AD-A186 360 CENTRIFUGAL AND NUMERICAL MODELING OF BURIED STRUCTURES 1/3
VOLUME 2 DYNAMIC..(U) COLORADO UNIV AT BOULDER DEPT OF
CIVIL ENVIRONMENTAL AND ARCH.. C SHIN 14 JUL 87
UNCLASSIFIED AFOSR-TR-87-1446 $AFOSR-84-0300 F/G 19/9 NL

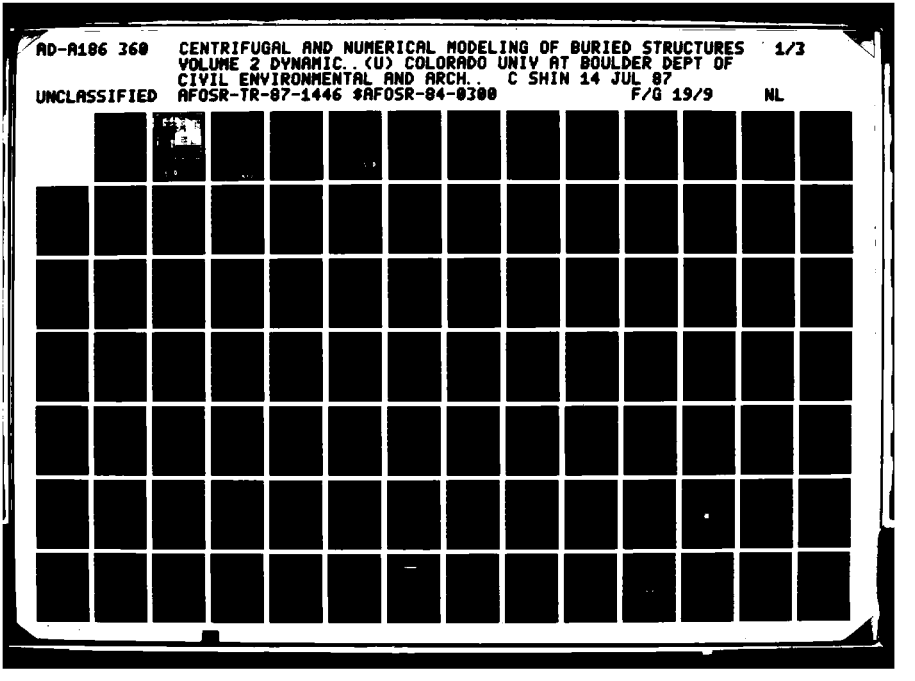

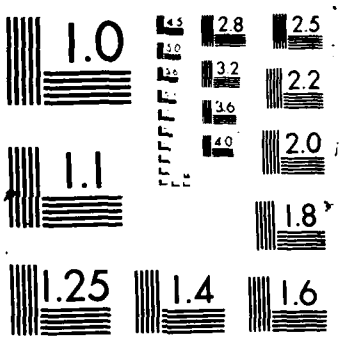
1.0
1.1
1.25
1.4
1.6
1.8
2.0
2.2
2.5
2.8
3.2
3.6
4.0

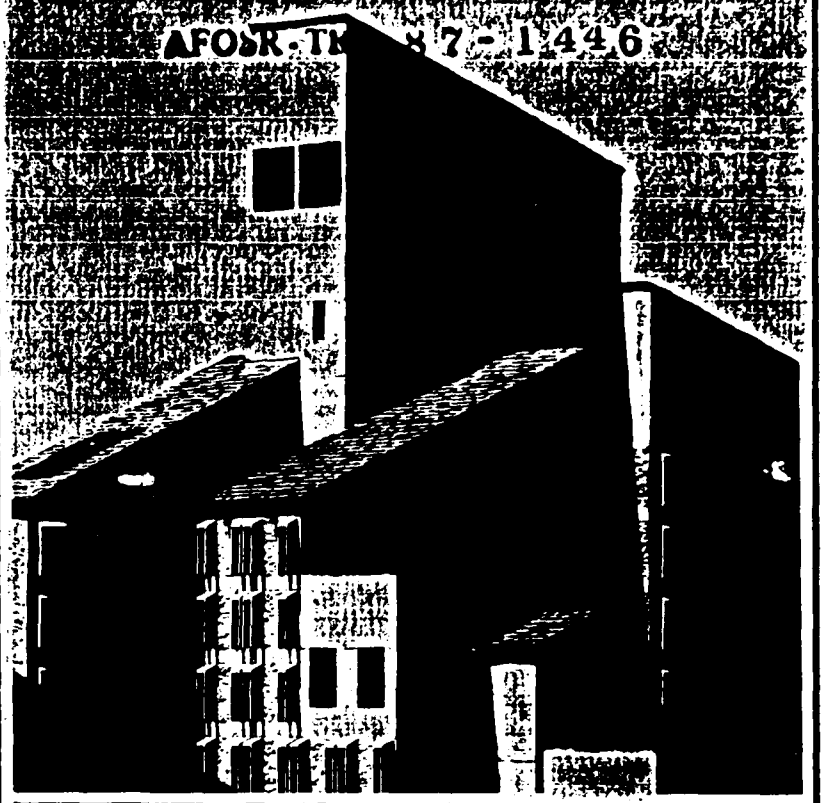

Department of Civil, Environmental, and Architectural Engineering

University of Colorado, Boulder
Box 428
Boulder, CO 80309

REPORT DOCUMENTATION PAGE

1a. REPORT SECURITY CLASSIFICATION Unclassified	1b. RESTRICTIVE MARKINGS
2a. SECURITY CLASSIFICATION AUTHORITY	3. DISTRIBUTION / AVAILABILITY OF REPORT Approved for public release; distribution is unlimited.
2b. DECLASSIFICATION / DOWNGRADING SCHEDULE	
4. PERFORMING ORGANIZATION REPORT NUMBER(S)	5. MONITORING ORGANIZATION REPORT NUMBER(S) AFOSR-TR- 87-1446
6a. NAME OF PERFORMING ORGANIZATION University of Colorado 6b. OFFICE SYMBOL (*If applicable*) CEAE Dept.	7a. NAME OF MONITORING ORGANIZATION AFOSR/NA
6c. ADDRESS (*City, State, and ZIP Code*) Civil, Environmental & architectural Engr. Campus Box 428, Boulder, CO 80309-0428	7b. ADDRESS (*City, State, and ZIP Code*) Bldg. 410 Bolling AFB, DC 20332-6448
8a. NAME OF FUNDING / SPONSORING ORGANIZATION Air Force Office of Scientific Research 8b. OFFICE SYMBOL (*If applicable*) AFOSR/NA	9. PROCUREMENT INSTRUMENT IDENTIFICATION NUMBER AFOSR-84-0300
8c. ADDRESS (*City, State, and ZIP Code*) Bldg. 410 Bolling AFB, DC 20332-6448	10. SOURCE OF FUNDING NUMBERS PROGRAM ELEMENT NO: 61102F; PROJECT NO: 2302; TASK NO: C1; WORK UNIT ACCESSION NO:
11. TITLE (*Include Security Classification*) (U) Centrifugal and Numerical Modeling of Buried Structures; Vol. 2: Dynamic Soil-Structure Interaction.	
12. PERSONAL AUTHOR(S) Shin, Charng-Jeng	
13a. TYPE OF REPORT Final 13b. TIME COVERED FROM _____ TO _____	14. DATE OF REPORT (*Year, Month, Day*) 7/14/87 15. PAGE COUNT 251
16. SUPPLEMENTARY NOTATION	

17. COSATI CODES		
FIELD	GROUP	SUB-GROUP

18. SUBJECT TERMS (*Continue on reverse if necessary and identify by block number*)
Soil-structure interaction; airblast loading simulator; dynamic stress gage; finite element method.

19. ABSTRACT (*Continue on reverse if necessary and identify by block number*)

Soil-structure interaction under blast laoding was investigated both experimentally in 10 g-ton centrifuge and analytically by finite element simulation. In the centrifuge experiments, circular pipes made of micro-concrete were buried in a dry sand and tested in the centrifuge to simulate the effects of gravity-induced overburden stresses which played a major role in controlling the soil stiffness and, subsequently, the response of the pipe.

The blast laoding was simulated by a pressure pulse generated by rupturing a burst disc in an impact generator. Surface stress gages and contact stress gages both made of poluvinylidene fluoride were built and caligrated to measure air blast magnitudes and contact pressures.

The centrifuge experiments provided insight into the dynamic response of buried pipes and a data base for the verification of numerical results. These results were obtained by linear and non-linear finite element analyses of the experiments duplicating the surface overpressure loading. The suitability of constitutive relations (cont'd on reverse)

20. DISTRIBUTION / AVAILABILITY OF ABSTRACT ☒ UNCLASSIFIED/UNLIMITED ☐ SAME AS RPT ☐ DTIC USERS	21. ABSTRACT SECURITY CLASSIFICATION Unclassified
22a. NAME OF RESPONSIBLE INDIVIDUAL Dr. Spencer T. Wu	22b. TELEPHONE (*Include Area Code*) (202) 767-6962 22c. OFFICE SYMBOL NA

ABSTRACT (cont'd)

for both soil and micro-concrte were verified by conparing test results and analysis. The effects of soil arching around the buried pipe was also delineated from both experiment and analysis.

2

CENTRIFUGAL AND NUMERICAL MODELING OF BURIED STRUCTURES

Vol. 2

DYNAMIC SOIL-STRUCTURE INTERACTION

by

Charng-Jeng Shin

TABLE OF CONTENTS

LIST OF TABLES

LIST OF FIGURES

CHAPTER I

INTRODUCTION

1.1 Statement of Problem

The problem of soil-structure interaction has been studied since the time of Rankine (1862) and Coulomb (1776). The former developed the famous Rankine active and passive earth pressure coefficients to account for movements of the soil behind a retaining wall through the limiting equilibrium conditions. At a time 86 years earlier than Rankine, Coulomb recognized that the friction between the wall and the backfill affects the pressure distribution on the wall.

In this century, the interaction between a buried structure and its surrounding soils became an important issue, since more underground structures were designed and larger as well as more expensive structures were constructed. These included traffic tunnels for highways, railways and subways; drainage lines; pipe lines; and protective shelters.

The loads imposed on a buried structure depend on the stiffness properties of both the structure and the surrounding soil. The stiffness mismatch of these

materials results in an indeterminate problem in which the pressures transmitted from the soil onto the structure produce deflections that in turn determine the pressures. The term "interaction" is used because of this indeterminate effect.

The most important component in the design of a soil-structure system is the load carrying capacity of the underground structure. The design methods developed in the past are based on the analysis of arching effects which are believed to be the dominating factor in the problem of soil-structure interaction. The arching effects around a buried structure are similar to that which occur at the back of a retaining wall; however, the former case is far more complicated to be quantified by just considering the passive and active states of soil.

The factors affecting the arching effects around a buried structure include the properties of the soil and the structural material, the shape of the structure, the burial depth of the structure, the friction at the soil-structure boundary, and the magnitude as well as the type of loading, that is, static or dynamic loading. The latter type of loading brings a new dimension to the indeterminacy of the problem. For geotechnical engineers, soil-structure interaction under dynamic loading is a new and challenging problem.

1.2 Solution Schemes

In this research, dynamic soil-structure interaction is studied both experimentally in a centrifuge and analytically by dynamic finite element analyses.

Testing a sub-scale model of a soil-structure system in a centrifuge is necessary if the response of the prototype is to be represented correctly by the response of the model. The behavior of a soil depends on the stress level. For most earth structures, this stress is generated primarily by the self-weight of the soil. In order to correctly simulate the stresses in the prototype, a geometrically similar model must be subjected, in a centrifuge, to an increased gravity whose ratio to earth's gravity is the inverse of the length scale by which the model is scaled down from the prototype.

Centrifuge modeling technique is also often used in conjunction with constitutive modeling and numerical analyses. In this case, the centrifuge test results become a basis for calibrating the numerical modeling or validating analytical schemes. Since the soil properties and the boundary conditions of a centrifuge model can be easily controlled in the laboratory, centrifuge modeling is ideally suited for collecting the data basis for calibrating numerical analysis. Once validated,

numerical analysis can be employed for prototype prediction.

Numerical analysis, in itself, has advantages in dealing with the studies of soil-structure interaction. For instance, the non-homogeneity of the system can be simulated, the non-linear behavior of materials can be represented, the interface movement can be mimicked, and the construction sequence can be followed. In addition, parametric studies can be easily performed by conducting numerical analysis.

1.3 Problem Description and Research Objectives

To execute the philosophical approach of linking centrifuge modeling with numerical analysis of a soil-structure system, circular micro-concrete culverts buried in a dry sand is chosen for the model study, as shown in Figure 1.1. An airblast load is applied to the soil surface. The failure mode of the culvert as well as the pressures transmitted by the soil onto the culvert are of primary interest in this study.

The objectives of this research are as follows:

(1) To develop a centrifuge model, which includes the model itself and an impact generator for the application of the airblast in the centrifuge.

(2) To develop two types of dynamic stress gages, one to measure the overpressure generated

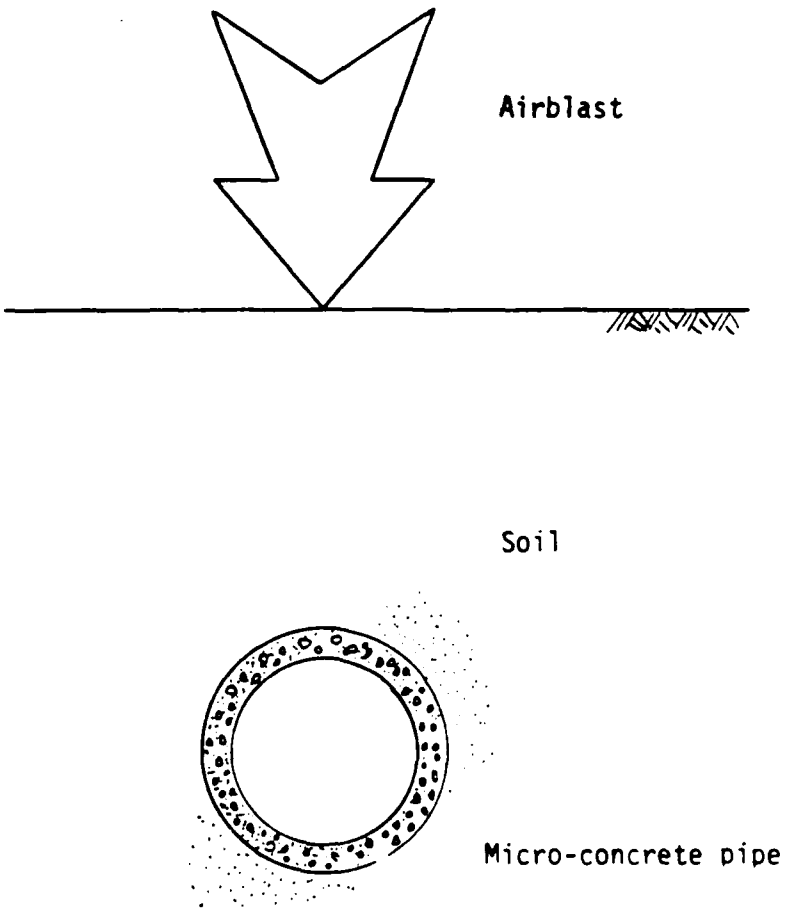

Figure 1.1 Plot shows a soil-culvert system subjected to an airblast on the soil surface

by the airblast, and the other to measure the pressures acting on the culvert.

(3) To initiate a parametric study using the centrifuge model test.

(4) To analyze centrifuge experiments by linear and non-linear dynamic finite element analyses, compare and interpret the results.

CHAPTER II

LITERATURE REVIEW

The subject of soil-structure interaction has been of technical interest for many decades. Numerous efforts have been devoted to this problem through research, analysis and testing. The accumulated knowledge from the past studies has contributed to the understanding of this complicated interaction phenomenon. In some cases, criteria have been developed to assist in the design of underground structures.

During and after the Second World War, the construction of military protective structures heightened the attention to soil-structure interaction under dynamic loadings. Since the design criteria developed before this time were based on static loadings, correlation between these two types of loading was needed. Research on the properties and behavior of the materials under dynamic loadings has been conducted since then.

After the 1950's, the advent of the digital computer has made numerical analyses feasible in solving the problems of soil-structure interaction. Since then,

sophisticated computer codes have been developed, in which the non-linear material properties and the interface behavior can be incorporated.

This chapter gives a review of the literature on the subject and is divided into three parts: (1) the study of soil-structure interaction under static loadings, (2) the study of soil-structure interaction under dynamic loadings, and (3) finite element analysis for soil-structure interaction.

2.1 Soil-Structure Interaction under Static Loadings

Basic knowledge on the subject was accumulated through the studies of soil-structure interaction under static loadings. A brief historical review on the development of soil-structure interaction concepts was provided by Linger (1972) who divided the review into two major areas: the development of concepts in classical culvert design and the development of phenomenological concepts in the response of buried structures. To assist in better understanding of the subject, a review following this division is presented.

2.1.1 Classical Design Concepts

The design of buried culverts was initiated in the early 1900's. Since then, the design of underground structures has been subdivided into a few general categories based on culvert flexibility, configuration,

and size. A structure would be classified as an arch or circular or box culvert based on shape, and the design procedures would be classified as rigid or flexible. The former usually represents reinforced concrete pipes, and the latter represents corrugated steel pipes. Each of these subdivisions had empirical design methods associated with it.

2.1.1.1 Design of Rigid Pipes

Marston (1913) was the first to recognize that the loading on an underground structure is dependent on the interaction of the structure and the surrounding soil. He published the important Marston theory at the Iowa State University. Spangler and Handy (1982) describe the basic concept of Marston theory as follows:

> "The basic concept of the theory is that the load due to the weight of the soil column above a buried pipe is modified by arch action in which a part of its weight is transferred to the adjacent side prisms, with the result that in some cases the load on the pipe may be less than the weight of the overlying column of soil. Or, in other cases, the load on the pipe may be increased by an inverted arch action in which load from the side prisms is transferred to the soil over the pipe. The key to the direction of load transfer by arch action lies in the direction of relative movement or tendency for movement, between the overlying prism of soil and the adjacent side prisms."

Figures 2.1a and 2.1b show a buried conduit and the arch action that may develop.

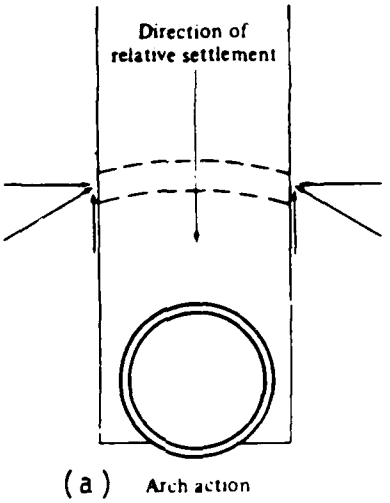

Figure 2.1 Plots show the arching action of a soil-pipe system (After Spangler and Handy, 1982)

Marston (1913) derived the maximum loads on ditch conduits by examining an element of soil as shown in Figure 2.2. The force equilibrium of the element requires that

$$V + dV + 2K\mu' V\, dh/B_d = V + r\, B_d\, dh \qquad (2.1)$$

where V = load on conduit,

B_d = horizontal width of ditch at top of conduit,

r = unit weight of back fill material,

K = coefficient of lateral to vertical pressure,

= coefficient of friction between fill material and sides of ditch.

The solution of Equation 2.1 is

$$V = C\ r(B_d)^2 \qquad (2.2)$$

where C is a load coefficient. Based on different assumptions, many researchers in the past have developed different load coefficient. A review of these is presented in Table 2.1.

2.1.1.2 Design of Flexible Pipes

The design of flexible conduits was first developed by the American Railway Engineering Association in 1926. The design criteria were based on empirical equations which neither considered the

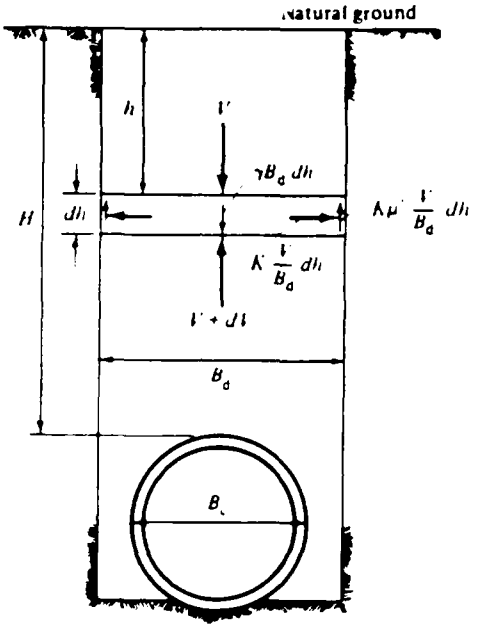

Figure 2.2 Free body diagram used in Marston theory (After Spangler and Handy, 1982)

Table 2.1

Summary of Load Coefficient
(After Matyas and Davis, 1983)

Equation	Remarks
$C = \exp[2K_a \mu \ H/B] - 1/(2K_a \mu)$	Spangler; complete pro-jection; $K_a \mu = 0.19$
$C = \exp[2K \mu \ H_e/B] - 1/(2K_a \mu) + [H/B - H_e/B] \exp[2K_a \mu \ H_e/B]$	Spangler; incomplete projection; $K_a \mu = 0.19$
$C = 1.961 \ H/B - 0.934$	Standand of American Water Works Association; $H_e/B = 1.75$; r_{sd} p=0.75
$C = H/B[0.289 \ H/B + 1]$	Vertical slip surface; $K_o = 0.5$; $\phi = 30^o$.
$C = H/B[0.577 \ H/B + 1]$	Frustum; $\theta = 45 + \phi/2$; $\phi = 30^o$.
$C = H/B[0.433 \ H/B + 1]$	Ladanyi and Hoyaux; $\phi = 30^o$.
$C = H/B[0.548 \ H/B + 1]$	Meyerhof and Adams; shallow, $H/B < 4$; $K' = 0.95$; $\phi = 30^o$.
$C = H_e/B[0.584(2H/B - H_e/B) + 1]$	Meyerhof and Adams; deep, $H/B > 4$; $K' = 0.95$; $\phi = 30^o$.
$C = H/B \ N_q$	Das and Seeley; length-width ratio =5; H/B = 1 3 5 8; N_q = 1.8 3.5 5.0 6.5
$C = H/B \ F_q$	Vesic; H/B = 0, 0.5, 1.0, 1.5 2.5, 5.0; F_q = 0, 0.45, 1.08, 1.45, 2.03, 3.30

where

K_a = coefficient of active earth pressure,

Table 2.1 (continued)

K' = nominal uplift coefficient of earth pressure on a vertical plane,

K_o = at-rest coefficient of lateral earth pressure,

H = vertical distance from the top of conduit to the soil surface,

H_e = vertical distance from the top of conduit to the plane of equal settlement,

r_{sd} = the settlement ratio,

p = the projection ratio,

N_q = a function a H/B as given in Table 2.1, and

F_q = breakout factor as given in Table 2.1

characteristic of the soil nor the concept of soil-structure interaction.

During the 1930's, the increase in highway construction increased the use of larger and more expensive drainage systems. Therefore, a more rational concept for the design of flexible pipes was needed. Spangler, a former student of Marston, recognized this need and published his Iowa formula in 1941. The formula predicted the deflection of a buried flexible pipe. Later, the first well-defined soil-structure interaction concept was formulated by Spangler, and presented by Spangler and Handy (1982) as follows:

> "The [flexible] pipe itself has relatively little inherent strength, and a large part of its ability to support vertical load must be derived from the passive pressures induced as the sides move outward against the soil. The ability of a flexible pipe to deform readily and thus utilize the passive soil pressure on the sides of the pipe is its principal distinguishing structural characteristic and accounts for the fact that these relatively lightweight, low-strength pipes can support earth fills of considerable height without showing evidence of structural distress. It is apparent from these considerations that any attempt to analyze the structural behavior of the flexible conduits must take into account the soil at the sides as an integral part of the structure, since such a large proportion of the total supporting strength is attributable to the side material."

Based on the above concept, the following expression was developed for computing the deflection of a flexible pipe. It was the first attempt to require the

evaluation and inclusion of soil properties in design procedures.

$$x = \frac{K W r^3}{EI - 0.061 (E')^3} \qquad (2.3)$$

where x = increase in horizontal diameter of the pipe,

K = a parameter which is a function of the bedding angle,

W = vertical load per unit length of the pipe at the level of the top,

r = mean radius of the pipe,

E = modulus of elasticity of the pipe material,

I = moment of inertia of the cross-section of the pipe, and

E' = modulus of soil reaction, a property of soil.

Deflection of the corrugated metal pipe, as computed from Equation 2.3 is recommended not to exceed 5% of the nominal pipe diameter.

White and Layer (1960) proposed the ring compression theory for the design of flexible pipes. The theory assumes that: (1) the compression in the wall of the pipe is equal to the overburden pressure at the crown of the pipe multiplied by the radius of the pipe; and (2) failure occurs by the crushing of the pipe wall.

Watkins (1960) conducted model tests to verify the ring compression theory. He found that under certain soil conditions and with certain values of pipe wall stiffness, the pipe failed by ring compression deformation, otherwise it failed by ring buckling of the wall. He also indicated that for a certain soil-pipe system there exists a buckling envelope separating the zone of deformation and buckling. As shown in Figure 2.3, the location of the buckling envelope depends on the properties of the soil-pipe system. In addition, the decreasing trend of the plots indicate the occurrence of stress release at the crown of the pipes.

By the middle 1960's, all the design schemes for the buried pipes were more or less developed from the Marston theory. The problem of soil-structure interaction had been defined but a rigorous analysis did not, as yet, exist.

Nielson (1967) introduced the concept of arching theory to find the vertical load on the buried pipes. He abandoned the flat element used by Marston (see Figure 2.2) and proposed a circular arch which was supported by two inclined planes. These planes had the maximum shear stress and the locations of the planes could be determined by the theory of elasticity. Figure 2.4 shows the free-body diagram used in the analysis. He also presented experimental and analytical results which were

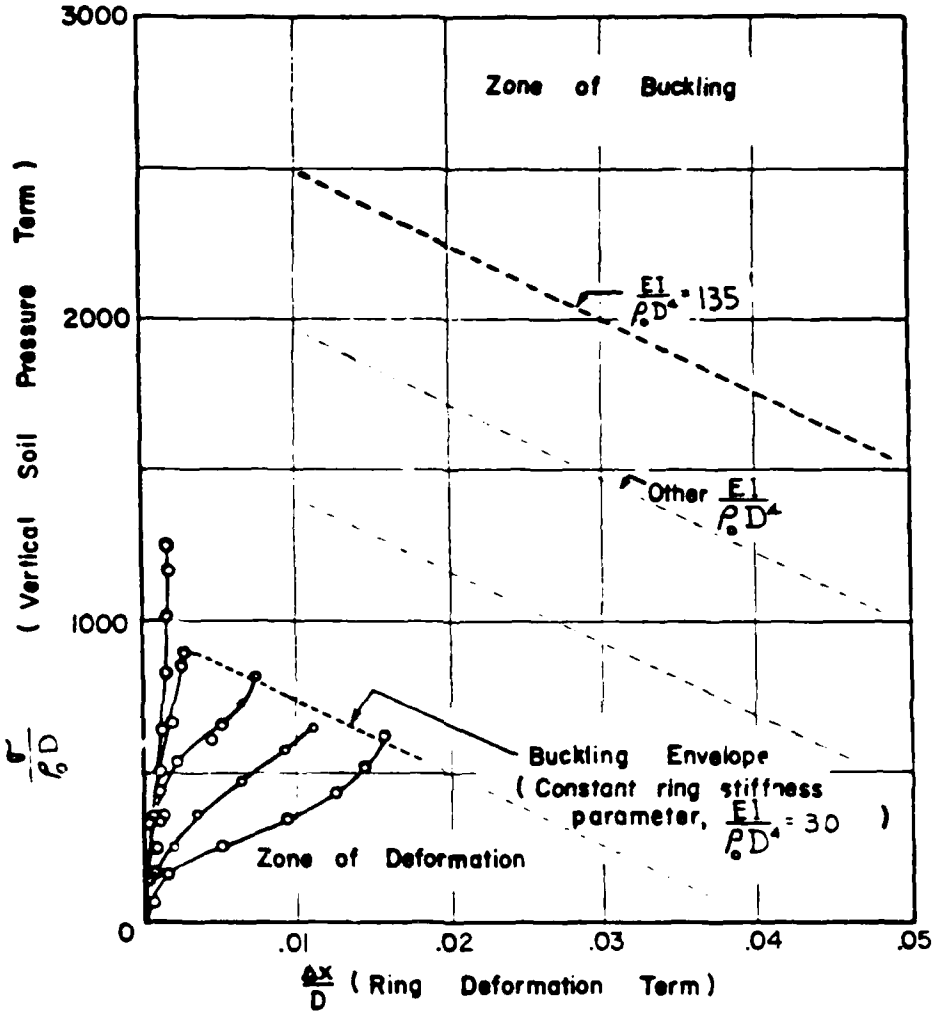

Figure 2.3 Plots show the buckling envelope of buried pipes. (After Watkins, 1960)

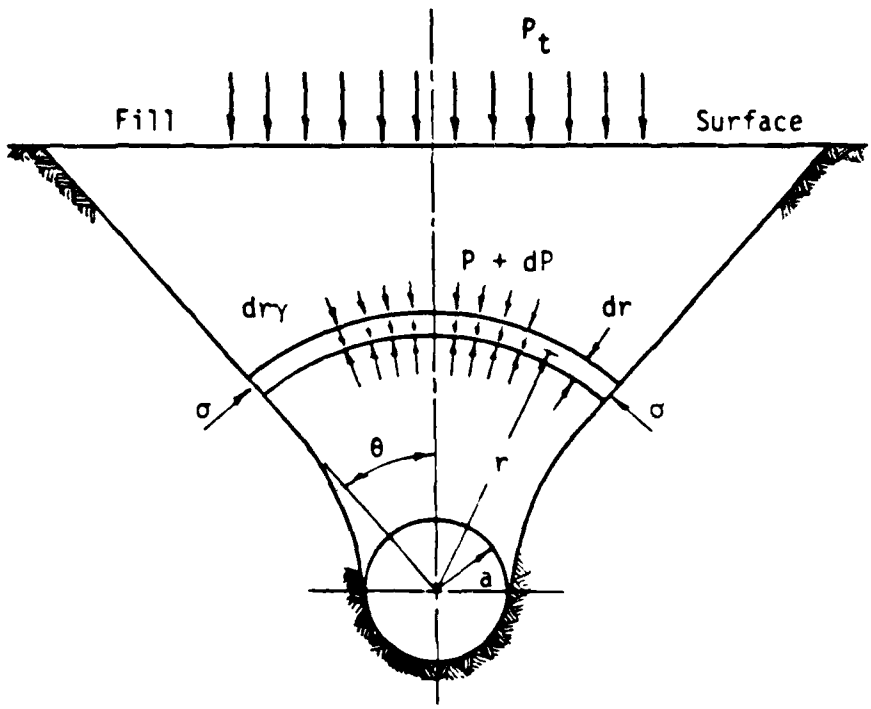

Figure 2.4 Free body diagram used in Nielson's theory (After Nielson, 1967)

in agreement. Nevertheless, little use has been made of this novel diversion from the classical Marston analysis.

2.1.2 Phenomenological Concepts-Study of Arching Effect

Arching effect has been recognized as the dominating phenomenon controlling the stress distribution in a soil-structure system subjected to loads. Terzaghi (1943) defined arching as follows:

> "If one part of the support of a mass of soil yield while the remainder stays in place the soil adjoining the yielding part moves out of its original position between adjacent stationary masses of soil. The relative movement within the soil is opposed by a shearing resistance within the zone of contact between the yielding and the stationary masses. Since the shearing resistance tends to keep the yielding mass in its original position, it reduces the pressure on the yielding part of the support and increases the pressure on the adjoining stationary part. This transfer of pressure from a yielding mass of soil onto adjoining stationary parts is commonly called the arching effect, and the soil is said to arch over the yielding part of the support. Arching also takes place if one part of a yielding support moves out more than the adjoining parts."

There have been many experimental studies to examine stress distribution and arching, the most famous being conducted by Terzaghi (1936) using a deflecting trapdoor in the base of a soil bin. He found that the pressure acting on a long trapdoor was independent of the state of stress in the soil located more than two or three door widths above the door. The experiments were concerned with a plane strain condition, with only two

plane surfaces of sliding. Figure 2.5 shows the results of one of Terzaghi's trapdoor tests.

McDonough (1959) studied the arching effect and concluded that an intermediate liner of very low modulus should be placed between a buried structure and the surrounding medium so that arching would develop around the structure and thus release the stress acting on the structure.

Whitman, et al., (1962) conducted a series of experiments on domes in sand. They observed that the rigidly supported structure would experience pressures greater than the surface pressure until the domes failed by yielding at the support. The resulting crown deflection caused a stress relief of about half of the load on the structure.

McNulty (1964) investigated the arching in sands using a circular trapdoor mounted at the bottom of a circular soil container. Figure 2.6 summarizes the test results. The curves in the figure show the relationship between the ratio of the average pressure on the door to the surface air pressure and the ratio between deflection and diameter of the door. The active arching in the figure occurs when the trapdoor moves away from the soil, whereas the passive arching occurs when the trapdoor moves into the soil. It can be seen from the figure that the pressure on the trapdoor reduces rapidly

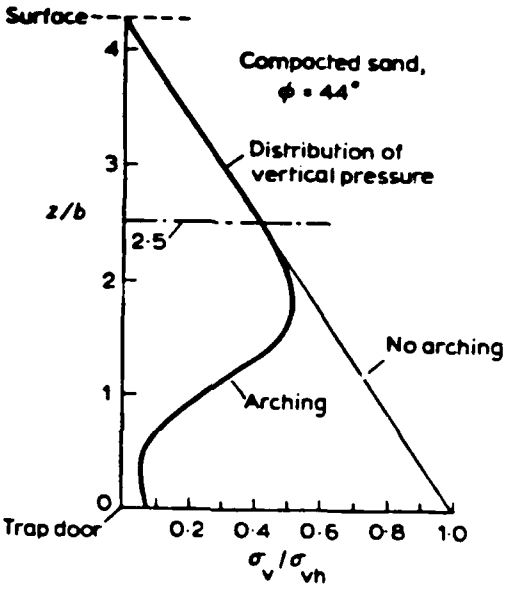

Figure 2.5 Plot of the vertical stress in Terzaqhi's trapdoor test (After Bulson, 1985)

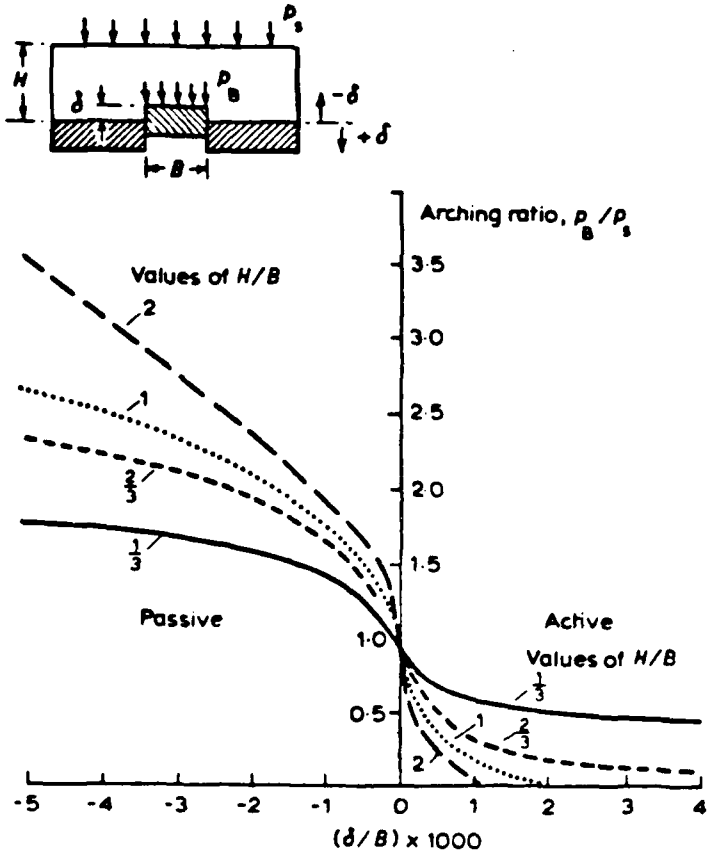

Figure 2.6 Test results of McNulty's trapdoor experiment (After McNulty, 1964)

to zero in the case of active arching and increase slowly to a ultimate value in the case of passive arching.

Getzler and Komornik (1968) investigated the arching phenomenon using a 10 by 20 by 40 cm model and a poorly graded medium sand. The study considered several parameters: the shape of the structure, the depth of soil cover, and the magnitude of surface load. The results of the tests indicated that:

1. Arching above structures with protruding roofs, that is, triangular or arched, is greater than above flat structures; it increases with the height of the roof, but this increase is partially a matter of definition of appropriate depth of the protruding shape. This influence vanishes with increasing depth.

2. The amount of arching increases with depth of cover but tends toward a definite value.

3. The amount of arching increases with the external load; the rate of this increase varies with depth.

Höeg (1968) conducted model tests with techniques to measure the contact stresses. The structure was a cylinder that consisted of twelve segments each supported by a load cell. The normal stress acting on the structure was measured directly. The test results indicated that for a perfectly rigid

cylinder, buried deeper than one cylinder diameter, the crown pressure was approximately 1.5 times the applied surface pressure, and the side pressure at the springline was 0.25 times the applied surface pressure and was independent of the soil modulus.

Allgood and Takahashi (1972) defined arching A as:

$$A = 1 - p_i/p_v \qquad (2.4)$$

where P_i is the vertical pressure on the structure at the crown, and P_v is the free field vertical stress at the elevation of the crown. Free field stress is defined as the stress in the soil when the structure is not present. In Equation 2.4, $A = 0$ if no arching or no change in the state of stress occurs because of the presence of the structure, $A < 0$ if there exists negative arching or stress concentration, and $A > 0$ indicates positive arching or stress relief.

In addition to the quantitative definition of arching, Allgood and Takahashi (1972) proposed a quantitative definition of flexible and rigid structures as follows:

Flexible:	$M_s D^3/EI > 10^4$
Intermediate:	$10 \leq M_s D^3/EI \leq 10^4$
Rigid:	$M_s D^3/EI < 10$

where E = the Young's modulus of the structural material,

I = the moment of inertia of the pipe,

M = the secant modulus of the soil, and

D = the outer diameter of the pipe.

They also indicated that structures in the rigid category will experience negative arching, whereas structures in the flexible category will experience positive arching.

2.2 Soil-Structure Interaction under Dynamic Loading

During and after the Second World War, soil-structure interaction under dynamic loading has received considerable attention in connection with the design of underground structures subjected to nuclear or high explosive blasts. Due to the inertial effect in a dynamic environment and the strain rate effect of the material involved, the procedures developed for static loadings in the past cannot be employed for the design of these protective structures. Thus, a new scheme in soil-structure interaction analysis and design was necessary to include the aforementioned effects.

Generally, a large explosion produces three mechanical phenomena (Whitman, 1970): (1) formation of a crater; (2) generation of an airblast wave which sweeps outward over the ground surface; and (3) generation of

the stress wave in soils. Figure 2.7 illustrates these phenomena.

The size of the crater is itself of interest in geotechnical engineering. However, the dynamic stresses in the soils are of more interest in the study of soil-structure interaction because these stresses cause the earth to deform, thus causing forces upon, and movements of, the structures located within the earth.

Past research efforts related to this subject can be divided into two general categorizes: characteristic studies and experimental studies. Studies of the first category was concerned with the propagation and attenuation of pressure waves in soils and dynamic properties of soils. Studies of the second category concentrated on using model tests to study the effects of wave induced loadings.

2.2.1 Characteristic Studies

2.2.1.1 Propagation and Attenuation of Stress Waves in Soils

An explosion on a soil surface will generate a stress wave in the soil immediately at the point of explosion. This stress wave is known as the directly induced ground shock. In addition, when the airblast sweeps out on the soil surface, the pressure in the air

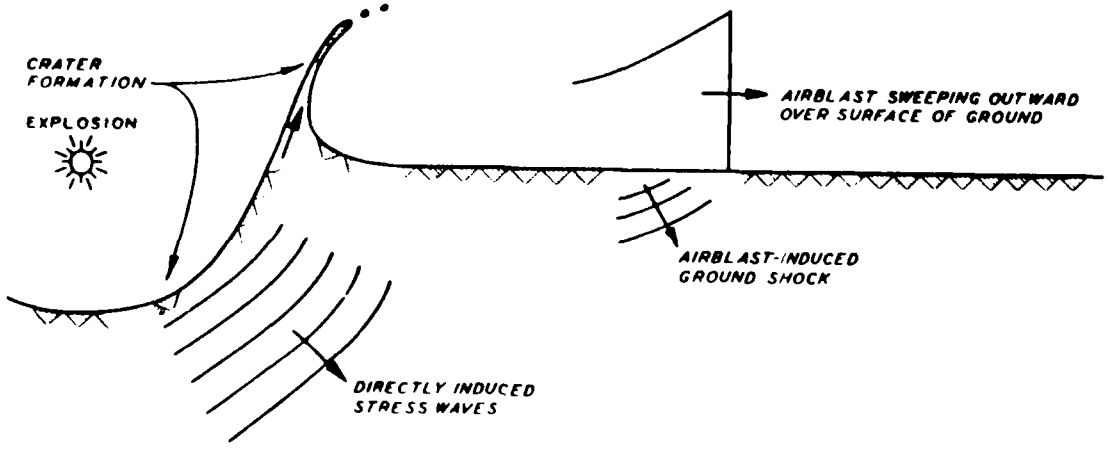

Figure 2.7 Plot shows the mechanical phenomena generated by a blast loading. (After Whitman, 1970)

produces a stress wave in the soil. This stress wave is known as airblast induced ground shock (Whitman, 1970)

Both the directly induced ground shock and the airblast induced ground shock travel in soils at seismic velocities. However, the directly induced ground shock propagates radially in the soil, whereas the propagation of the airblast induced ground shock depends upon the speed of the airblast travelling in the air.

There are three possible cases when the airblast induced ground shock is generated (Das, 1983):
(1) At a small distance from ground zero, the speed of the airblast overpressure front, V, is large. If V is greater than the dilatational seismic velocity, V_p, it is referred to as a superseismic case. This is shown in Figure 2.8a. The slopes of the dilatational wave front, V_p, and the shear wave front, V_s, with the horizontal ground surface is given by:

$$\alpha_1 = \sin^{-1}(V_p/V) \tag{2.5}$$

$$\alpha_2 = \sin^{-1}(V_s/V) \tag{2.6}$$

(2) As the overpressure front moves forward, its velocity, V, gradually decrease. When the condition, $V_s < V < V_p$, is reached, it is called the transeismic case, as shown in Figure 2.8b. (3) At larger distances, the blast front velocity, V, becomes less than V_s. This condition is called subseismic case.

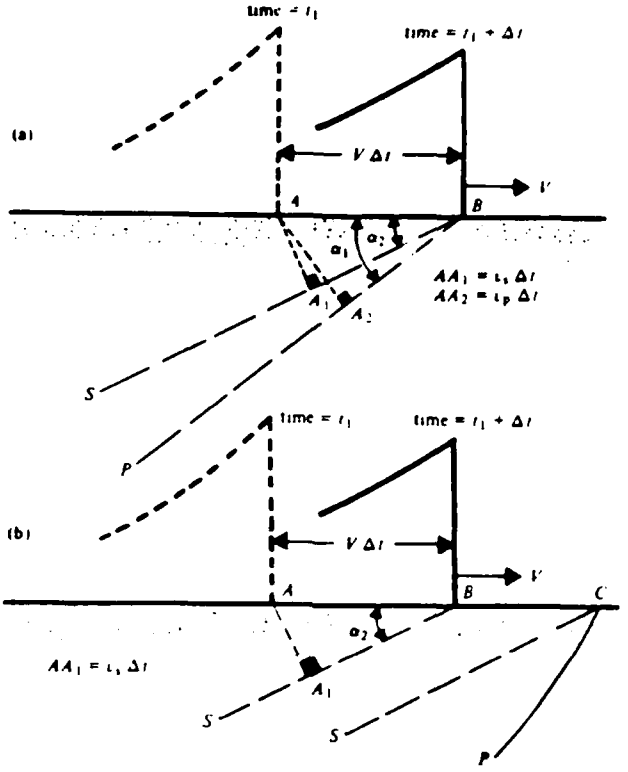

Figure 2.8 Propagation of airblast induced ground shock (a) Superseismic case (b) Transeismic case (After Das, 1983)

Since regions in the near vicinity of ground zero are especially of interest with regard to protective construction, the superseismic region is of special concern. Note that when $V/V_p = 2.25$ (which is not uncommon for high explosions), the angle α_1 is equal to 26 degrees. The motion are predominantly vertical.

Whitman (1970) compared the superseismic case of blast wave with $V/V_p = 2.25$ to a one-dimensional confined compression case. The results showed that the vertical stresses and motions were similar for the two cases and they differed mostly with regard to the horizontal motions. However, it was also shown that the horizontal motions in the superseismic case could be approximated by multiplying the vertical component by $\tan(\alpha_1)$. This comparison suggested that the simpler one-dimensional problem might be used by estimating the response in the more complicated superseismic problems.

Newmark (1964) discussed the attenuation of the pressure wave with depth. Figure 2.9 shows a typical pressure history curve for an explosion. At the soil surface, the response includes a short rise-time followed by an exponential decay. However, when the wave front propagates in the soil, the rise-time increases and the pressure history curve becomes smoother in shape. Newmark also found that for most pressures, the

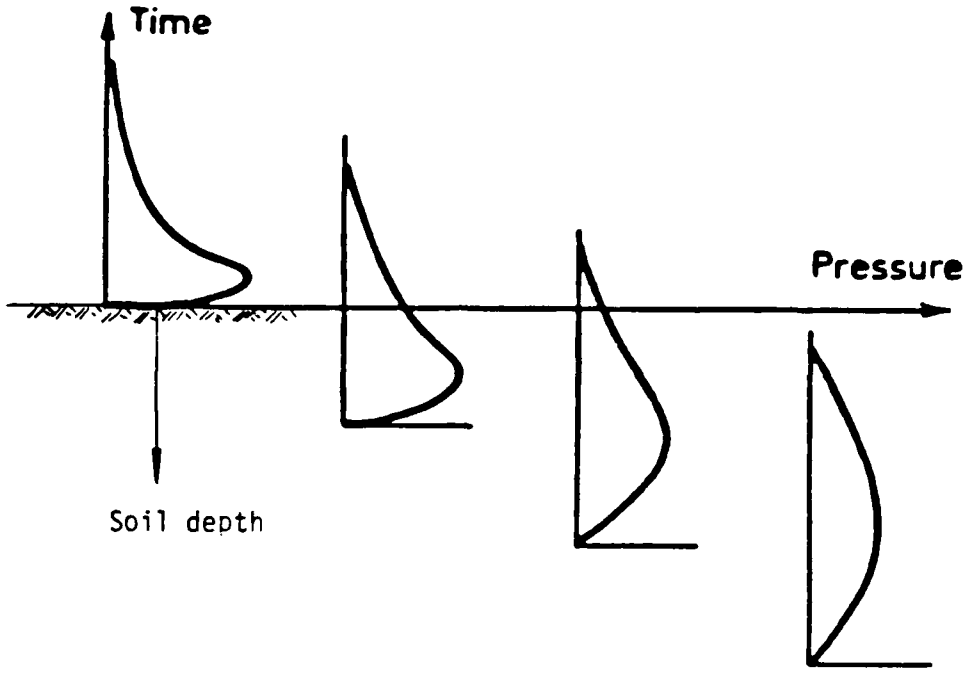

Figure 2.9 Attenuation of pressure wave with depth. (After Newmark, 1964)

impulse remains fairly constant even though the shape changes.

2.2.1.2 Dynamic Properties of Soils

The most distinct dynamic property of soils is the strain rate effect, that is, the strength and moduli of soils increase with increased strain rate. This effect introduces a new factor in the analysis of dynamic soil-structure interaction. In the past decades, this effect has been investigated by many researchers (e.g.,Seed and Lundgren (1954), Moore (1963), Whitman (1963), Whitman and Healy (1963), Schindler (1968), Jackson (1980)). However, the fundamental mechanisms causing this effect are still not clear (Jackson, 1980).

Due to its direct linkage to the velocity of compression wave in soils, the constrained modulus has an especially significant role in the problem of dynamic soil-structure interaction. For practical applications, the laboratory tests should aim at measuring the constrained modulus under the stress level and loading rate of interest.

It has been found that when the rise-time of loading is reduced to 1 millisecond or less, the constrained modulus increased drastically (Jackson, 1980). However, when dynamic loading with rise-time of 1 millisecond or less is applied to a test specimen, it is possible that the rate of stress application overcomes

that of stress wave propagation velocity in the specimen. Consequently, non-uniform strains are produced over the thickness of the specimen, hence making the results either useless or difficult to interpret.

Another concern related to testing with sub-millisecond rise-time is the inertial effect. That is, the inertial force in the specimen may reduce the applied stress, so that the actual stress in the specimen is smaller than that measured.

Das (1983) indicated that there is always a great discrepancy between the modulus measured in a compression test and that back-calculated from an ultrasonic or resonant column test. In order to account for this discrepancy and to select the proper modulus for the calculation of soil movement, Wilson and Sibley (1962) proposed to use confined compression test results for shallow depth of fields and to use the vibration test results for the greater depths. Moore (1963) proposed using the modulus from the confined compression test after three repeated cycles of load.

2.2.2 Experimental Studies

After the 1960's, the construction of blast simulators and horizontal, as well as vertical shock tubes, enabled a number of experimental studies to be carried out. These studies investigated the static and dynamic behavior of thin-wall cylinders in sand and

clay. Although these model tests were conducted at 1 g condition and hence the body forces, present in their prototypes were not accounted for, they provided valuable information about the different responses of sands and clays to static and dynamic loadings. This section summarizes the most important findings from these studies.

Dorris (1965) tested horizontally buried aluminum pipes using a blast simulator which can generate uniform surface overpressure as high as 500 psi in about 3 milliseconds. He summarized his test results in a plot of surface pressure versus average springline thrust. This plot is shown in Figure 2.10. It is noticed that the values of the thrust for a given surface overpressure are about 20% greater for rapid loading than for static loading and that the overpressure to cause collapse is about 20% higher for rapid loading than for static loading. Test results on a stiffer pipe showed values of the thrust more than 50% greater for rapid loading than for static loading.

Dorris (1965) repeated identical tests at the U.S. Waterways Experiment Station using a smaller blast generator. The simulator can generate an overpressure of 150 psi in about 0.3 milliseconds. The tests results are shown in Figure 2.11. Note that the thrust at the springline increases with the speed of loading.

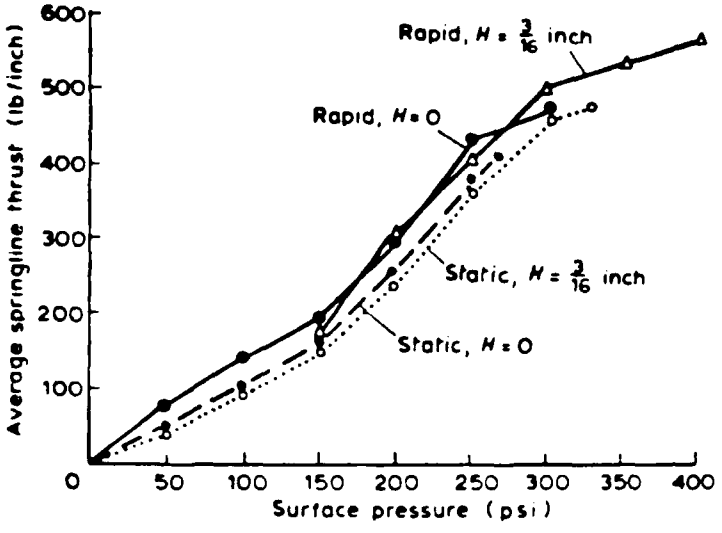

Figure 2.10 Surface pressure vs. average spring trust (After Dorris, 1965)

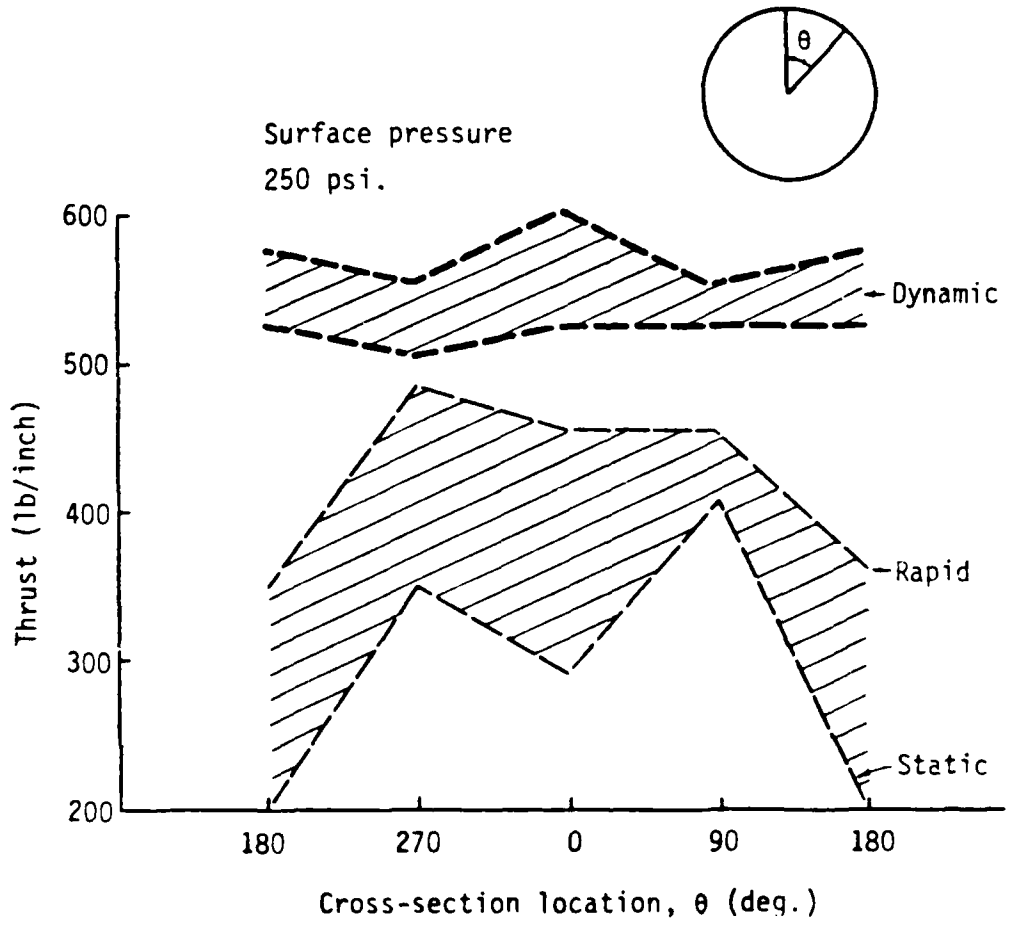

Figure 2.11 Plots show the trust increases with the increase of loading speed (After Dorris, 1965)

Albritton, et al., (1966) used the above test apparatus to test 6 inch diameter steel cylinders buried in a sand. They drew the following conclusions from the test results: (1) the dynamic strains are 20-40% higher than strains at an equivalent static load; (2) the cylinder responses at the 12 and 6 inch depths of burial were very similar; and (3) hoop strains were not a linear function of applied overpressure. Tensile strains tended to become constant for pressures greater than 100 psi and at least up to 350 psi.

A further series of tests were conducted jointly by Dorris and Albritton (1966) to examine the response of a 4 inch diameter, 18 inch long steel cylindrical tube. The model was used to simulate a prototype protective structure. The experiments were conducted in a dense, dry sand (dry density = 108.5 lb/ft^3), and a stiff, wet clay (wet density = 120 lb/ft^3, water content = 25%). The results of the tests indicated that: (1) the maximum hoop strains in the tube walls under dynamic loading were about 25% greater than the strains at the equivalent static loads; and (2) the strains in the conduit were much larger in clay than in sand at comparable pressures, and in both soils strain was a non-linear function of overpressure.

Bulson (1985) performed a series of tests on model thin-walled cylinders in a vertical shock tube

built at the Atomic Weapons Research Establishment. The tests utilized both brass and steel tubes in a sand and a clay under similar conditions of moisture and compaction. The most important conclusion from the tests was that the static collapse pressures in sand were about four times as large as in clay but the dynamic collapse pressure was about the same for both sand and clay.

2.3 Finite Element Analysis for Soil-Structure Interaction

Before the 1960's most culvert designs in the United States were based on semi-empirical methods. The shortcoming of these traditional design methods is the lack of proper representation of soil-structure interaction. Close-formed, plane strain solutions were developed to assist in the design of underground structures. But these methods cannot deal with complex boundary conditions nor can they incorporate non-linear material properties.

After the 1960's the application of the finite element method became the main trend of study. Numerous studies have been performed since then and the technique has improved from constant strain triangular elements with elastic material law to the present 3-dimensional elements and sophisticated plasticity material law.

In the 1970's, the American Concrete Pipe Association undertook a long term research project with the objective of developing finite element codes to conduct both analysis and design of buried culverts. The well-known program CANDE (Culvert ANalysis and DEsign) was developed with these objectives in mind (Katona, 1976).

The finite element code CANDE has quadrilateral or triangular elements for soil and thrust-bending elements for pipe. Interface behavior can be simulated by interface elements which allow for frictional sliding, separation, and rebonding. The stress-strain relation of soils can be described by incremental elastic model wherein the elastic moduli are dependent on current fill height or variable modulus model utilizing a modified version of the Hardin soil model. The latter model employs a variable shear modulus and variable Poisson's ratio which are dependent on maximum shear strain and hydrostatic pressure.

The advances of constitutive modeling of soil in the 1970's have made finite element analysis a even more powerful tool to solve various geotechnical problems. Duncan and Clough (1971) analyzed the construction of Port Allen Lock of Mississippi River by finite element analysis. Elastic material representation was used for concrete whereas both elastic and hyperbolic models (an

incremental linearly elastic model) were used for the soil. The construction was monitored by various instrumentations and the analytical prediction was checked during the construction. It was found that the analysis with linearly elastic soil model predicted the response poorly. On the other hand, the analysis with the non-linear soil model provided good predictions which included the heaving of soil during excavation, the settlement during construction, and the structural deflections after filling.

Corotis and Krizek (1976) conducted finite element analyses of buried concrete pipes. The soil was represented by piece-wise linearly elastic, plane strain quadrilateral and triangular elements. The soil elements were subtracted or added to simulated the sequence of excavation and backfilling. The modulus of the concrete elements was dependent on the major principal stress, and their tensile strength was a function of the specified ultimate compressive strength of the concrete. A cracking mechanism was incorporated into the pipe model to simulate the development of cracks upon loading. The study indicated that the change in diameter of the pipe compared well between the analysis and the field measurements.

Selig, et al., (1982) analyzed a buried concrete pipe by the non-linear finite element program SPIDA. The

concrete model in the program allows for the non-linear load-deformation relationship observed in three-edge bearing tests. The hyperbolic model was used for the stress-strain behavior of the soil. The conclusions of the study were: (1) The choice of soil model and values of soil parameters were important for accurate modeling of the soil-pipe interaction; (2) the overburden-pressure-dependent soil model often used in the past is not satisfactory because the model assumptions were inconsistent with the stress states at many locations in the soil.

Walters and Thomas (1982) used elasto-plastic finite element analysis to model shear zone localization. They conducted the Terzaghi's trapdoor experiment and compared the shear zone developed in the sand box to the analytical results. They demonstrated that elasto-plastic finite element analyses with Drucker-Prager type yield conditions and associated flow rules could only model initial shear zone development. However, when a non-associated flow rule was used the subsequent shear zone development could be accurately simulated.

Nelson and Goldstein (1984) used non-linear dynamic finite element analyses to study the blast wave reflections in soil from a buried, dome-shaped rigid structure. The study was conducted using TRANAL explicit

finite element code (Baylor and Wright, 1975; and Baylor et al., 1979). The constitutive law of the soil was described by the cap model (DiMaggio and Sandler, 1971; and Sandler and Rubin, 1979). The study demonstrated that the contact stress near the crown of the dome could be 4 times higher than the free field stress. On the other hand, the contact stress below the springline was smaller than the free field stress.

Townsend, et al. (1985) conducted linear and non-linear dynamic finite element analysis by the NONSAPC program. In the case of non-linear analysis, the Modified Duncan Model was used to represent the sand, while an orthotropic variable modulus model was used to represent the non-linear concrete behavior. The study indicated that non-linear finite element analyses of a buried structure subjected to blast loading produce higher stresses and displacements than linear analyses.

Ni (1986) studied soil-structure interaction using centrifuge modeling and finite element analyses. The centrifuge model consisted of a thin-walled metal tube buried in a moist silt. The model was spun in a centrifuge while a static pressure was applied to the soil surface. The strains on the tube and the diameter change of the tube were measured and the stresses in the wall of the tube were calculated. The centrifuge test results were analyzed by non-linear finite element

analyses using hyperbolic and Lade's soil models. From this study, Ni concluded that: (1) under-integration could reduce the shear locking of the element and was essential for the four-node quadrilateral elements; (2) the hyperbolic and Lade's model could simulate the hardening system; (3) the hyperbolic model was able to represent the stress-strain behavior but not the dilatant behavior of the tested soil. However, Lade's model could simulate both aspects fairly well; and (4) an anisotropic soil model with principal stress rotation is necessary to predict the soil-culvert system's response.

CHAPTER III

DEVELOPMENT OF DYNAMIC STRESS GAGES

The primary unknown in the problem of soil-structure interaction is the surface overpressure and the pressure transmitted by the soil onto the structure. For any model or field test, instrumentation is needed to obtain this information. The pressure measurement in a dynamic test requires more elaborate consideration than a static one. For instance, the response frequency of the stress gage has to be higher than the highest significant frequency component of the loading history, so that the gage will respond to the loading truly. Another major factor in dynamic testing is the hostile environment of the dynamic loading. Gages have to be strong and rugged to survive in the test.

To obtain the stress distribution on the underground structure is a challenging task. The two most suitable ways for dynamic tests are to measure strains on the wall of structure and then back calculate the stresses in the structure, and to utilize stress gages to measure the stresses on the structure directly. The first method requires the stress-strain relationship

of the structure material to be well defined. The second method, to measure soil stress directly, is the preferred one but is also the more difficult one.

The development of a soil stress gage has been pursued by soil engineers for decades. Generally, the problems related to a soil stress gage are (1) the problem of the inclusion of the gage; and (2) the problem of non-uniform stress distribution on the gage.

Two types of dynamic stress gages were developed and used for the centrifuge test in this research program. The first type was used to measure the air blast pressure applied to the soil sample surface. Gages of this type are called surface stress gages. The second type was used to measure the normal stress acting on the structure. Gages of this type are called contact stress gages.

The gages built are of the piezoelectric type. The sensing material is polyvinylidene fluoride (PVDF). This type of gage was first developed by Chung, et al., (1985) at the National Bureau of Standard (NBS). The gage built here differs from the NBS gage in two ways. First, the shape and structure of the gage are different. Second, the electric circuits for conditioning the gage signal are different. Design and construction details of UCB (the University of Colorado

at Boulder) gages are presented in the following section.

The PVDF film used in the present study was supplied by Systron Donner Company. The film is 0.025 inches in thickness, 1.05 inches wide and has various lengths. It has a conductive layer coated on both sides, and is ready to use upon arrival at UCB. PVDF is a semi-crystalline thermoplastic polymer. It has good impact resistance, good abrasion resistance, low creep, outstanding weather and aging resistance. It is unaffected by ultraviolet light and is highly stable to gamma radiation. The temperature range for normal operation lies between -50 and +150 ^{o}C. PVDF is a good electrical insulator, with a high dielectric constant, especially when oriented. This high dielectric constant means that the material has strong piezoelectric and pyroelectric effects. In another words, the material is very sensitive to stress and temperature changes. PVDF has a wide range of application in food, chemical, and nuclear industries. Table 3.1 lists the properties of PVDF film.

3.1 Gage Design and Construction Detail

Considerable amounts of effort have been spent in the past to develop stress gages to measure soil stresses. A review of these studies show that the most important factors in the design of stress gage are: (1)

Table 3.1

Properties of low molecular weight PVDF film (Supplied by Systron Donner Company)

Property	Typical Value	Comments
Density	1780 kgm^{-3}	1750 kgm^{-3} for high mol.wt.
Tensile Modulus	1.9 GPa	1.2-1.6 for high mol.wt
Compressive Modulus	1.3 GPa	
Flexural Modulus	2.2 GPa	
Torsion Modulus	0.8 GPa	
Tensile Yield Strength	50-60 MPa	~ 45 MPa for high mol.wt.
Compressive Yield Strength	90-100 MPa	
Flexural Yield Strength	55 MPa	
Shore D Hardness	78	Test Method DIN 53 505
Brittle Temperature	-40°	
Vicat Softening Temperature	147°C	165° quoted for "KF 1000"
Heat Distortion Temperature	150°C at 0.45 MPa	98°C at 1.84 MPa
Crystalline Melting Point	178°C	160°C for high mol.wt.
Moulding Temperature	190 - 260°C	
Coefficient of Linear Expansion	12×10^{-5} $°C^{-1}$	Average, 20 - 150°C
Thermal Conductivity	0.13 $WK^{-1} m^{-1}$	
Specific Heat	1.3 $kJkg^{-1} K^{-1}$	
Latent Heat of Fusion	6.3×10^{4} Jkg^{-1}	
Volume resistivity	5×10^{12} Ωm	10^{13} Ωm, if oriented
Surface resistivity	10^{13} Ω	
Dielectric Strength AC	150V μm^{-1}	Considerably higher
on 20μm sheet DC	400V μm^{-1}	for oriented material
Water Absorption	0.03-0.04%	
Average Refractive Index	1.42	
Piezoelectric coefficient d_{31}	20.9 pCN^{-1}	
d_{32}	1.4 pCN^{-1}	
d_{33}	-33.1 pCN^{-1}	

the aspect ratio (the ratio of gage thickness to gage diameter); (2) the modulus ratio (the ratio of gage modulus to soil modulus); (3) gage deflection or arching effect of soil on and around the gage; (4) the uniformity of stress distribution over the gage; and (5) lateral stress rotation which was defined by Weiler and Kulhawy (1982) as: "the disruption of a multi-axial stress field by an inclusion causes a portion of the applied lateral stress to be felt normal to the cell ".

Taylor (1945) studied the behavior of soil stress gages and recommended that the aspect ratio of a stress gage be less than 0.2 to minimize the error caused by gage thickness. This criterion was verified by subsequent investigations and has been followed since. Many researchers in the past have found that a stress gage stiffer than the soil will over-register, and a gage softer than the soil will under-register. However, a study by Tory et al., (1967) revealed that the change in the registration ratio, i.e., the ratio of gage stress to applied stress, is negligible as long as the gage is rigid relative to the soil. Chung and Bur (1985) also concluded that a gage should have an aspect ratio less than 0.1 and the modulus ratio should be greater than unity. In the same paper, they also mentioned that a gage with low aspect ratio and high modulus ratio can also minimize the development of arching in soil.

The uniformity of normal stress over the gage surface was examined by Monfore (1950), Peattie and Sparrow (1954), and Hvorslev (1976). These studies showed stress concentrations around the outer perimeter of a gage. It is necessary to design a gage with the sensitive area of the gage being smaller than the total area, so that the stress distribution will be uniform over the sensitive area of the gage. Monfore (1950) suggested that the sensitive area be less than 45 percent of its total area. Peattie and Sparrow (1954) recommended the ratio being less than 25 percent.

Weiller and Kulhawy (1982) investigated the factors affecting the measurement of soil stresses and showed that the Poisson's ratio of a soil is the dominating factor that controls the amount of lateral stress transfer.

The gage design criteria listed above are for a gage embedded in soil. However, the surface stress gage and the contact stress gage in the present study are used in different situations. That is, the surface stress gage will have one face seated on the soil surface with the other face of the gage open to the air while the contact stress gage will be seated on the structure with the other face contacting with the soil. Since none of these gages is used to measure free field stresses (which are the soil stresses when no buried

structure presents), the above mentioned criteria need to be adjusted for the design of both the surface and the contact stress gages. For the surface stress gage, the aspect ratio is no longer a factor since there is no inclusion problem for the gage. Also, the criterion for the modulus ratio is meaningless for the surface stress gage. The uniformity of stress distribution on the gage is still important for the surface stress gage. Nevertheless, there will not be any lateral stress rotation since the gage will be embraced by a retaining bracket to preclude lateral stress on the gage. For the contact stress gage, the design criteria of the past study are still appropriate except that the contact stress gage, like the surface stress gage, also has a retaining bracket to prevent the lateral stress from exerting an influence on the gage response.

The ability of the gage to survive in the violent blast is an important concern in the design of surface stress gage. In order to have a strong, rugged gage the PVDF film needs to be protected. A polycarbonate sheet is used as the protective layer after high strength epoxy was tried and abandoned due to the fact that the sand grain will make indentions on the surface of epoxy. Polycarbonate is a stiff plastic. Its Young's modulus is about 350,000 psi at room temperature and its unit weight is 75.0 pcf. The surface stress gage

is built of two 0.0625-inch-thick polycarbonate sheets sandwiching the PVDF film. The film and the protective layers are glued together with high strength epoxy. Figure 3.1 shows the construction of the surface stress gage and the retaining bracket. Signal from the gage is carried out by a coaxial cable which provides good noise shielding. The outer diameter of the coaxial cable is 0.056 inches. The cable is very flexible. It is believed that the cable will have a minimum inclusion effect on the gage response when buried in soil. The resonant frequencies of the gage calculated with the stiffness and the mass density of the polycarbonate sheets are 60 khz and 80 kHz for the surface stress gage and the contact stress gage respectively.

Figure 3.2 shows the contact stress gage along with its retaining bracket. The PVDF film is protected by two 0.0375-inch-thick polycarbonate sheets. The gage has a curved face with the curvature being the same as that of the outer face of the test structure. The curved face of the contact stress gage is achieved by baking the polycarbonate sheets while it is held on a cylinder with the proper curvature.

The contact stress gage has a square shape, sized 1.1 X 1.1 inches. Its equivalent diameter, i.e., the diameter of the gage as if it was circular with a same area, is equal to 1.24 inches. The gage is 0.10

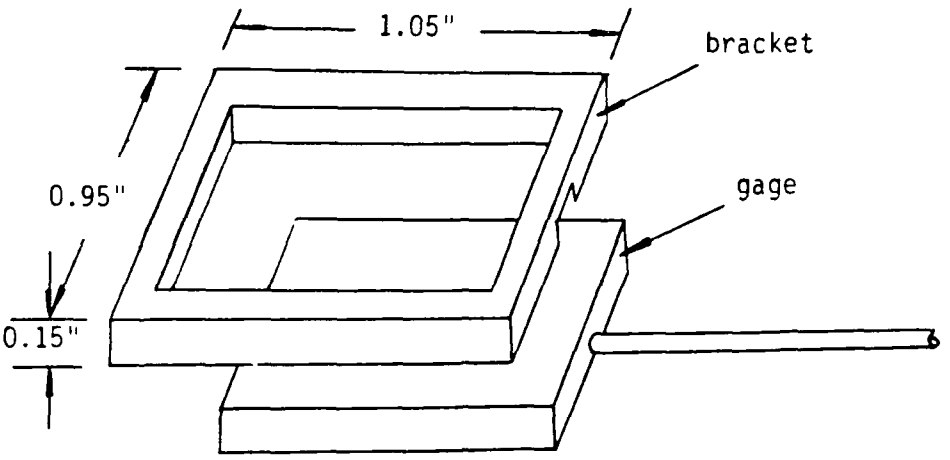

Figure 3.1a Surface stress gage and retaining bracket

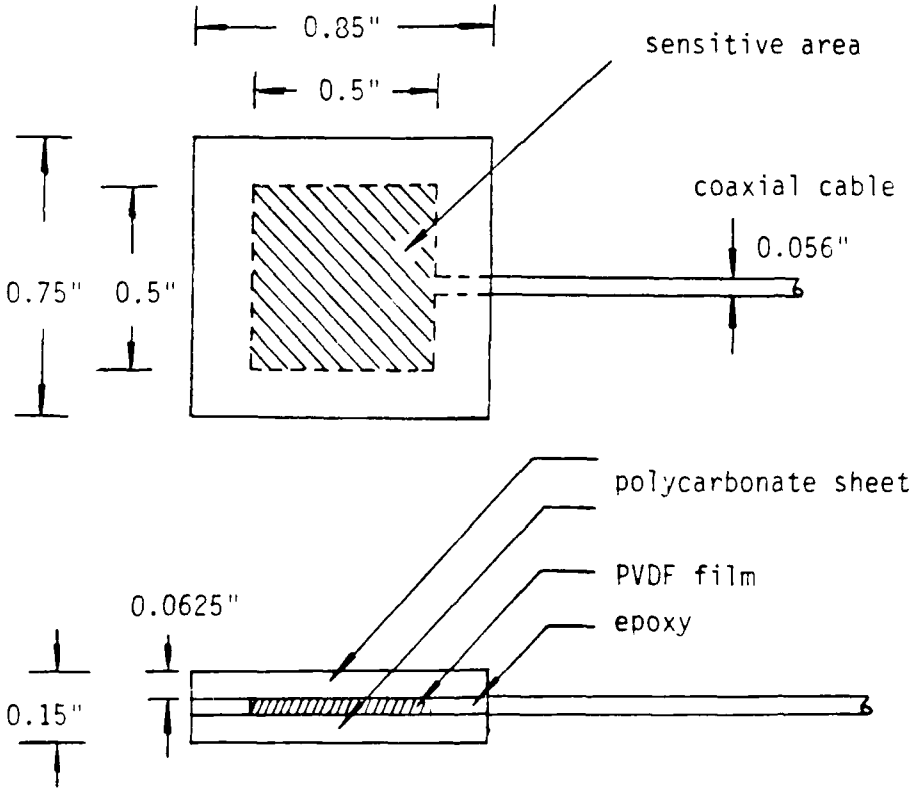

Figure 3.1b Surface stress gage

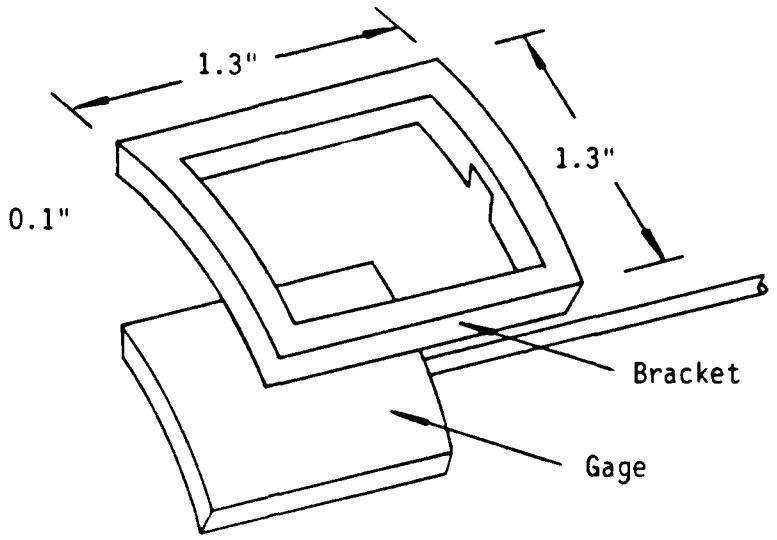

Figure 3.2a Contact stress gage and retaining bracket

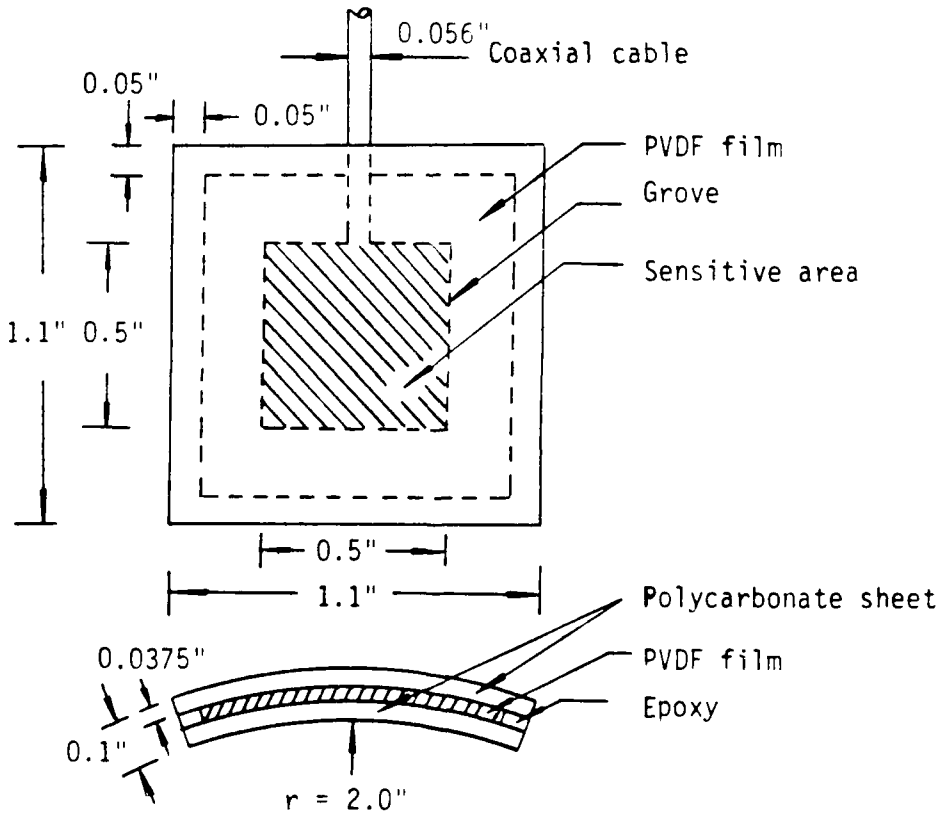

Figure 3.2b Contact stress gage

inches thick, so that the aspect ratio of the gage is 0.081. According to the previous gage design criteria, an aspect ratio of 0.081 is satisfactory in minimizing the intrusion of the gage.

The ratio of the sensitive area to the total area of the contact gage is 0.2. According to the design criteria of the past studies, a uniform distribution of normal stress will be obtained over the sensitive area of the gage. The modulus ratio of the contact stress gage is less than 0.1 which is appropriate according to the gage design criteria. The excellent performance of the surface stress gage and the contact stress gage is confirmed in the section of gage calibration.

3.2 Gage Theory

This section addresses two basic questions about the stress gage: (1) how does the PVDF film work as a pressure sensing device? and (2) how to convert the gage signal to a pressure history ?

Before the discussion on this issues, several terms need to be defined first:

(1) An electric dipole is a pair of positive and negative charges, +q and -q, separated by a distance d.

(2) The dipole moment, p, of an electric dipole is the product of the charge and the distance, i.e.,

$$p = qd \tag{3.1}$$

(3) The dipole potential is the potential of an electric dipole. Dipole potential is proportional to dipole moment.

A polarized material possesses a potential which is proportional to the total dipole moment in the material. Figure 3.3 shows a segment of PVDF film. The film has been subjected to a stretching in the 1-direction and to a polarization in the 3-direction. The polarization is accomplished by a high electric field.

When the film is stressed, the dipole potential of the film changes. This is analogous to changing the separation distance of a parallel capacitor. The change of potential results in a change in the electric field. When the film is short-circuited, such as connecting both sides of the film to a measuring instrument, the unbalanced electric field will force electric charges to flow in or out of the film in order to maintain equilibrium. The amount of charge flowing in the circuit can be calculated as:

$$Q_i = A\sum_j (d_{ij}\delta\sigma_j) - \beta A\delta T \tag{3.2}$$

where

i = 1 to 3 and j = 1 to 6,

Q_i = electric charge in the i-direction,

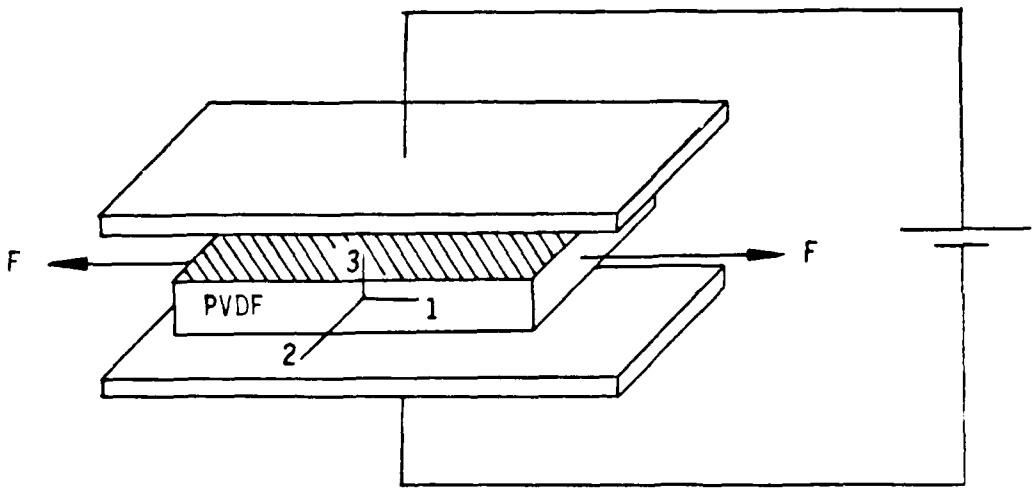

Figure 3.3 A segment of PVDF film under mechanical drawing and electrical polarization

A = sensitive area of the film,

d_{ij} = matrix of piezoelectric coefficients,

$$= \begin{bmatrix} 0 & 0 & 0 & 0 & d_{15} & 0 \\ 0 & 0 & 0 & d_{24} & 0 & 0 \\ d_{31} & d_{32} & d_{33} & 0 & 0 & 0 \end{bmatrix}$$

$\delta\sigma_{ij}$ = changes of the six stress components,

= pyroelectric coefficient, and

δT = temperature change of the PVDF film.

The temperature change of the PVDF film may be generated by the temperature pulse which follows the stress pulse in a dynamic loading. Bur and Roth (1985) studied the pyroelectric effect of the PVDF film and concluded that for gage thickness over 0.028 inches and pressure measurement shorter than 0.04 seconds, no active temperature compensation is needed, but an 8 % correction applied to the gage signal was recommended in considering the adiabatic heating of the PVDF film. In order to investigate how the pyroelectric effect of the PVDF film affects the performances of the surface and the contact stress gages, a surface stress gage was tested. Dynamic loading was applied to the gage repeatedly with same loading amplitude for ten times. The results showed no recognizable change of the calibration constant of the gage. This can be explained

as the pressure level of the loading being too small to cause noticeable adiabatic heating of the PVDF film. It was thus concluded that the temperature correction is not necessary for the surface and the contact stress gages when the working pressure is under 100 psi which is the pressure range used in both the centrifuge test and the investigation described above.

Once the pyroelectric effect of the PVDF film is ignored, the second term at the right hand side of Equation (3.2), $\beta A \Delta T$, can be taken off. Thus, Equation (3.2) is reduced to

$$Q_i = A \sum_j (d_{ij} \sigma_j) \qquad (3.3)$$

Let $\sigma_1 = \sigma_2 = \sigma_3 = \sigma_h$ for a hydrostatic loading, then

$$Q_3 = A(d_{31}+d_{32}+d_{33})\sigma_h \qquad (3.4)$$

Current, I, is defined as amount of charge passing through a cross-sectional area in a unit time, i.e.,

$$I = \frac{dQ_3}{dt} \qquad (3.5)$$

According to Ohm's law

$$V = IR$$

$$= \frac{dQ_3}{dt} R \qquad (3.6)$$

Substituting Equation (3.4) into Equation (3.6), the only time variable in Equation (3.4) is σ_h, thus

$$V = AR(d_{31}+d_{32}+d_{33}) \frac{d\sigma_h}{dt} \qquad (3.7)$$

Equation (3.7) indicates that when PVDF film is stressed, the signal measured by an instrument, in term of a voltage output, is proportional to the sensitive area of the film, the impedance of the instrument, the piezoelectric coefficient of the film, and the time derivative of the applied stress.

The impedance, R, serves as an amplification factor for the gage signal. Since PVDF film can only send out very small current, a high impedance resistor is needed to amplify the gage signal to a certain level so that a regular recorder can read and store the signal.

The applied stress, σ_h, can be obtained by integrating Equation (3.7),

$$\sigma_h = \frac{1}{AR(d_{31}+d_{32}+d_{33})} \int V dt \qquad (3.8)$$

Equation (3.8) implies a linear relationship between the applied stress, and the integrated gage signal. The constant, $1/AR(d_{31}+d_{32}+d_{33})$, is the calibration constant of the stress gages under hydrostatic loading.

For the gage stressed with one-dimensional loading in the 3-direction, Equations (3.7) and (3.8) become

$$V = ARd_{33} \frac{d\sigma_3}{dt} \tag{3.9}$$

and

$$\sigma_3 = \frac{1}{ARd_{33}} \int V dt \tag{3.10}$$

The calibration constant in this case is $1/ARd_{33}$.

Numerical values for the piezoelectrical coefficients can be found in Table 3.1. Note that constant d_{33} has different sign than d_{32} and d_{31}. This implies that the calibration constant of a gage under hydrostatic loading is greater than that of the gage under one dimensional loading. The calibration results of the next section confirm this point. The ratio between the calibration constants of these two loading conditions is found to be about one-third.

The circuit used for the surface stress gage and the contact stress gage is shown in Figure 3.4. A

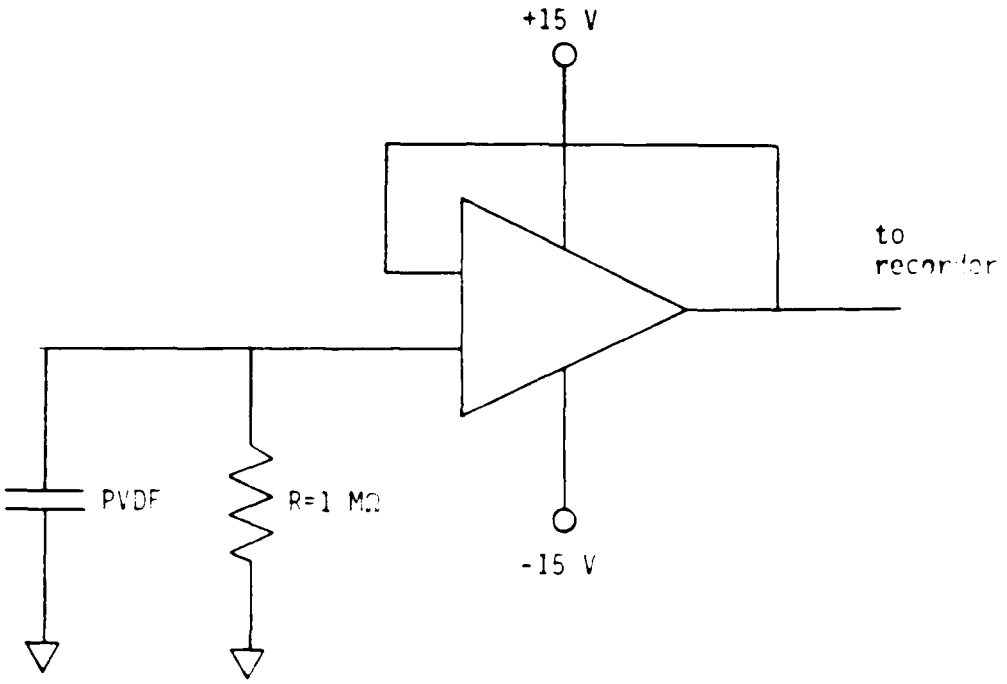

Figure 3.4 High impedance amplifier for dynamic stress gage

resistor of one mega-ohm was adopted after five and ten mega-ohm resistors were tried and found to produce too much noise. The signal recorded with this circuit needs to be integrated with respect to time to obtain the applied stress. Rather than integrating this signal electronically, numerical integration is performed. The trapezoidal rule is used in the numerical integration algorithm.

3.3 Calibration of the Surface Stress Gage

3.3.1 Test Hardware

Hardware for calibrating the surface and the contact stress gages includes a hydrostatic loading chamber, a reference pressure transducer, a dynamic loading system, and a data acquisition system.

The hydrostatic loading chamber is bored from a solid aluminum cylinder. The chamber has two parts, the upper and the lower chambers. The calibration of the contact stress gage will use both chambers, but, the calibration of the surface stress gage (as shown in Figure 3.5), uses only the lower chambers. There are four electrical fit-throughs and one pressure transducer port at the bottom of the lower chamber. Four surface gages can be calibrated against the pressure transducer at the same time. The reference pressure transducer for calibrating the surface stress gage is the CEC 4-313

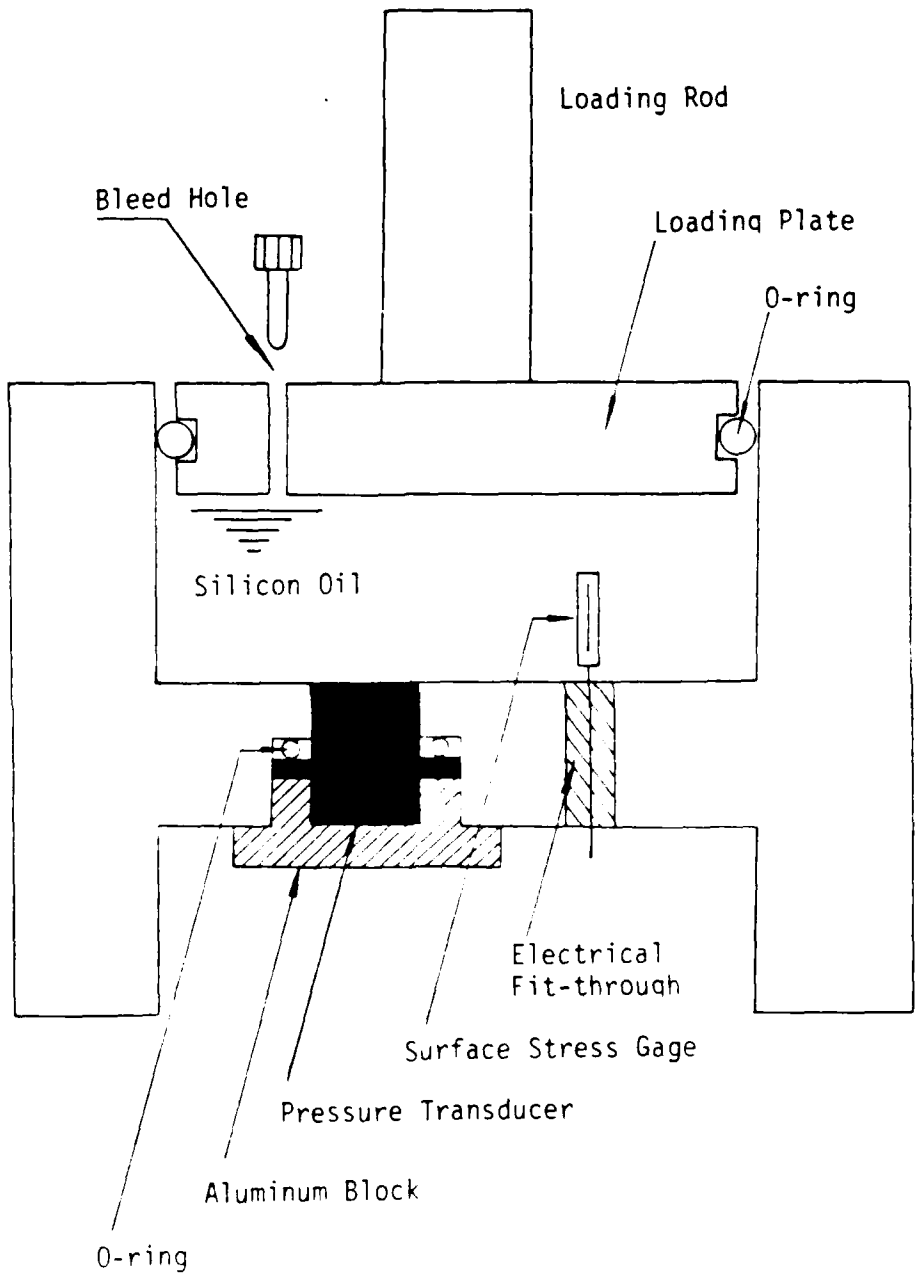

Figure 3.5 Calibration of surface stress gage under 3-D loading

pressure transducer. Its frequency response is 5 kHz which is capable of catching the highest loading frequency of the loading machine. The transducer is calibrated before and after the calibration of the gages.

The dynamic loading is carried out in a load frame manufactured by Material Testing System (MTS), which is capable of delivering an impulse with a rise time of 10 milliseconds. Figure 3.6 is a schematic view of the test set-up. The amplified stress gage and pressure transducer signals are recorded by a TEAC DC to 20 kHz, 14-channel analog tape recorder. The signals are digitized by an analog-to-digital (A to D) converter. Data are stored on a floppy disk by an IBM personal computer.

3.3.2 Data Reduction

An example is presented herein to explain how to obtain the calibration constant of the stress gages. The example is one of the calibration of the surface stress gage subjected to hydrostatic loading.

Figure 3.7 shows the plot of a surface stress gage signal. The abscissa is real time in milliseconds. The ordinate represents voltage which has been scaled up about two hundred times in the A to D conversion. As indicated in Equation (3.7), the voltage is really the derivative of the applied pressure with respect to time.

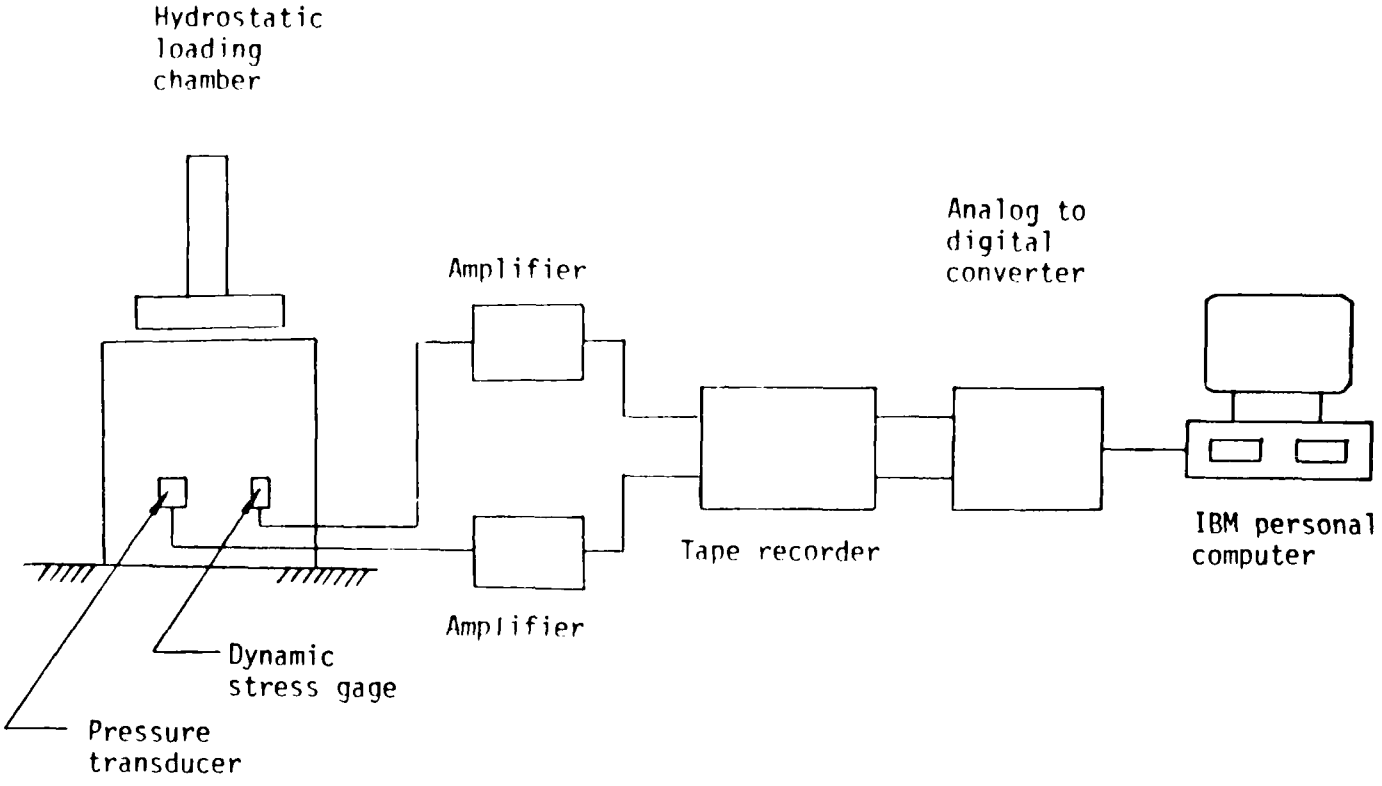

Figure 3.6 Schematic view of stress gage calibration test set-up

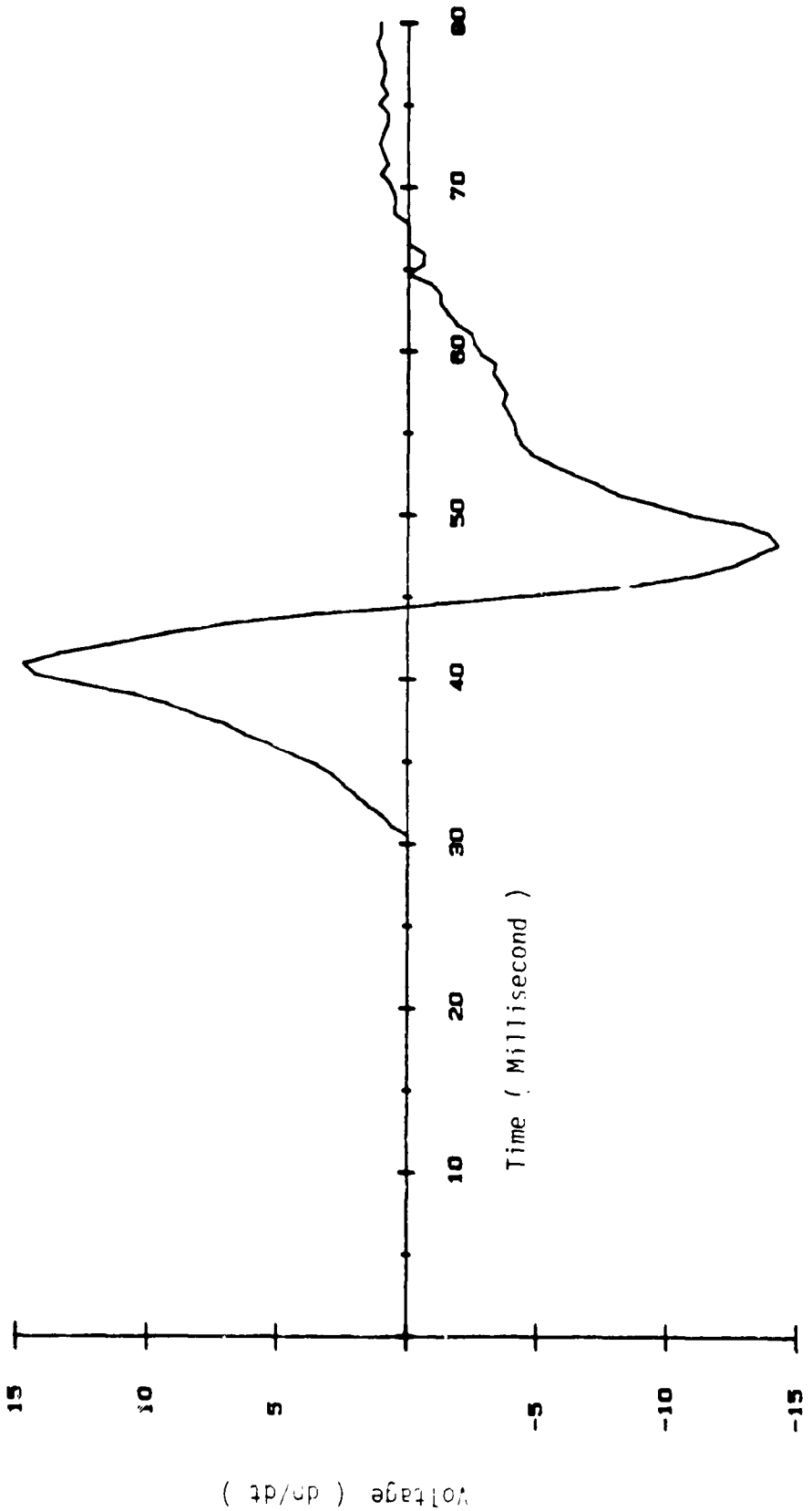

Figure 3.7 Unintegrated dynamic stress gage signal, test 1SGPT.3D

Figure 3.8 shows the pressure history recorded by the pressure transducer. Figures 3.7 and 3.8 are sychronized by using the same signal to trigger the A to D conversion for both channels.

Numerical integration is then performed on the curve of Figure 3.7. The integrated curve is shown in Figure 3.9. Note that the curve has a similar shape as the pressure history shown in Figure 3.8.

Equation (3.8) suggests a linear relationship between the applied stress and the integrated gage signal. Therefore, the calibration constant of the gage can be taken as the ratio of the applied stress to the integrated voltage at any time of the loading history. For easy programming, the ratio between the maximum pressure and the maximum integrated gage signal is used.

In order to confirm the methodology, the integrated gage signal is multiplied by the calibration constant and then compared to the pressure history. The comparison is given in figure 3.10. This plot demonstrates the retrieval of a pressure history by integrating the gage signal and multiplying it by the calibration constant.

3.3.3 Rubber Pad for the Surface Stress Gage

The uniformity of the stress over the sensitive area of the surface stress gage depends upon such factors as the flexibility of the gage, the stiffness of

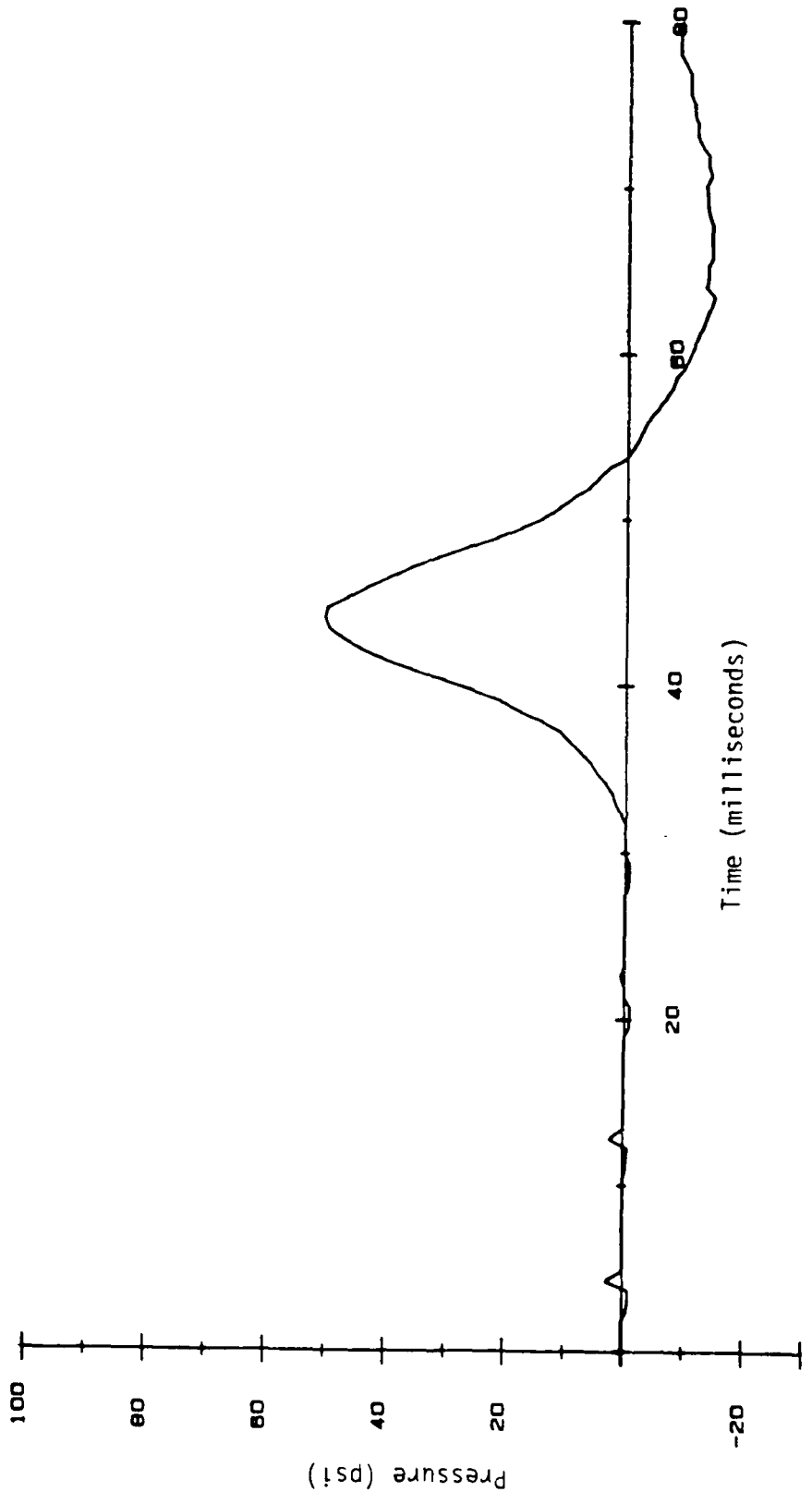

Figure 3.8 Pressure transducer output

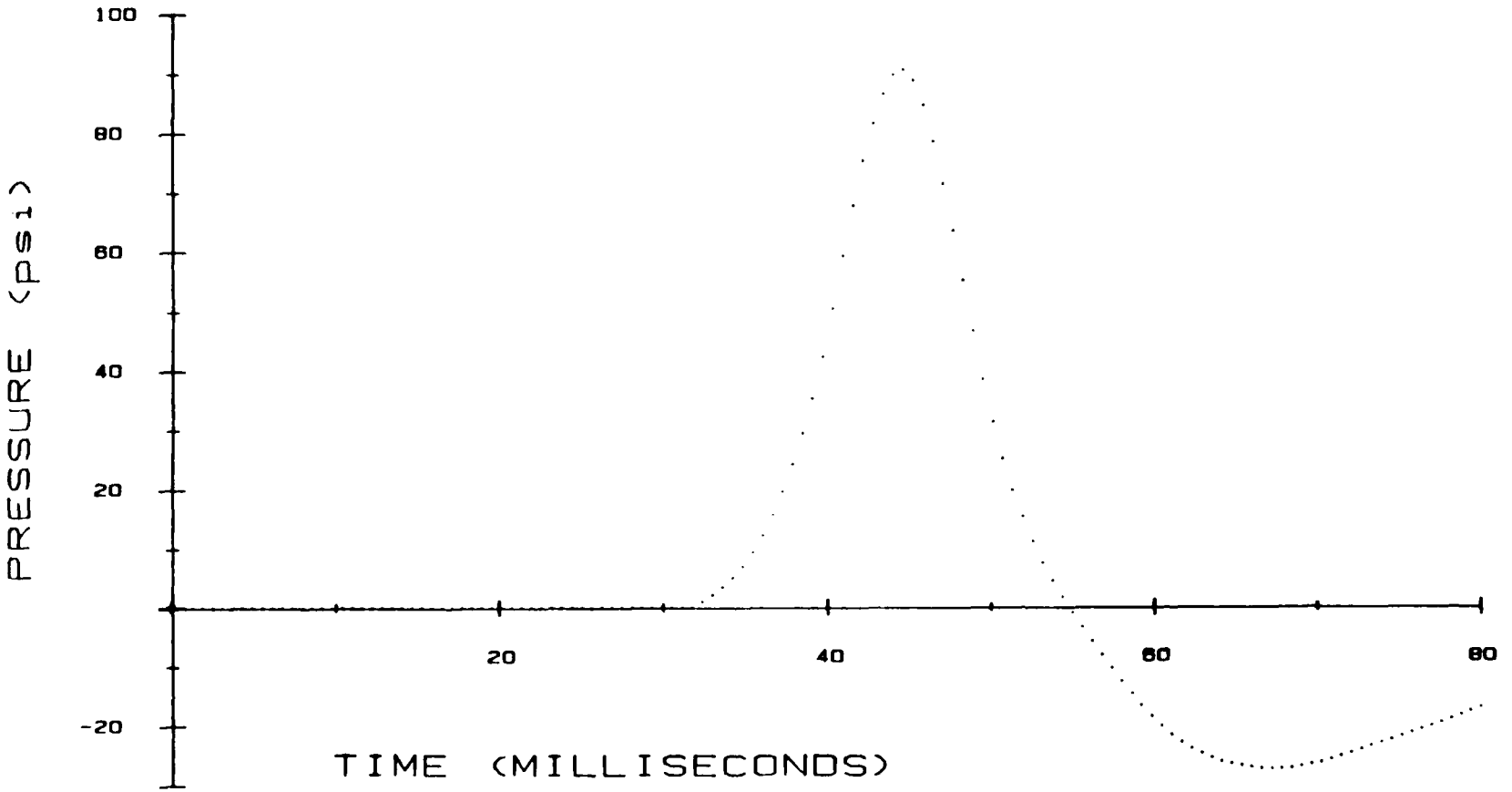

Figure 3.9 Integrated, uncalibrated gage output

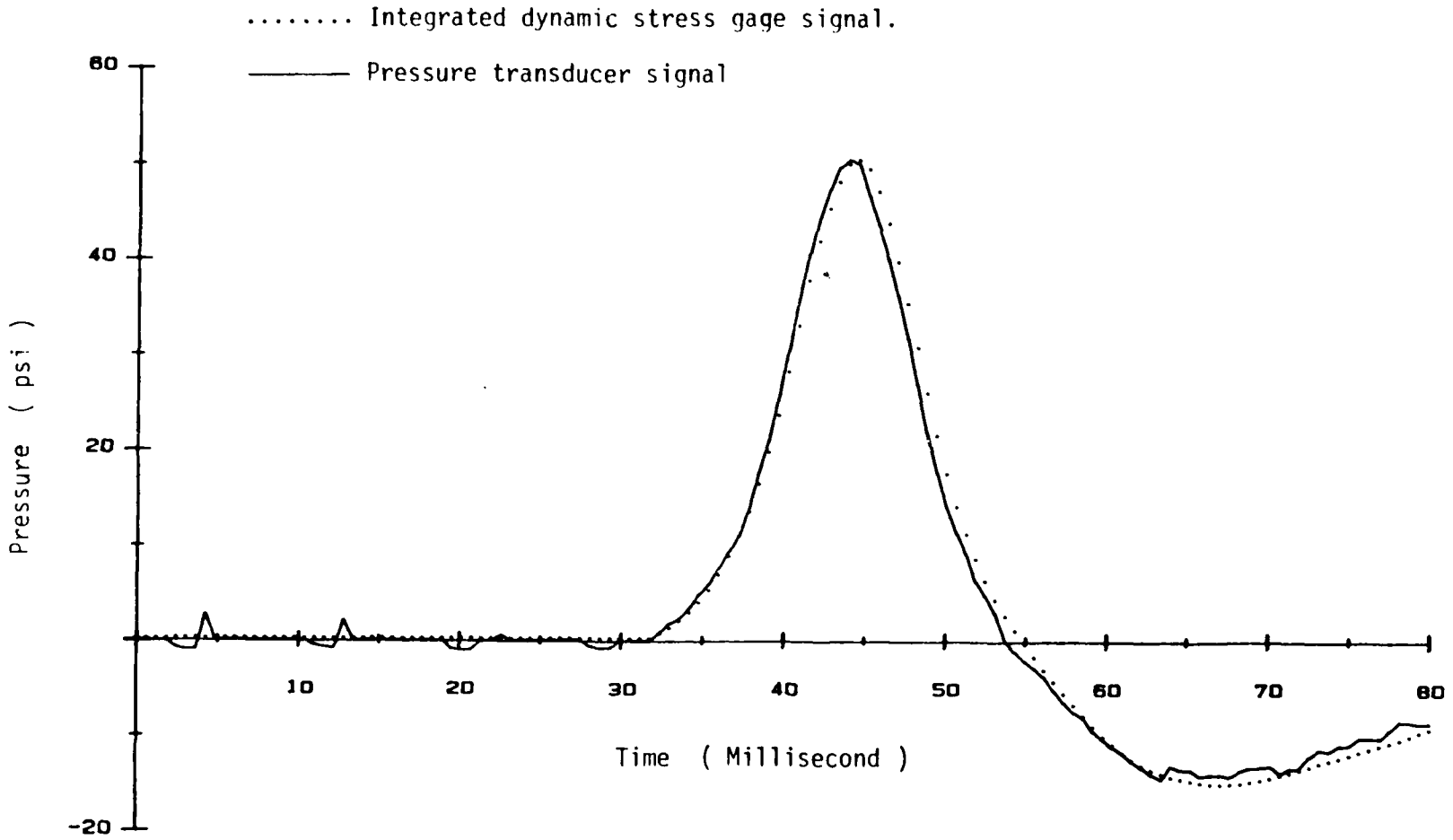

Figure 3.10 Calibration of dynamic stress gage, test 1SGPT.3D

the material on which the gage is placed, and the ratio of the sensitive to the total area of the gage. Since the surface stress gage may be seated on different materials like concrete, metal, or soil for the present study, it is desirable to have the gage possess a calibration constant independent of the material that the gage is sitting on. In light of this desire, a Nitrile rubber pad is attached to the lower face of the gage. The purpose of the rubber pad is to produce a uniform contact stress distribution over the gage. Two questions need to be answered before the rubber pad is considered to be appropriate. The first one is how to justify the uniform stress distribution when the rubber pad is used and the second one is whether the existence of the rubber pad will reduce the response time of the gage to an unacceptible level.

To answer the first question, Terzaghi's concept of contact stress distribution under a rigid foundation is reviewed. Figure 3.11a shows the distribution of contact pressure on the base of a smooth rigid footing supported by a foundation. According to Terzaghi and Peck (1948), the curve C_1 represents the contact stress distribution when the load is small, the curve C_u is the distribution after the subgrade fails by plastic flow, and the curve C_2 is at an intermediate stage. If a surface stress gage is free floating in silicon oil and

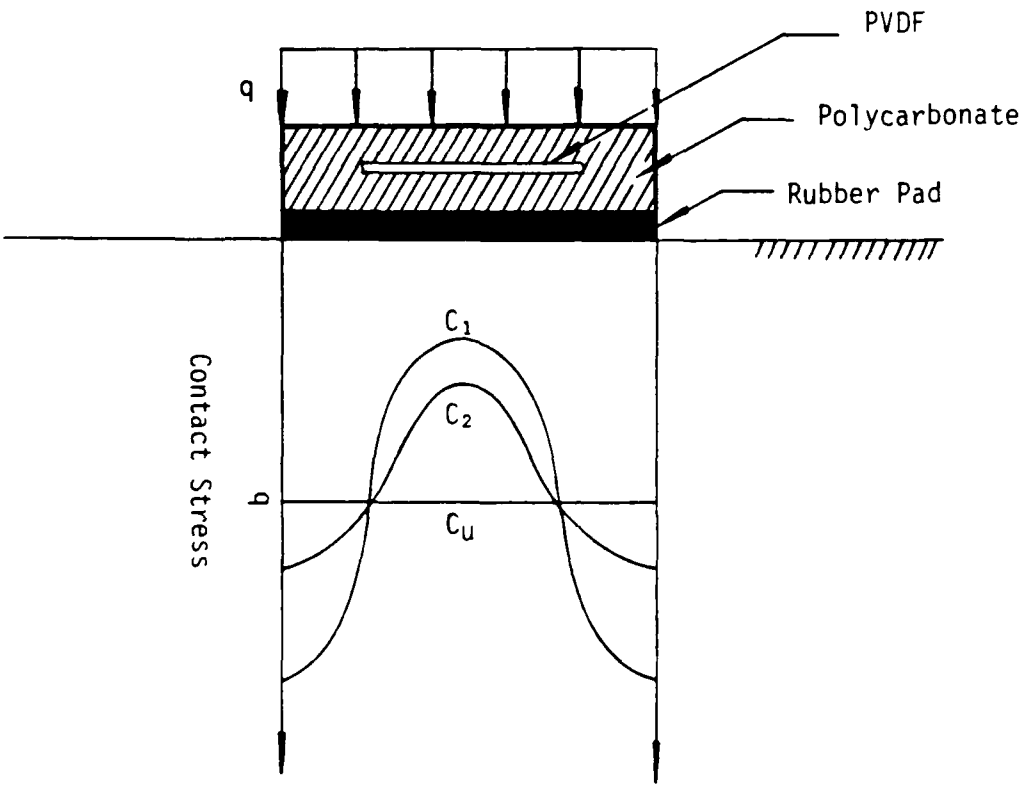

Figure 3.11a Contact stress distribution

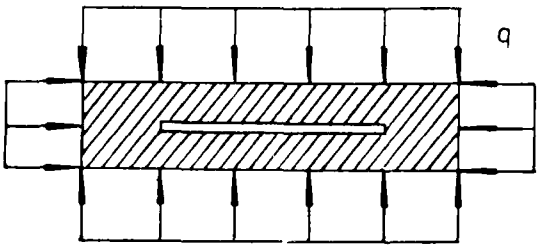

Figure 3.11b Stress distribution on a stress gage in hydrostatic loading

subjected to a hydrostatic loading, the stress distribution on the gage will be uniform as it is shown in Figure 3.11b. If the calibration constant obtained in this situation is considered as the true calibration constant of the gage, then whatever subgrade condition which can produce the same calibration constant will have the same uniform stress distribution on the gage. The results of calibrations using rubber pads of different thicknesses reveals that only when a rubber pad thicker than 0.11 inches is used can the gage produce the true calibration constant. Also, when a thinner rubber pad is used the calibration constant is larger than the true calibration constant. The above results are comparable to Terzaghi's contact stress distribution curves in Figure 3.11a, provided that curve C_1 is considered as the distribution when the deformation of the subgrade is small and curve C_u is the distribution when the deformation of the subgrade is large.

Calibration results also show that when a rubber pad thicker than 0.11 inches is used, common calibration constants were obtained for the cases when the gage was seated on an aluminum plate and when the gage was seated on a dry sand.

The response time of the gage when used with the rubber pad will be about the same as that of the rubber

pad. This can be seen by considering the gage and the rubber pad being connected in series in a single-degree-of-freedom-system. The stiffness of the gage is K_g and the stiffness of the rubber is K_r. The equivalent stiffness, K_e, of the system is

$$K_e = \frac{K_g K_r}{K_{g+K_r}} \tag{3.11}$$

Since $K_g >> K_r$,

$$K_e \simeq K_r$$

The stiffness of the rubber pad is difficult to measure. In order to ensure that the gage and the rubber pad system can respond fast enough to be used to measure the dynamic stress in the centrifuge test, surface stress gages with and without a rubber pad were loaded by air blast. The results show that both gages registered pressures of the same rise time (about one millisecond) but different magnitudes. This implies that the 0.11-inch-thick rubber pad can be used along with the surface stress gage for dynamic stress measurement as long as the rise time of the loading is not less than one millisecond. Nevertheless, if it ever happened that a thinner or stiffer rubber pad is required in regard to the response time of the gage, a uniform stress

distribution on the gage can still be achieved by increasing the dimensions of the gage.

Much effort was devoted to the calibration of the surface stress gage under 3-D loading. Investigation of the pyroelectric effect of the gage has been described in section 3.2. The conclusion was that no temperature compensation is needed for working pressure under 100 psi. The uniformity of the stress over the sensitive area of the gage was examined above.

When a surface stress gage is placed on a flat surface and subjected to an airblast, it is not sure that the gage will be stressed in a hydrostatic loading condition. However, 1-D loading of the gage can be ensured by placing a retaining bracket around the gage and a flexible membrane covering the gap between the gage and the bracket. Therefore, the surface stress gage shall only be used to measure the normal stress applied to the gage. Figure 3.12 shows the calibration of the surface stress gage under 1-D loading.

3.3.4 Calibration Results

Ten surface stress gages were calibrated with 3-D loading. Each gage was calibrated eight times. The mean value of the calibration constants and their standard deviations of the ten gages are listed in table 3.2. The average value of the means of the ten gages is shown at the last line of the table. Although the gages

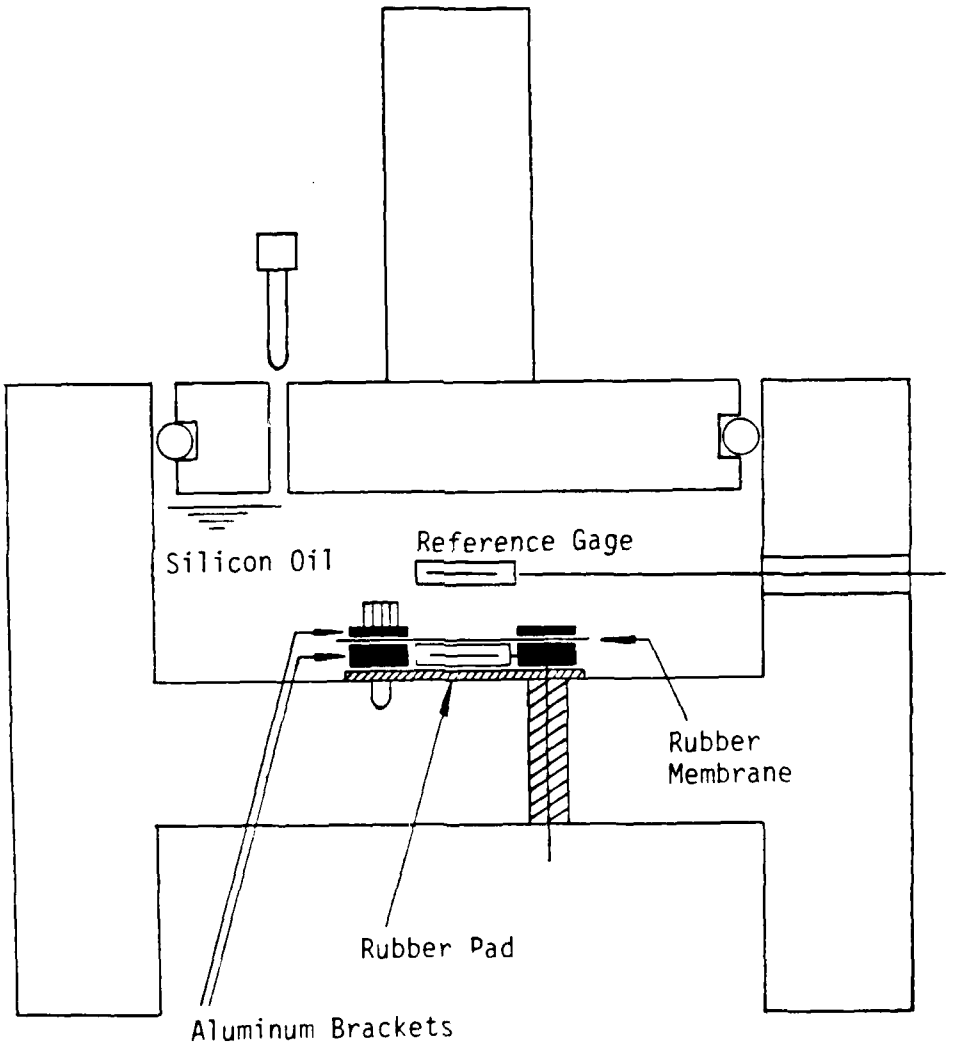

Figure 3.12 Calibration of surface stress gage under 1-D loading

Table 3.2

Calibration results of the surface stress gage under 3-D loading

Surface stress gage number	Mean value of the calibration constant	Standard deviation
1	0.550	0.01
2	0.618	0.02
3	0.526	0.01
4	0.623	0.01
5	0.582	0.01
6	0.653	0.01
7	0.572	0.02
8	0.568	0.02
9	0.543	0.01
10	0.537	0.02
average	0.577	

all have the same sensitive area their calibration constants vary up to seven percent. This is attributed to the variation of the contact condition between the PVDF film and the polycarbonate protective layers when the gages were built.

Seven of the ten surface stress gages were recalibrated four months later. The calibration constants were found to have remained the same even though the gages were used intensively during this period of time.

Seven surface stress gages were calibrated under 1-D loading. Each gage was calibrated eight times. The mean value of the calibration constants and their standard deviations are listed in table 3.3.

3.4 Calibration of the Contact Stress Gage

3.4.1 Test Set-up

Figure 3.13 shows the hydrostatic loading chamber with a contact stress gage placed on top of a aluminum block. A 0.03-inch-thick rubber pad is placed beneath the contact stress gage for the same reason as for the surface stress gage. The lower chamber is filled with soil. A rubber membrane is placed on the soil surface and the upper chamber is mounted. The upper chamber is filled with silicon oil which will transmit a uniform stress to the soil surface during the test.

Table 3.3

Calibration results of the surface stress gage under 1-D loading

Surface stress gage number	Mean value of the calibration constant	Standard deviation
1	0.184	0.007
4	0.186	0.01
6	0.187	0.02
7	0.177	0.02
8	0.186	0.01
9	0.169	0.008
10	0.179	0.03
average	0.181	

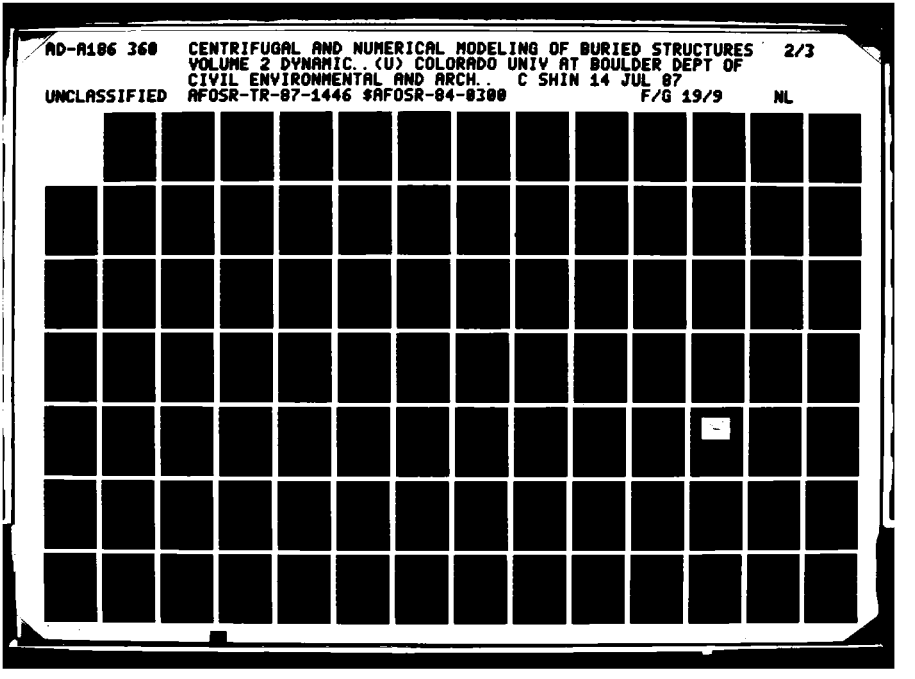
AD-A186 360 CENTRIFUGAL AND NUMERICAL MODELING OF BURIED STRUCTURES 2/3
VOLUME 2 DYNAMIC..(U) COLORADO UNIV AT BOULDER DEPT OF
CIVIL ENVIRONMENTAL AND ARCH.. C SHIN 14 JUL 87
UNCLASSIFIED AFOSR-TR-87-1446 $AFOSR-84-0300 F/G 19/9 NL

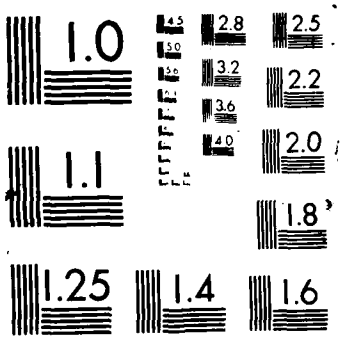
1.0
1.1
1.25
1.4
1.6
1.8
2.0
2.2
2.5
2.8
3.2
3.6
4.0
4.5
5.0
6.3

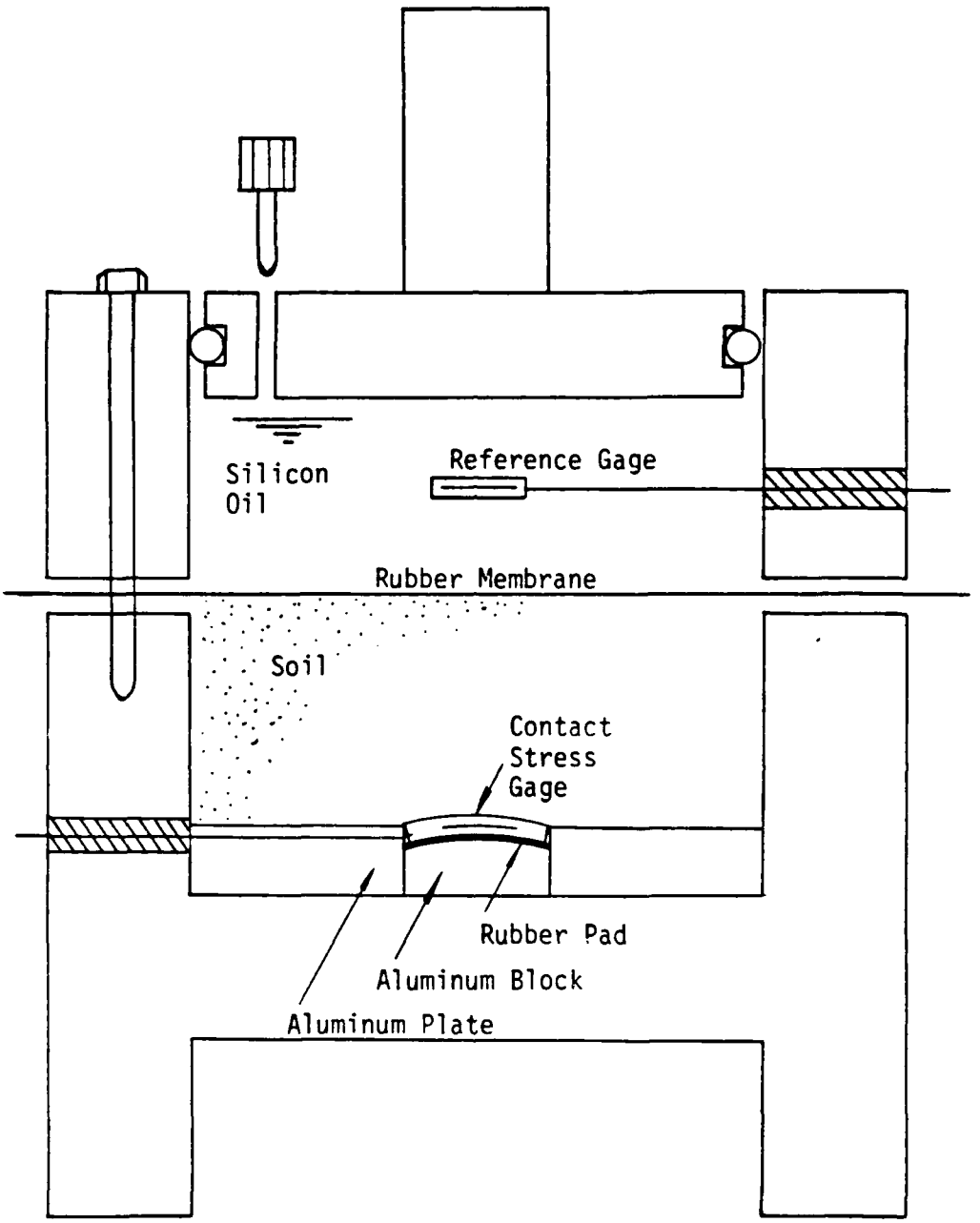

Figure 3.13 Calibration of contact stress gage

There is one electrical fit-through on the wall of the upper chamber. A calibrated surface stress gage can be used as a reference gage for the contact stress gage calibration.

The aluminum block has a curved surface. The area and the curvature of the curved face is the same as that of the contact stress gage. The block with the contact stress gage and the rubber pad will fit into the square opening of a circular aluminum plate which rests against the bottom of the chamber. Figure 3.13 is drawn to scale. It can be seen that the curved face of the gage occupies a relatively small area compared to the circular plate. Hence, it was assumed that the planar pressure wave transmitted from the soil surface will remain planar when it arrived at this section.

As shown in Figure 3.13 the edges of the gage are located below the square opening of the circular plate. The gap (0.002 inches) between the edges of the gage and the opening allows the free expanding of the gage and thus the 1-D loading on the gage. Play-dough was applied at the edge of the gage to prevent soil particles from entering the gap.

When the gage is used in a centrifuge test, a retaining bracket and a thin membrane covering the gage and the bracket are used to achieve a 1-D loading condition.

The lower chamber was designed to have a height to diameter ratio equal to 0.5, in order to minimize the effects of wall friction, and to ensure that the applied pressure was transmitted uniformly throughout the soil in the vertical direction.

The effect of wall friction was examined by employing a friction-reducing membrane which has been shown to reduce the friction between soil and aluminum to one-seventh of the original amount. Several calibrations were conducted with the friction-reducing membrane mounted on the wall of the lower chamber. The same calibration constant was obtained as when no friction-reducing membrane was used. This means that the height to diameter ratio equal to 0.5 was satisfactory in preventing the effect of wall friction.

3.4.2 Rubber Pad for the Contact Stress Gage

The choice of the rubber pad for the contact stress gage is very important for the performance of the gage. The requirements for the surface stress gage also apply to the contact stress gage, namely, the stress distribution on the gage needs to be uniform, and the response time of the rubber pad needs to be short. In addition, the deformability of the rubber pad needs to be small to prevent positive arching. This last requirement works in an opposite way to the first one, i.e., the rubber pad needs to be able to deform enough

to generate a uniform stress distribution on the gage. The only way to reconcile this contradiction is to increase the dimension of the gage, so that only a very small deformation of the pad is needed to give a uniform stress distribution on the gage. Several sizes of contact stress gage were tried with the same rubber pad. These included dimensions of 0.625 X 0.625 inches, 0.8 X 1.0 inches, and finally 1.1 X 1.1 inches. The gage sized 1.1 X 1.1 inches gave the most repeatable calibration constant. However, the adequacy of this constant still needs to be verified.

It is very difficult, if not impossible, to find the right size of the rubber pad analytically. The performance of the chosen 0.03-inch-thick rubber pad was judged experimentally. Note that the contact stress gage and the surface stress gage have common sensitive areas. If the rubber pad was acceptable in regard to the uniformity of stress and the arching effect, the contact stress gage should have same calibration constant as the surface stress gage under 1-D loading. The calibration results presented in the next section show that this was indeed the case.

3.4.3 Calibration Results

Table 3.4 lists the results of the calibration of five contact stress gages. Each gage was calibrated three times. Each calibration used a new soil sample.

Table 3.4

Calibration results of the contact stress gage

Contact stress gage number	Mean value of the calibration constant	Standard deviation
3	0.17	0.005
4	0.20	0.03
5	0.178	0.03
6	0.167	0.01
7	0.175	0.02
average	0.178	

Using new soil sample for each test is imperative since the sand grains will likely get trapped in the gap between the edge of the gage and the wall of the circular plate after each loading. Sand grain get trapped in the gap is reflected by a higher calibration constant due to the lateral stress acting on the gage.

The average value of the five contact stress gages calibration constants is 0.178, whereas that of the surface stress gage under 1-D loading is 0.181. The difference of these two numbers is less than two percent. This verifies the belief that there is no arching effect on the contact stress gage and that the stress distribution is uniform for both gages. As a result, the gage response is independent of the medium, and the calibration constant is only dependent on the sensitive ares of the gage, the resistance of the instrument, and the piezoelectric coefficient of the PVDF film.

The 0.03-inch rubber pad used for the contact stress gage is stiffer than the 0.11-inch rubber pad used for the surface stress gage. Knowing the 0.11-inch rubber pad can respond fast enough to the blast loading in the centrifuge, the 0.03-inch rubber pad can certainly respond fast enough to the same loading.

The contact stress gages are used to measure the normal stresses acting on a model or prototype structure

buried in soil. The gages will experience static overburden pressures before the dynamic overpressures arrive at the gages. Thus, it is important to know how the overburden pressure affects the calibration constant of the contact stress gage. Other questions also arise. Such as will the calibration constant change for different soil densities ? Will the calibration constant change for different soils ? And finally, will the calibration constant change for different loading rates ?

A thorough investigation was conducted to answer these questions. Parameters investigated include five different overburden pressures ranging from 1 to 200 psi, three different soil densities (dense, medium, and loose), and two different soils (Kaoline and Coyote concrete sand). The last question was answered by calibrating the surface stress gage with loading rise time varies from 5 milliseconds, which is the limit of the MTS machine, to 100 milliseconds. Results from these tests led to the conclusions that the calibration constant of the contact stress gage is independent of the overburden pressure, the density of soil, the type of soil, and the loading rate.

3.4.4 Correction for the Bending of the Contact Stress Gage

A bending moment applied to the PVDF film will cause the film to send out a signal similar to the one caused by normal stresses. The surface stress gages will not experience bending moment. However, the contact stress gages can be loaded in situations where they are bent. Therefore, it is necessary to determine the correction that must be applied to the signal from a contact stress gage.

The signal from a contact stress gage has two contributions, one from normal stress, the other from bending moment. In order to obtain just the normal stress a correction scheme is needed to isolate the bending contribution. Figure 3.14 shows the test set-up for calibrating the bending response of the gage. Two contact stress gages were attached firmly to a thin-walled aluminum pipe, one at the crown, the other at the springline. Two strain gages were mounted adjacent to the contact stress gages. The pipe was loaded by the MTS machine under deformation control. The loading head had a hole in the middle as shown in Figure 3.14.. The hole accommodates the stress and the strain gages so that they will only receive bending strain when the pipe is deformed. A calculation based on elastic solution shows that the deformation of the pipe at the mid-third

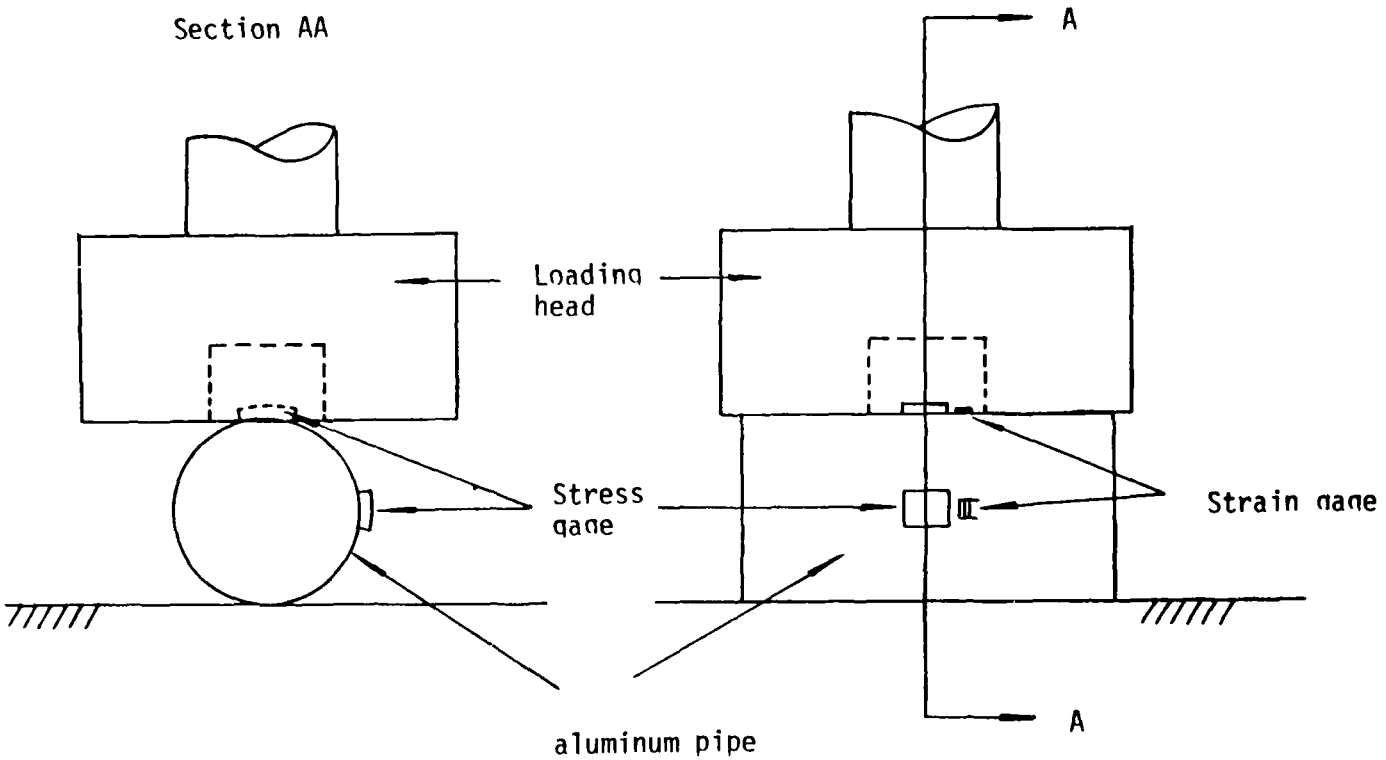

Figure 3.14 Bending calibration of the contact stress gage

section is only 1.6 percent different than the deformation of the pipe if it were loaded along its full length. Thus, it is safe to assume that the stress gages will have the same bending strain as the strain gages do. The bending strains measured by the strain gages will be used to correlate the bending signals of the stress gages.

If the bending signal of the stress gage is integrated, and then multiplied by the calibration constant of the gage, a stress history will be obtained. Because the stress gage does not really receive a normal stress, this normal stress due to the bending of the gage is called fictitious normal stress. Test results indicate that the fictitious normal stress is linearly related to the bending strain. Figure 3.15 shows that the bending strain can be scaled by a bending-correction factor to match up with the fictitious normal stress.

The fictitious normal stress is positive when the contact stress gage is subjected to tensile strain, and is negative when the contact stress gage is bent with compressive strain. The bending-correction factor is defined as the ratio of the fictitious normal stress to the bending strain.

If tensile strain is defined as positive, then the bending-correction factor will always be positive. Thus,

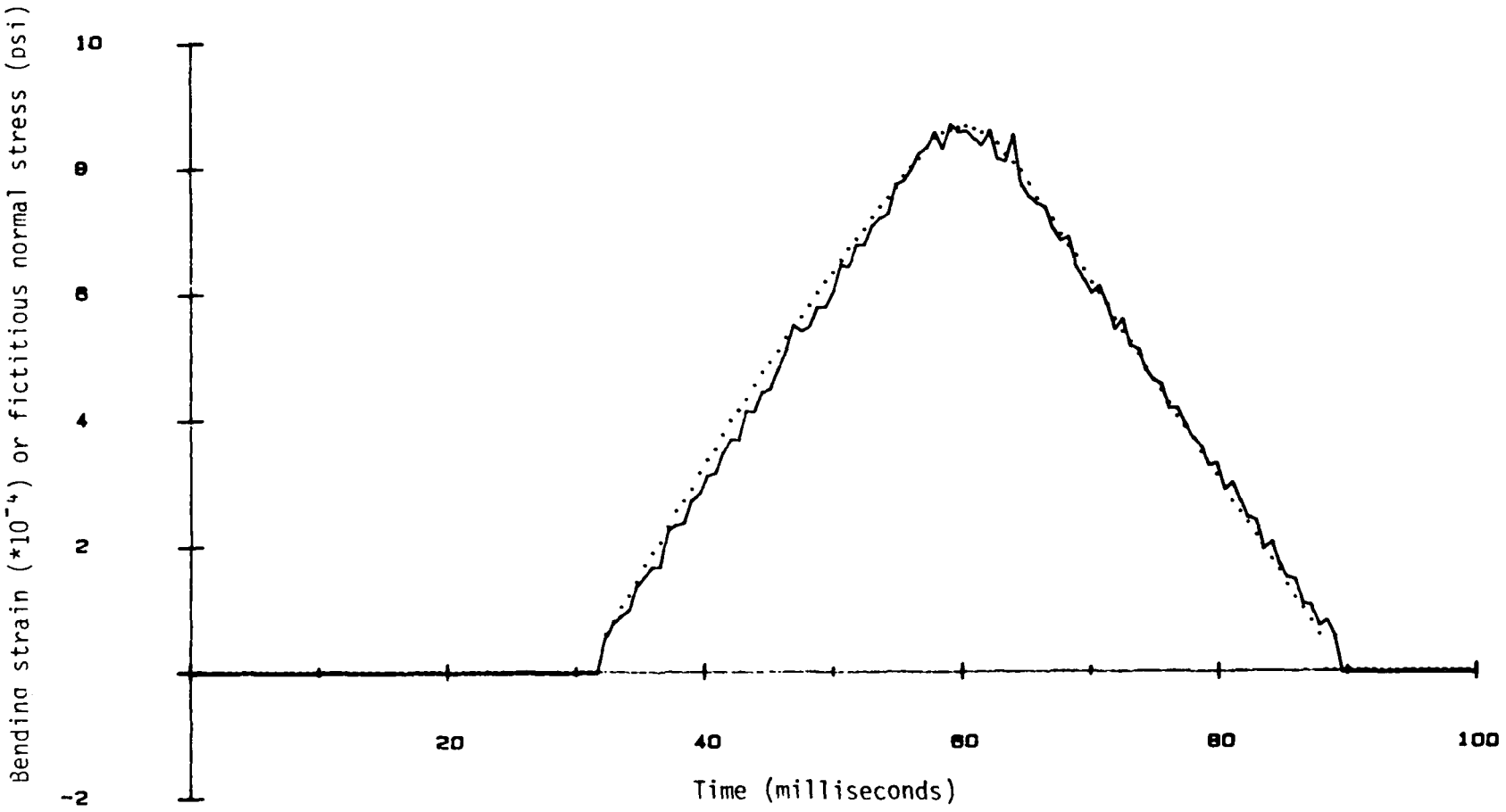

Figure 3.15 Plot shows the linear relationship between the bending strain and the fictitious normal stress

$$\sigma_f = B\varepsilon \quad (3.14)$$

$$\sigma_c = \sigma - B\varepsilon \quad (3.15)$$

where

σ_f = fictitious normal stress,

B = bending-correction factor,

ε = bending strain,

σ_c = corrected normal stress, and

σ = uncorrected normal stress.

To find the bending-correction factor of the contact stress gage, ten bending calibration tests were conducted for each contact stress gage. Among them, five tests were performed with the gage located at the crown of the pipe so that the gage received compressive strain, the other five were carried out with the gage located at the springline of the pipe so that the gage received tensile strain.

Figure 3.16 shows a typical plot of peak fictitious normal stresses versus peak bending strains. The slope of the curve is the bending-correction factor which is different for tensile strain and for compressive strain. Table 3.5 summarizes the results of bending correction tests.

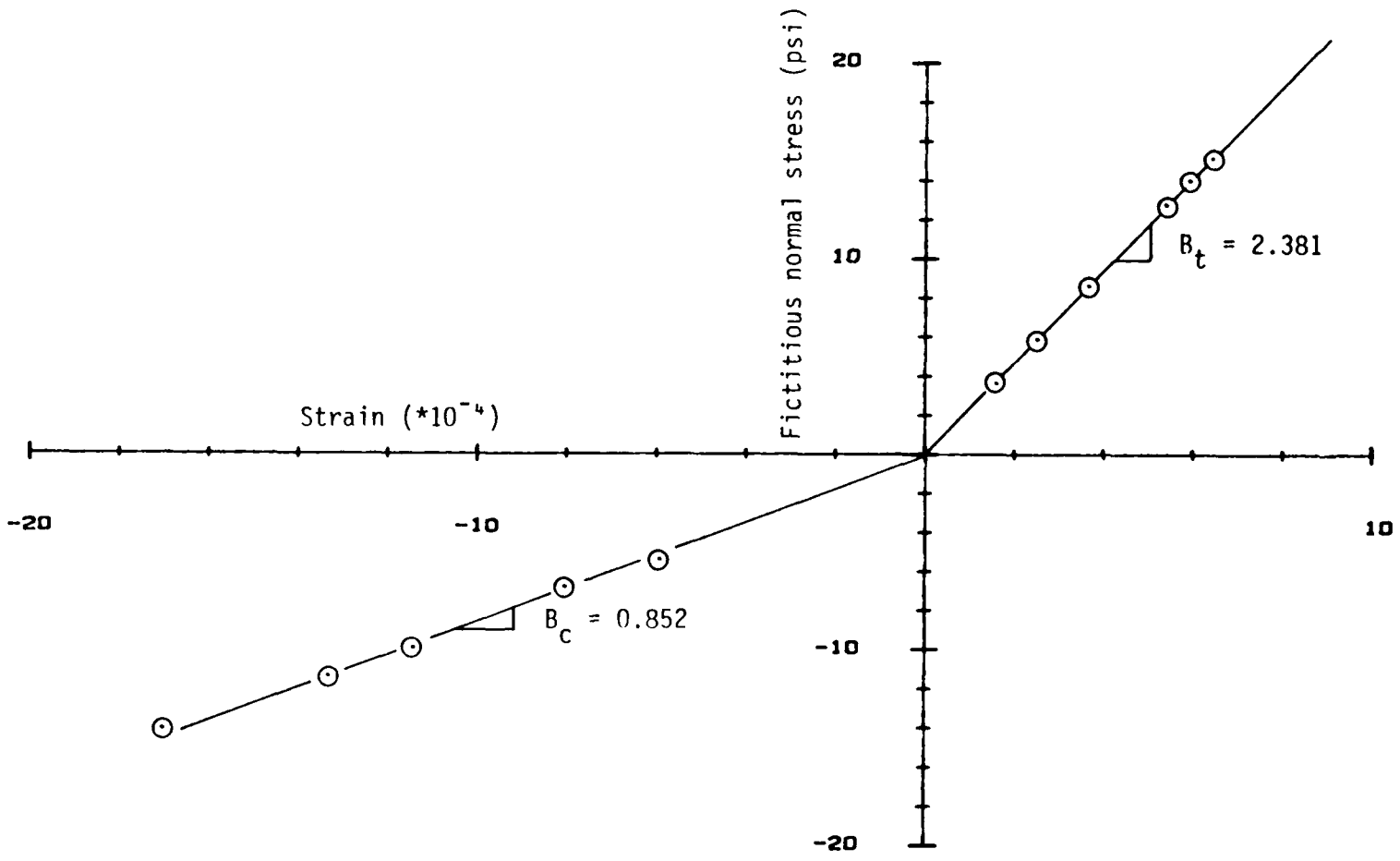

Figure 3.16 Bending calibration of contact stress gage, gage no. 4

Table 3.5

Bending calibration results of the contact stress gages

Contact stress gage no.	B_t*	B_c*
3	2.174	1.667
4	2.381	0.852
5	1.709	1.111
6	1.905	1.408
7	2.128	1.471

* B_t = Bending-correction factor for tensile strain.

* B_c = Bending-correction factor for compressive strain.

3.5 Conclusions for the Development of the Dynamic Stress Gages

Two types of dynamic stress gage were built at UCB. The first type is the surface stress gage which is used to measure the overpressure of an air blast loading. The second kind is the contact stress gage which is used to detect the dynamic normal stress acting on an underground structure. The design of the gages follows most of the criteria given from the past studies.

Numerical integration is employed in converting the gage signal to a pressure history. Data reduction, starting with the analog signal of the gage and resulting in a pressure history, has been shown to work easily and successfully. Calibrations of the gages include the surface stress gage under 3-D loading, the surface stress gage under 1-D loading, and the contact stress gage under 1-D loading. The results of these calibrations confirm the good performance of both types of gages. The bending response of the contact stress gage necessitates the strain measurement at the location of the contact stress gage in order that the correction of the bending response could be deduced and applied to the gage output.

The contact stress gage has been found to work independently of the overburden pressure, the density of the soil, and the type of soil. Calibration conducted on the surface stress gage also shows that the surface stress gage calibration constant is independent of the loading rate.

The advantages of these dynamic stress gages include the following: (1) the gages are very light in weight so that the inclusion of the gage is very small (the surface stress gage weights 1.8 grams and the contact stress gage weights 1.7 grams); (2) they are rugged and durable; (3) the calibration constant is stable; and (4) most importantly, they deliver reliable pressure measurements.

CHAPTER IV

CENTRIFUGE TEST HARDWARE

The most important ingredients in a centrifuge test are: (1) the centrifuge itself; (2) the loading system; (3) the test model including the soil; and (4) the instrumentation and data acquisition system. This chapter first describes the centrifuge. Then the design and construction of the model and the loading system are detailed. The instrumentation and data acquisition system are presented in Chapter 6.

4.1 The Centrifuge

A centrifuge provides an artificial gravity field that elevates the stress level in the centrifuge test soil model so that the stress field of the prototype is properly simulated. Since the properties of soil depend very much on the stress level, a centrifuge becomes a powerful tool for the model testing of soil. The centrifuge used in this research is located in the Geotechnical Laboratory of the Civil Engineering Department at UCB. The centrifuge has two swinging baskets, 56 electric slip rings, and 2 hydraulic slip rings. The machine is rated as 10 g-tons.

Figure 4.1 shows a schematic view of the centrifuge. Table 4.1 lists the dimensions and the specifications of the machine.

4.2 The Loading System

To generate a controlled impact loading in the centrifuge was one of the most challenging parts of this research. Past researchers utilized explosive and projectile guns to produce impact loading in centrifuges (Schmidt, 1978; Schmidt and Holsapple, 1980; Nielson, 1983). The present research employs an impact generator which works in a different way than the above mentioned methods. The impact generator was designed and built at UCB. Figure 4.2 shows an expanded view of the impact generator mounted on the centrifuge sample container.

The impact generator works like a shock tube which is often used to create a shock wave for the study of supersonic aerodynamics. When conducting a test, the pressure vessel is pressurized by a nitrogen tank to a desired pressure level. A pressure regulator located between the tank and the pressure vessel is used to keep a constant pressure supply. A rupture disk placed in the middle of the rupture disk holder will hold this pressure for a certain amount of time which is termed the yielding time. After the yielding time has elapsed, the disk will rupture suddenly and send out a pressure

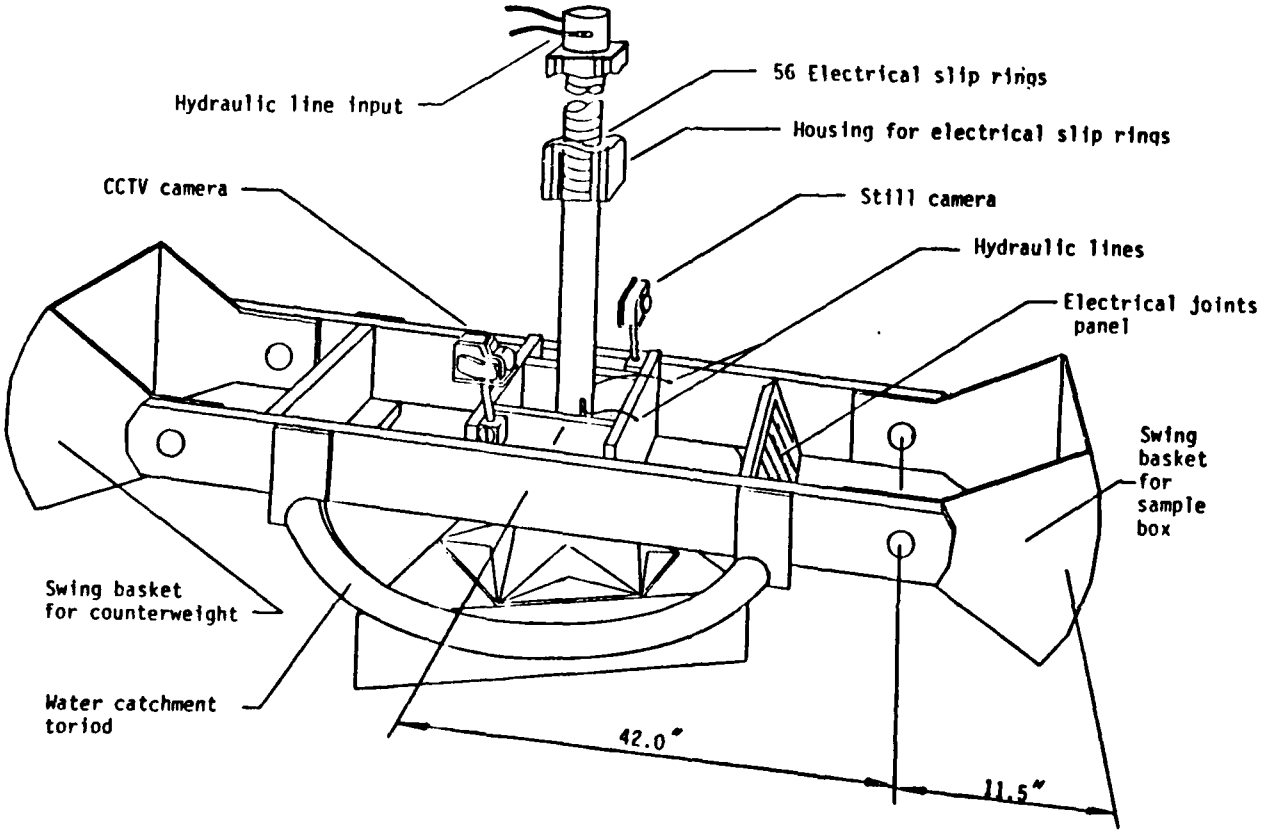

Figure 4.1 Schematic view of CUB 10 g-tons centrifuge

Table 4.1

Centrifuge specifications

Manufacturer	Genisco
Model	1230-5
G-Range	Variable 1 to 262 g at 42 in nominal radius
Driving System	25 HP hydraulic
Working Radii	42.0 in - center to basket hinge 11.5 in - hinge to basket floor
RPM Range	0-470 RPM
Payload Capacity	20,000 g lbs (200 lb at 100 g)
Test Package Size	18 in^3 maximum
Electrical Pick-ups	56 slip rings
Fluid Transfer	2 hydraulic slip rings
Test Recording	Closed circuit TV 35 mm SLR camera

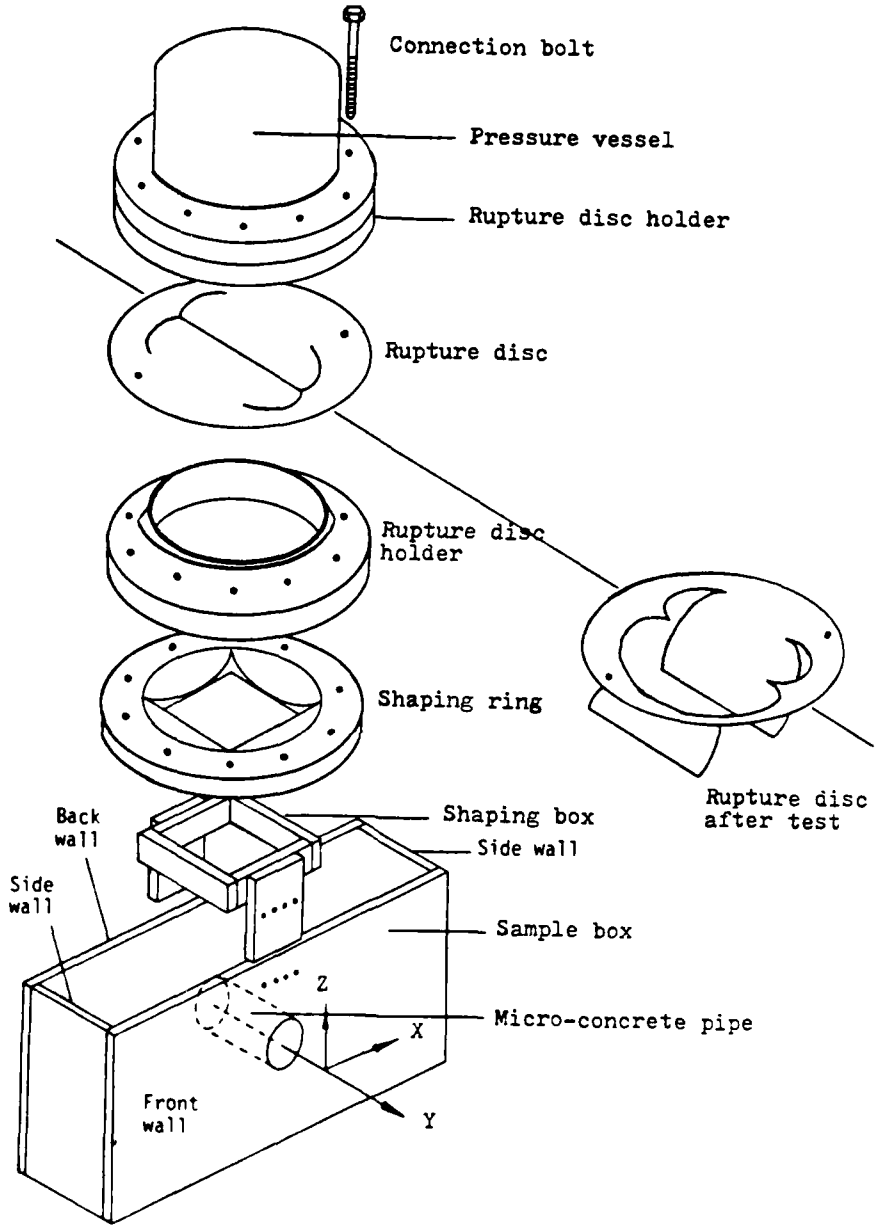

Figure 4.2 Expanded view of impact generator and centrifuge sample box

wave. This wave will pass through the shaping ring which has a circular opening on the top and a square opening at the bottom. The wave will keep travelling downward through the shaping box until the surface of the sample is encountered.

The rupture disk holder was purchased from Fike Company. In industrial application, the rupture disk and its holder are used as an emergency pressure release device. Fike Company also supplies rupture disks. However, in considering the large number of tests in the present program, it was decided to manufacture the rupture disks in house.

Before the impact generator was built, a calculation was made for estimating the air blast pressure that can be generated by the impact generator. The equation used is :

$$p = \rho v^2/2 \qquad (4.1)$$

where p : pressure,

ρ : mass density of the fluid, and

v : speed of the fluid.

If it is assumed that the average velocity of the nitrogen after the rupture occurs is equal to the speed of sound, knowing the mass density of nitrogen at the atmospheric pressure, the pressure, p, is calculated to be equal to 37 psi. This rough estimation is very

close to the value calculated from the shock strength analysis which is presented next.

A further evaluation of the air blast pressure was conducted utilizing the shock strength calculation. The term, shock strength, is the magnitude of the shock wave generated by a shock tube. Figure 4.3 shows a shock tube. A diaphragm located at the middle of the shock tube is used to separate the high and the low pressures on opposite sides of the tube. When the diaphragm breaks, a shock wave will travel from the location of the diaphragm to the low pressure (left) side of the tube and at the same time an expansive pressure wave will travel to the high pressure (right) side of the tube. The shock strength p_2, i.e., the magnitude of the shock wave, can be calculated by the basic shock strength equation:

$$\frac{p_4}{p_1} = \frac{p_2}{p_1}\left[1 - \frac{(r_4-1)(a_1/a_4)(p_2/p_1-1)}{\{2r_1[2r_1+(r_1+1)(p_2/p_1-1)]\}^{1/2}}\right]^{-2r_4/(r_4-1)} \tag{4.2}$$

Where

p_4 : initial high pressure or upstream pressure,

p_1 : initial low pressure or downstream pressure,

p_2 : shock strength or air blast pressure,

a_4 : speed of sound in the high pressure chamber,

a_1 : speed of sound in the low pressure chamber.

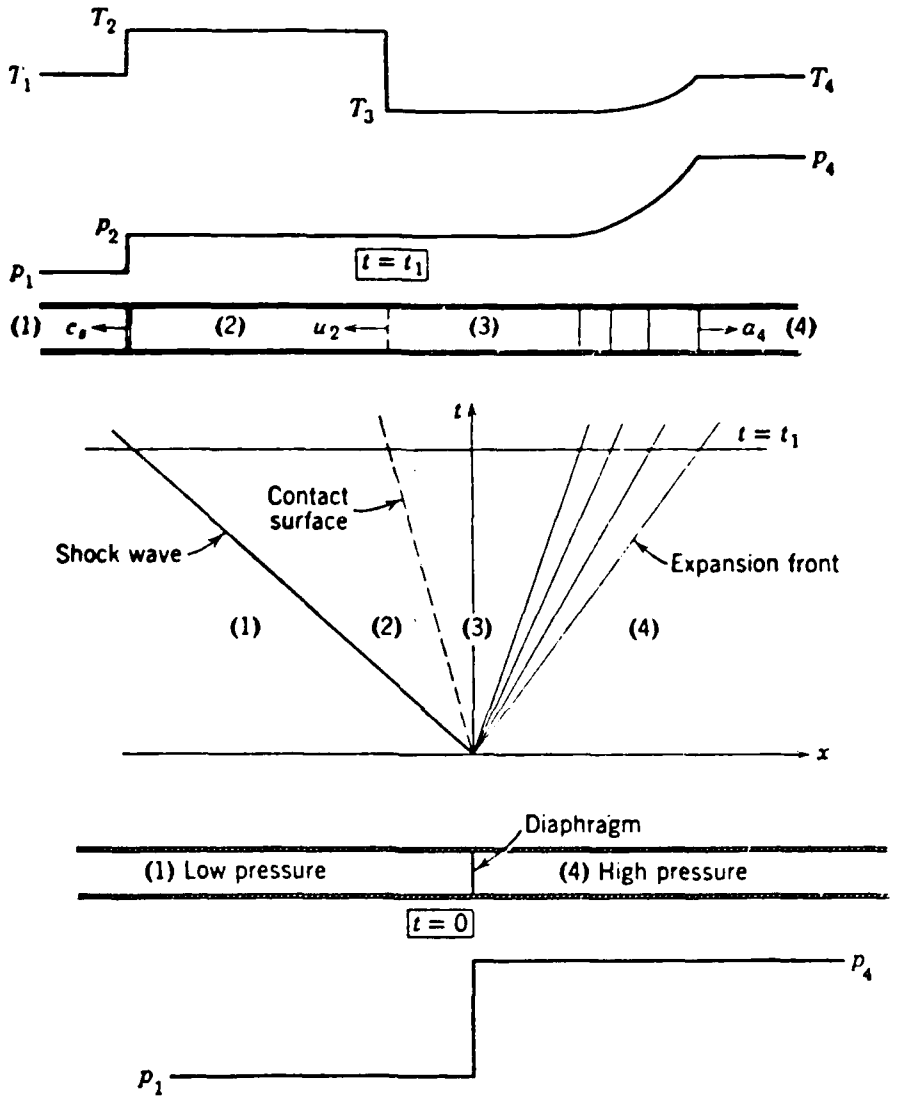

Figure 4.3 Motion in a shock tube. (After Liepmann and Roshko, "Element of Gasdynamics", 1957, pp. 81)

Subscripts 1 and 4 in Equation (4.2) stand for the low pressure chamber and the high pressure chamber, respectively. The term, r, is the gas constant which is equal to the ratio of C_p/C_v, i.e., the ratio between the specific heat of the gas at constant pressure to the specific heat of the same gas at constant volume.

The speed of sound in a gas, a, is related to the thermodynamic temperature, T; the universal gas constant, R; and the specific heat ratio, r:

$$(a_1)^2 = r_1RT \quad \text{and} \quad (a_4)^2 = r_4RT \qquad (4.3)$$

In a short time interval after the rupture of the diaphragm, the temperature can be assumed to be the same on both sides of the diaphragm. The ratio of a_4/a_1 can be obtained by knowing r_4 and r_1, which are the gas constants of nitrogen and air, respectively.

Knowing the ratio of a_4/a_1, the shock strength, p_2, in Equation (4.2) can be calculated for any pressure ratio, p_4/p_1, where p_1 is taken as the atmospheric pressure. Results of calculations show that for an upstream pressure of 90 psi the shock strength is 34 psi. This pressure is very close to the estimated value of 37 psi obtained by Equation (4.1).

After the impact generator was built, a series of tests were performed to measure the magnitude and the

distribution of the air blast. These tests are called stress distribution tests, and they will be presented later. For now, it is worth mentioning that the results of the stress distribution tests show that the air blast pressure generated by a 90 psi upstream pressure is about 30 psi. These results confirm the shock strength calculations.

4.2.1 The Rupture Disk

The key feature of the impact generator is the rupture disk. It determines the shape of the pressure wave. This is important because if a uniform pressure distribution on the soil surface can be achieved, the soil-structure system can be treated as a two-dimensional boundary value problem provided that the properties of the soil and the structure are also uniform.

It can be seen from Figure 4.2 that a plane strain simulation in the x-z plane can be applied to the soil-structure system if the following conditions are true: (1) the applied pressure is uniform in the y-direction; (2) the properties of the model pipe are uniform in tne y-direction; (3) the properties of the soil is uniform in the y-direction; and (4) the wall friction is negligible.

Conditions (2), (3) and (4) are not difficult to achieve, and will be justified later. Condition (1) requires more elaboration and will be discussed herein.

Thin aluminum plates were considered the ideal material for making the rupture disks because they are soft enough that the plate can be deformed by the edge of the rupture disk holder to achieve an air-tight seal, and aluminum has a high tensile strength such that a high pressure can be held before rupture.

The aluminum plates were ordered from Ryerson Aluminum. Plates of different thicknesses and made of aluminum alloys of different heat treatments are available. Different heat treatments of the material produce different stiffnesses. Generally, a stiffer plate is preferred because it is more brittle; thus, when they rupture, they generate a higher fluid velocity and, hence, a stronger impact. However, the plate cannot be too stiff for the reason of the air-tight seal.

Four different aluminum plates were tried. The first three were all of 3003 series alloy having different thicknesses, 0.015, 0.020 and 0.025 inches respectively. The results indicated that the 3003 aluminum is too soft, hence when the disk ruptured it did not open fully. A stiffer aluminum plate, 5052-H32, 0.020-inch-thick, was then tried. The results showed that the disk ruptured forcefully and opened fully.

Thus, this material was chosen for making the rupture disk.

After the material was decided upon, the stress distribution under the shaping box was measured. A special way of scratching the rupture disk was employed to do a repeatable and uniform stress distribution. This is presented in the following section.

4.2.2 Stress Distribution Test

The purpose of the stress distribution test is twofold; first, to find the stress distribution of the air blast loading that is produced by the impact generator, and, second, to find a way of scratching the rupture disk so that a uniform stress distribution can be achieved.

It has been shown in Chapter 3 that if a 0.1-inch-thick rubber pad is used along with the surface stress gage, its performance is independent of the material that the gage is sitting on. According to this conclusion, the stress distribution measured by having the surface stress gages and the rubber pads seated on a thick aluminum plate will be the same as having the gages and the rubber pads seated on the soil directly. This make the stress distribution tests very easy, because the stress distribution can be obtained by just mounting the gages on a thick aluminum plate. This aluminum plate was 1 inch thick and was bolted to the

bottom of the shaping box as shown in Figure 4.4. Eleven gages were used in the stress distribution tests.

At first, a uniform stress distribution in the x-y plane was sought. The rupture disk without any scratch was used; however, it was soon found out that the rupture pattern of the disk varied randomly. The next trial was to make a small indention at the center of the disk. It was hoped that the rupture of the disk would initiate from the indention and end up with an axi-symmetric opening. This idea did not work because the indention caused a significant stress concentration so that the disk simply split a small distance at the center without giving a sudden rupture.

The next idea was to make a cross-shaped scratch at the center of the disk as shown in Figure 4.5. If the scratch can have a uniform depth then the disk should open into four slices when it breaks. It was expected that a uniform pressure distribution can be obtained in this way.

A spring-loaded cutter was built for making scratches of uniform depth. The cutter is shown in Figure 4.6. It is made of a wooden block. A slot at the bottom of the block is made to accommodate a steel bar which is hinged on the wooden block. A blade is mounted on one end of the bar. The other end of the bar is attached to a spring. While there is no load on the

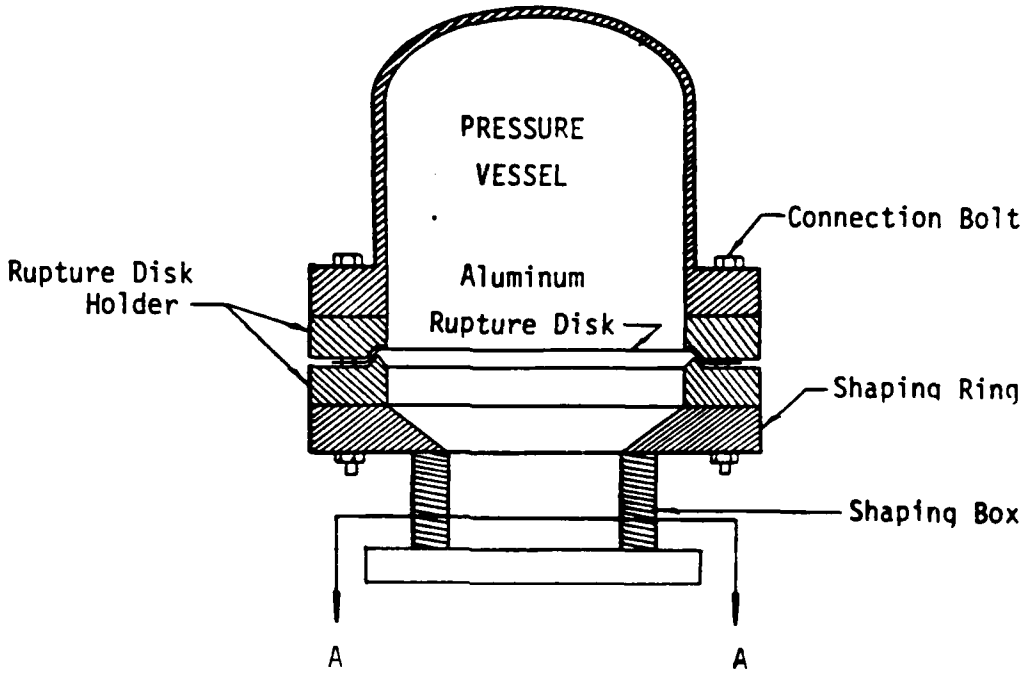

Section A-A

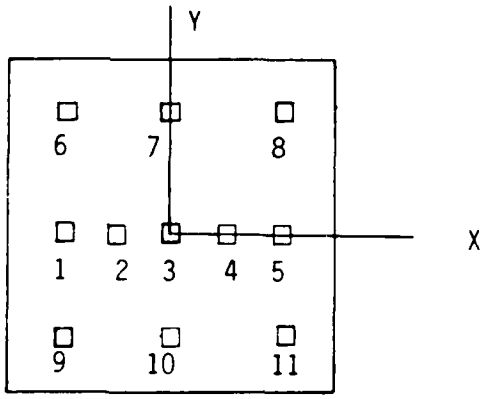

Figure 4.4 Test set-up for stress distribution measurement

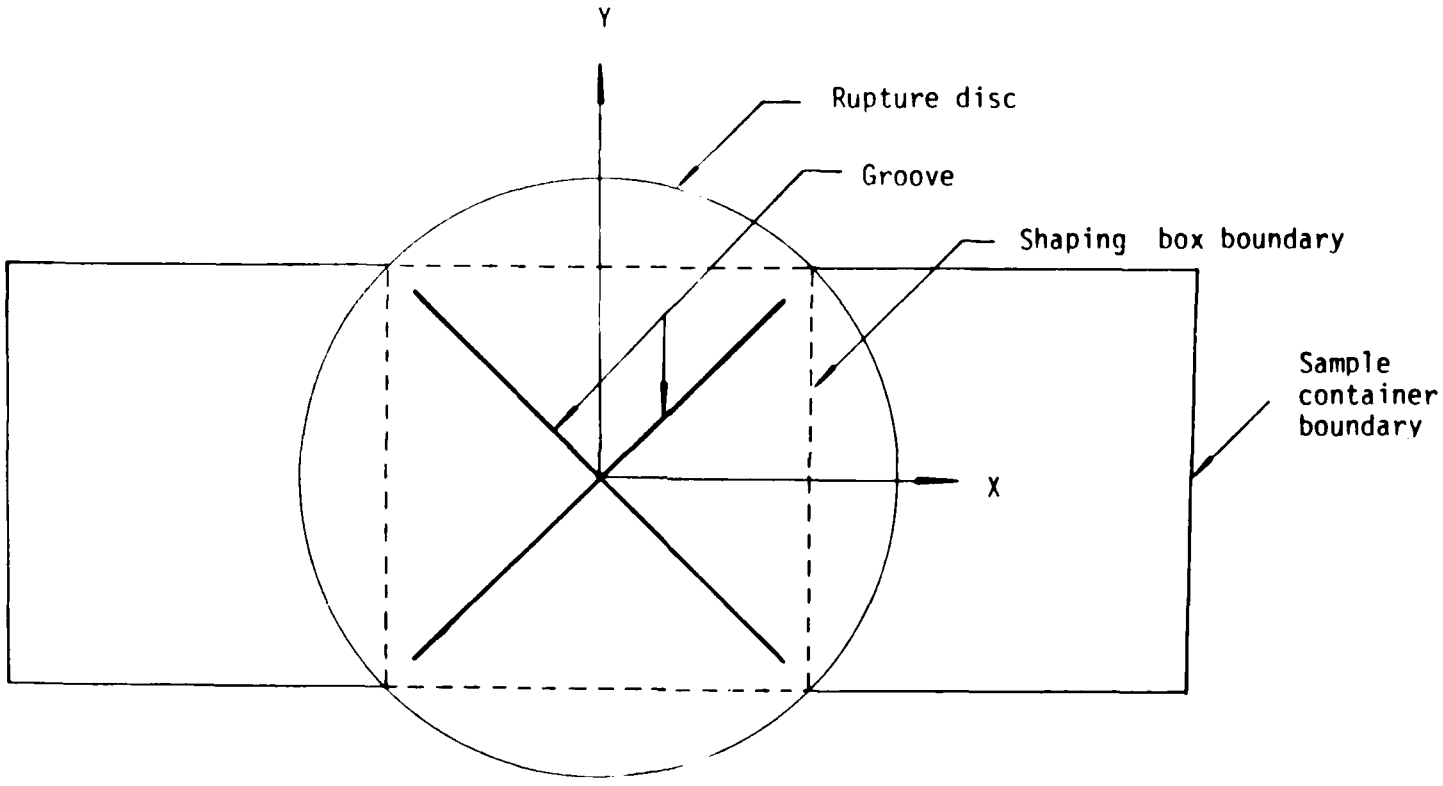

Figure 4.5 Rupture disc with a cross-shaped scratch

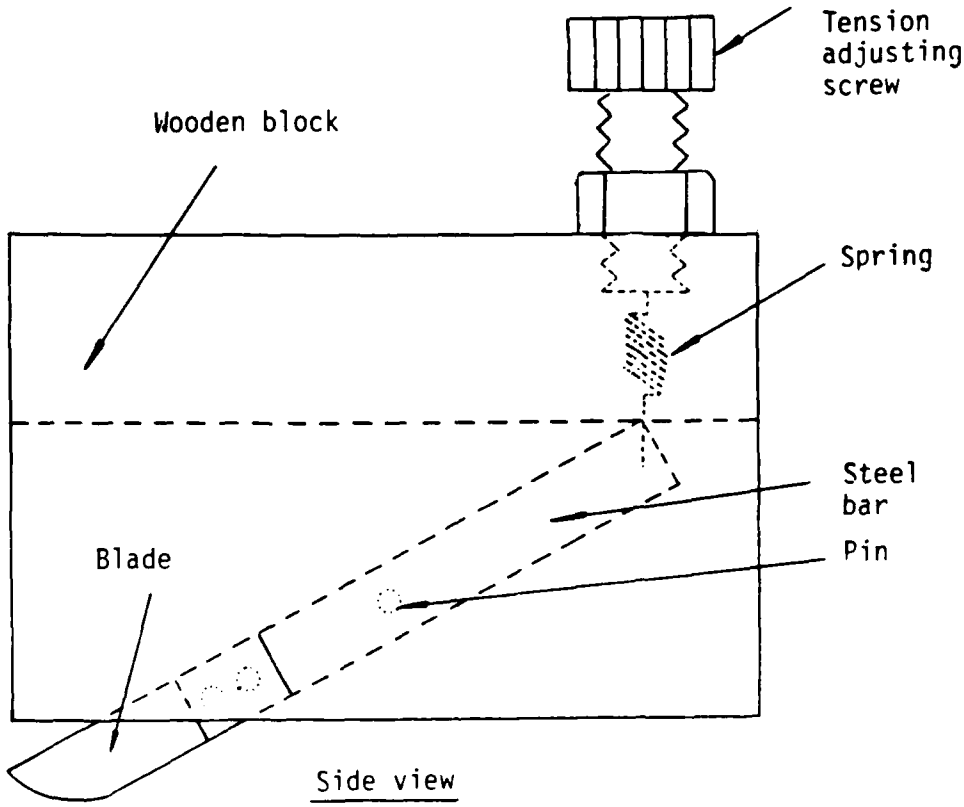

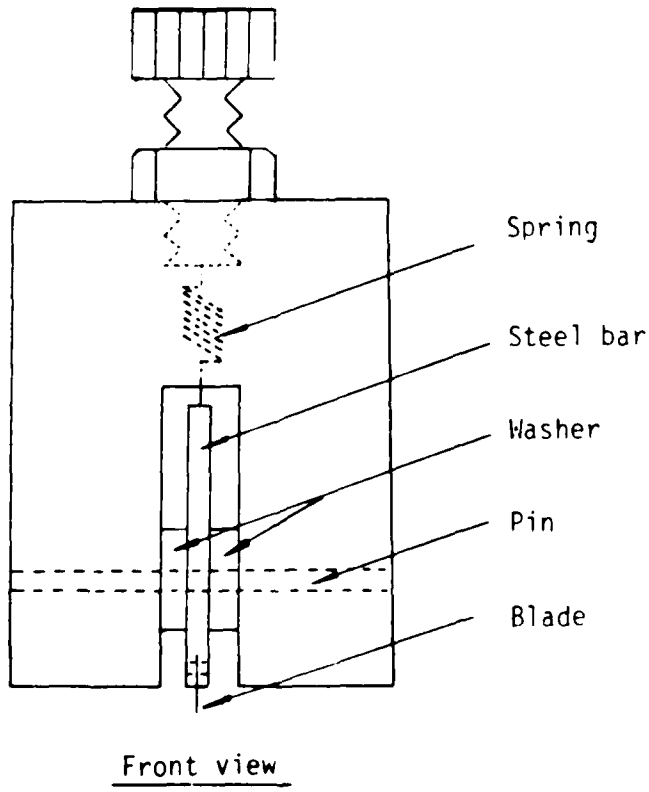

Figure 4.6 Groove cutter for rupture disc

spring, the blade projects out of the bottom face of the cutter. When the cutter is pressed down the spring load increases until the bottom face of the cutter contacts the rupture disk. At this point, The blade exerts a constant load on the disk. Hence, sliding the cutter on the surface of the disk will make a scratch on the disk of a uniform depth. The spring is attached to a bolt which can be adjusted to go up and down with respect to the body of the cutter so that the spring load on the steel bar can be adjusted and thus scratches of different depths can be achieved.

Rupture disks with cross-shaped scratches made by the cutter were tried. Test results showed that the disk always open into two halves instead of four slices. This result was attributed to the anisotropy of the aluminum plate.

The above test results inspired a new idea. That is, instead of making two grooves on the disk and have no control of which one will be followed when the disk ruptures, it might be better to have only one scratch in the y-direction as shown in Figure 4.7. It was expected that if the rupture disk is oriented in this way the stress distribution of the air blast could be uniform in the y-direction. This is one of the requirements for the plane strain assumption. Also, if the disk opens evenly, the stress could be symmetric about the center line of

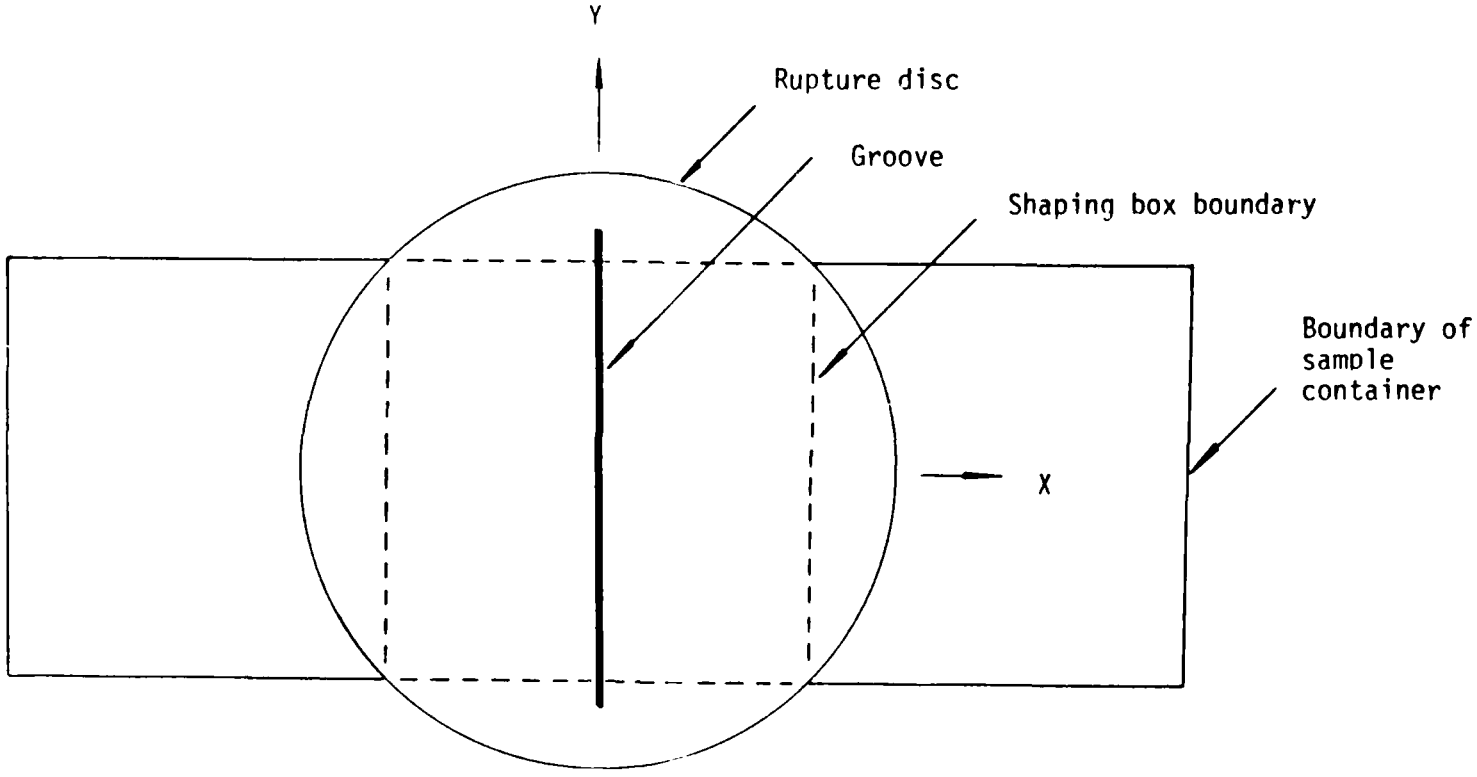

Figure 4.7 Rupture disc with a scratch in the y-direction

the x-z plane. This adds one more advantage to the analysis since only half of the x-z plane would be required.

Several tests were conducted with only one scratch at the center of the rupture disk. The results showed that not all the ruptured disks rupture into two halves. For those disks which did rupture into two halves, a crack at both ends of the scratch developed along the x-direction. Hence, in order to have better control with the opening of the disk, an I-shaped scratch, as shown in Figure 4.8, was attempted.

The I-shaped scratch did increase the consistency of rupturing into two halves. However, a close examination on the pattern of the ruptures revealed that they did not turn with a 90-degree angle from the y to the x-direction like the scratches do. Instead, they changed direction with a curved path.

An improved I-shaped scratch as shown in Figure 4.9 was thus tried. It was found that with the main axes of the improved I-shaped scratch aligned with the grain of the aluminum plate (as shown in Figure 4.9), the disk ruptured in a very consistent manner. Hence, the curved I-shaped scratch was considered the best scratch pattern and was used for the stress distribution and the centrifuge tests. Figure 4.10 shows the result of a typical stress distribution test. The figure indicates

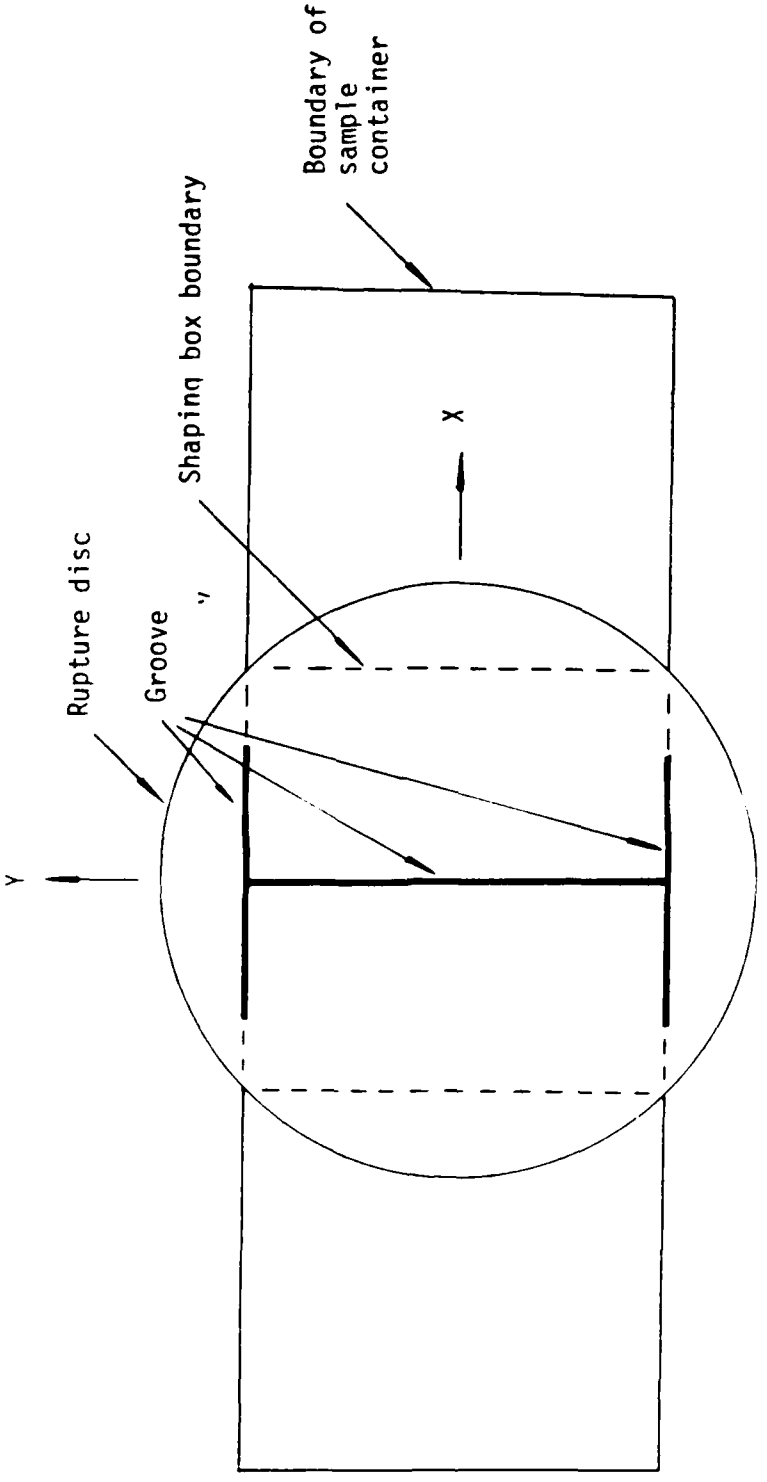

Figure 4.8 Rupture disc with an I-shaped scratch

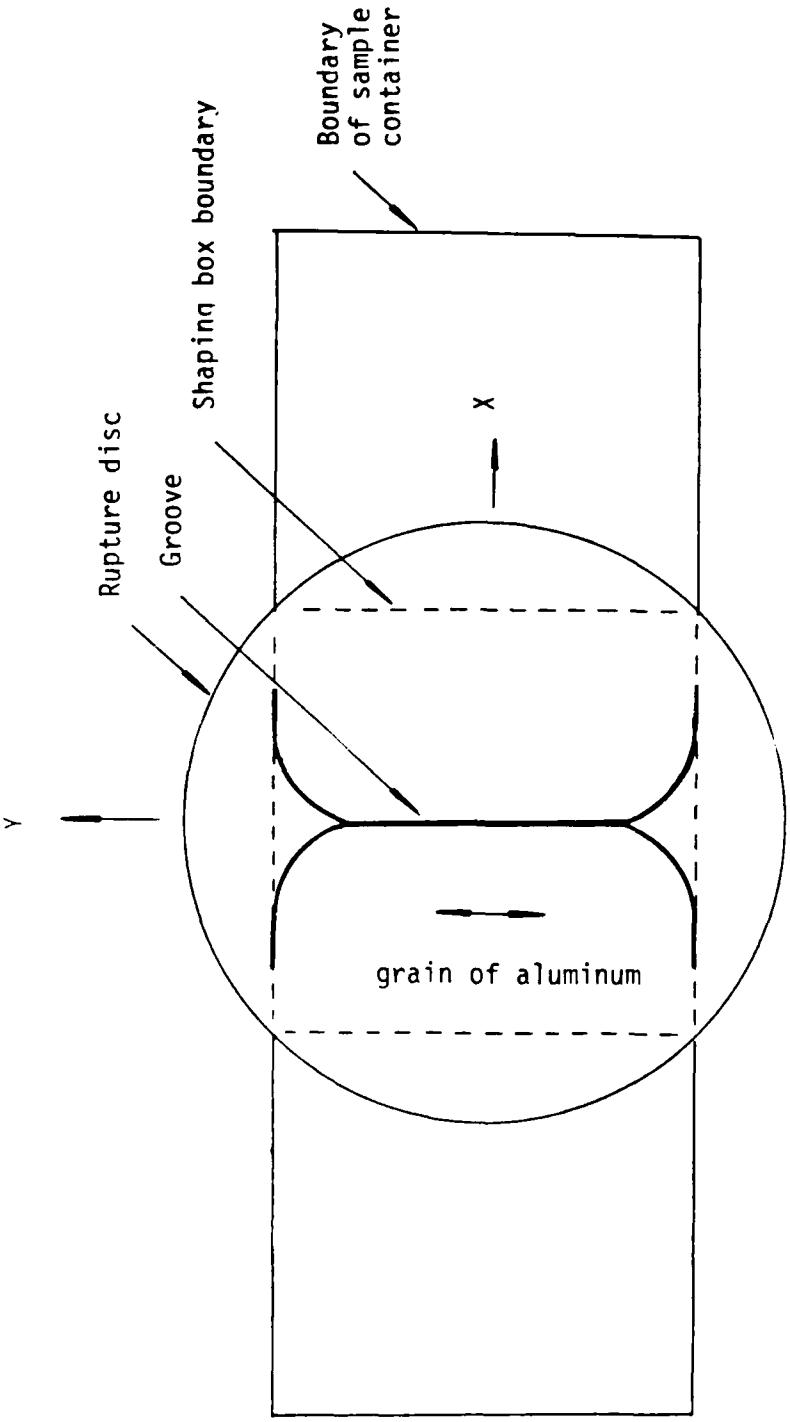

Figure 4.9 Rupture disc with an improved I-shaped scratch

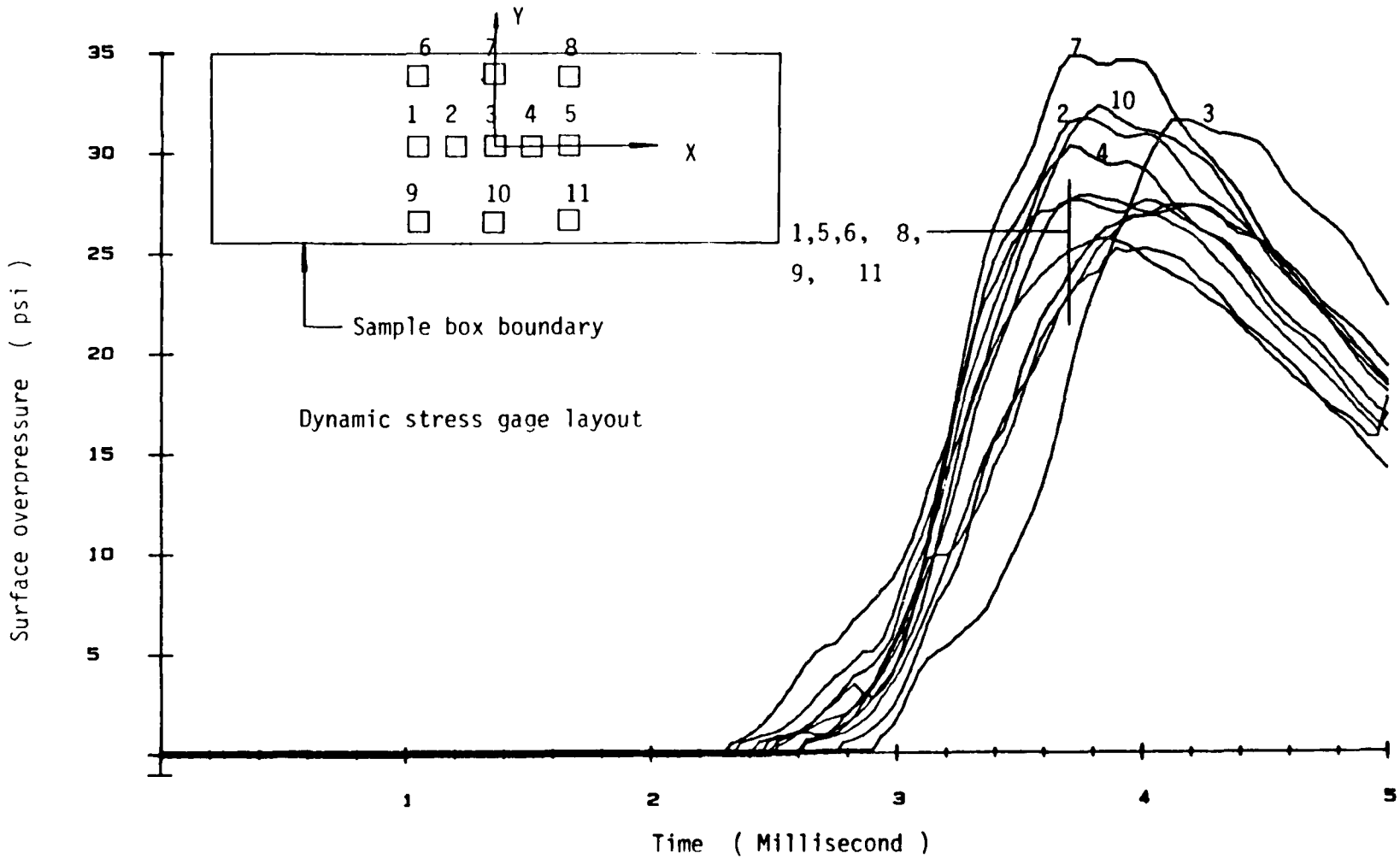

Figure 4.10 Measurement of surface overpressure distribution, test 12PCSG

that the pressure of the air blast is uniform in the y-direction and symmetric about the y axis. In addition, the magnitude of the pressure is about 30 psi for an upstream pressure of 90 psi, which is very close to the result of the shock strength calculations.

4.3 Centrifuge Test Model

4.3.1 Sample Container

The sample container is made of high strength aluminum plates. Figure 4.11 shows the centrifuge sample container with a coordinate system. The x-z plane is the plane of plane strain. It may seem that the width of the sample in the y-direction is too small for the plane strain assumption. However, it will be shown later that the friction on the side walls of the sample can be reduced effectively by a friction-reducing membrane.

The width of the sample container was chosen to be 5.5 inches such that the air blast loading could cover the whole width of the sample. The 8 in. diameter rupture disk holder was chosen mainly because of the payload limitation of the centrifuge.

Figure 4.12 shows the in-flight position of the sample container with respect to the rotation axes of the centrifuge. Centrifugal acceleration is equal to rw^2, where r is the radius of rotation and w is the angular velocity. It can be seen from the figure that

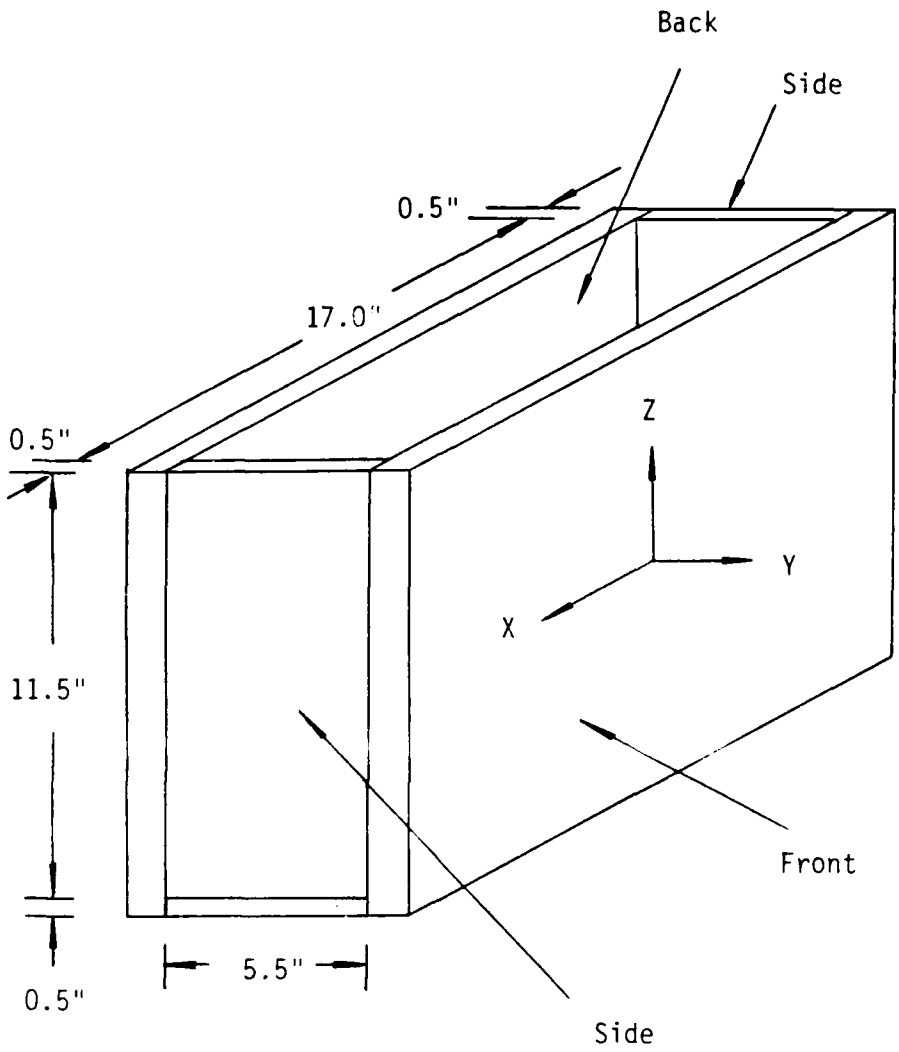

Figure 4.11 Schematic of sample container

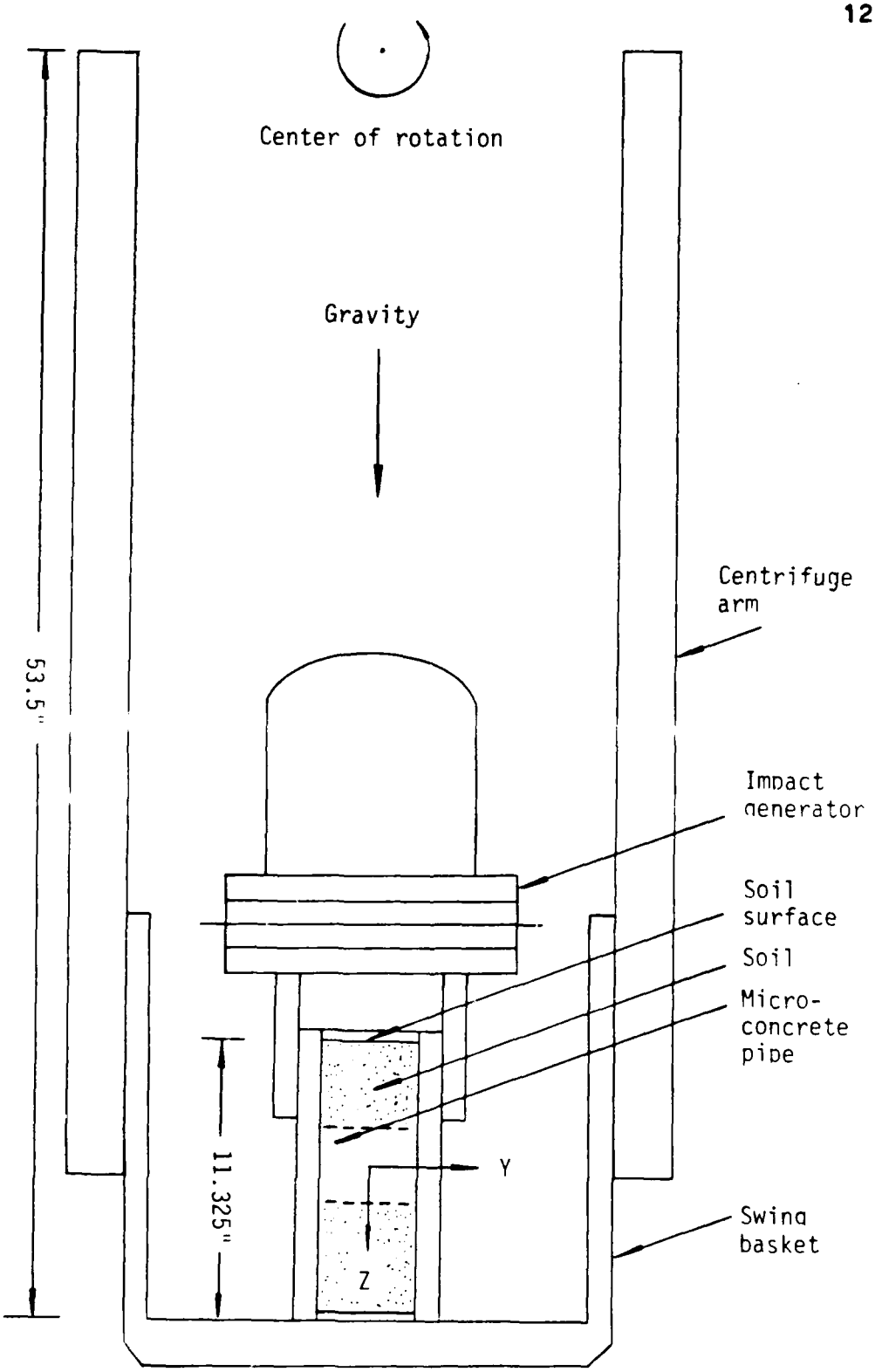

Figure 4.12 The in-flight position of the sample container and the impact generator

the radius of rotation varies from point to point in the centrifuge sample. That is, the acceleration field that the sample is subjected to during the test is not uniform in the sample. This nonuniform centrifugal acceleration field in the sample is a common problem for centrifuge tests. An increase in the length of the arm of the centrifuge will lead to a smaller variation in the acceleration field, which is the advantage of a larger machine. In this research, the variation of acceleration field along the width of the sample is trivial because the width of the sample is small. The height of the soil sample is 11.325 inches, thus the acceleration varies 11 % from the top to the center of the sample.

The front and back walls of the sample container (perpendicular to the y-direction) each has a 3-inch-diameter hole. These holes allow the wires of the stress gages and those of the strain gages to pass from the inside to the outside of the sample container. The two walls are 1 in. in thickness. They have to be strong to sustain the static weight of the impact generator which will weigh about 4,450 pounds if the centrifuge is spinning at 50 g.

4.3.2 Friction Reducing Membrane

As mentioned before, in order to achieve a plane strain condition, the friction on the two faces of the

sample will have to be small. This is especially crucial for the narrow sample like the ones used in this research.

A search for a material to use to minimize the wall friction was therefore taken. The material tried was a latex membrane. This is the material used to make the sample membrane for standard triaxial tests. The membrane is very elastic. It was found that a thin layer of Mobil multipurpose grease in between the wall and the membrane could reduce the wall friction. Nevertheless, it also found that the membrane will absorb the grease in a couple of hours and increase the friction. Since it takes several hours for a centrifuge sample to be tested after it is made, it is not desirable to use the greased latex membrane. A thick layer of grease was tried but it was found that the membrane starts to deteriorate after several hours.

The next step was to submerge membranes in several different lubrication oils for 24 hours. Then the membranes were taken out of the oil pans and were cleaned and placed on an aluminum plate for another day. The best lubrication oil for the membrane was then decided by choosing the strongest and the most oily membrane. The best lubrication oil decided by this way was Mobil DTE medium heavy oil.

Careful observation revealed that when the membrane was submerged in the oil, it absorbed the oil at a noticeable rate in the first 7 days. This was recognized by noticing that the size (area) of the membrane keep expanding in this period of time. After 7 days, the membrane reached an area increment as much as 40%. At the same time the thickness of the membrane increased from 0.009 inches originally to about 0.012 inches.

Another observation was made on the following set-up: A piece of well-soaked membrane was wiped clean first and then placed on a clean aluminum plate, a layer of sand was rained on the top of the membrane and a small weight was put on the soil. The observation revealed that the oil in the membrane seeped into the soil continuously while a thin layer of oil was always maintained in between the aluminum plate and the membrane. The soil kept soaking the oil from the membrane until after about three days the membrane dried out and stuck to the aluminum plate.

A test was performed to determine the coefficient of friction between the friction-reducing membrane and the aluminum wall of the container. The test set-up was very similar to the set-up for the observation described above except that a load was added to the soil and the pulling force was measured. The test

set up is shown in Figure 4.13. A vertical load was applied to the block and the horizontal forces were taken at the moment the membrane started to slide over the aluminum plate. The ratio of the vertical load to the horizontal force is the coefficient of friction which is calculated as 0.0075. This is about one-seventh of the coefficient of friction between the soil and aluminum without the friction-reducing membrane.

4.3.3 Model Structure

The model structure is an important component in the study of soil-structure interaction. Past studies revealed that the arching effect of soil around a buried structure depends upon the shape and the rigidity of the structure (Getzler and Komornik, 1968; Allgood and Takahashi, 1972).

The shape of underground structures vary in a wide range. Since this research is not pertaining to any specific prototype, a pipe with a circular cross-section was chosen for this research.

A special material is used to construct the pipe. This material has properties similar to regular concrete but uses a finer aggregate. The advantages of using this material are: (1) the model pipe can have a very thin wall; (2) the rigidity of the pipe can be changed by changing the thickness of the pipe; and (3) the interface behavior is preserved in the model test.

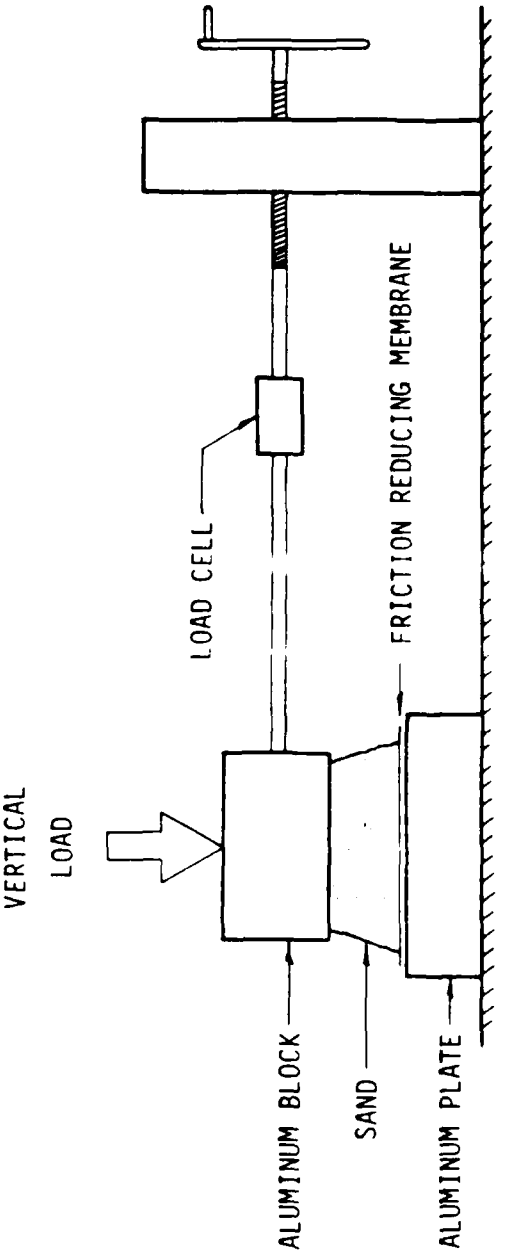

Figure 4.13 Test set-up for determining the coefficient of friction between the friction-reducing membrane and aluminum

The material used to construct the model pipe is called micro-concrete, and was developed by Townsend et al., (1985). Micro-concrete is made of a mixture of high strength gypsum, sand and water. When dry gypsum is mixed with water and sand, it crystallizes and grasps the sand together tightly. According to the recipe given by Townsend, micro-concrete is made of one part of high strength gypsum, 0.8 parts of sand and 0.25 part of water. Townsend also found that in order to produce a micro-concrete with a constant property, it is important to let the cast model or test specimen cure for 48 hours and then coat it with shellac to stop curing of the gypsum.

The high strength gypsum used in this research is purchased from U.S. Gypsum. The series number is ULTRACAL # 60. This particular gypsum has an additive to retard the crystallization process of the gypsum. But even so, the workable time after mixing is less than 15 minutes for the mixture with 0.25 parts of water. For this research, since the thickness of the thinnest pipe is only 0.2 inches, a low viscosity mixture is necessary so that it can be cast into the mold. This is achieved by using 0.35 parts of water. The higher water to gypsum ratio also increases the workable time of the mixture.

The micro-concrete is made by mixing one part of gypsum with 0.8 parts of Coyote Concrete sand in a

mixing bowl for 2 minutes, and then after 0.35 parts of water are added, mixing for an additional 2 minutes.

Coyote Concrete sand is a cohesionless medium sand. The sand was not only used for the aggregate of the micro-concrete but also used for the soil sample of the centrifuge model. The grain size distribution curve of the sand is shown in Figure 5.1.

Figure 4.14 shows the mold for making the model pipes from micro-concrete. The mold is composed of 4 detachable parts to allow casting and extraction. The pipes are formed by casting the micro-concrete in between the outer tube and the inner core of the mold. The top and bottom plates have two concentric slots which are used to hold the tube and the core in place. The top plate has an opening to allow the micro-concrete to flow into the mold.

The outer tube and the top and bottom plates are made of acrylic, whereas the inner core is made of cardboard pipe. Cardboard pipes are used because they can be torn down after the micro-concrete has set. This allows an easy extraction of the micro-concrete pipe from the acrylic tube.

The inner diameter of the outer tube is 4.0 inches. This is the outer diameter of the micro-concrete pipe. This dimension is fixed. However, the inner diameter of the micro-concrete pipe can be changed by

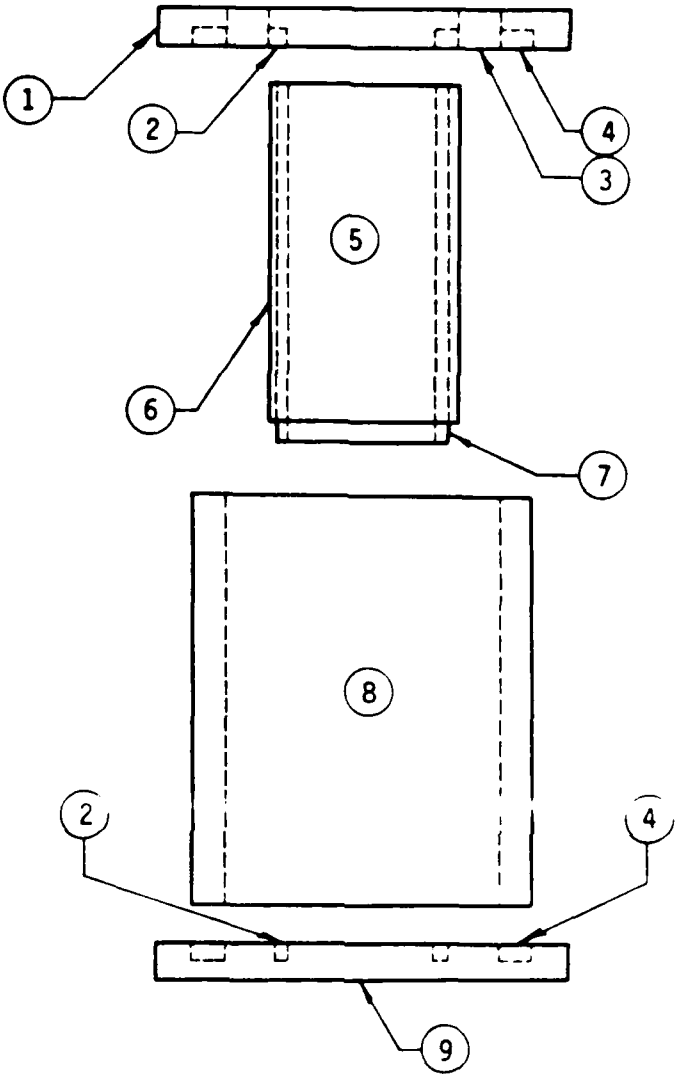

1) Acrylic Top Plate

2) Slot Accomodating the Inner Core

3) Slot for Casting the Micro-Concrete into the Mold

4) Slot Accomodating the Acrylic Outer Tube

5) Cardboard/Paper Inner Core

6) Adustable Paper Layers

7) Cardboard Core

8) Acrylic Outer Tube

9) Acrylic Bottom Plate

Figure 4.14 Mold for the construction of micro-concrete pipes

changing the outer diameter of the carboard core. This is achieved by wrapping layers of construction board on the core.

Casting the micro-concrete into the mold is accomplished with the help of a mechanical vibrating table and a tamping rod. The transparent acrylic allows viewing the micro-concrete in the mold to make sure all major voids have been eliminated. After the mold is filled, about 5 pounds of surcharge is placed on the top of the mold. The surcharge has been found to be necessary in keeping the micro-concrete from expanding and thus reducing the tendency to develop cracks. Test cylinders of 2 inches in diameter and 4 inches in height were made at the same time. These specimens were used in the determination of the strength properties of the micro-concrete. The tests included uniaxial compression and split tension tests. The results are presented in Chapter 6.

Both the micro-concrete pipe and the test cylinders were cured at room temperatures in the laboratory where the moisture content in the air is usually less than 20%. For the first 24 hours they were cured in the molds, and then they were cured for an additional 24 hours after extraction.

For the extraction of the micro-concrete pipe, the base and top of the mold were removed and then the

inner core was torn out. The micro-concrete pipe was then pushed out by a soil sample extruder.

After the curing was complete the micro-concrete pipe and the test cylinders were coated with shellac to arrest the curing.

Figure 4.15 shows a schematic view of a micro-concrete pipe with contact stress gages, strain gages, and rubber end pads mounted on it. The length of the micro-concrete was sanded down to 5.26 inches. Center and parallel lines were drawn on the pipe to position the contact stress gages and the strain gages. Five notches were cut on one end of the pipe. Each of the notches was located on the end of the parallel lines. The notches were 0.06 inches deep and 0.06 inches wide. They allowed the wires of the contact stress gages and those of the strain gages to pass from the surface of the pipe to the inside of the pipe.

The contact stress gages and the strain gages were placed at the center of the pipe as shown in Figure 4.15. The contact stress gages were attached to the pipe using double sided tape. Each contact stress gage was embraced by a curved retaining bracket to prevent the lateral stress from acting on the contact stress gages. A strip of friction-reducing membrane covering the contact stress gages and their retaining brackets was

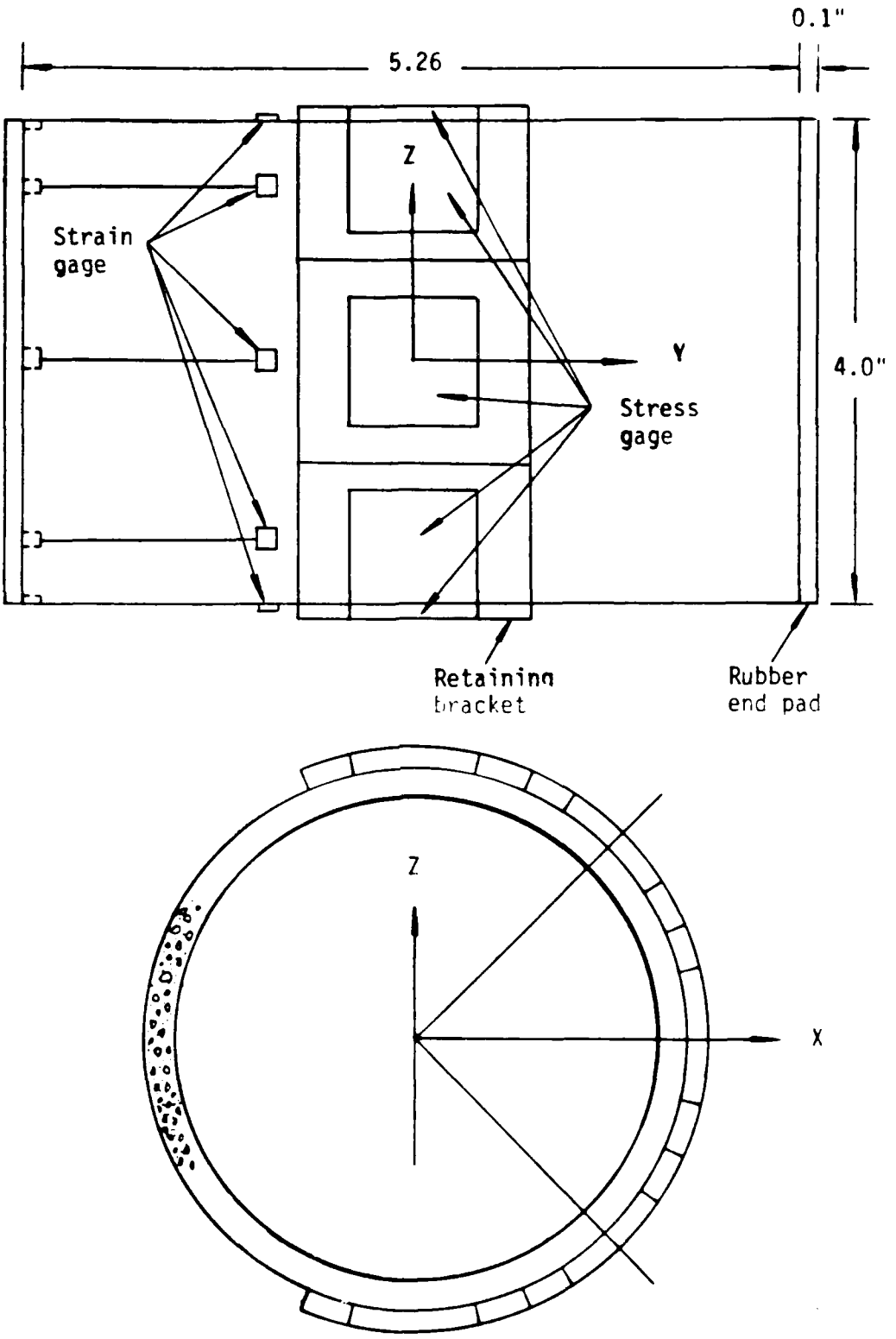

Figure 4.15 Instrumented micro-concrete pipe

used to keep the soil particles from falling into the gap between the gage and the bracket.

The strain gages were positioned besides the contact stress gages. The gages were Micro Measurement's foil gages, series number CEA-13-125UW-120. They were glued on the pipe by M-bond 200 which cures within 5 minutes under thumb pressure. The gages were protected by applying a layer of M-coat D which usually takes 12 hours to cure.

A ring of rubber pad was glued to each end of the micro-concrete pipe. These rubber pads ensure good contact with the friction reducing membranes in the centrifuge sample container. The thickness of these pads was 0.1 inches. The addition of the pads increased the total length of the pipe to 5.46 inches. Since the thickness of the friction reducing membrane is 0.012 inches, the micro-concrete pipe, the rubber pads and the friction reducing membranes fit between the front and back walls of the sample container exactly.

CHAPTER V

TEST PROCEDURE

The objectives of the experimental phase of this research are threefold: first, to develop dynamic stress gages for measuring dynamic overpressures produced by blast loadings on the soil surface and the soil pressures generated by the blast loadings on the model structure; second, to develop the test hardware for performing the centrifuge model test; and third, to establish a procedure for conducting the centrifuge test. The first and the second objectives were covered in Chapter 3 and Chapter 4, respectively. This chapter describes how the centrifuge tests were performed.

5.1 Test Preparation

5.1.1 Description of soil

The soil used in this research was a soil used in previous research conducted for Martin Marietta Corporation at the University of Colorado, Boulder. The soil was obtained from Coyote Concrete Company of Albuquerque, N.M., and is called Coyote Concrete Sand. It is a cohesionless medium sand, light brown in color

and odorless. Classical soil property tests were performed in the previous research. These tests include specific gravity test, grain size analysis, relative density tests, permeability tests, and triaxial shear tests (Ko, et al., 1984). Figure 5.1 shows the grain size distribution curve of the soil and Table 5.1 lists the results of the classical soil property tests.

The above test results were only used as a reference for this research because of the following two reasons: first, the soil was sieved by a no. 20 sieve for this research, and second, the soil used in this research was at its air-dry conditions, whereas the soil was tested with 7% moisture content in the previous research.

It was necessary to remove the soil grain larger than the no. 20 sieve because the larger soil grains might destroy the friction-reducing membrane in the centrifuge test. Also, since the soil was also used as the aggregate for the micro-concrete, the larger soil grains had to be removed for the construction of the 0.2-inch-thick micro-concrete pipe. Air-dry soil was used because it allowed an easier preparation of the centrifuge sample.

Conventional triaxial compression tests, hydrostatic compression tests, and one-dimensional confined compression tests were conducted for the

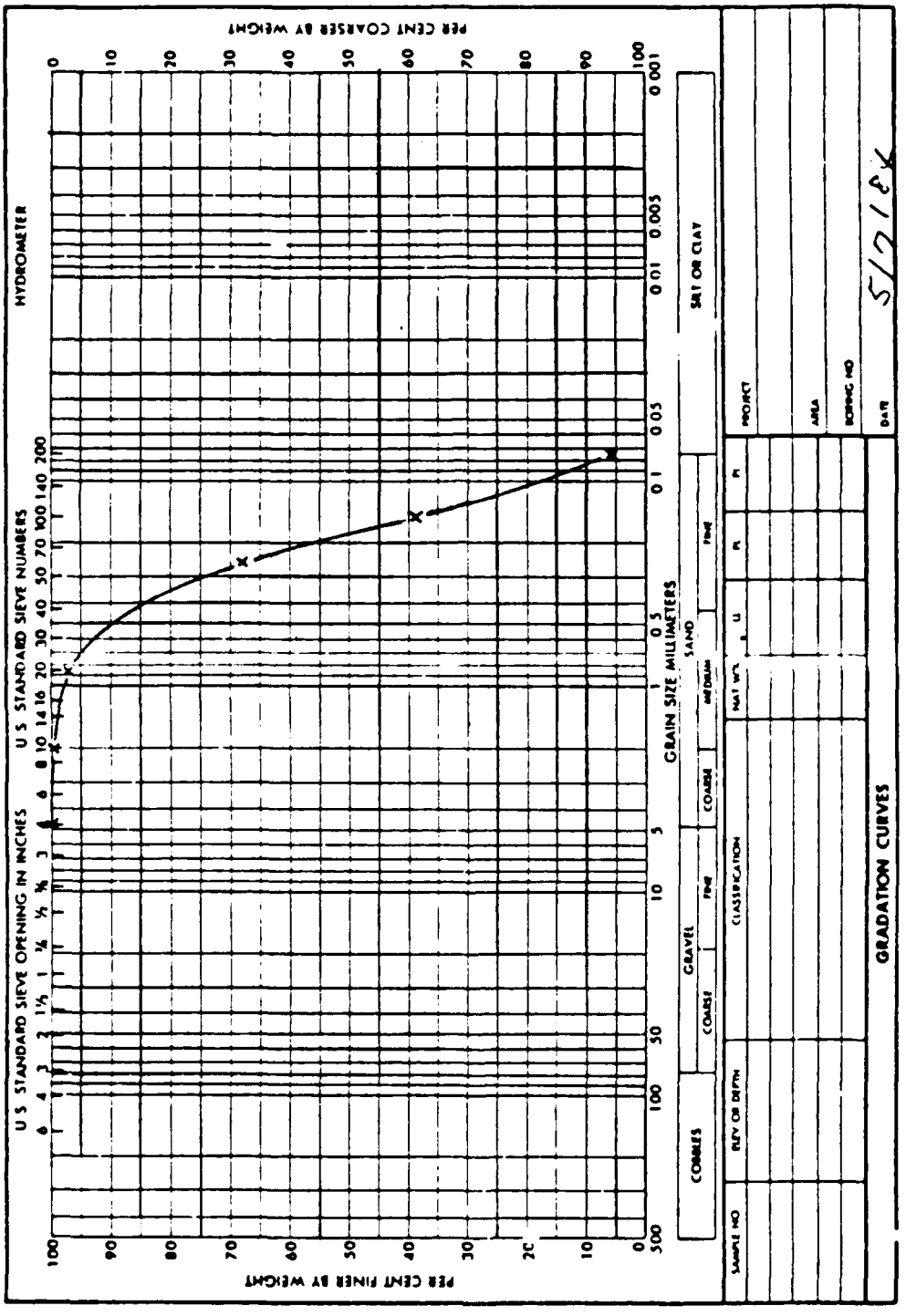

Figure 5.1 Grain size distribution curve of Coyote Concrete sand

Table 5.1

Properties of Coyote Concrete Sand

Maximum dry density	113.3 pcf
Minimum dry density	90.8 pcf
Maximum void ratio	0.89
Minimum void ratio	0.49
Specific gravity	2.71

Relative density (%)	Internal friction angle (degree)
60	38.3
80	39.8
90	40.6

Relative density (%)	Permeability (ft/sec)
60	6.9×10^{-6}
80	5.2×10^{-6}
90	4.6×10^{-6}

sieved, air-dry Coyote Concrete Sand. The results of these tests were used to calibrate a non-linear constitutive soil model which will be described in Chapter 6.

5.1.2 Sample Preparation

In many engineering fields, model tests are frequently used to verify designs or to validate analytical solutions. It is trivial, yet it is very important, to a modeler to recognize that the essence of his work is the quality of the test sample. A sample is considered to have a high quality provided that: (1) its boundary conditions are well controlled; (2) the properties of the sample material are well defined; and (3) the sample can be reproduced from test to test.

In tests involving soil-structure interaction, it is difficult but critical to make a sample with good contact between the soil and the structure. This research utilized a vibrating table to construct the samples. Satisfactory results were obtained in regard to the contact condition. In addition, the samples made by the vibrating table were found to be uniform and a consistent relative density was always achieved.

Figure 5.2 shows the vibrating table, the sample container, and the two wooden collars for the sample preparation. Note that the sample was made by placing the soil in the y-direction which is perpendicular to

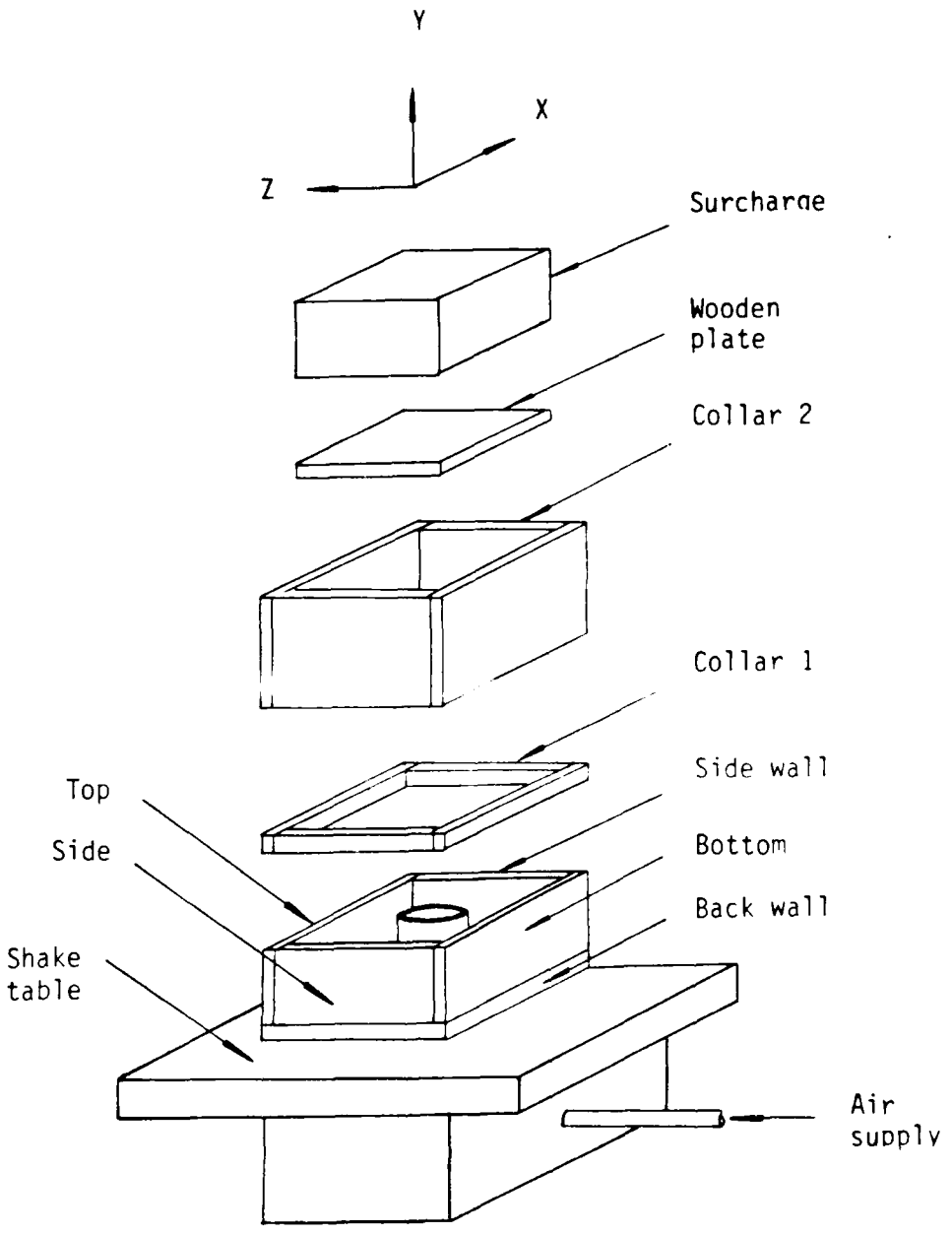

Figure 5.2 Plot shows the equipments for sample preparation

the directions of the air blast and the gravity loading. There are two advantages to this sample making scheme: (1) good contact between the soil and the pipe is achieved, and (2) uniform soil sample is obtained.

The density of the sample made by the vibrating table depends on: (1) the time of vibration; (2) the frequency of vibration; and (3) the amount of surcharge. The vibrating table is activated by pneumatic pressure and the frequency of vibration is dependent on the air pressure. Generally, a high air pressure (hence, a high frequency) will produce a high density sample, however, segregation will occur if the air pressure exceeds 40 psi. Segregation of the soil can be detected as its large particles merge to the soil surface. An air pressure of 30 psi was found to be adequate to make a dense sample without causing the soil to segregate. The following steps are followed in the sample preparation procedure.

(i) Two sheets of friction-reducing membrane (described in Chapter 4) were trimmed and placed on the front and back walls of the sample container. These two walls were the ones parallel to the x-z plane (see Figure 4.11). The air bubbles and the excess oil under the membranes were removed and the faces of the membranes were wiped clean.

(ii) As shown in Figure 5.2, the sample container was assembled except for the front wall, and placed on the vibrating table. The instrumented micro-concrete pipe was placed on the center of the back wall which has vertical and horizontal lines to match up the lines on the crown and the spring line of the pipe. The yires of the stress gages and the strain gages were passed through the hole on the back wall of the container.

The container was held in place using two wooden brackets which were clamped to the vibrating table. Two wooden collars, one 0.75 inches and the other 5.5 inches in height, were mounted on the sample container.

(iii) The vibrating table was activated by supplying a pneumatic pressure. The soil was poured into the container and the micro-concrete pipe using a scoop. Once the soil entered the container and the pipe, the soil would spread out due to the vibration of the table. The speed of pouring the soil was about 1 minute per scoop of soil. The volume of scoop was about 0.25 ft^3.

After the soil was filled to an elevation above the top edge of collar 1 (see Figure 5.2), the vibrating table was stopped for the preparation of the surcharge loading. Collar 2 was dismounted and the soil surface was scraped flush with the top edge of collar 1. Collar 2 was then remounted and a wooden plate, 11.25 x 16.5 x

0.75 inches, was placed on the soil surface. A surcharge, in the form of dead weight, of 120 pounds was added to the plate and the vibrator was reactivated for 10 minutes.

After the 10 minutes of final vibration with the surcharge, the surcharge and the wooden plate were removed.

(iv) The two wooden collars were removed next. The surface of the soil was then scraped flush with the edges of the sample container. This was followed by the mounting of the front wall.

The sample was then tilted up slowly to stand on its bottom plate. The soil inside the pipe would drop out of the pipe from the hole on the back wall. The sample was weighed and the relative density of the soil was calculated. Samples prepared with these procedures were found to have a consistent relative density of 90± 2%. After the weight of the sample was checked, the top plate was removed from the sample container and the sample was ready to be transferred into the centrifuge.

5.1.3 Instrumentation

The instrumentation used in the test consisted of five contact stress gages, five strain gages, and three surface stress gages. The contact stress gages and the strain gages were mounted on the micro-concrete pipe before the soil sample was made. The surface stress

gages were placed on the sample afterward. The contact stress gages were used to detect the dynamic normal stresses acting on the pipe, which were the most important unknowns of the test. The strain gages were used to measure the strains on the outside surface of the pipe, which would allow the bending correction of the contact stress gages. The surface stress gages were used to determine the dynamic overpressure applied to the soil surface. This surface overpressure would be used as an input pressure in the analysis. The contact stress gages and the strain gages were positioned at the middle section of the pipe as shown in Figure 4.15. Note that only half of the section of the pipe was instrumented, due to symmetry in the geometry as well as the applied load.

The surface stress gages and their retaining brackets were attached to a 5.5 x 17 x 0.125 inch Nitrile rubber pad using a double sided tape. The gages and the retaining brackets were covered by a thin rubber membrane which prevented the lateral stress from acting on the gages. The top 0.175 inches of soil was removed to accommodate the 0.125-inch-thick rubber pad. Figure 5.3 shows a schematic view of the soil model with the impact generator.

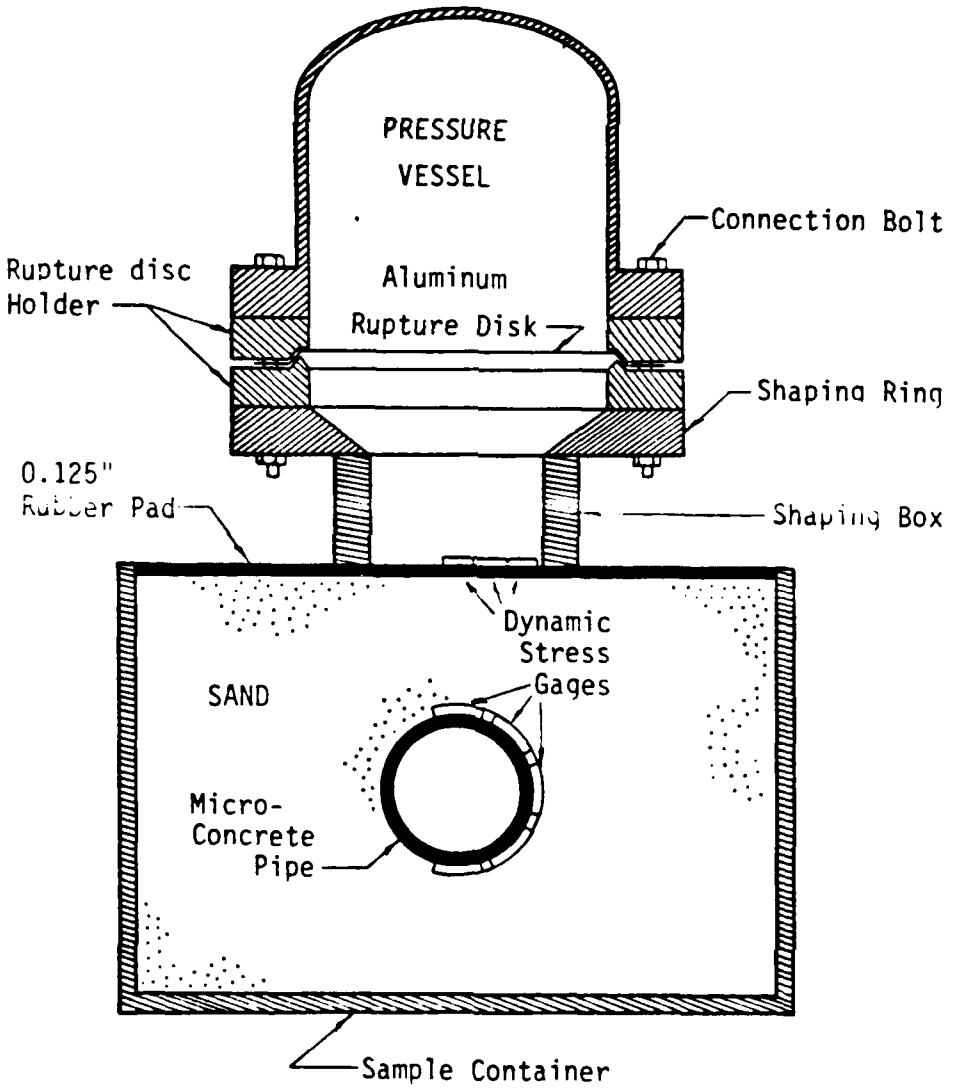

Figure 5.3 A schematic view of the centrifuge model

5.1.4 Data Acquisition

The dynamic nature of the centrifuge tests necessitates a data acquisition system which must respond fast enough to capture the changes of the measured quantities. Data recording rate need not be considered for tests of steady events for which digital data acquisition system is overwhelmingly used nowadays. However, digital data acquisition systems are not adequate for the centrifuge tests of this research, because the responses of the tests contain high frequency components, and because there are 13 different quantities to be measured at the same time, which increase the demand on the response time of the digital system.

A multichannel analog tape recorder was considered to be the most reliable means of data acquisition for the dynamic centrifuge tests. However, an important question needed to be answered before the employment of the recorder: What is the necessary frequency response of the tape recorder for a true recording of the dynamic centrifuge tests?

In order to answer this question, an investigation was performed on the response of a surface stress gage to the air blast loading generated by the impact generator. The signal, shown in Figure 5.4a, was recorded by a 20 megahertz oscilloscope. The trace in

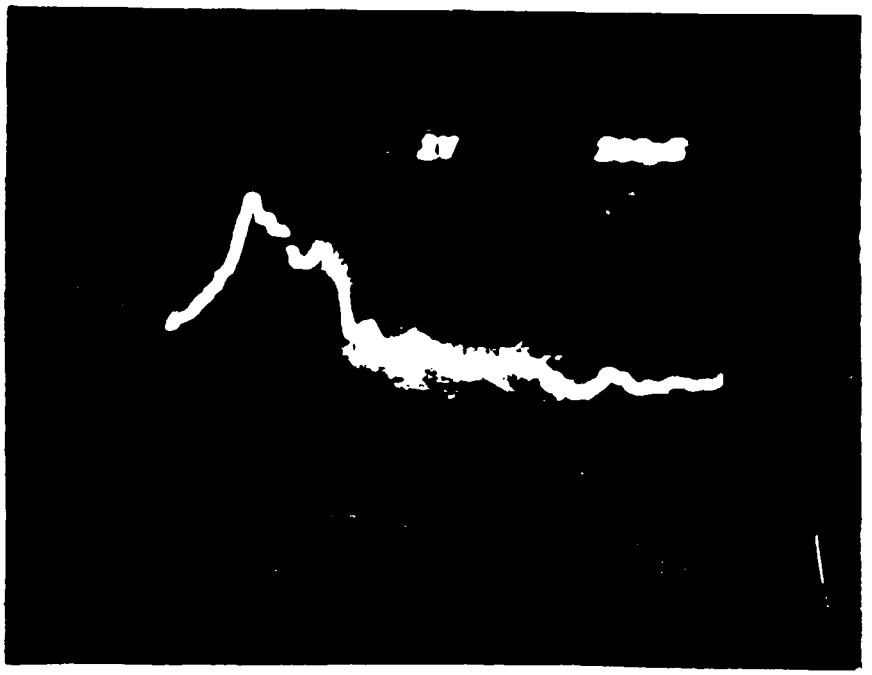

Figure 5.4a Response of a surface stress gage subjected to an airblast Loading

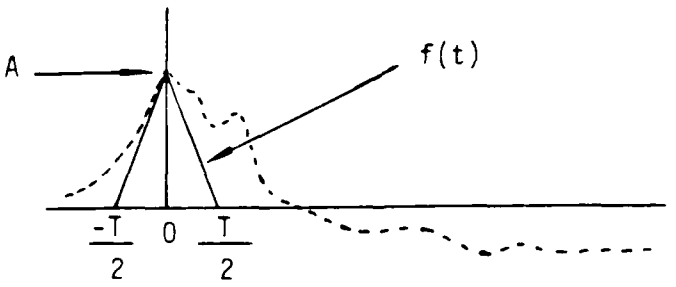

Figure 5.4b Gage response and a time function, f(t)

the picture is the response of the gage subjected to the first pressure wave of the air blast loading. Since the frequency response of the oscilloscope is practically infinite, this signal can be considered as the true response of the gage. The purpose of the following paragraphs is to find the frequency components whose powers compose of at least 99% of the total power. This information can be used to determine the necessary frequency response of the tape recorder to be used for the centrifuge tests.

Figure 5.4b shows a simple time function, f(t) which has frequency components higher than the true gage response shown in Figure 5.4a. This function can be represented by the exponential Fourier series:

$$f(t) = \sum_{-\infty}^{\infty} (F_n e^{jnwt}) \qquad (5.1)$$

where

$$F_n = \frac{1}{T} \int_{T/2}^{T/2} [f(t)e^{-jnwt}]\, dt, \quad \text{and}$$

$$n = 0, \pm 1, \pm 2, \ldots\ldots \qquad (5.2)$$

The function, f(t), in Figure 5.4b can be written as:

$$f(t) = (2At/T + A) \quad \text{for } -T/2 \leq t \leq 0, \quad \text{and}$$

$$= (-2At/T + A) \quad \text{for } 0 \leq t \leq T/2 \qquad (5.3)$$

Substituting Equation (5.3) into Equation (5.2) and performing the integration, we obtain

$$F_n = \frac{A}{2} \text{sinc}^2 (n\pi/2) \qquad (5.4)$$

where $\text{sinc}^2 x = \sin^2 x / x^2$

Equation (5.4) allows the calculation of the frequency spectrum for n = ± 1, ± 2,....,etc. However, since Equation (5.4) is not defined for n = 0, the d.c. response spectrum of the function have to be calculated using Equation (5.2).

The power of a time signal is often an important characterization of the signal. The total power, P_t, of the time signal, f(t), can be expressed in the time domain as well as in the frequency domain, i.e.,

$$P_t = \frac{1}{T} \int_{-T/2}^{T/2} f^2(t) \qquad (5.5)$$

or

$$P_t = \sum_{n=-\infty}^{\infty} (F_n)^2 \qquad (5.6)$$

Equation (5.6) indicates that the power in f(t) can be calculated by adding together the powers associated with the frequency components in f(t).

The power associated with the frequency component at nw radians is $(F_n)^2$ and that at -nw is

$(F_{-n})^2$. Since it takes both frequency components at $\pm nw$ to form a single harmonic, and since

$$F_n = F_{-n} \tag{5.7}$$

the power in the nth harmonic of f(t) is

$$P_n = 2(F_n)^2 \tag{5.8}$$

Hence, Equation (5.6) can be written as:

$$P_t = (F_0)^2+2(F_1)^2+2(F_2)^2+.....$$

From the above equations, the percentage of the power in the nth harmonic can be obtained. For instance, if an instrument is capable of capturing the third harmonic of a specific function, the percentage of power that the instrument can capture is:

$$[(F_0)^2+2(F_1)^2+2(F_2)^2+2(F_3)^2] \; / \; P_t$$

The total power, P_t, of the time function, f(t), can be calculated by substituting Equation (5.3) into Equation (5.5). The result of integration shows that:

$$P_t = A^2/3 \tag{5.9}$$

To find the power associated with the d.c. component of the time function one must substitute both n = 0, and Equation (5.3) into Equation (5.2). The result of integration shows that:

$F_0 = A/2$, thus $(F_0)^2 = A^2/4$

Using Equation (5.4), the frequency spectra for $n = \pm 1, \pm 2, \pm 3$, were calculated to be as follows:

$F_{\pm 1} = 0.20264A \qquad (F_{\pm 1})^2 = 0.04106A^2$

$F_{\pm 2} = 0$

$F_{\pm 3} = 0.02252A \qquad (F_{\pm 3})^2 = 0.000507A^2$

The percentages of power contained in the different frequency components are calculated in the following:

n	% of power	Accumulated
0	$(A^2/4)/(A^2/3) = 75.0\%$	75.0%
1	$(0.08212A^2)/(A^2/3) = 24.6\%$	99.6%
3	$(0.00101A^2)/(A^2/3) = 0.3\%$	99.9%

The above results indicate that for the time function shown in Figure 5.4b, the first harmonic plus the d.c. component contain 99.6% of the actual power.

Since $f_n = n/T$, thus for n = 1 and T=0.0003,

$f_1 = 1/T = 3.3$ khz.

This means that an instrument with a frequency response of 3.3 khz is adequate for recording the signal shown in Figure 5.4b. Since this signal has higher

frequency components than the true gage signal, the latter can be recorded by the same instrument as well.

A 20 khz frequency response tape recorder was purchased to acquire the centrifuge tests data. From the above arguments, the machine is adequate for the centrifuge tests. This was confirmed by comparing the signal recorded directly by the oscilloscope to the play-back signal that was stored on the tape. The results showed an identical signal in both cases.

The tape recorder was purchased from TEAC Corporation. The machine has 14 channels. Different input levels can be chosen for each channel to obtain signal with the smallest noise to signal ratio. The recorder has 7 tape driving speeds with the maximum speed corresponding to 20 khz frequency response. The tests were conducted with the maximum speed. After the test, the signals were digitized with a slower play-back speed.

The test results were digitized by an analog to digital (A-D) converter which was controlled by an IBM personal computer. Two data channels were digitized at a time. Sychronization of the 13 data channels was achieved by choosing one of the channel as a reference channel and using it in the digitization of the rest of the channels. Since the A-D converter can convert 27 data points in one millisecond, the time lag between two

conversions is approximately 0.037 milliseconds. Hence, the shift between the reference channel and each of the other data channel is about 0.037 milliseconds which is a negligible amount. The digitized data were stored on a diskette for future analysis.

5.2 Procedure for Conducting the Test

The procedure of conducting the centrifuge test included the following 3 steps: (1) mount the test hardware and balance the centrifuge; (2) hook up the instrumentation circuits; and (3) operate the centrifuge and apply the air blast. Detailed descriptions of these steps are presented as follows:

(1) The test hardware mounted in the centrifuge consisted of the sample container and the impact generator. After they were mounted on one end of the rotor arm, both swing baskets of the centrifuge were fixed to their in-flight position for balancing the rotor arm.

(2) As mentioned previously, the instrumentations of the test included three surface stress gages, five contact stress gages and five strain gages. Figure 5.5 shows the wiring in the centrifuge. The signals of the contact and the surface stress gages were first sent to the high impedance amplifier. Then, the amplified signals were sent out of the centrifuge through the slip rings.

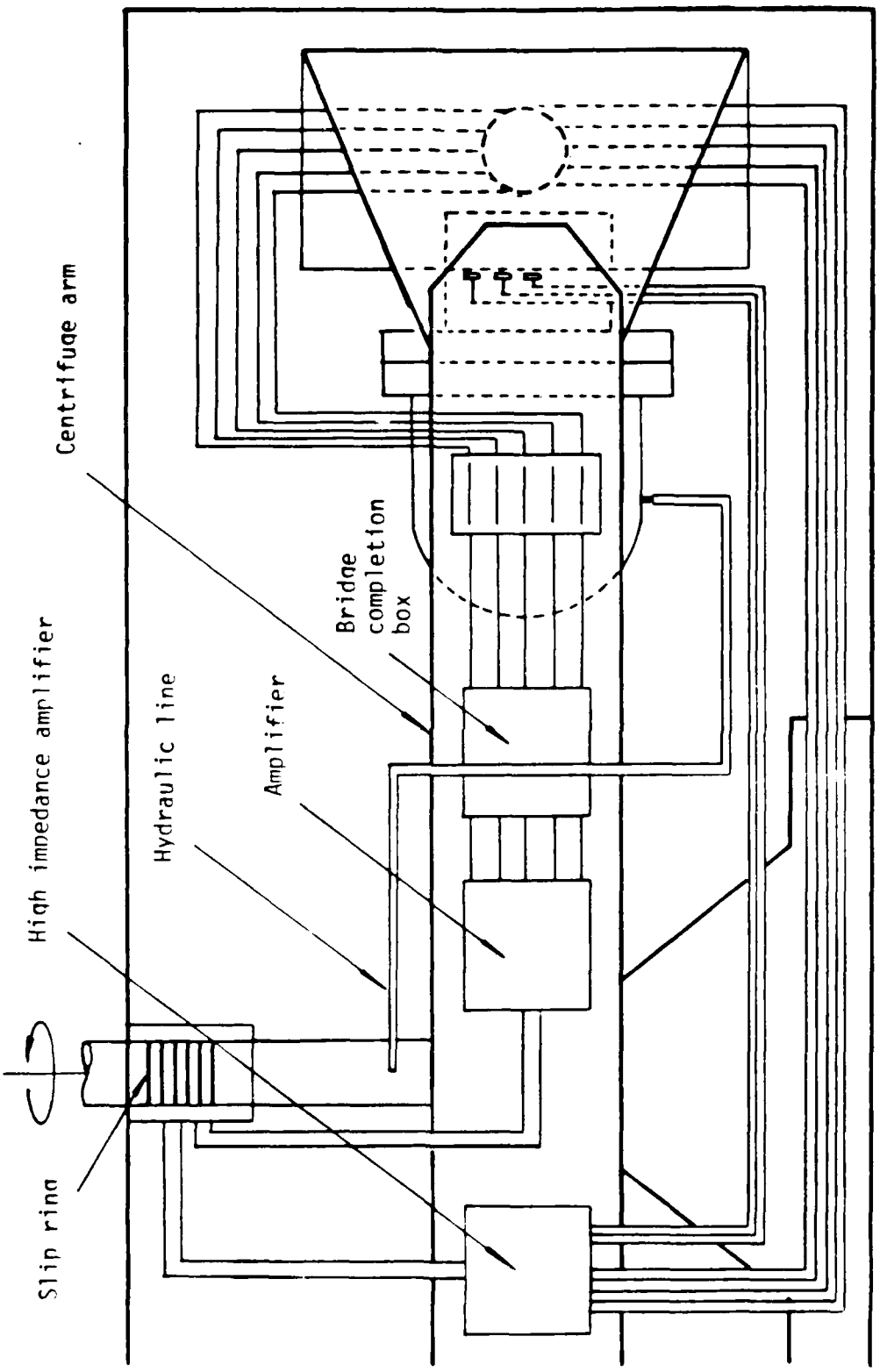

Figure 5.5 Wiring in the centrifuge

The signal of each of the strain gages was sent to a Wheatstone bridge completion box as shown in Figure 5.5. The signals were amplified 900 times before they were sent to the slip rings. To send amplified signals through the slip rings was necessary because the vibration of the centrifuge would cause the slip rings to generate an electric noise.

The centrifuge has two hydraulic slip rings. One of them was used to sent the pressurized nitrogen from outside to inside of the centrifuge.

On the outside of the centrifuge, signals transmitted through the slip rings were all sent to the TEAC recorder. The recorder was set to record with its maximum speed which corresponded to a frequency response of 20 khz. The optimum input level for each channel was chosen. Figure 5.6 shows a schematic of the test set-up.

After all the circuits had been completed, they were checked to ensure all the connections were correct. Checking the circuity was important because the test would take only several milliseconds to complete, hence adjustment during the test was impossible.

(3) The centrifuge was spun up slowly to 194 revolutions per minute which corresponded to 50 g at the center of the sample container. After the centrifuge had reached a steady speed, the recorder was activated and the pressure supply from the nitrogen tank was released.

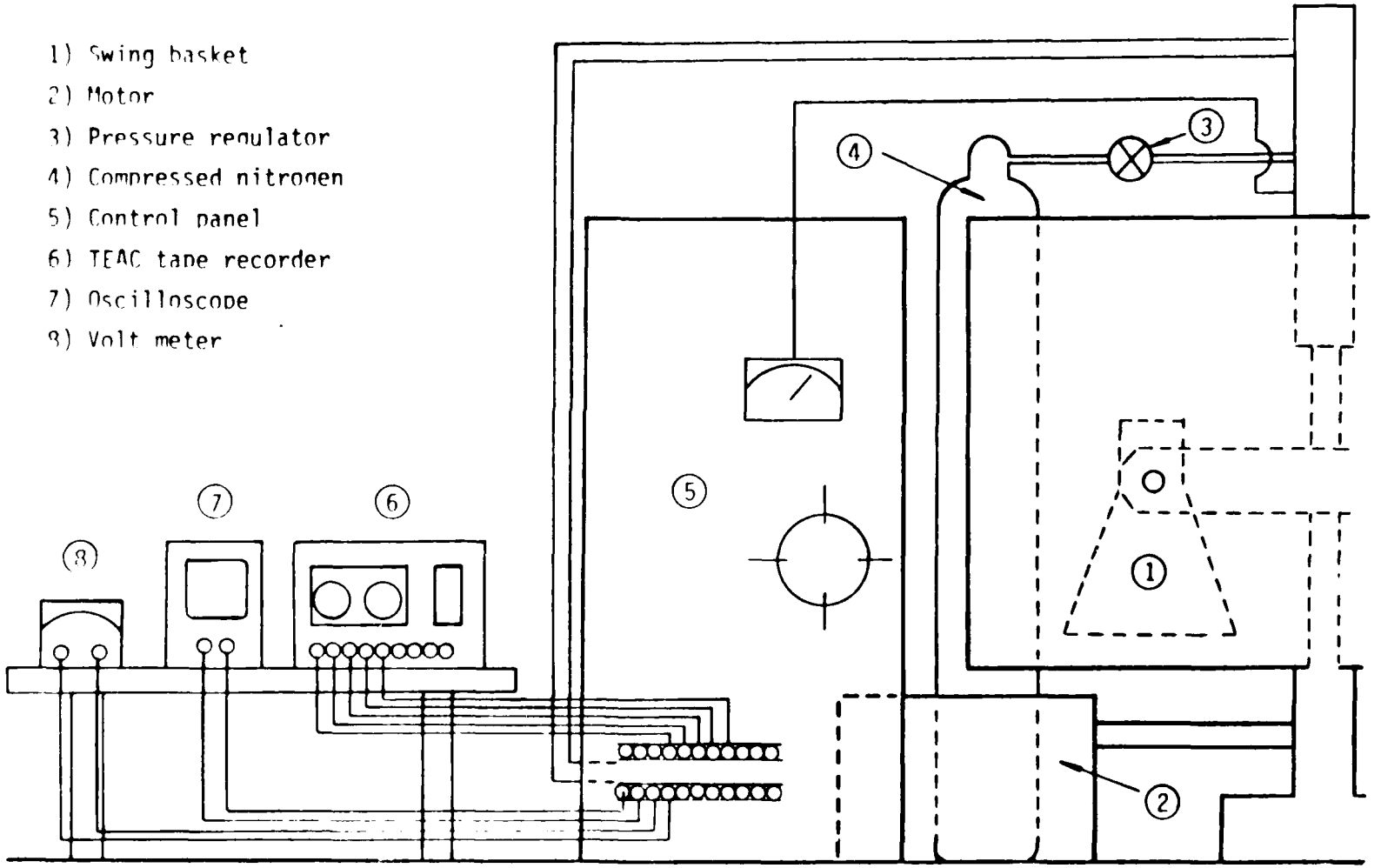

Figure 5.6 Schematic of centrifuge test set-up

CHAPTER VI

NUMERICAL ANALYSIS

The experimental phase of the research has been discussed in Chapters 3,4, and 5. This chapter introduces the numerical analysis, which is the solution scheme parallel to the centrifuge tests. The experimental and analytical results are presented in the following chapter.

Chapter 1 has discussed the advantages of numerical analysis in solving the problem of soil-structure interaction. The advantages can be summarized as the following: (1) a numerical model, like a physical model, can properly simulate the arching effect in a soil-structure system; (2) the non-linear constitutive laws of the soil and the structural material can be incorporated; (3) the slipping boundary at the soil-structure interface can be modeled by interface elements; and (4) parametric study can be performed easily.

6.1 Description of SAMSON2

The finite element code, SAMSON2, used in this research was obtained from U.S. Air Force Weapons

It usually took about 30 seconds for the rupture disk to rupture. The pressure supply was brought down immediately after the shot.

Laboratory. SAMSON2 is a two-dimensional finite element code developed primarily for dynamic analyses of plane and axisymmetric solids. It is used mainly for analysis of blast types of loading such as high explosions. The main features of the code include the following:

1. Central different explicit time integration.
2. Cap model for soil.
3. Engineering model for concrete.
4. Interface elements.

The central difference time integration scheme discretizes the time domain by a time step Δt. The nodal point velocities, $\dot{u}$, and displacements, u, are updated by the formulas:

$$\dot{u}_{i+1/2} = \dot{u}_{i-1/2} + \ddot{u}_i \Delta t \qquad (6.1)$$

$$u_{i+1} = u_i + \dot{u}_{i+1/2} \Delta t \qquad (6.2)$$

where $\ddot{u}$ denotes acceleration.

The solution of an explicit integration scheme is conditionally stable and the stability depends on the time-step size, Δt. For a stable solution Δt is limited by

$$\Delta t \leq \frac{2}{\omega_{max}} \left(\sqrt{1+\xi^2} - \xi\right) \qquad (6.3)$$

where w_{max} is the maximum frequency of the system and is the fraction of critical damping. Note that when μ is small the term $(\sqrt{1+\mu^2} - \mu)$ approaches unity.

Since the highest frequency can be estimated by

$$w_{max} = \frac{2C}{L} \tag{6.4}$$

where C is the maximum wave speed in the material and L is the minimum element dimension, the time-step size can be approximated by

$$\Delta t \leq \frac{\lambda L}{C} \tag{6.5}$$

where λ is a reduction factor that can be used to reduce the size of the time-step.

The instability can be detected by examining the solution since it is always accompanied by an obvious oscillation of the solution. Once instability occurs, a smaller λ is used until a stable solution is obtained. Reducing the time-step means increasing computing time which can be enormous for the non-linear analysis.

6.2 Description of the Cap Model

The cap model is an elastic-plastic model developed for granular soils by DiMaggio and Sandler (1971). The following lists the main features of the model:

1. The model is defined in a three-dimensional stress space.

2. The yielding of the material is controlled by a fixed Coulomb-Mohr failure surface and a moving hardening cap whose position is a function of plastic volumetric strain.

4. An associated flow rule is used, that is, the plastic potential is described by the yielding surface.

DiMaggio and Sandler, (1971), and Sandler et al., (1976) showed that the model was shown to control excessive dilatancy and allowed hysteresis. These will be confirmed in the next section where the model calibration is presented.

Figure 6.1 shows the failure surface and the hardening cap of the cap model. The failure surface is defined by

$$\sqrt{J_2'} - [A-C \exp(BJ_1)] = 0 \qquad (6.6)$$

where

J_1 = the first stress invariant. J_1 is negative for compression,

J_2' = the second deviatoric stress invariant,

A,B,C = model parameters.

The hardening cap is described by an ellipse whose equation is:

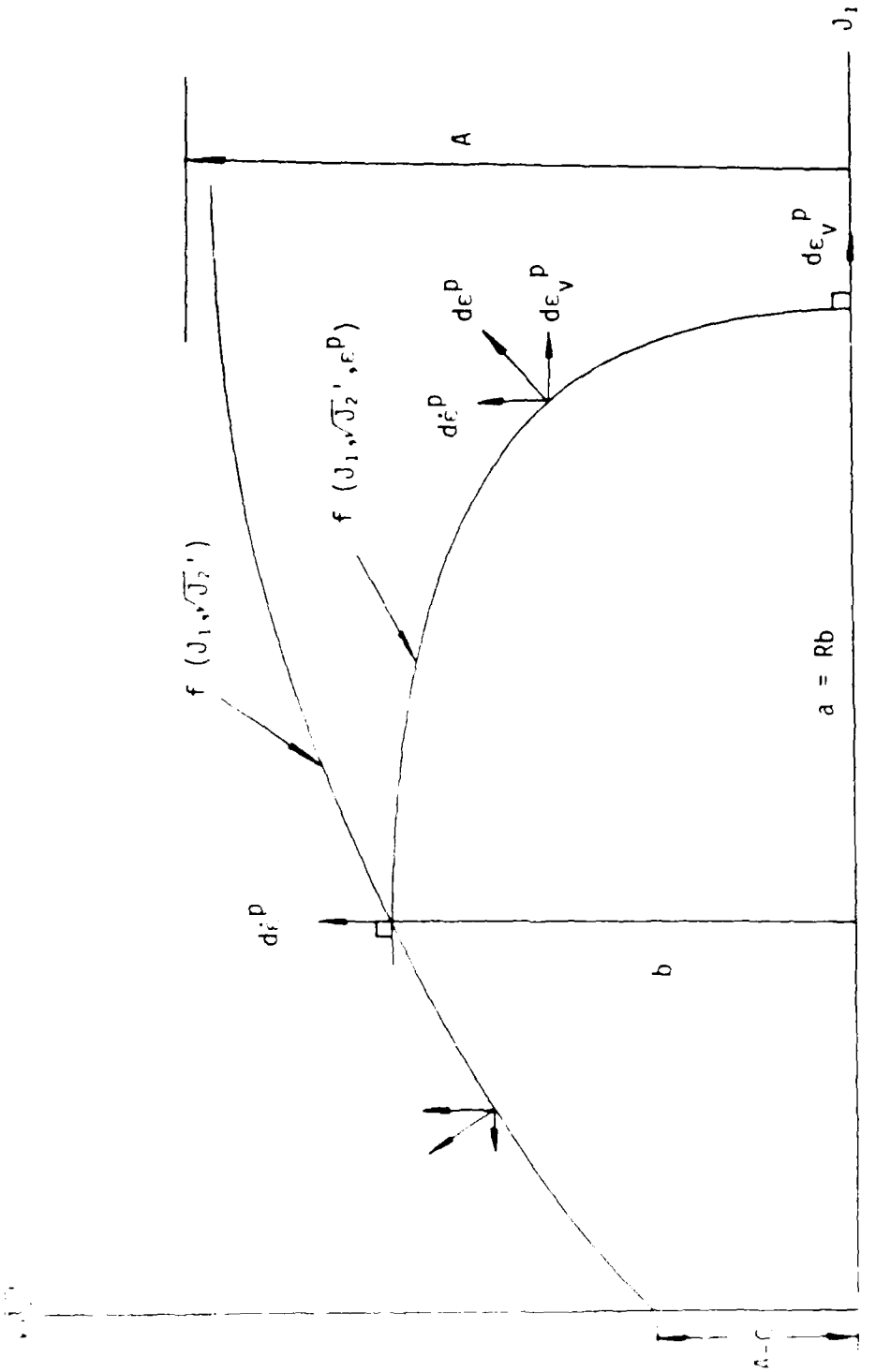

Figure 6.1 Plot shows the failure surface and the yield cap of the cap model

$$R^2 J_2' + (J_1 - C)^2 = R^2 b^2 \qquad (6.7)$$

where

C = the value of J_1 at the center of the ellipse,

R = the ratio of the major to minor axis of the ellipse, and

b = the value of $\sqrt{J_2'}$ when J_1 equals to C.

The hardening parameter, X, is negative for compression. X is dependent on the plastic volumetric strain, ε_v^p, and is expressed as

$$\varepsilon_v = \varepsilon_v^p + \varepsilon_v^e$$

$$= \varepsilon_v^p + \frac{(-J_1/3)}{K}$$

$$= W[\exp(DX) - 1] \qquad (6.8)$$

where

ε_v = total volumetric strain,

ε_v^e = elastic volumetric strain,

K = elastic bulk modulus, and

W,D = model parameters.

The elastic response of the soil is controlled by the two elastic parameters, K and G, where G is the elastic shear modulus of the soil.

According to the rule of normality, the incremental plastic strain vector, ε^p, is perpendicular to the yield surface and can be decomposed into incremental plastic volumetric strain and incremental plastic shear strain as shown in Figure 6.1. The cap model assumes that the fixed failure surface and the moving cap intersect in such way that the tangent to the yield surface at the intersection is parallel to the J_1-axis. Hence, the incremental plastic strain vector at this intersection is pointing upward implying that there is no incremental plastic volumetric strain and that only incremental plastic shear strain exists at this point. On the other hand, the model assumes that the hardening cap intersects the J_1-axis at right angles. Hence at this intersection, the incremental plastic strain vector is pointing toward the right implying zero incremental plastic shear strain. As the state of stress reaches the failure surface at the left of the intersection of the failure surface and the hardening cap, the incremental plastic volumetric strain has a negative value, implying shear dilatancy.

6.3 Calibration of the Cap Model

Four conventional triaxial compression tests and one hydrostatic test were conducted on Coyote Concrete sand. The soil used for these tests were in the air-dry conditions and at 90% relative density, which are

similar to those conditions used in the centrifuge tests.

Figure 6.2 shows the deviator stress versus axial strain response of the soil tested under different confining stresses, and Figure 6.3 shows the volumetric response of the soil from the same tests. Figure 6.4 shows the Mohr failure envelope obtained from the four triaxial compression tests. It is also shown in Figure 6.4 that the internal friction angle of the soil is 45 degrees. The results of the hydrostatic test are shown in Figure 6.5.

It can be seen from Figure 6.2 that all the unloading parts of the tests approach a series of parallel, straight lines. Since the cap model assumes the soil response is elastic in the unloading path, the slope of the straight line represents the elastic Young's modulus of the soil. The Poisson's ratio of the soil is assumed to be equal to 0.33 which is a reasonable value for a sandy soil.

The maximum deviator stresses of the four triaxial tests allow the definition of the failure surface, and the model parameters, A, B, and C to be obtained.

The shape of the elliptical hardening cap is controlled by the parameter, R, which usually has a value between 1.5 to 2.5. To obtain the exact value of R

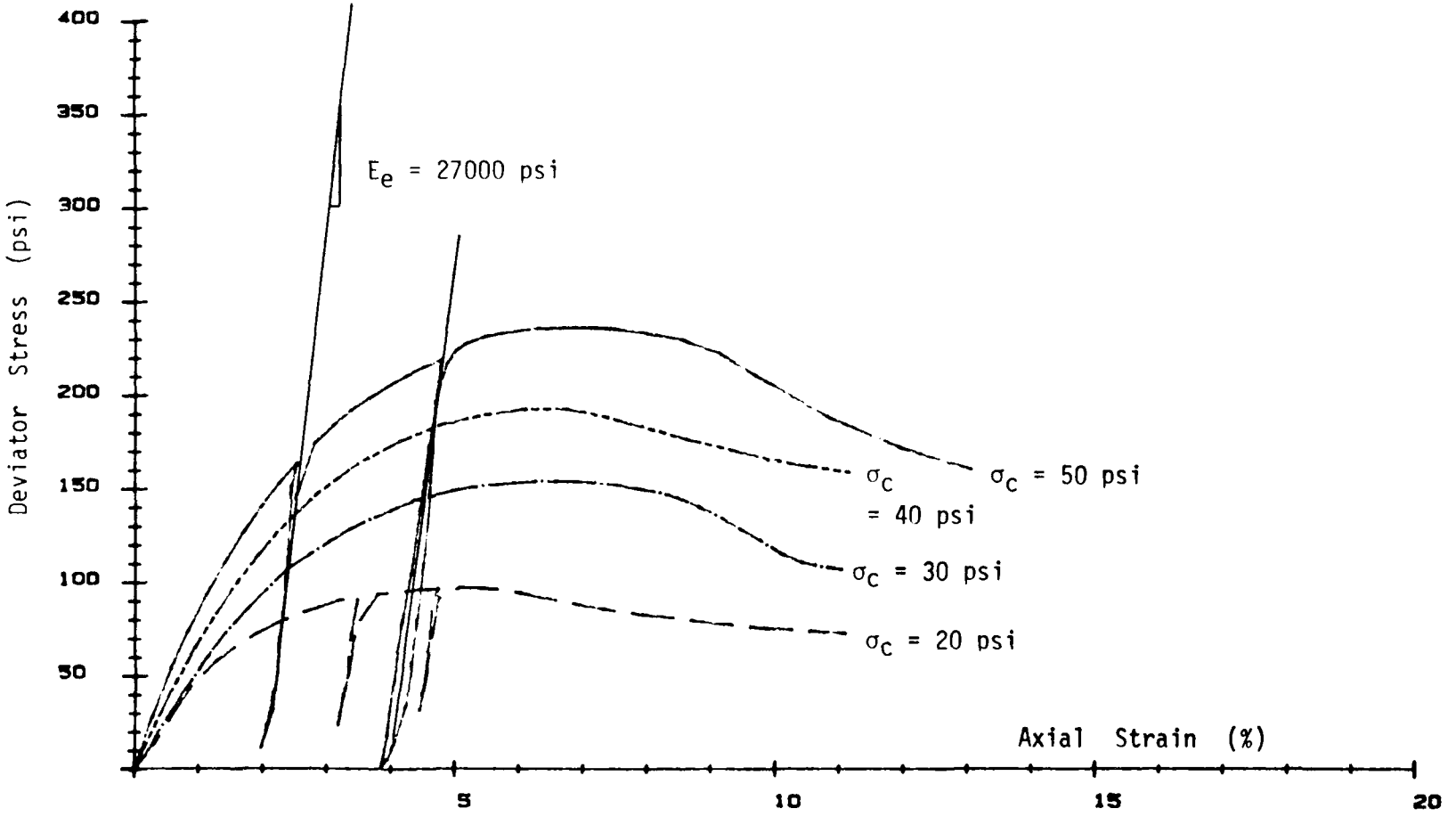

Figure 6.2 Deviator stress vs. axial strain response: Relative density = 90%

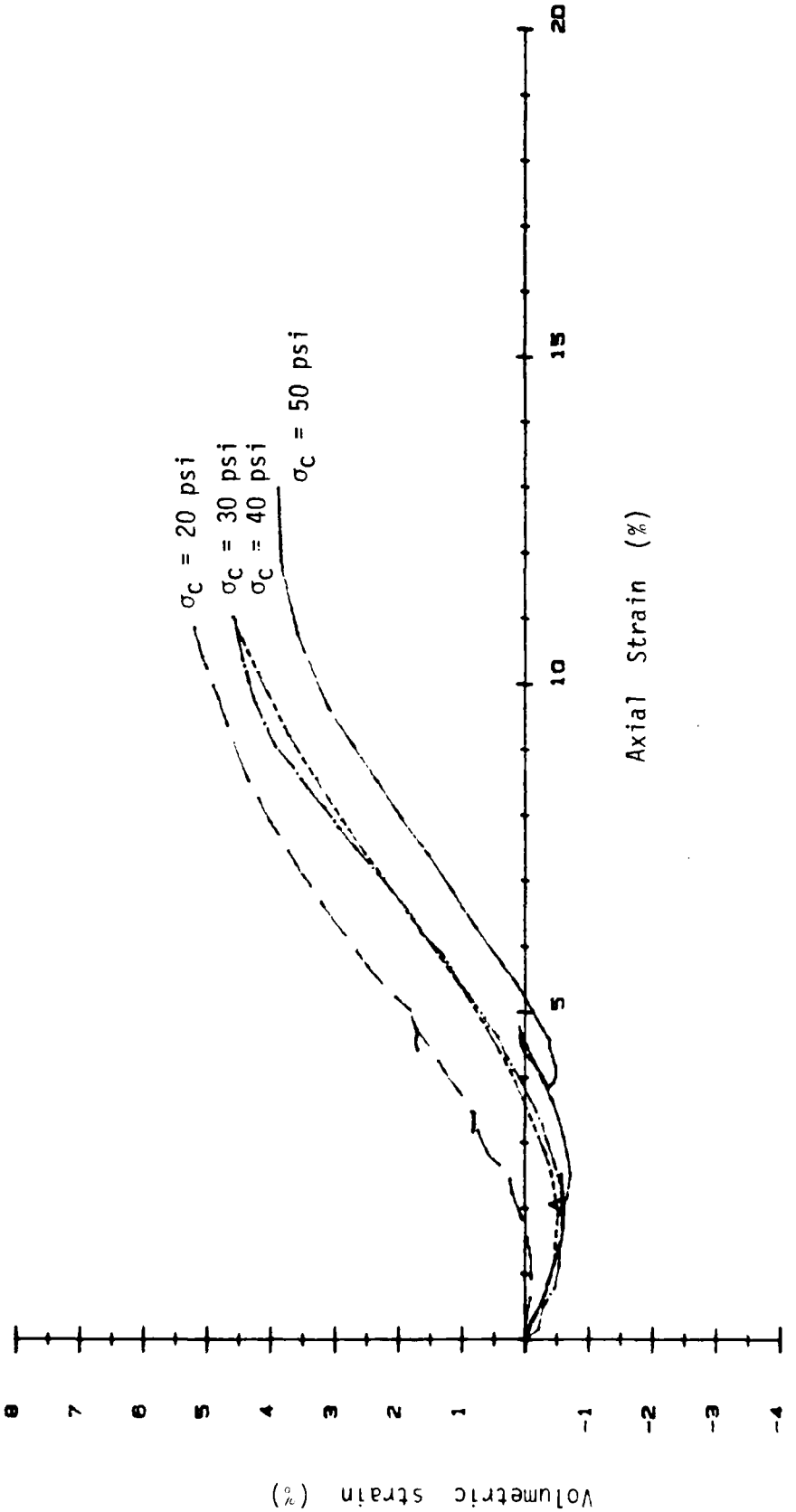

Figure 6.3 Volumetric strain vs. axial strain; relative Density = 90%

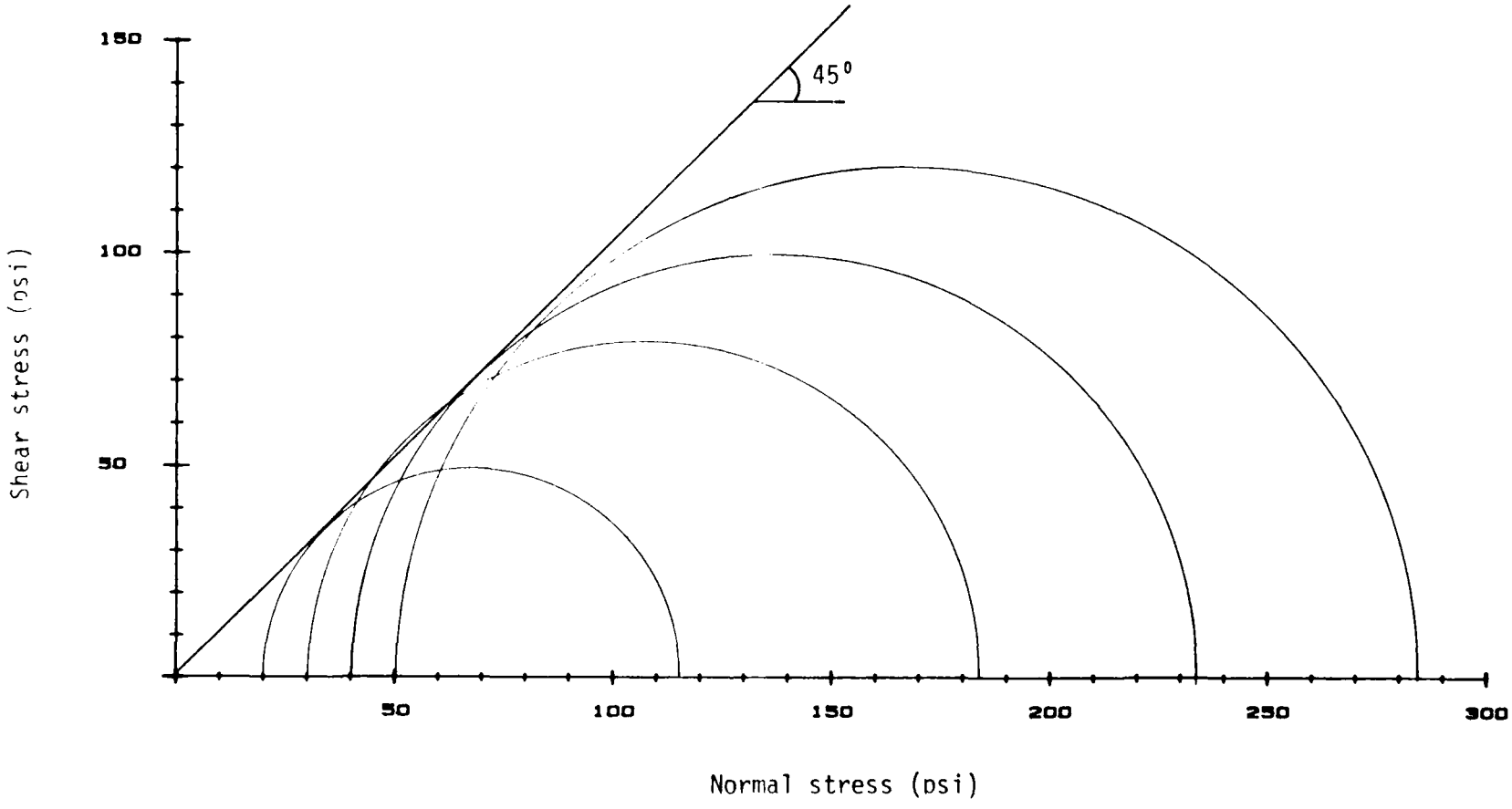

Figure 6.4 Failure envelope of Coyote Concrete sand at air-dry and 90% relative density

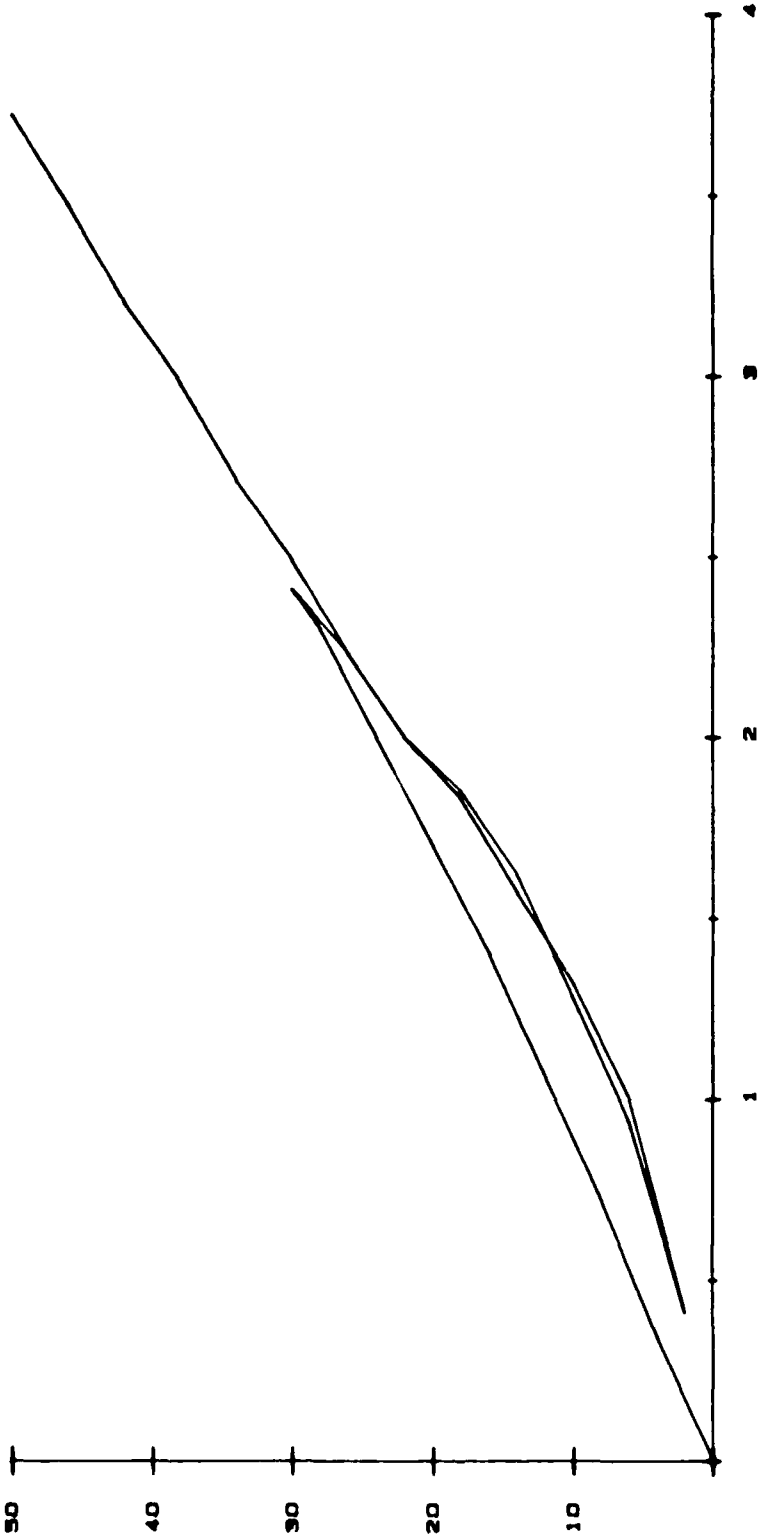

Figure 6.5 Volumetric strain vs. hydrostatic stress response

requires the volumetric response of the soil from laboratory tests with different stress paths. However, preliminary calculations using SAMSON2 showed that the response of the Coyote Concrete sand was not sensitive to the value of R. Therefore, it was assigned a value of 2.0.

To determine parameters D and W, Equation 6.8 is rewritten as

$$\varepsilon_v = W[\exp(DX) - 1] + \frac{\sigma_h}{K} \qquad (6.9)$$

where σ_h is the hydrostatic stress. Taking two points from the hydrostatic loading curve shown in Figure 6.5 and with the value of K known, one can obtain two equations with two unknowns D and W. These parameters can then be found by trial and error.

The parameters determined by the four triaxial and one hydrostatic tests are listed as follows

A = 250 psi, B = 0.01554 psi^{-1}, C = 246 psi,
K = 26000 psi, G = 10000 psi, R = 2.0,
D = 0.003 psi^{-1}, W = 0.006.

After the model parameters were determined, the next step was to exercise the model to predict the triaxial and hydrostatic test results. Figure 6.6 shows the two one-element finite element models for the triaxial and

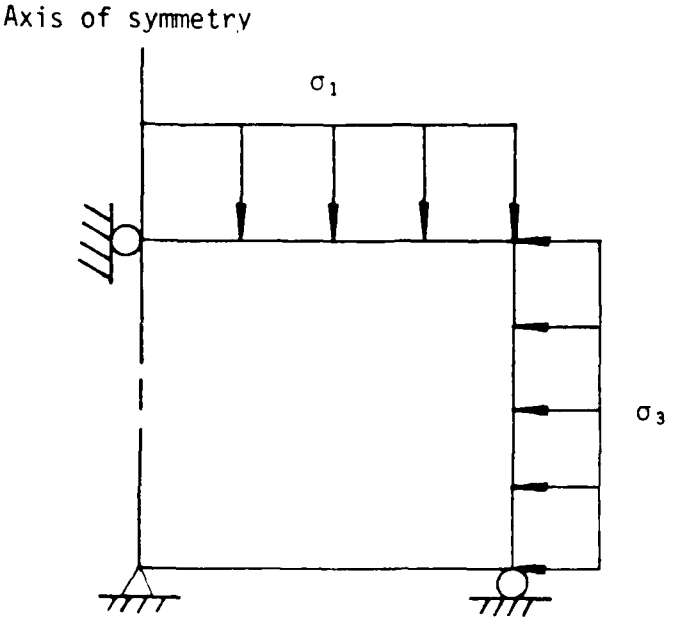

Finite element model of triaxial test

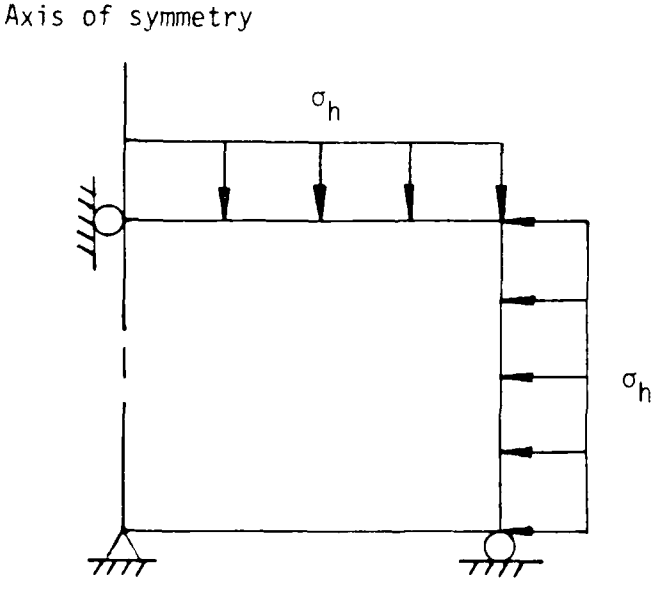

Finite element model of hydrostatic test

Figure 6.6 Finite element models of triaxial and hydrostatic test

the hydrostatic tests. The results showed good predictions of the triaxial tests but the prediction of the hydrostatic test was rather poor. The volumetric strain from the prediction was only about one tenth of the experimental results. The difference was contributed to first, the membrane penetration effect and second, the leakage of the triaxial cell, so that the volume change of the sample was over-registered in the experiment.

In order to investigate further the model capability in predicting the volumetric behavior of the soil, a confined compression (uniaxial strain) test was conducted in an oedometer. The reason of choosing this test was that in the centrifuge experiment, the soil around the pipe was very likely to be subjected to such a loading condition.

The results of the confined compression test are shown in Figure 6.7. As mentioned before, hydrostatic test data are needed to determine the parameters D and W (which, along with the parameter R, control the plastic volumetric strain). Thus, it was necessary to deduce a pseudo-hydrostatic test from the confined compression test. To do so the coefficient of lateral pressure at rest, K_o, was assumed to be

$$K_o = 1 - \sin \phi \qquad (6.10)$$

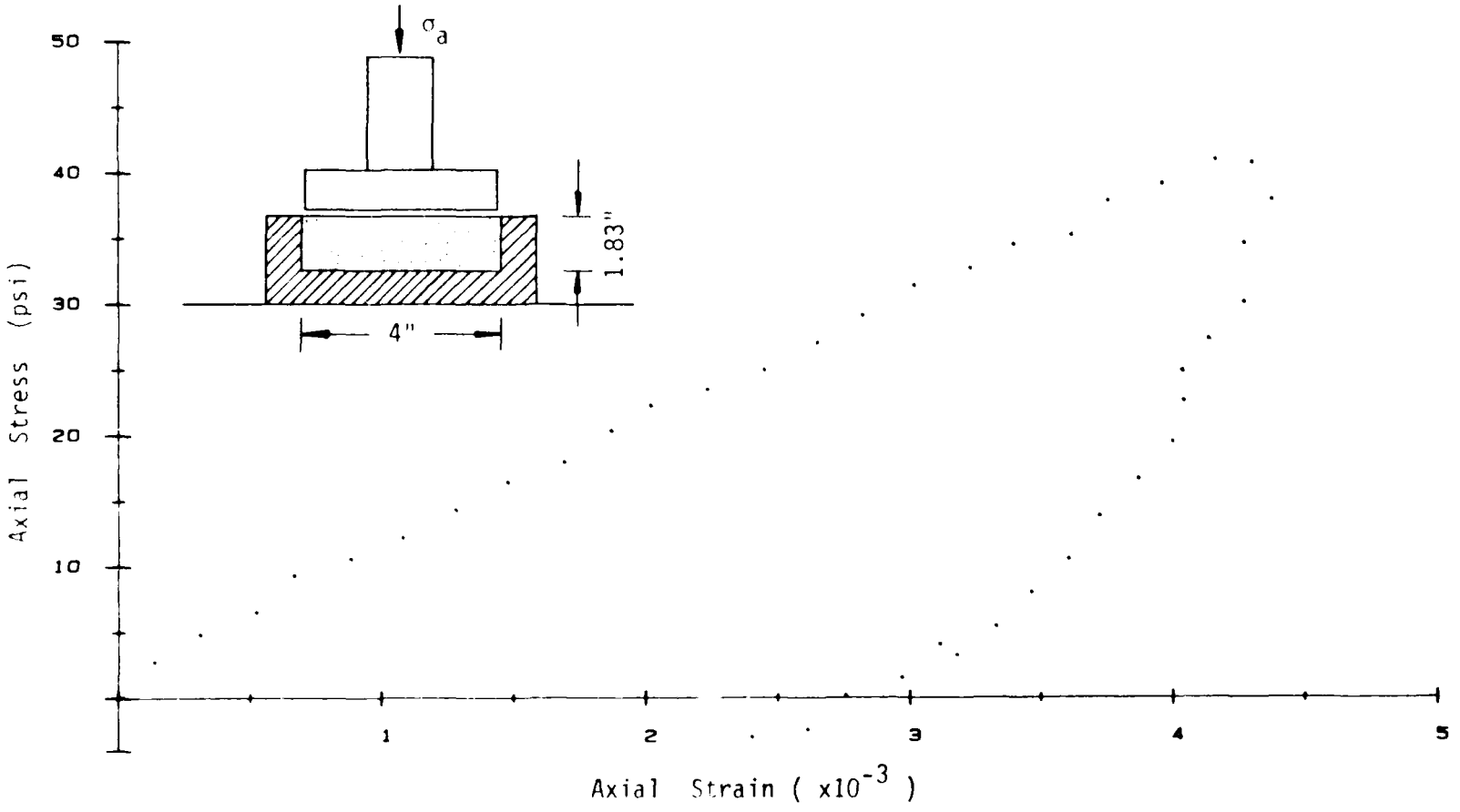

Figure 6.7 Axial stress vs. axial strain response of confined compression test.

where ϕ is the internal friction angle of the soil. A pseudo-hydrostatic stress, σ_h^s, can be obtained as

$$\sigma_h^s = \frac{\sigma_a(1 + 2K_o)}{3} \qquad (6.11)$$

where σ_a is the axial stress of the confined compression test. Since the axial strain is equal to the volumetric strain in the confined compression test, a plot of pseudo-hydrostatic stress versus volumetric strain can be generated. The plot is shown in Figure 6.8. Following the same procedure described previously, the parameters D and W became:

$$D = 0.001, \quad W = 0.0021$$

With these new values, the model was exercised again to predict the experimental results

Figure 6.9, Figure 6.10, and Figures 6.11 to 6.16 show the comparisons between the model prediction and the experimental results for the confined compression test, the pseudo-hydrostatic test, and the triaxial tests, respectively. It can be seen from Figure 6.9 that the model allows hysteresis of soil to occur, and from Figure 6.10 that the assumption of K_o being equal to $(1 - \sin \phi)$ was very reasonable. The prediction of the triaxial tests indicate that the model is able to

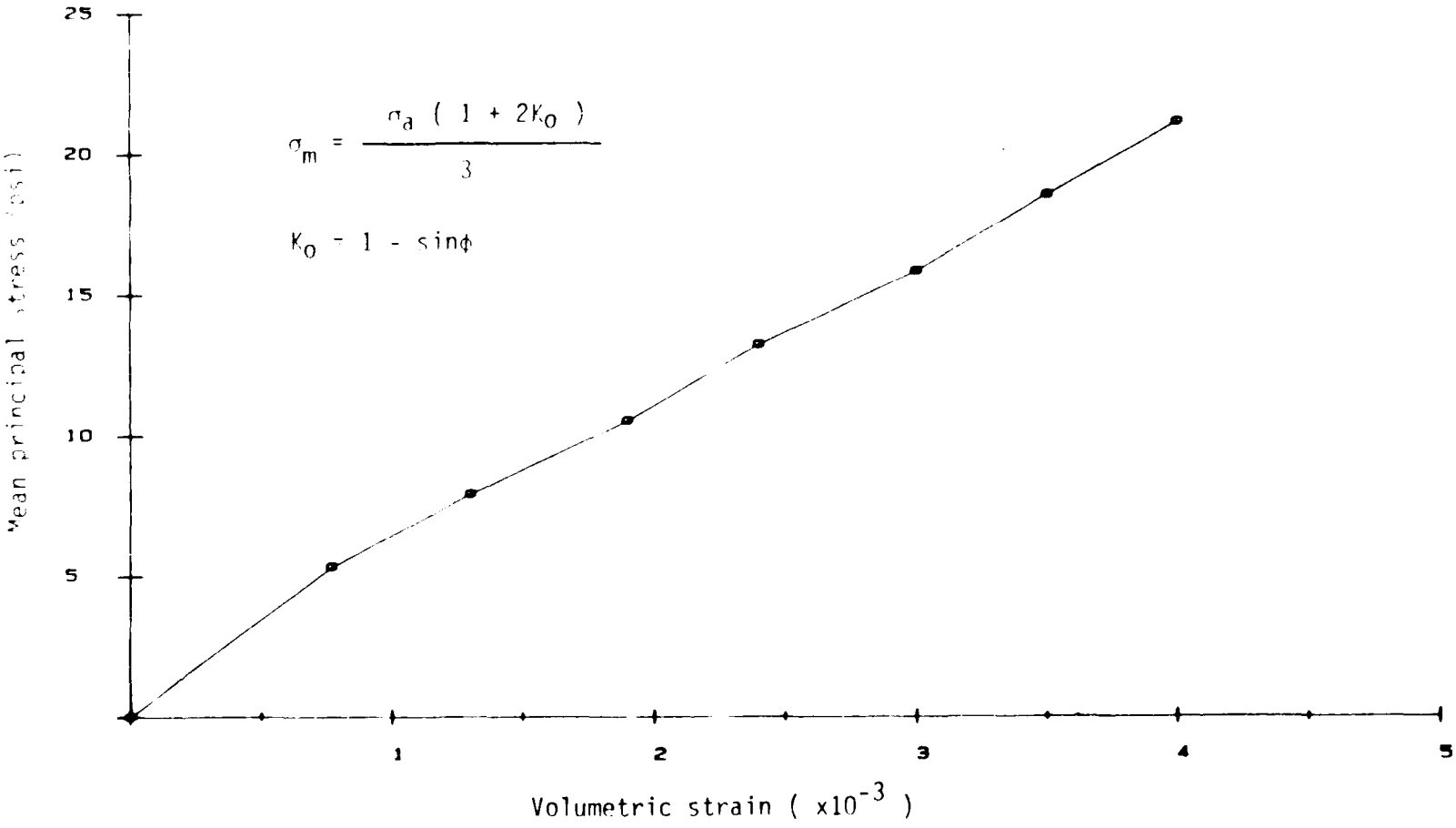

Figure 6.8 Response of mean principal stress vs. volumetric strain obtained from the confined compression test.

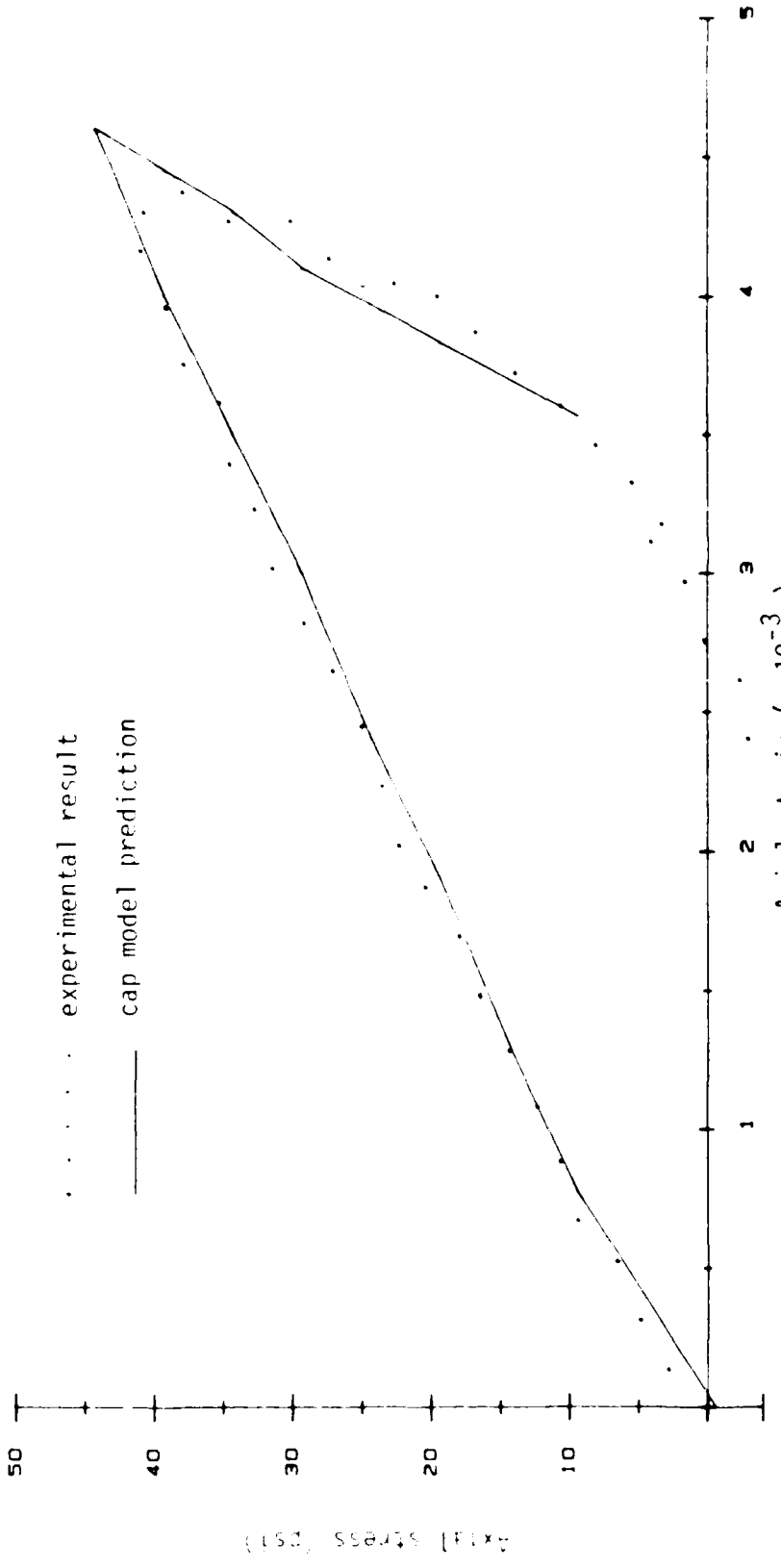

Figure 6.9 Comparison between the cap model prediction and the experimental result of the confined compression test.

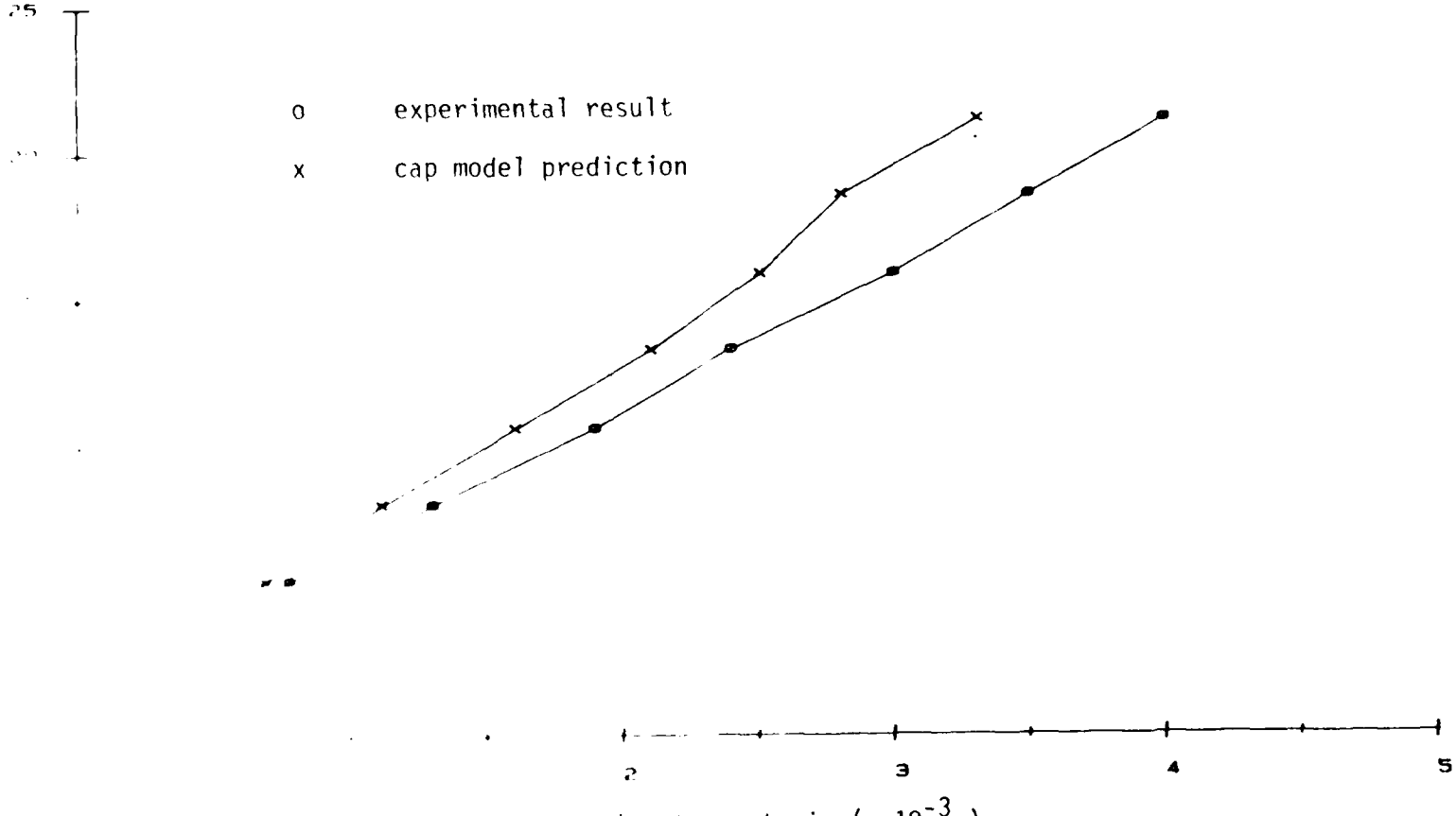

...lumetr c strain (x10^{-3})

...between the cap model prediction
...experimental result of the
...r of soil.

AD-A186 360 CENTRIFUGAL AND NUMERICAL MODELING OF BURIED STRUCTURES 3/3
VOLUME 2 DYNAMIC.. (U) COLORADO UNIV AT BOULDER DEPT OF
CIVIL ENVIRONMENTAL AND ARCH.. C SHIN 14 JUL 87
UNCLASSIFIED AFOSR-TR-87-1446 $AFOSR-84-0300 F/G 19/9 NL

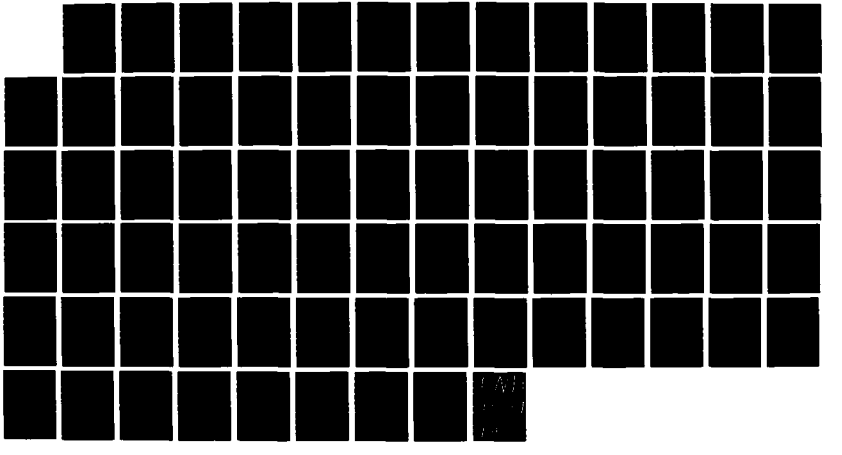

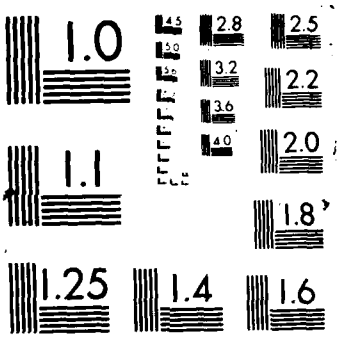
1.0
1.1
1.25
1.4
1.6
1.8
2.0
2.2
2.5
2.8
3.2
3.6
4.0

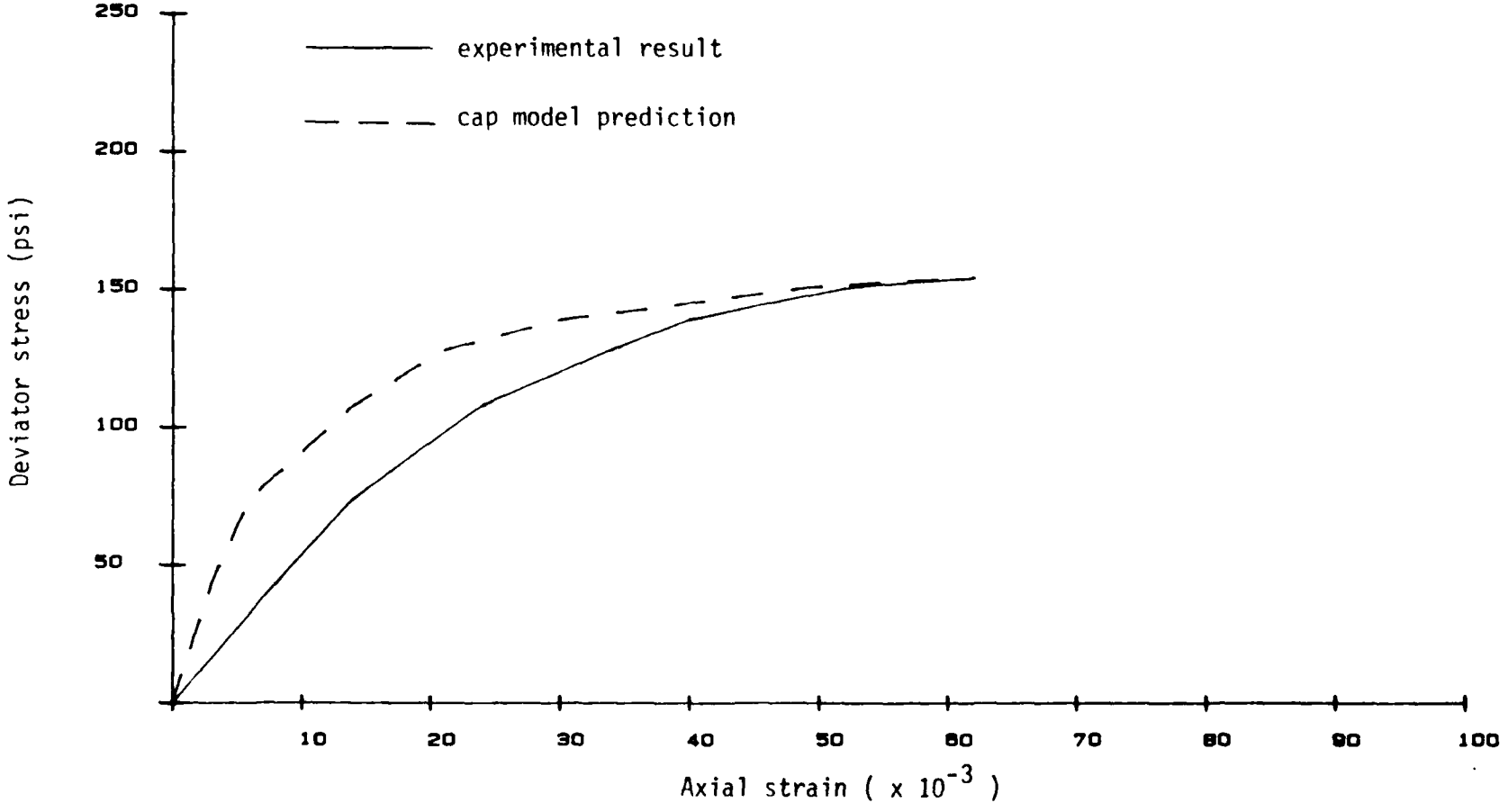

Figure 6.11 Comparison between the cap model prediction and the experimental result of the triaxial compression test, confining stress = 30 psi.

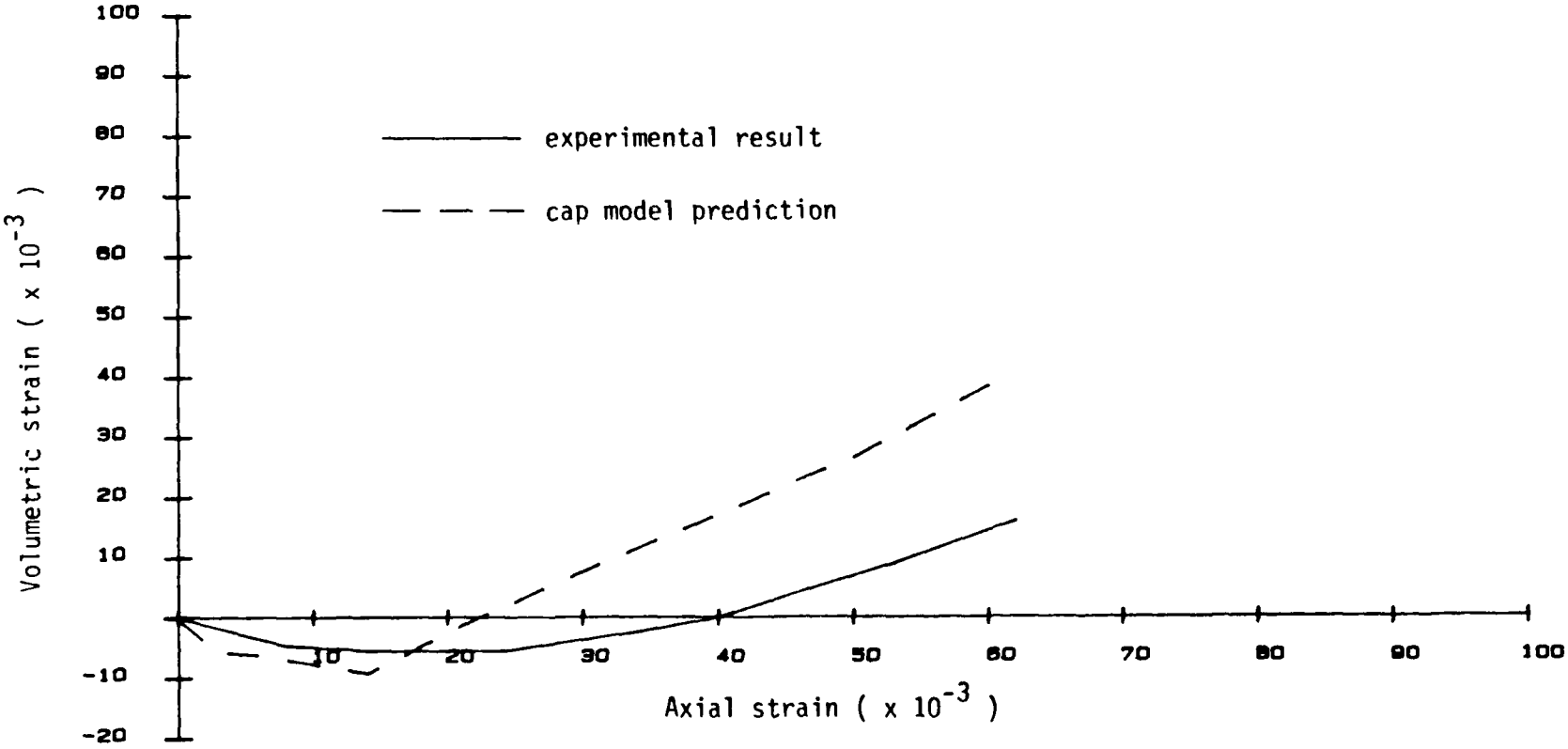

Figure 6.12 Comparison between the cap model prediction and the experimental result of the volumetric strain vs. axial strain response of triaxial test with confining stress = 30 psi

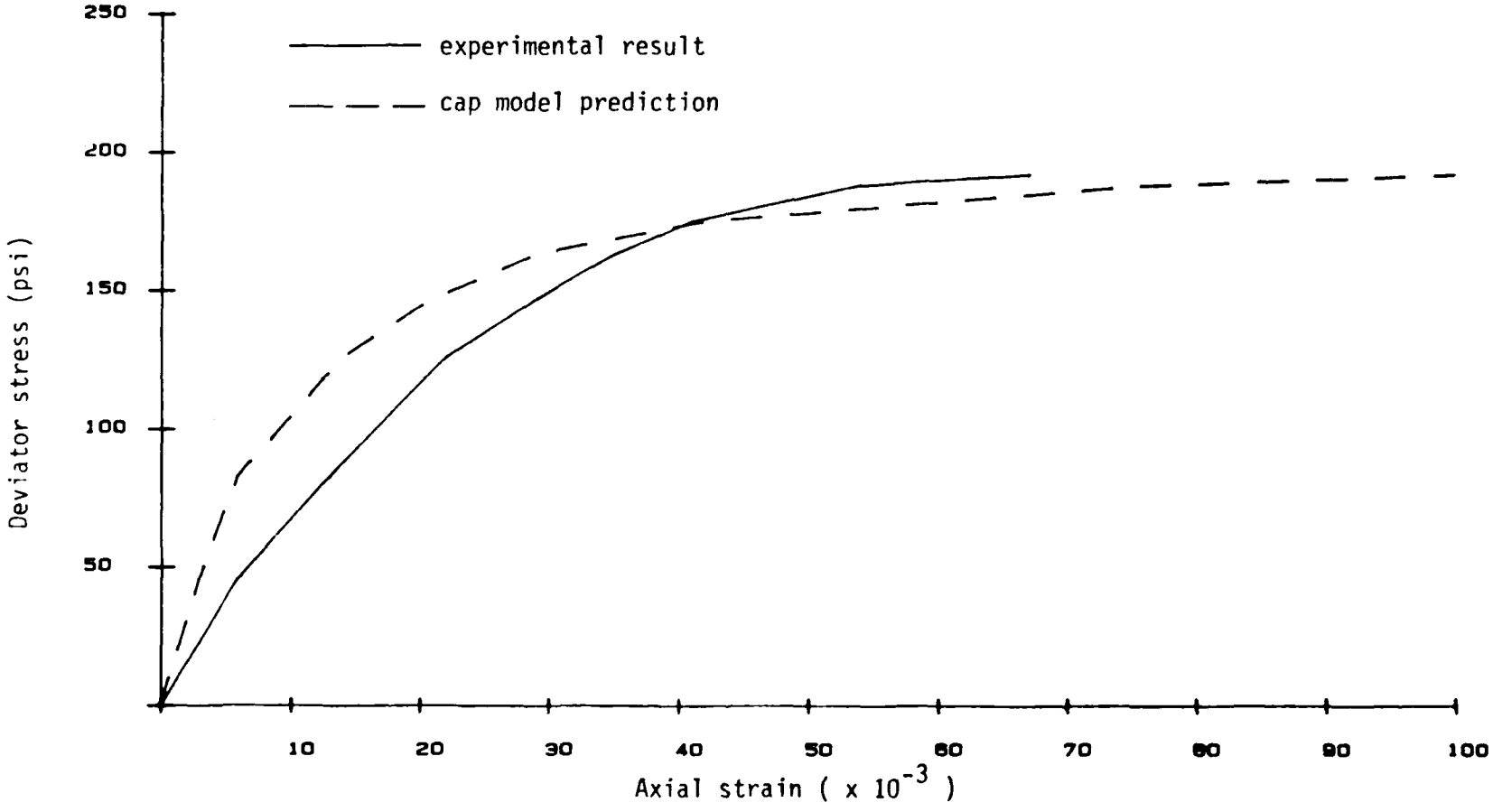

Figure 6.13 Comparison between the cap model prediction and the experimental result of the triaxial compression test with confining stress = 40 psi.

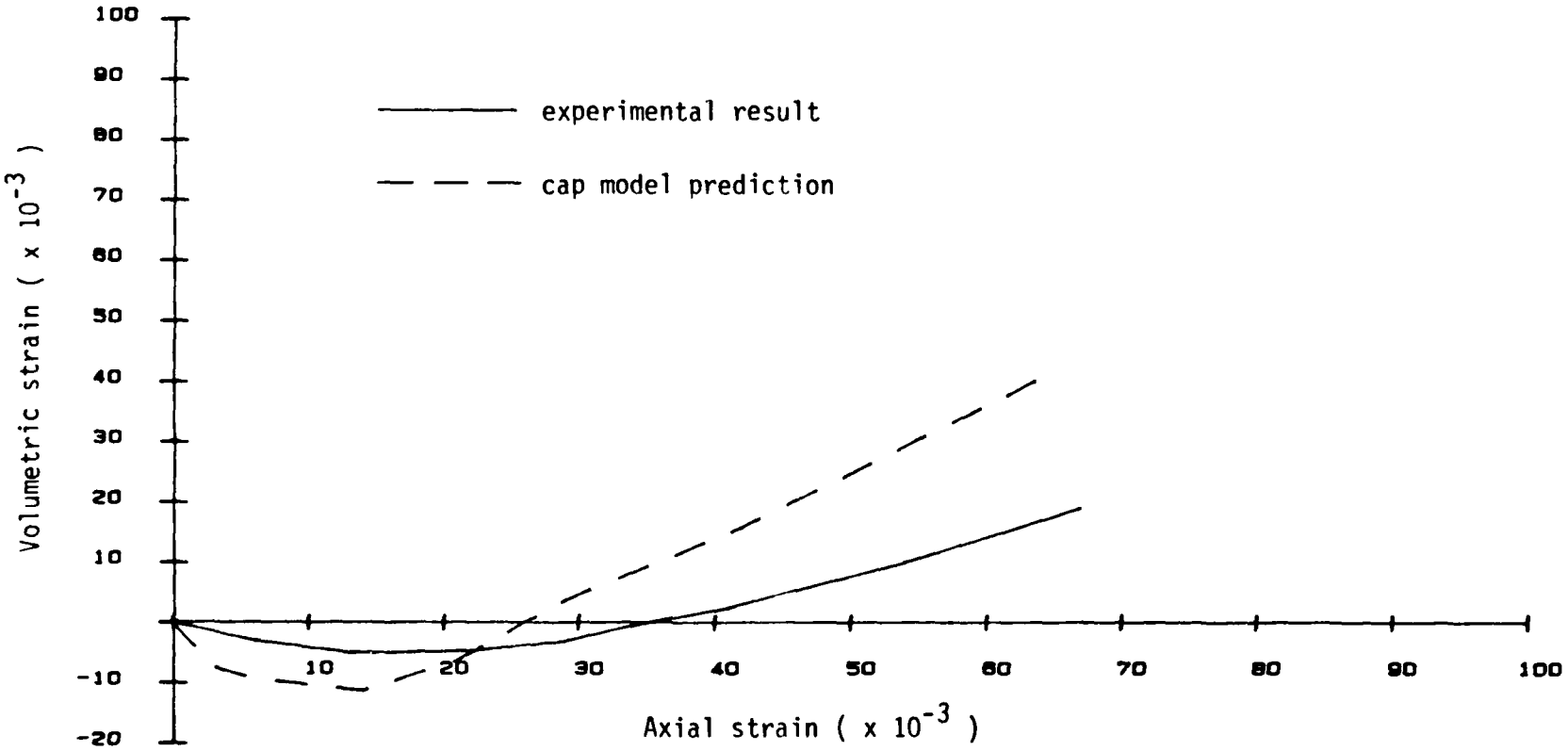

Figure 6.14 Comparison between the cap model prediction and the experimental result of the volumetric strain vs. axial strain response of the triaxial test with confining stress = 40 psi.

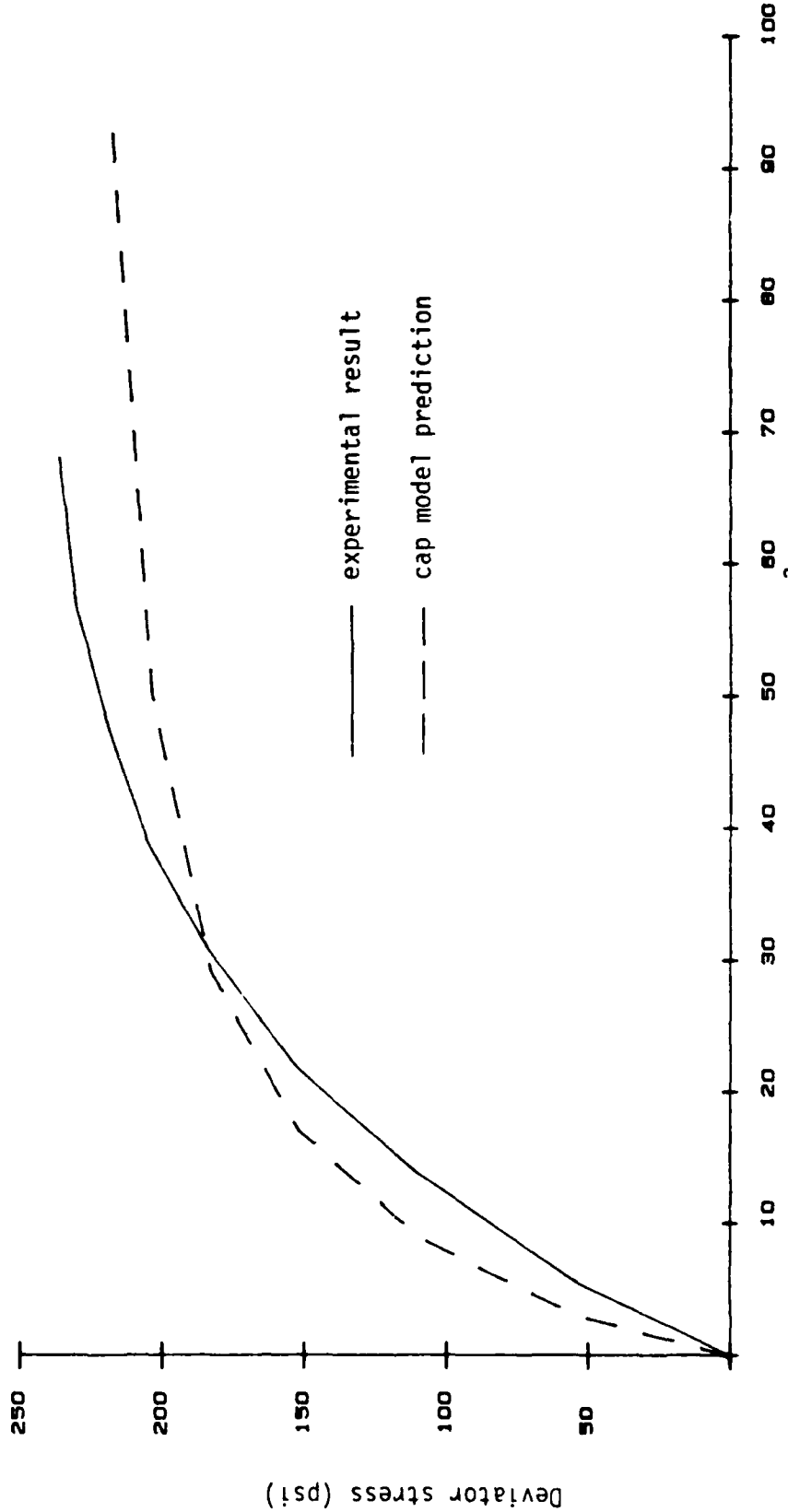

Figure 6.15 Comparison between the cap model prediction and the experimental result of the triaxial compression test with confining stress = 50 psi.

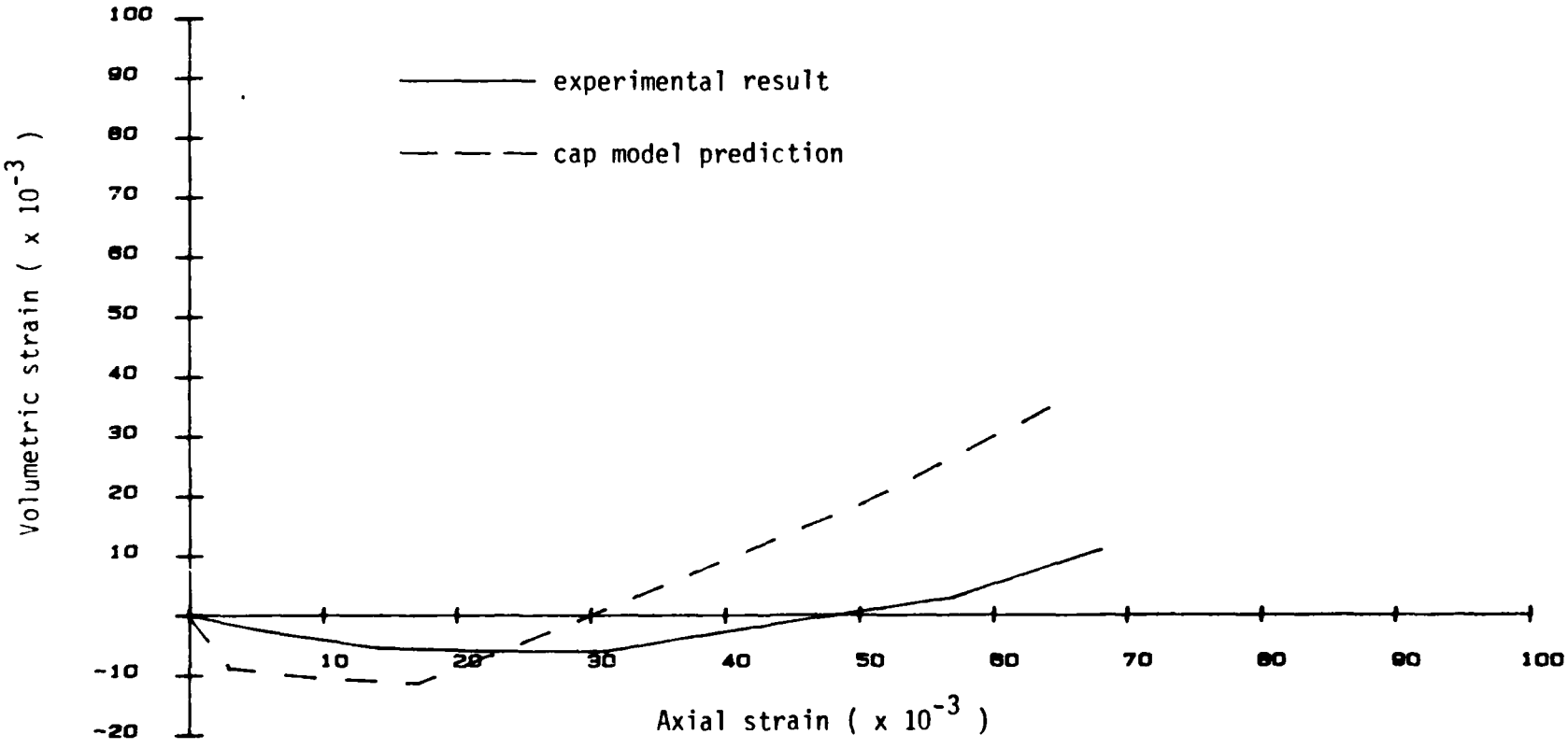

Figure 6.16 Comparison between the cap model prediction and the experimental result of the volumetric strain vs. axial strain response of the triaxial test with confining stress = 50 psi.

account for the non-linearity and the shear dilatancy of the soil.

6.4 Description and Calibration of Engineering Model

The engineering model was developed in-house at the U.S. Air Force Weapons Laboratory. The model was used for the micro-concrete in this study.

The model describes the failure surface of the material by a multilinear approximation of $\sqrt{J_2'}$ versus P function, where J_2' is the second deviatoric stress invariant and P is the mean normal stress. The failure surface is shown in Figure 6.17. Note that point A in the figure represents a tension cut-off for the material. According to the model, if at any time the stress state is described by a point outside the failure surface, the deviatoric stresses are corrected in simple proportions to a position on the yield surface. The correction is accomplished by bringing the value of $\sqrt{J_2'}$ vertically downward to an intersection with the failure surface.

The model describes the volumetric response of the material by a multilinear approximation of the mean normal stress versus the volumetric strain as shown in Figure 6.18. The different slopes of the curve are represented by different bulk moduli of the material.

Two experiments were needed for the calibration of the model, one was the uniaxial compression test and

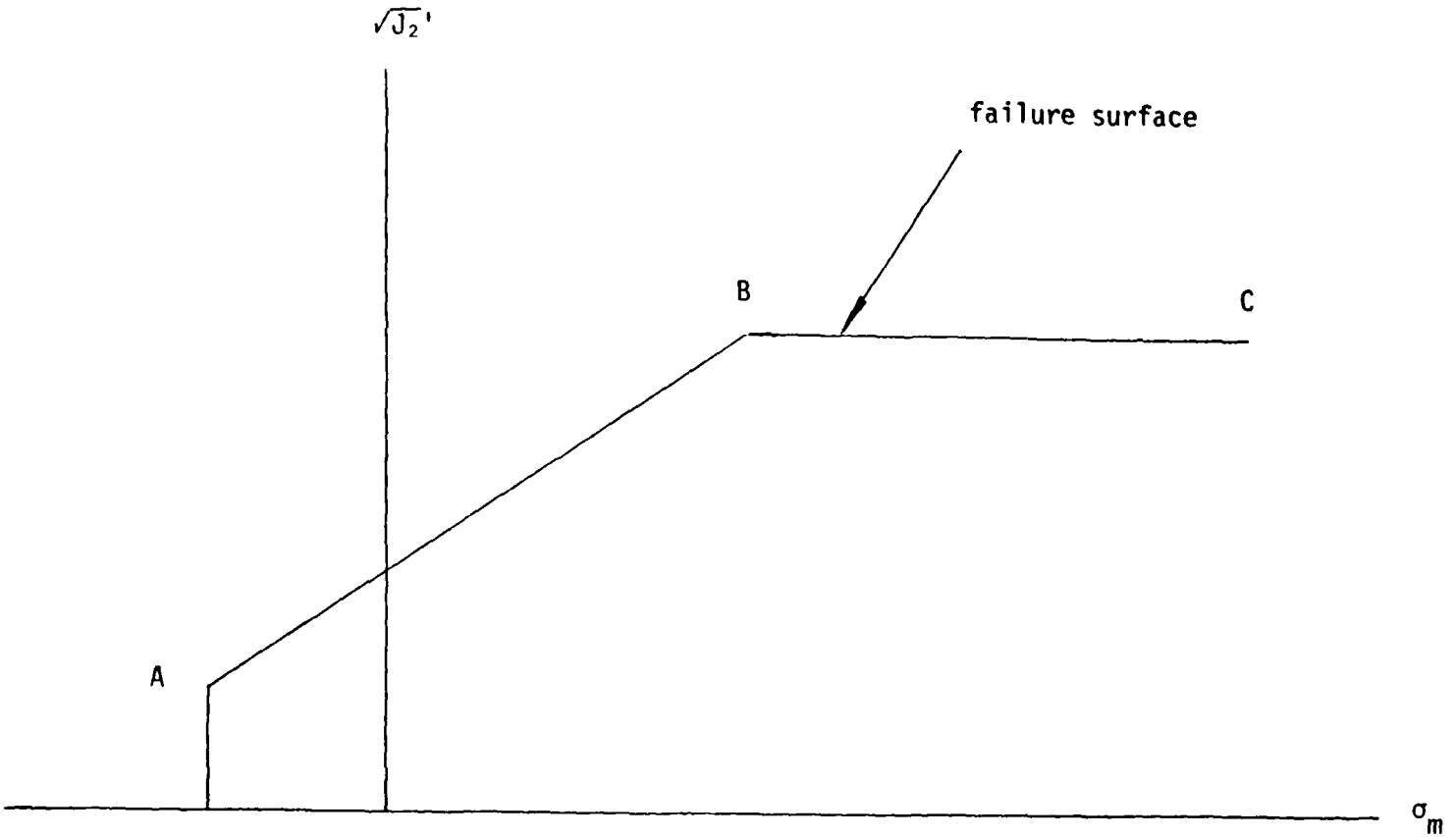

Figure 6.17 The failure surface of engineering model

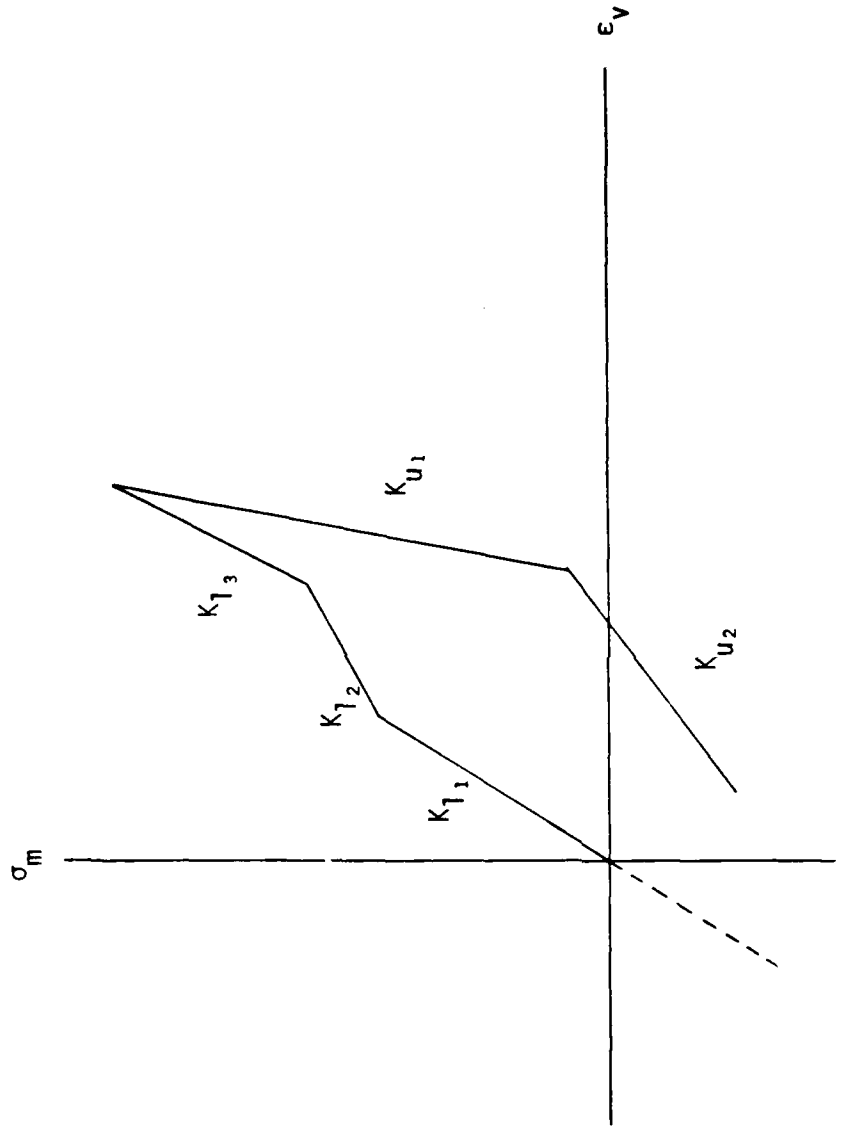

Figure 6.18 Engineering model description of mean stress vs. volumetric strain response

the other was the split tension test. The test procedures follow standard ASTM test procedure C39 (Compressive Strength of Cylindrical Concrete Specimens) and C469 (Splitting Tensile Strength of Cylindrical Concrete Specimens). Curved steel end platens were used in the Brizilin splitting tension tests to reduce local crushing of the test sample.

All tests were performed on an MTS machine at the standard loading rates. Figures 6.19 shows the stress-strain relationship of the micro-concrete obtained from one of the unconfined compression tests. Table 6.1 lists the test results of all the strength tests.

The unconfined compressive strength and the tensile strength of the material allows point A and point B in Figure 6.17 to be defined. Point C on the curve is obtained by extending the curve from B parallel to the P-axis to an arbitrary value.

Figures 6.19 indicates that the micro-concrete responded linearly throughout the entire loading. Since the working load of the centr fuge experiment was only about 100 psi, it was reasonable to assume that the bulk moduli of the loading and the unloading parts of material were the same. Knowing the Young's modulus and assuming the Poisson's ratio of the material to be 0.25, the elastic bulk modulus of the material could be

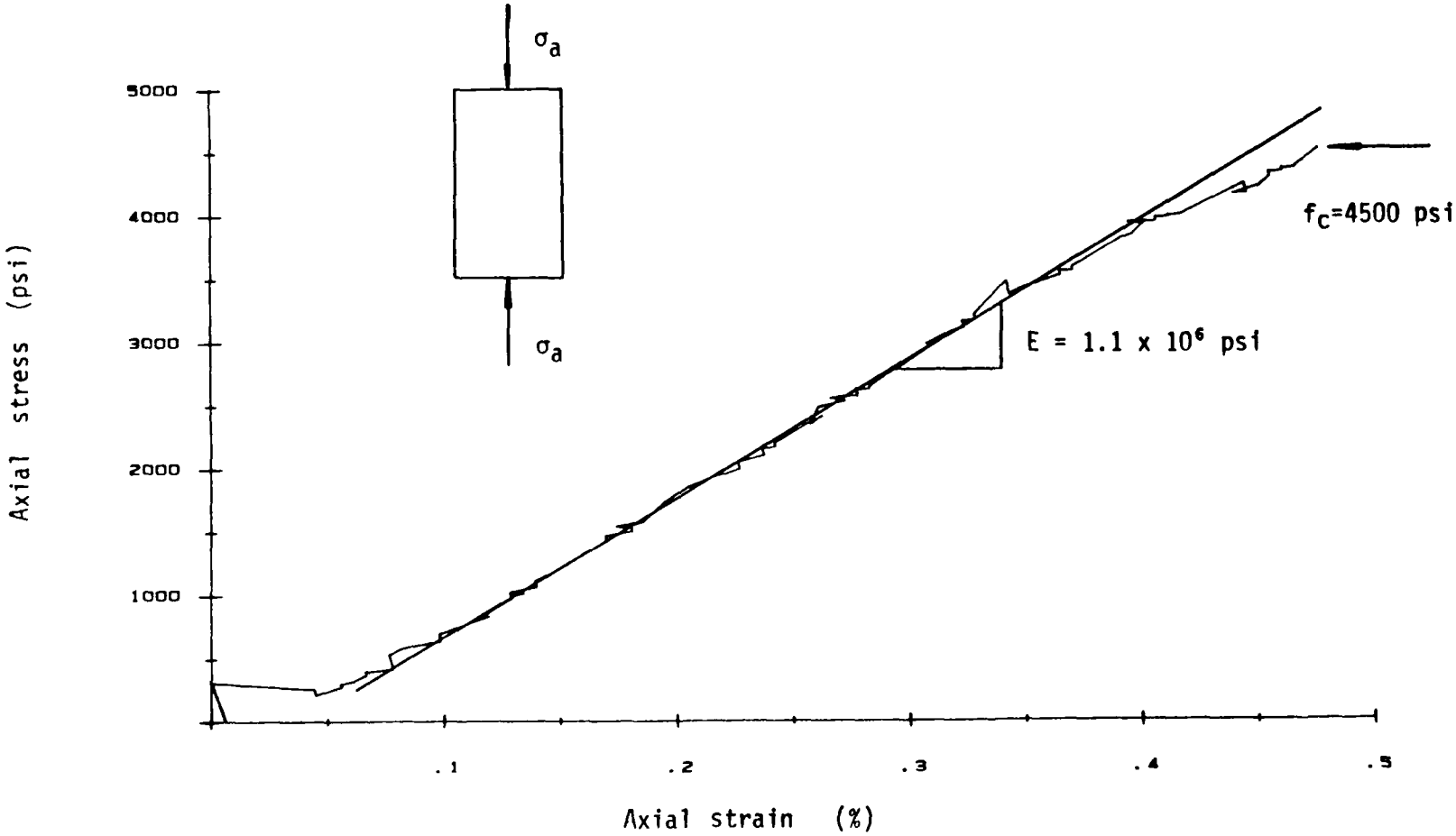

Figure 6.19 Axial stress vs. axial strain response of micro-concrete under uniaxial compression.

Table 6.1

Results of micro-concrete strength tests

test number	Young's modulus (psi)	Unconfined compressive strength (psi)
1	1.1×10^6	4,500
2	0.9×10^6	4,500
3	1.0×10^6	4,500
4	1.1×10^6	4,500
Ave.	1.0×10^6	4,500

Test number	Split tensile strength (psi)
1	558
2	485
3	516
4	578
Ave.	534

obtained. Hence, the volumetric response of the material could be defined.

Figure 6.20 shows the comparison between the model prediction and the experimental result of the uniaxial compression test.

6.5 Parameters for Linear-Elastic Analysis

The parameters required to represent a linear-elastic material include the Young's modulus and the Poisson's ratio. For Coyote Concrete sand, the Young's modulus is obtained from the unloading curve in the stress-strain response as shown in Figure 6.2 and the Poisson's ratio is assumed equal to 0.33. For the micro-concrete, the Young's modulus is obtained from the uniaxial compression test as shown in Figure 6.19 and the Poisson's ratio is assumed equal to 0.25.

6.6 Direct Shear Test and Interface Elements

As described previously, interface elements which can properly simulate the relative movements between the soil and structure are important in the analysis of soil-structure interaction. This relative movement will redistribute the stresses around the structure, and the degree of stress redistribution depends on the magnitude as well as the type of movement. Generally, the relative movements are controlled by the interface friction angle.

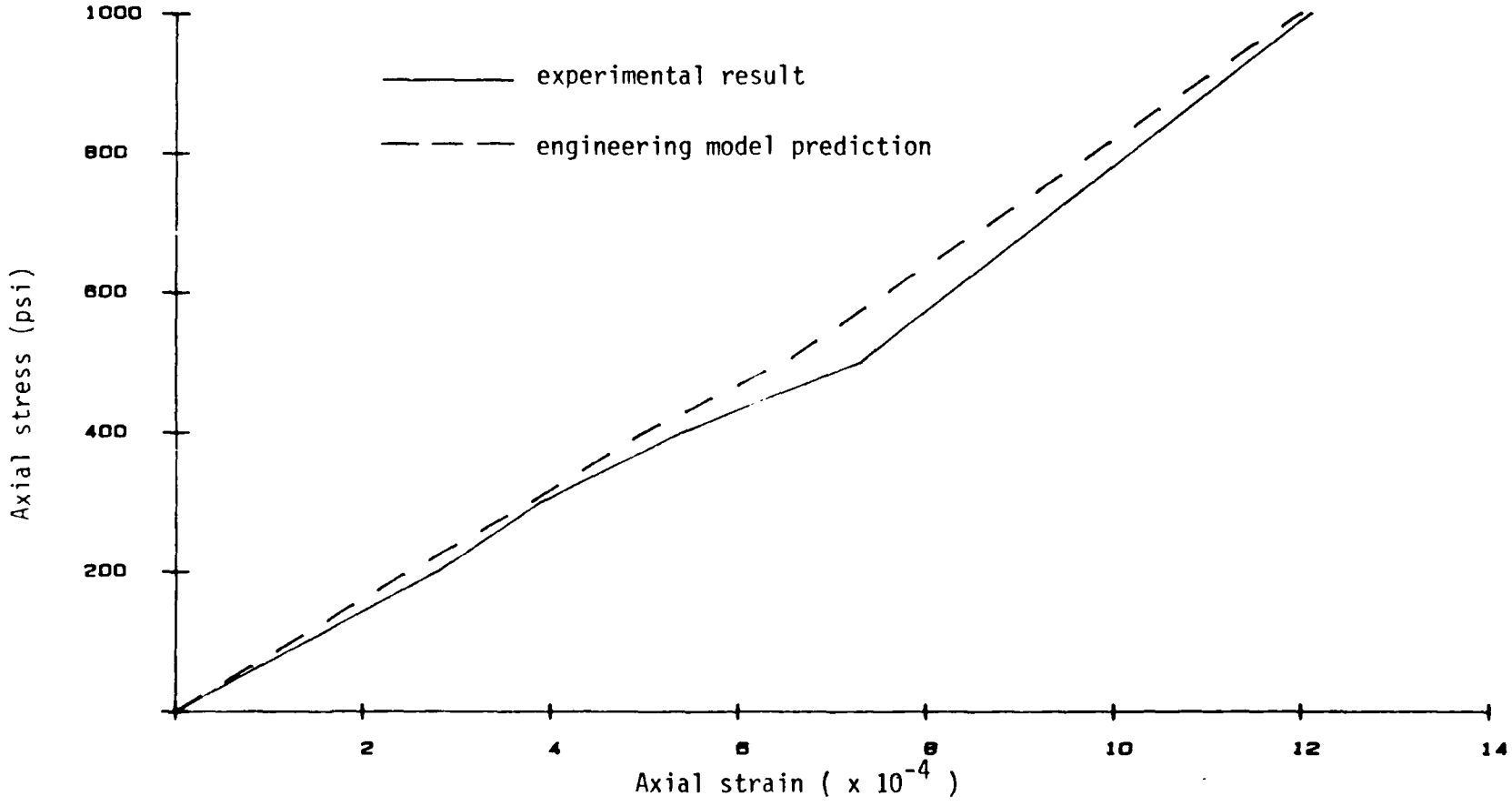

Figure 6.20 Compression between the engineering model prediction and the experimental result of the uniaxial compression test.

The study of interface element in finite element method was initiated by Goodman et al., (1968). Their interface element was used to represent the discontinuity in rock. Zienkiewicz (1970) used an isoparametric element with adjacent nodal points on opposite sides of the element having the same initial coordinates. Ghaboussi et al., (1973) derived an interface element by considering relative motions between surrounding solid elements as an independent degree of freedom. Desai (1981) developed a thin-layer element which has very small compressibility in the direction normal to the boundary.

All of these above-mentioned interface elements require the value of interface friction angle to simulate the interface motion. In order to determine this angle and to investigate the shearing behavior between the soil and the micro-concrete, a series of interface shear tests were conducted. The tests were conducted on a direct shear test machine that is used for conventional soil testing. The test procedure for the interface shear test followed that of the soil-soil direct shear test. In fact, the only difference between the interface shear test and the regular soil-soil direct shear test was that in the former the bottom half of the shear box was replaced by a fixed micro-concrete block.

The test program included testing the Coyote Concrete sand at densities, 50%, 70%, 80% and 90% under five different normal stresses. Figure 6.21 shows a typical shear stress versus displacement response. The interface friction angle can be obtained by plotting the normal stress versus the shear stress as shown in Figure 6.22. The results show that the interface friction angle is independent of the relative density of the soil.

6.7 Body Force

One of the major advantages of using a geotechnical centrifuge is that the centrifugal acceleration increases the self weight of the soil so that the stress level of the prototype is properly simulated in the model, which in turn assures that the soil response will be properly replicated.

In the non-linear finite element analysis, it is also necessary to include the body force which will produce an initial stress that allow the soil to react to loading differently than if the body force is absent.

The program SAMSON2 does not allow the application of the body forces. This is understandable because the code was originally developed for the analysis of ground shock effects resulting from nuclear or high explosive sources. The body forces of the soil in this case become minute as compared to the live loads. However, it is obviously that the body forces are

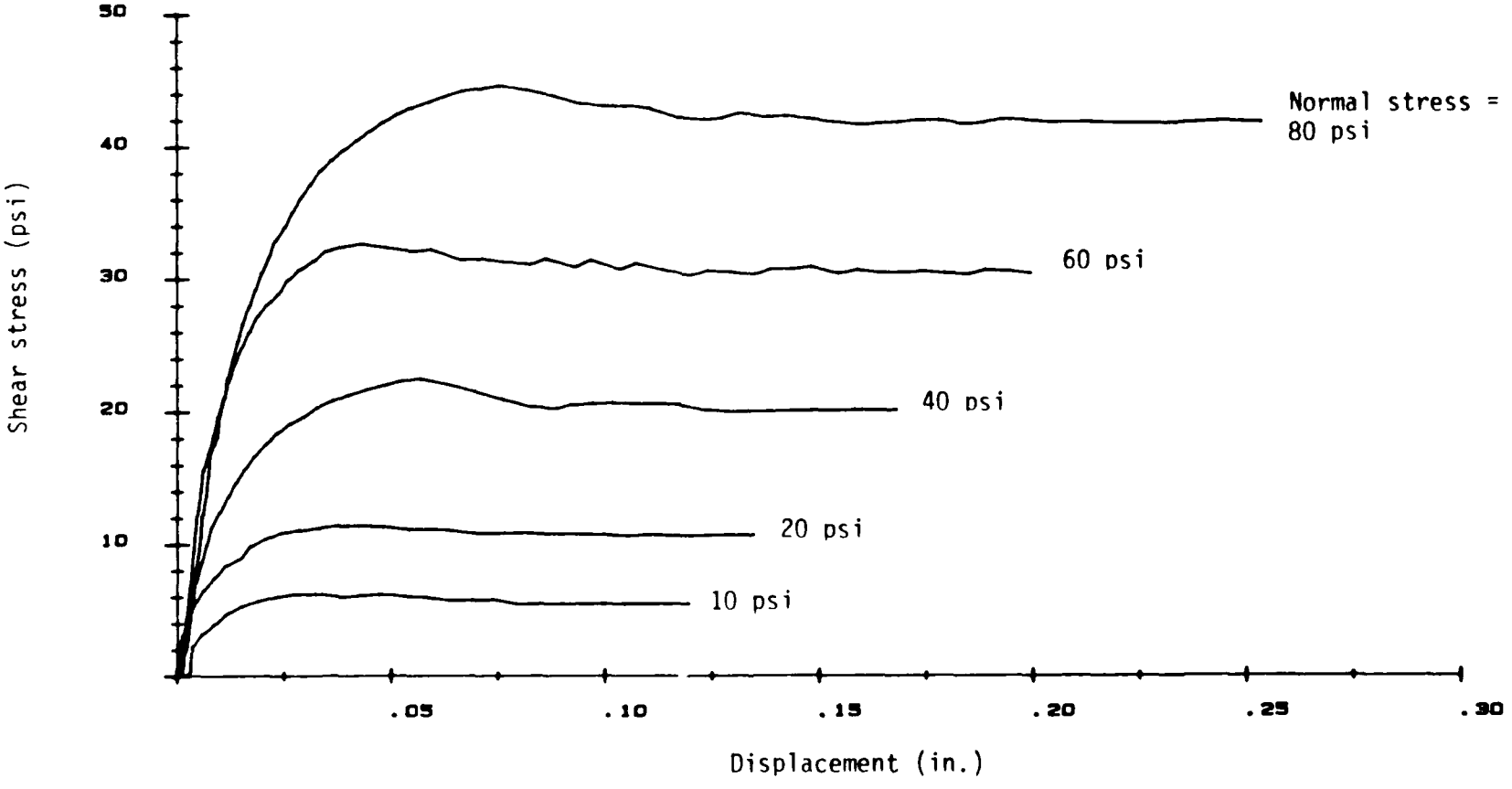

Figure 6.21 Shear stress vs. displacement response, relative density= 50%

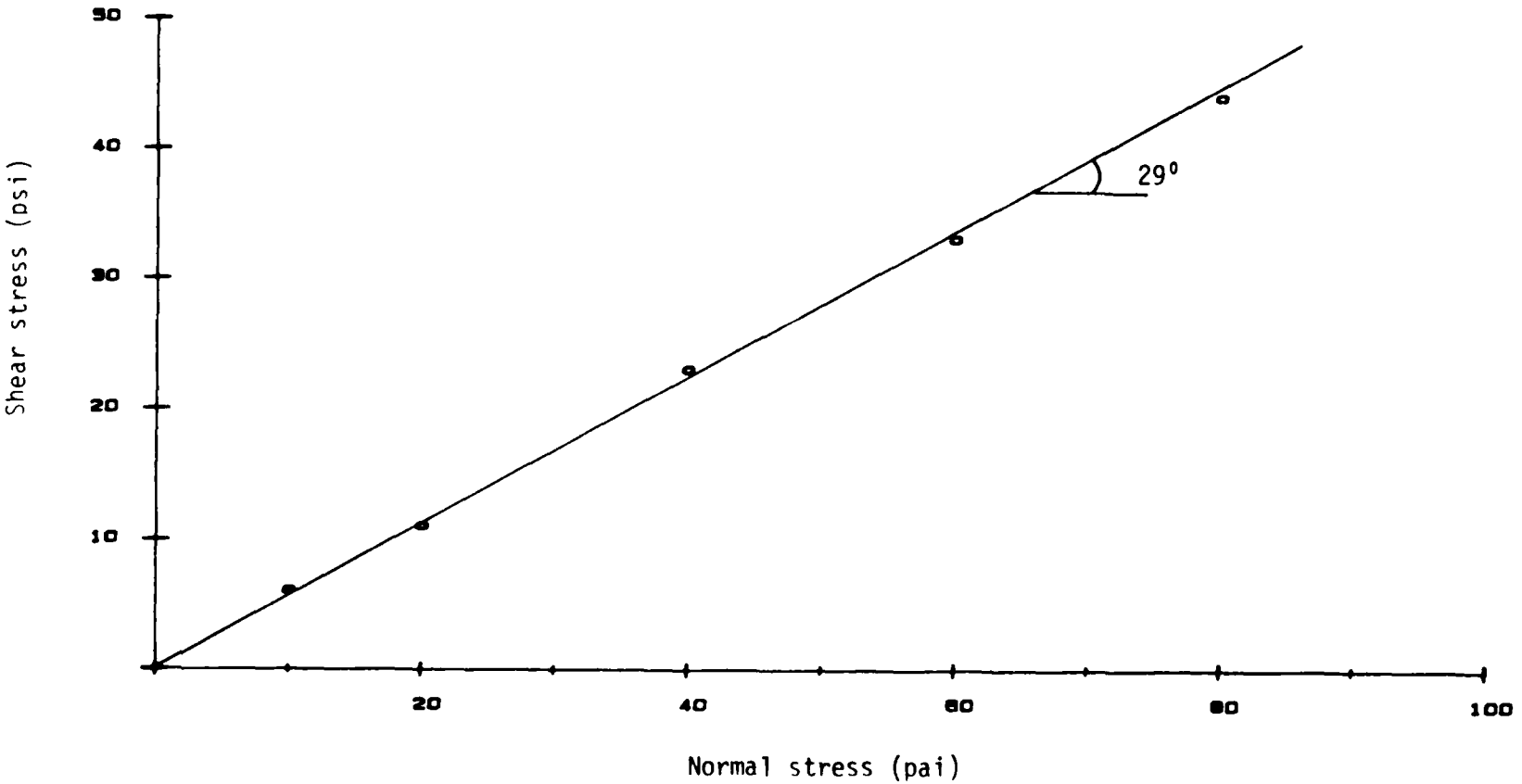

Figure 6.22 Plot of strength envelope: Relative density = 50%

critical for the analysis of the centrifuge experiments. In addition, the unit weight of the soil has to be varied along the depth of the soil since the centrifugal acceleration varies in that direction.

The easiest way to allow the application of the body forces without changing the code is to use a pre-processer to generate the consistent nodal forces due to the body forces and prescribe the nodal forces at the SAMSON2 input level. The consistent nodal forces due to the body force can be calculated by

$$\{q\}_b = t \iint [\mathbf{N}]^T \gamma \, dxdy \qquad (6.12)$$

where

$\{q\}_b$ = the consistent nodal force due to the body force,

t = element thickness,

$\mathbf{N}$ = shape function,

γ = unit weight which is a function of the depth of the soil.

To perform the above calculations, a subroutine generating the shape function for eight-node elements, and another subroutine conducting numerical integration, were implemented in an instructional finite element code MICROFEM. The calculated consistent nodal forces were written in a SAMSON2 input format and used as input to the SAMSON2 analysis.

The analysis of the centrifuge experiments will be in a dynamic environment; however, the body forces are initially applied static loads. Hence, in performing the non-linear dynamic analysis with body forces, it is necessary to apply the body forces with a long rise time at the beginning of the analysis. The dynamic load shall be applied only after the response of the system to the application of the body force becomes stable. Figure 6.23 shows the method of load application for the non-linear dynamic analysis.

6.8 Finite Element Model of Centrifuge Test

Figure 6.24 shows the finite element model used for the analysis of the centrifuge experiments. Eight-node elements were used in the analysis. The four-node elements shown in the mesh are only for illustration.

The mesh represents only half of the centrifuge model reflecting the symmetry of the surface overpressure and the geometry of the model. Surface overpressure was applied to the center portion of the soil surface just like it was in the experiment. In the case of non-linear analysis, surface overpressure was applied after the application of the body forces.

Rollers are shown at the right boundary of the mesh. However, analysis with hinges at that boundary showed no noticeable difference in the stress field around the pipe. This might be due to the fact that the

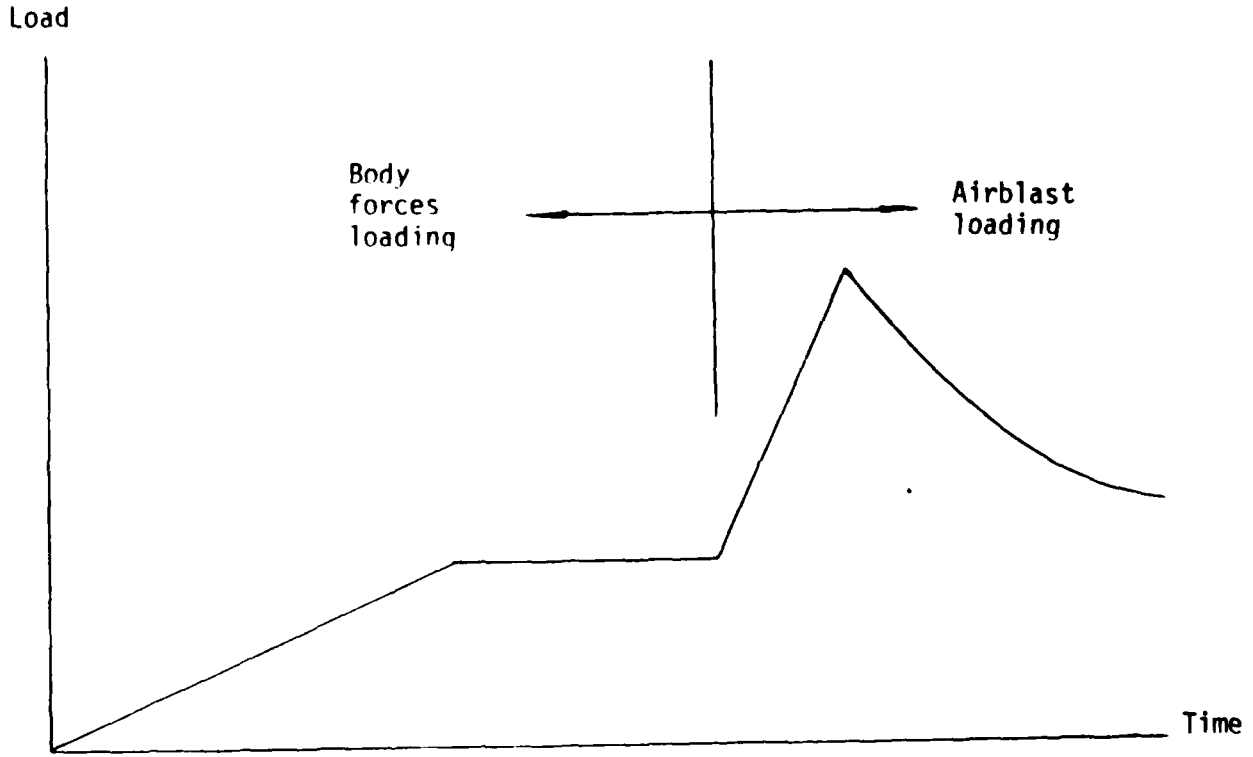

Figure 6.23 Method of load application for non-linear analysis

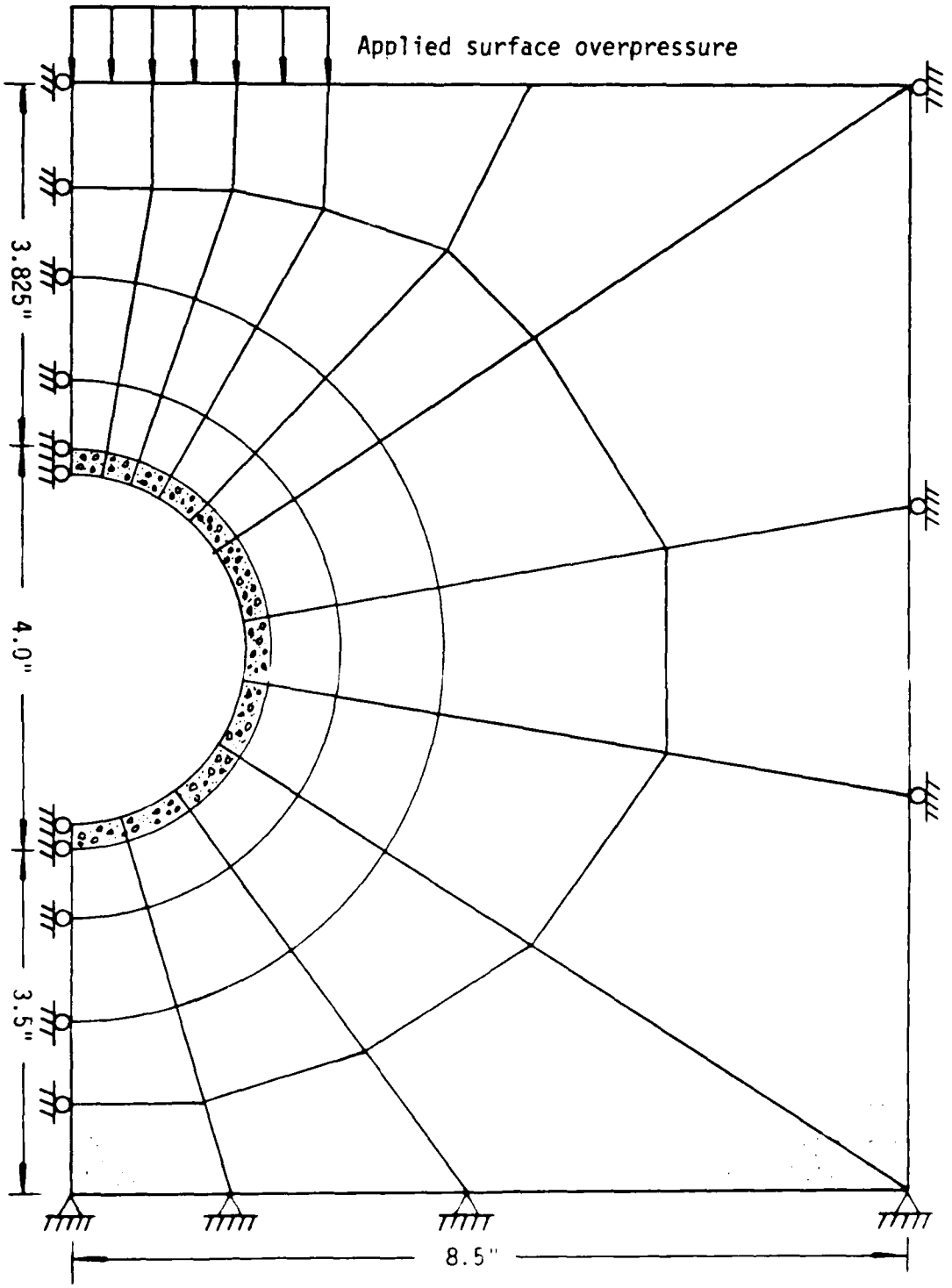

Figure 6.24 Discretization of the centrifuge model, mesh 2

applied loading was too far from the boundary to induce significant shearing at that boundary.

Interface elements were used to investigate the effects of relative motion at the soil-structure interface. The results showed that the incorporation of the interface element did not change the stresses around the pipe. This is probably due to the following reasons: (1) the initial confining pressure produced by the self-weight of the soil under 50 g provides a shear resistance at the interface; (2) the applied surface pressure (maximum 38 psi) was too low to induce interface shearing.

6.9 Convergence Study

A convergence study was conducted using three difference meshes, shown in Figures 6.24 to 6.26. Meshes 1, 2 and 3 have 224, 356 and 749 degrees of freedom, respectively. Two by two and three by three integration rules were used for each of these meshes in this study.

The typical surface overpressure distribution as seen in the centrifuge tests (as shown in Figure 6.27) was applied to these meshes. Strain energy and kinetic energy of the system were calculated at 1.0 msec. for the three meshes and plotted versus the degree of freedom as shown in Figure 6.28. The energy convergence as shown in the figure is a necessary condition for the convergence of the system. In addition, the convergence

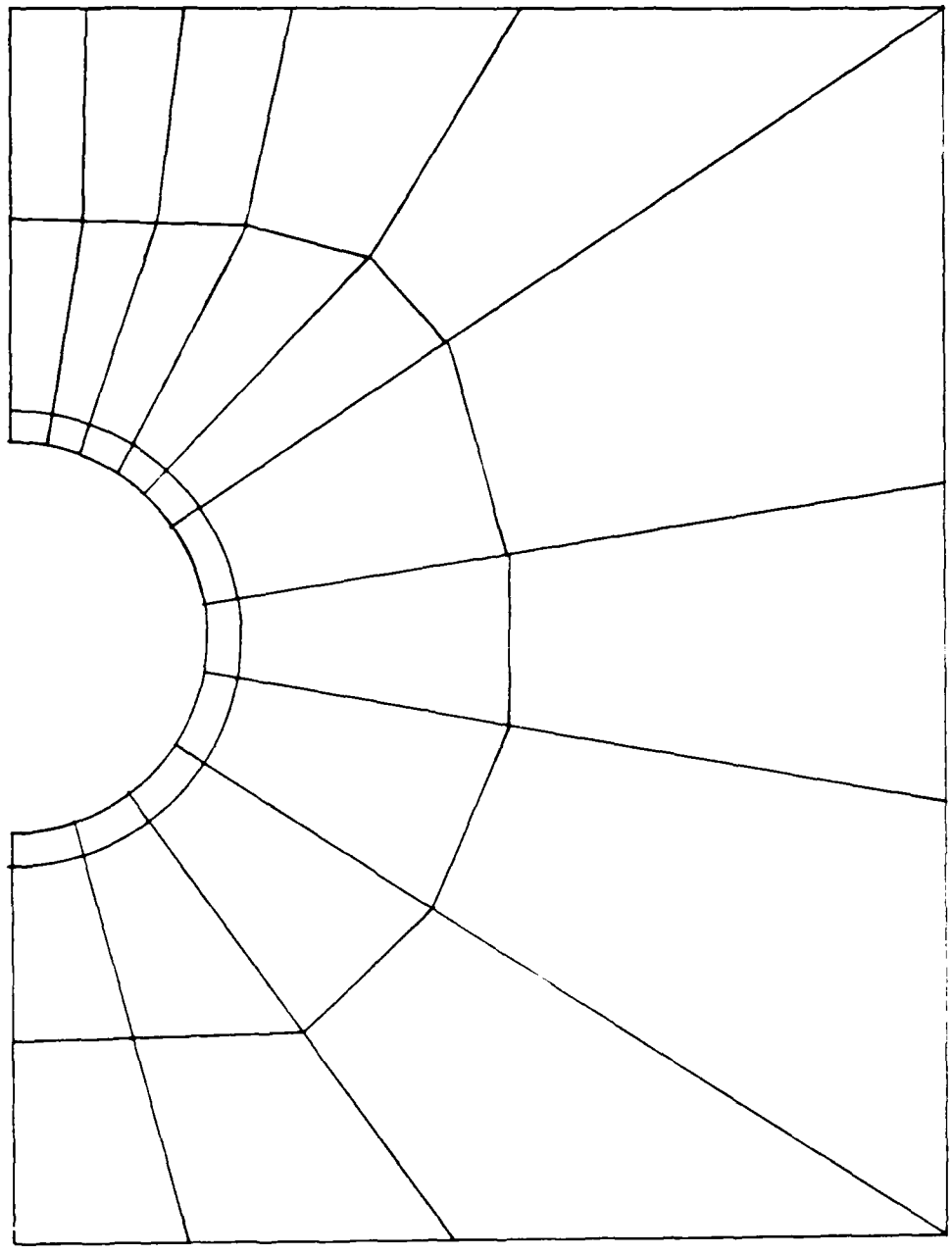

Figure 6.25 Convergence study, mesh 1

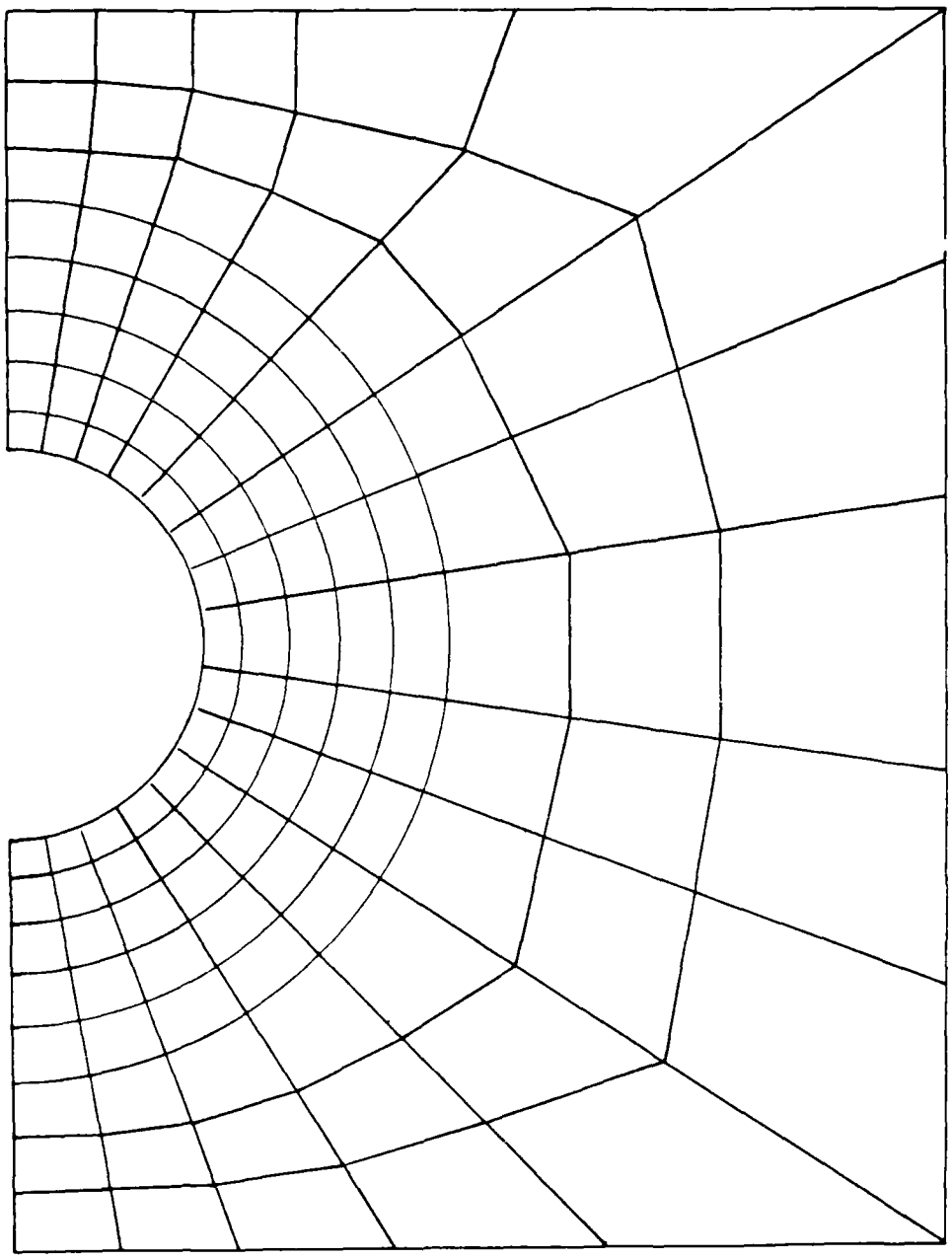

Figure 6.26 Mesh 3 for convergence study

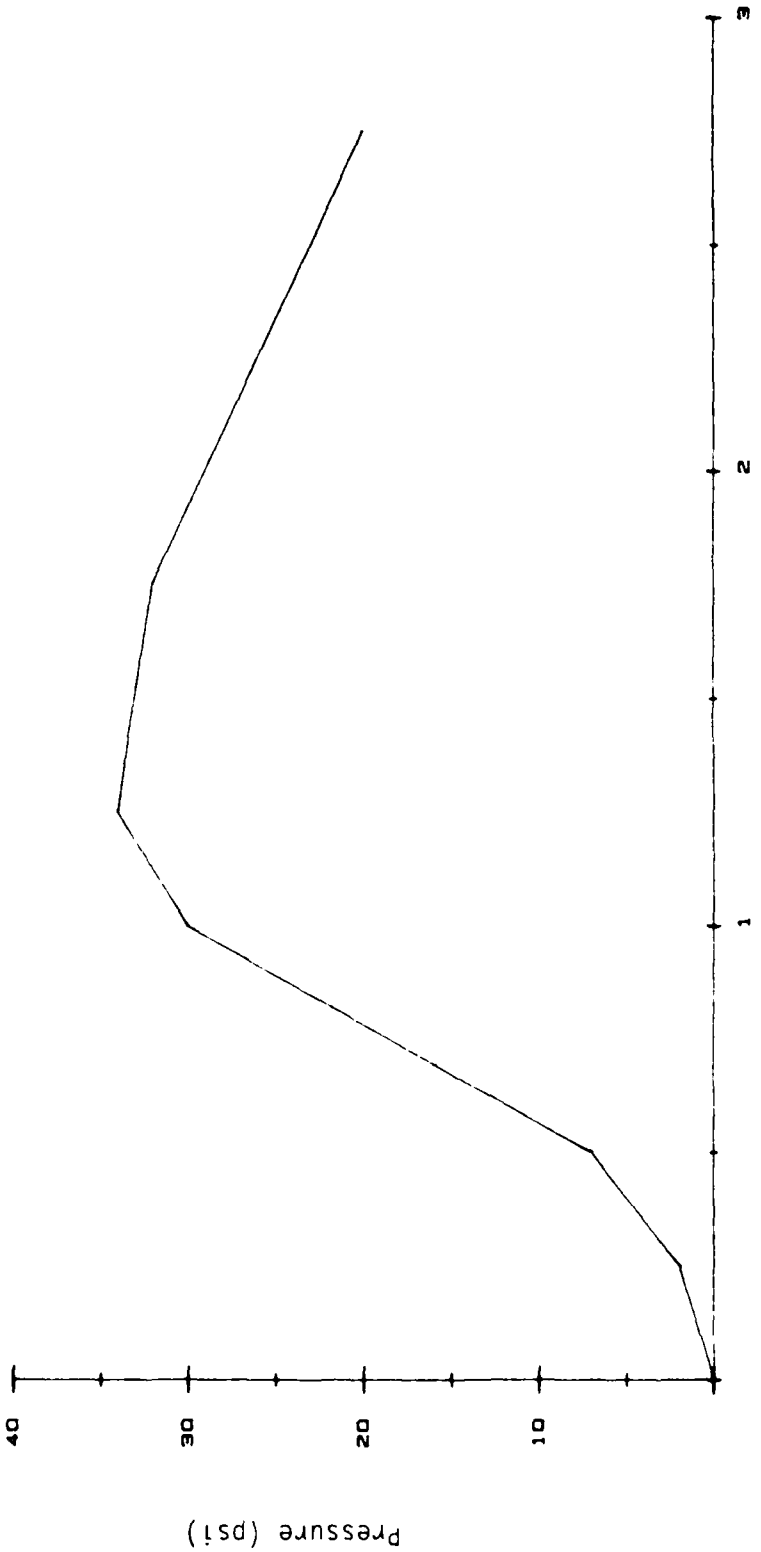

Figure 6.27 A typical surface overpressure in the centrifuge test

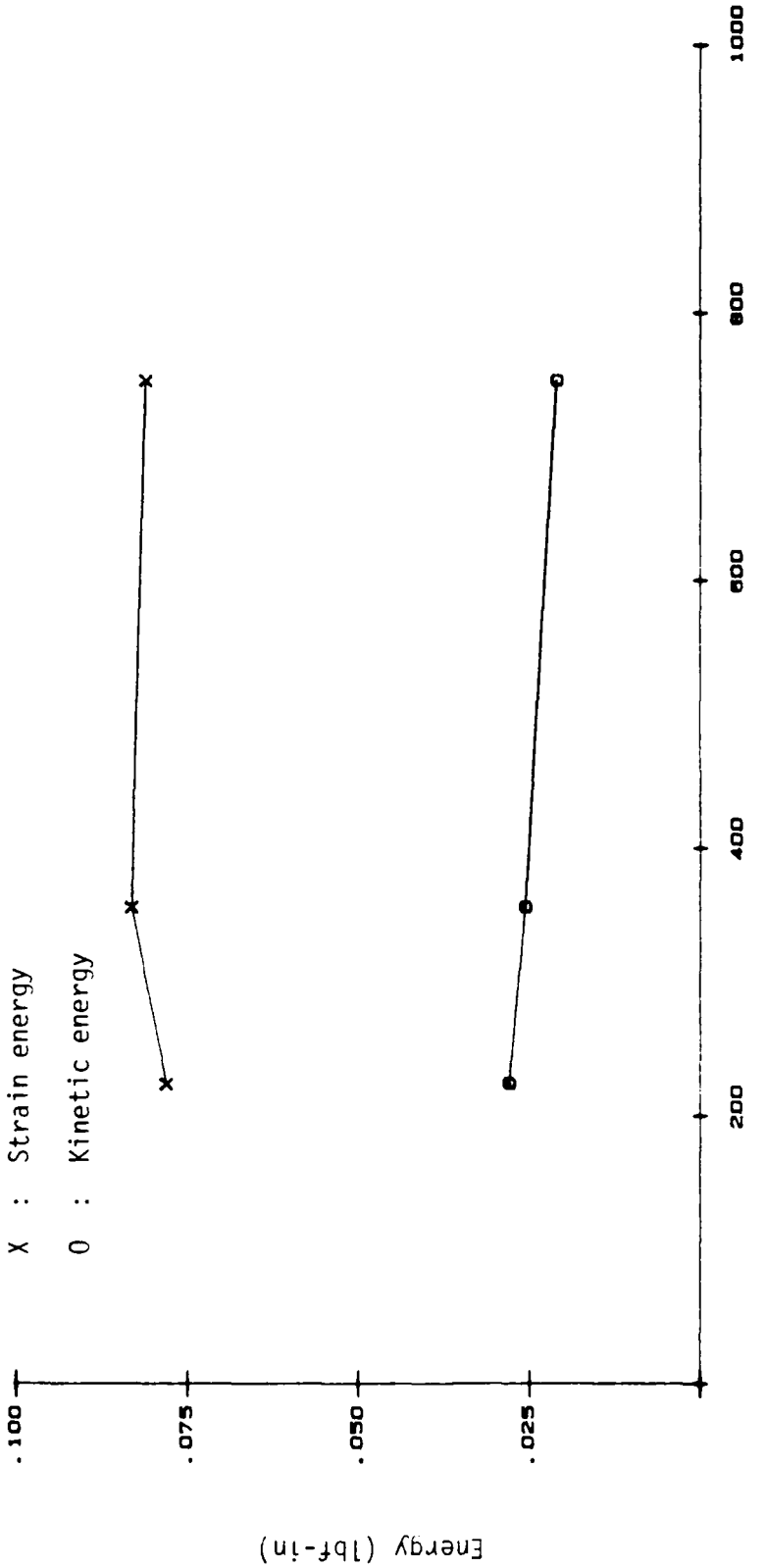

Figure 6.28 Energy versus degrees of freedom.

of the contact pressures need to be ensured since they are the ones to be compared to the experiment.

The contact pressure histories at the crown, springline and invert of the pipe, obtained from these meshes with the two integration rules, are shown in Figures 6.29, 6.30 and 6.31. It can be seen from these figures that for each mesh the results obtained by using 2x2 integration are close to those obtained by using 3x3 integration, and that the results obtained from the medium mesh (356 d.o.f.) are close to those obtained from the fine mesh (749 d.o.f.). Judging from the accuracy and the computing cost of these results it is concluded that reliable solutions can be obtained using the medium mesh with 2x2 integration rule.

The dynamic pressure profile along the center of the soil model, as obtained by using mesh 2, was plotted at three different times as shown in Figure 6.32. The plot demonstrates that the pressure profile in the soil can be obtained.

Figure 6.33 shows a mesh with 554 d.o.f. It was found that when 2x2 rule is used, this mesh generates instability problems at about 0.3 msec and when 3x3 rule is used, the same problems occur at about 1.75 msec. The reason for this instability remains unknown.

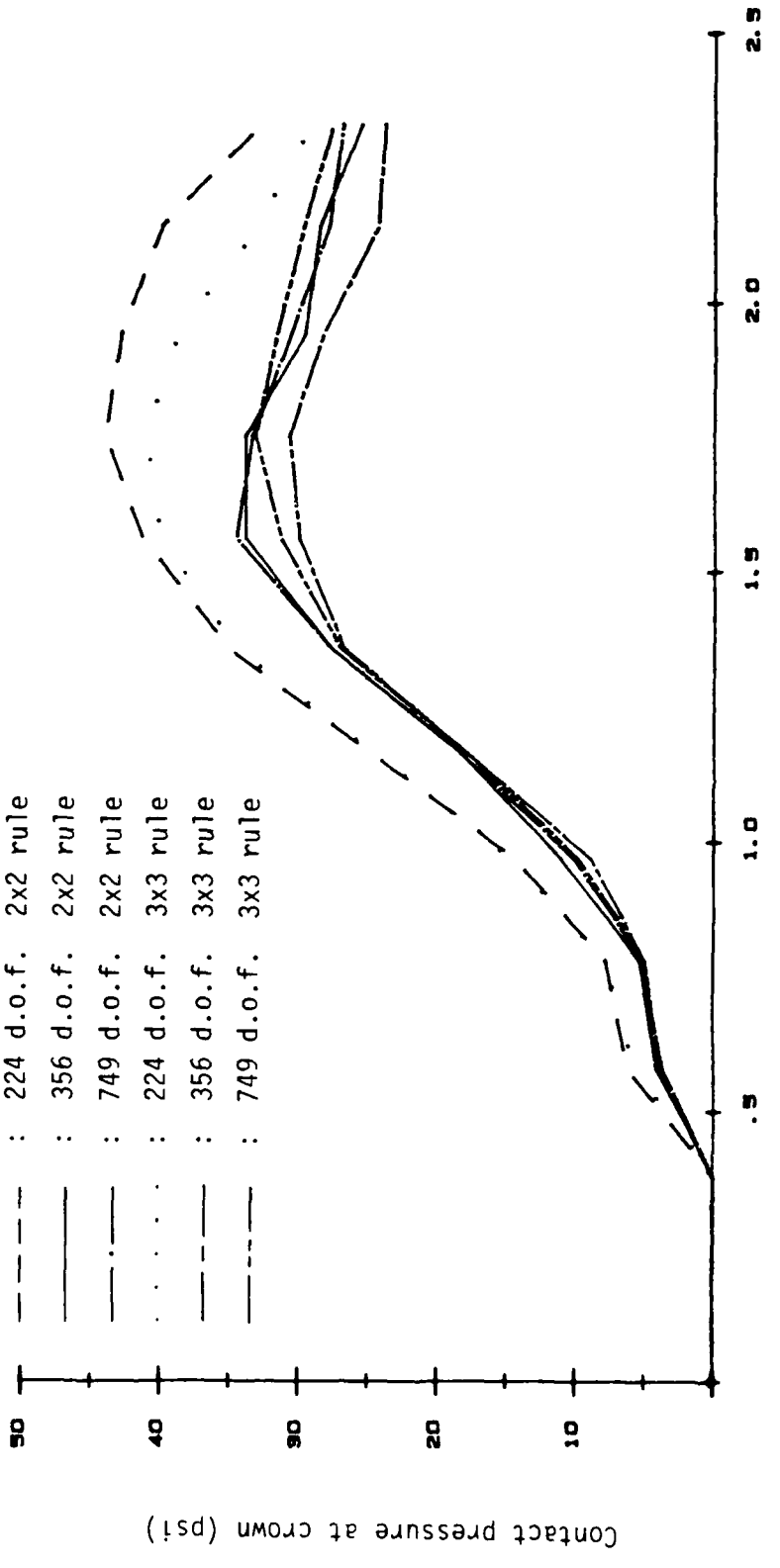

Figure 6.29 Comparison of contact pressure at crown obtained from three meshes using two integration rules.

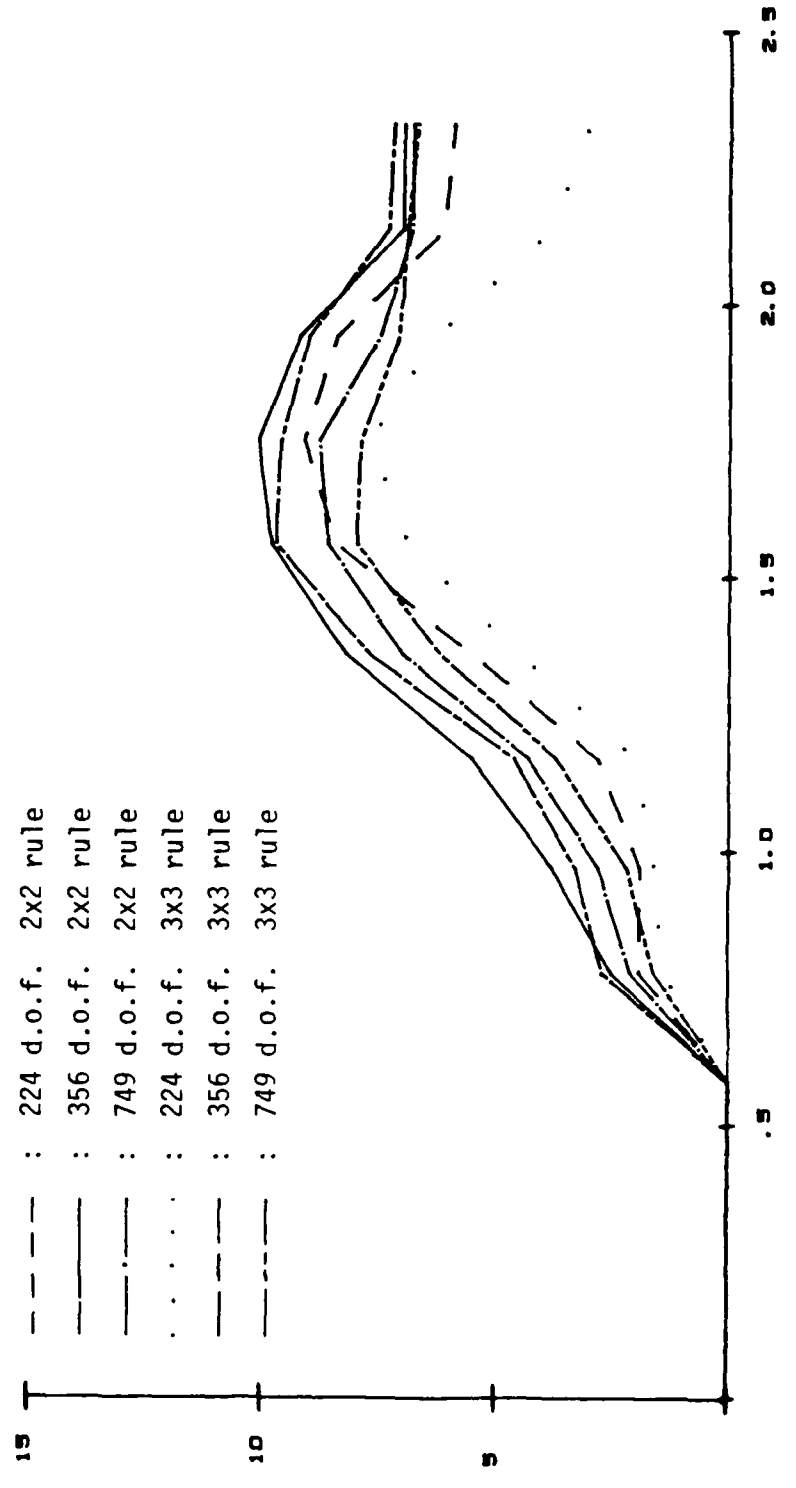

Figure 6.30 Comparisons of contact pressure at springline obtained from three different meshes using two integration rules.

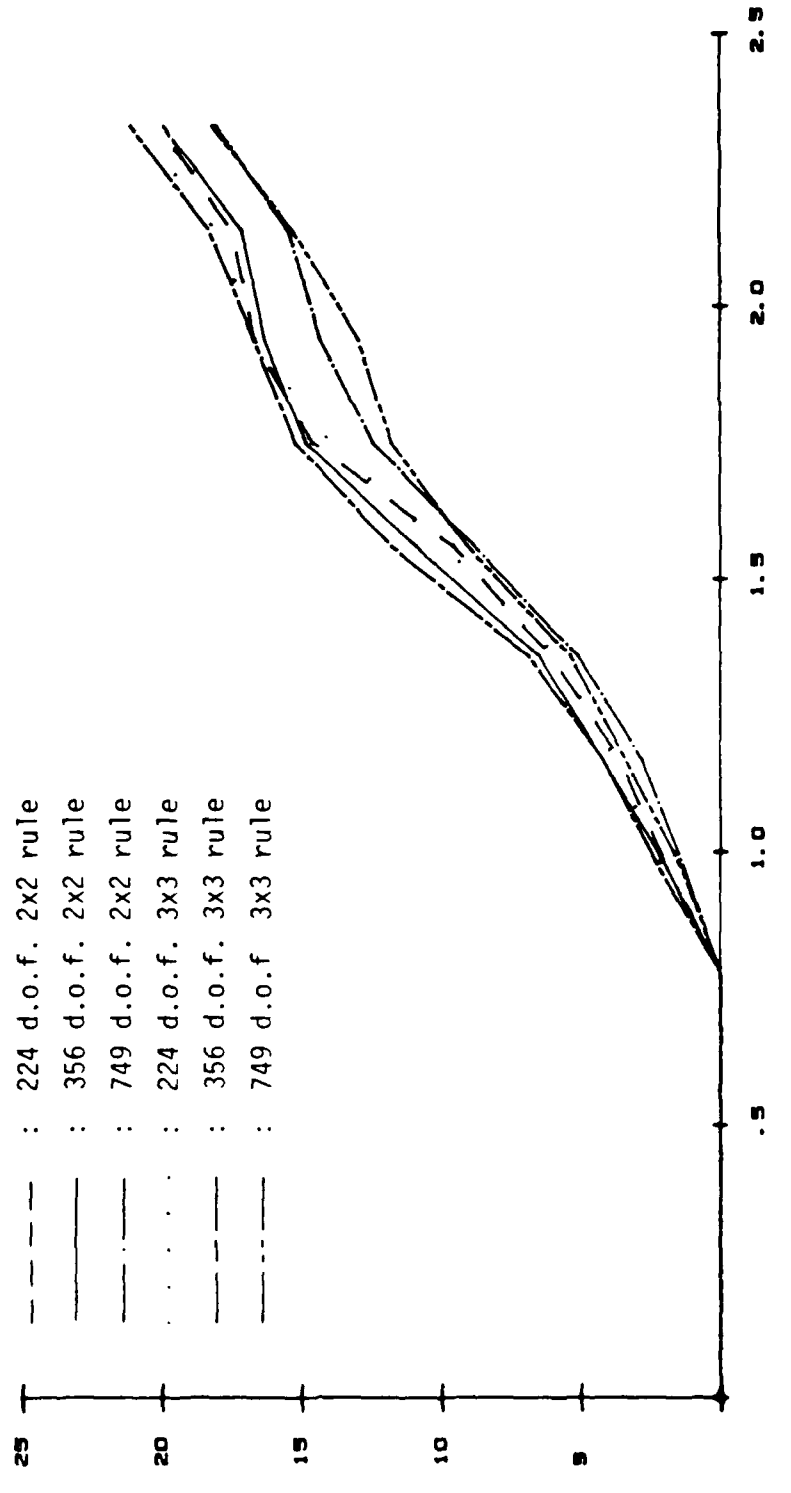

Figure 6.31 Comparisons of contact pressure at invert obtained from three meshes using two integration rules.

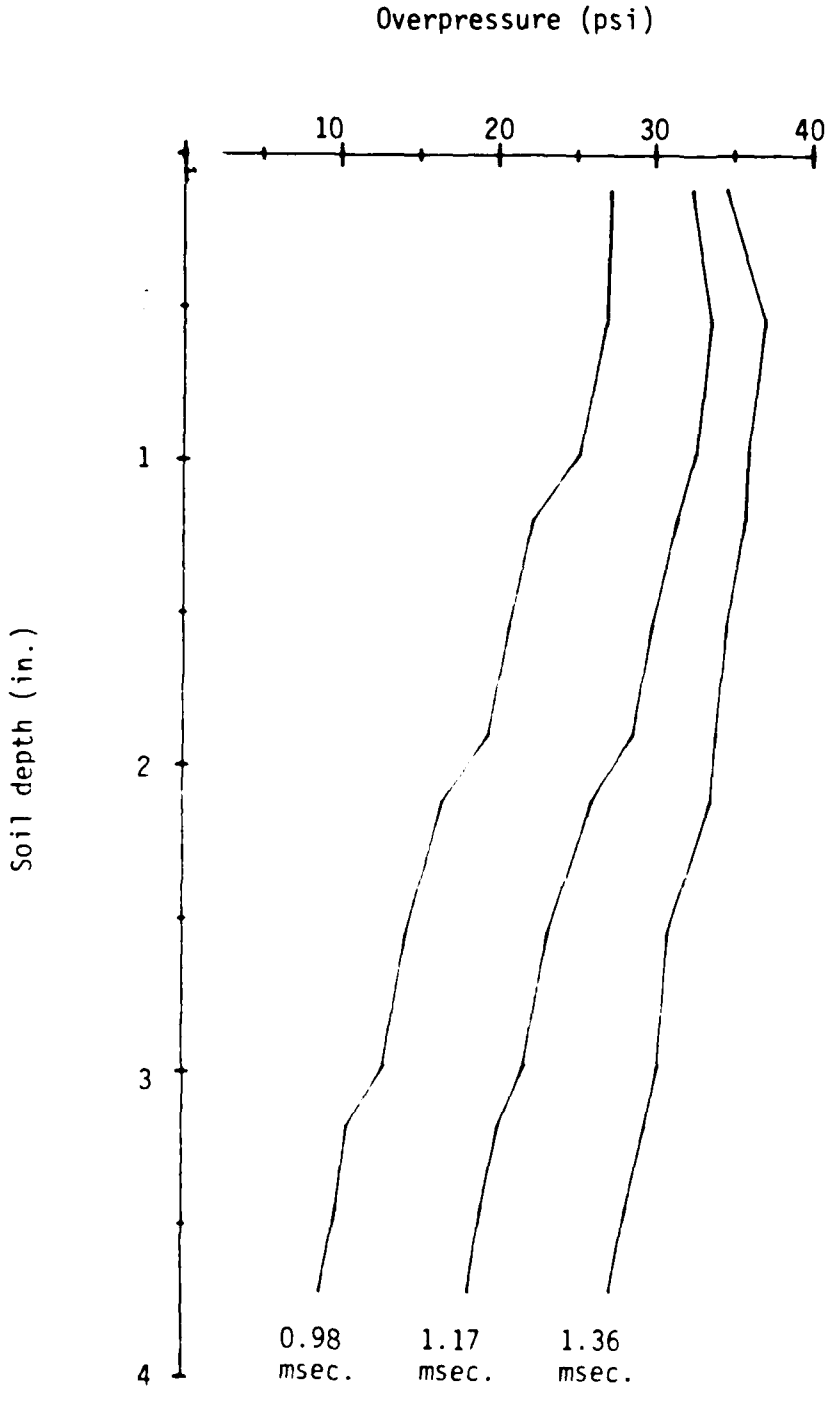

Figure 6.32 Pressure profile in a pipe test

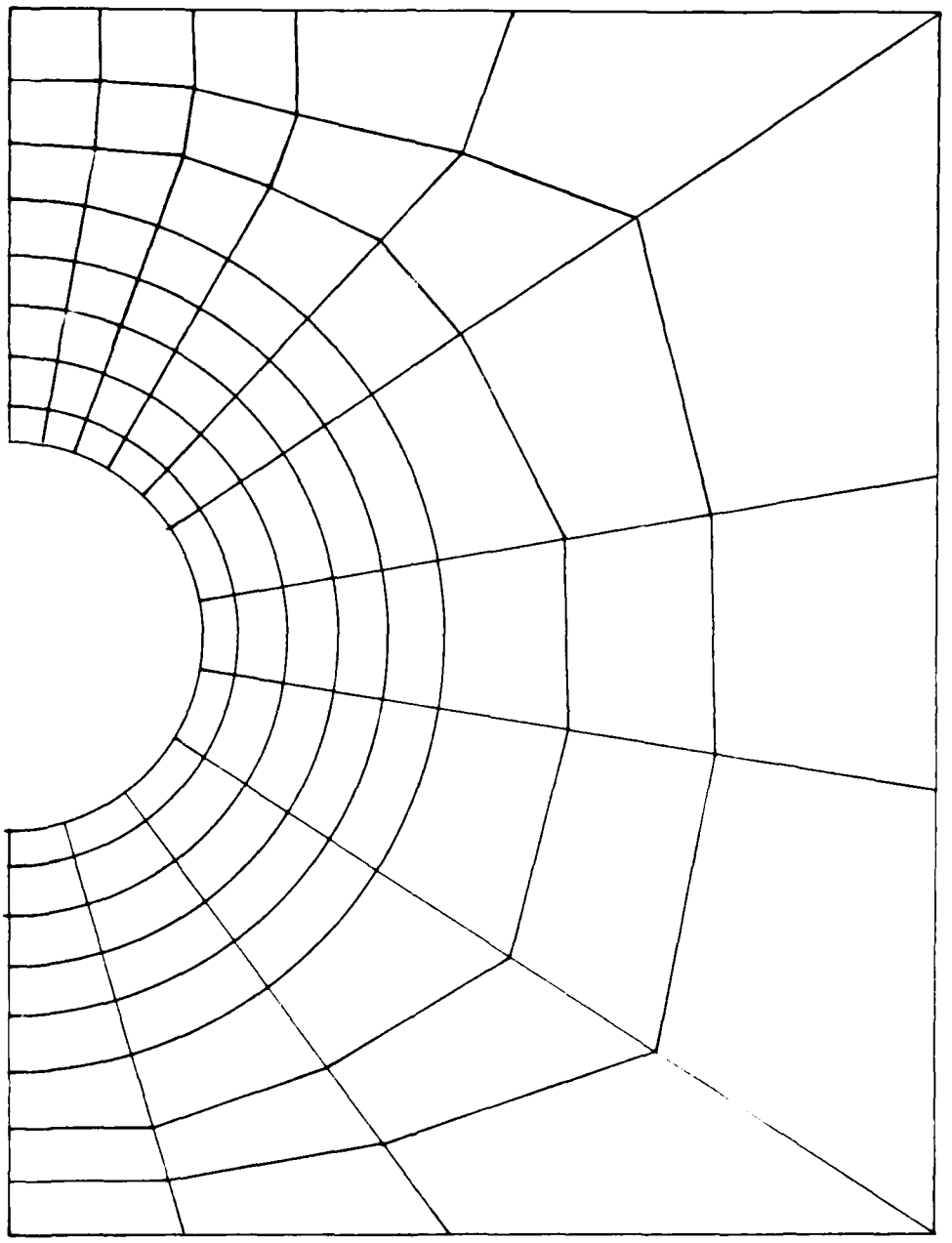

Figure 6.33 Finite element model, mesh

6.10 Finite Element Model of Free Field Analysis

Figure 6.34 shows the finite element model for the analysis of free field stresses. The loadings were applied to the soil in the same manner as in the soil-pipe system, i.e., the body forces were applied first with a slow rise time and were followed by the application of the surface overpressure. The dynamic pressure profile along the center of the soil model was plotted at three different times as shown in Figure 6.35.

The free field stresses are used to show the effect of the existence of the pipe. The results of the analysis are presented in the following chapter.

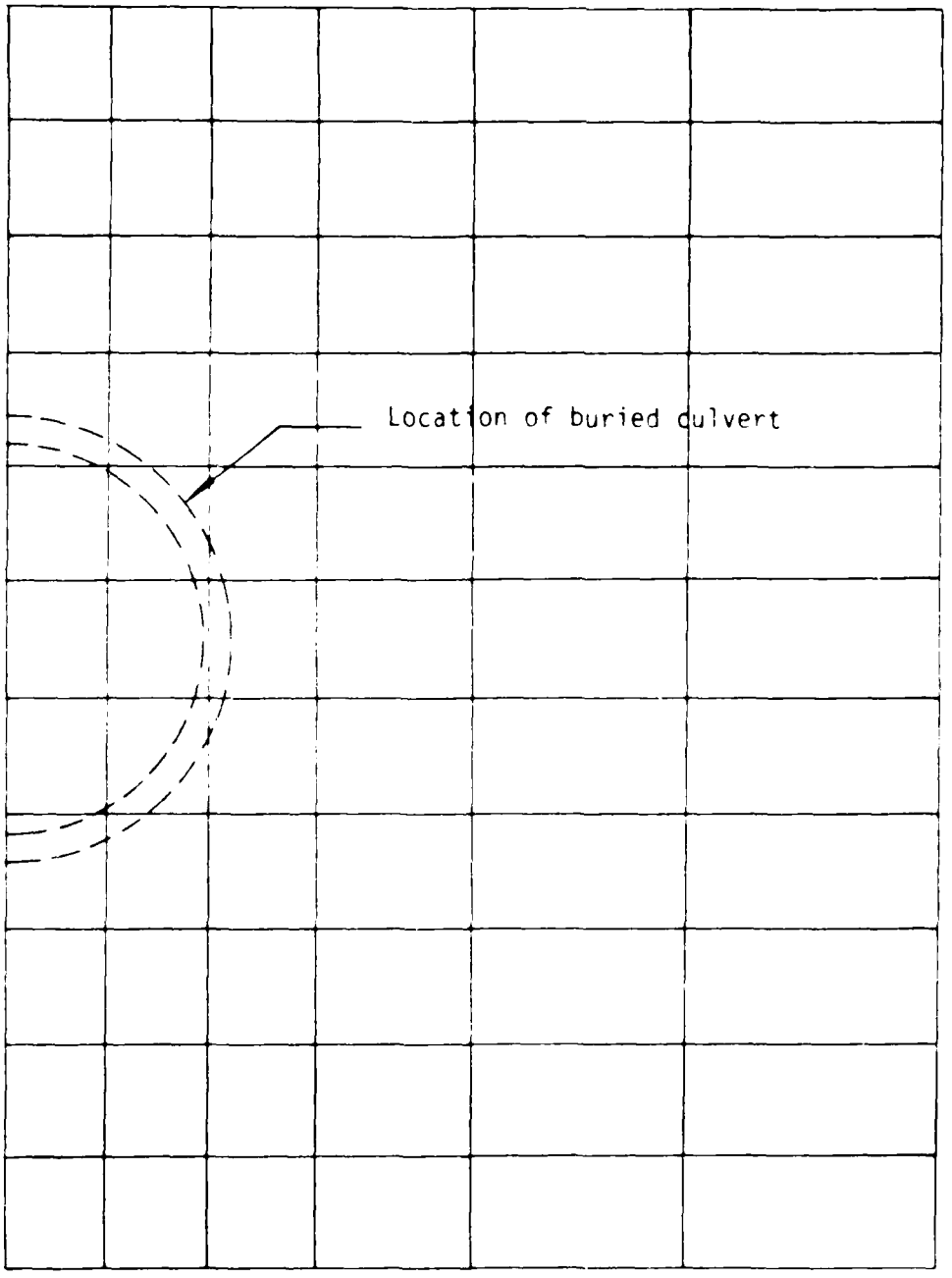

Figure 6.34 Discretization of the centrifuge model for free field analysis

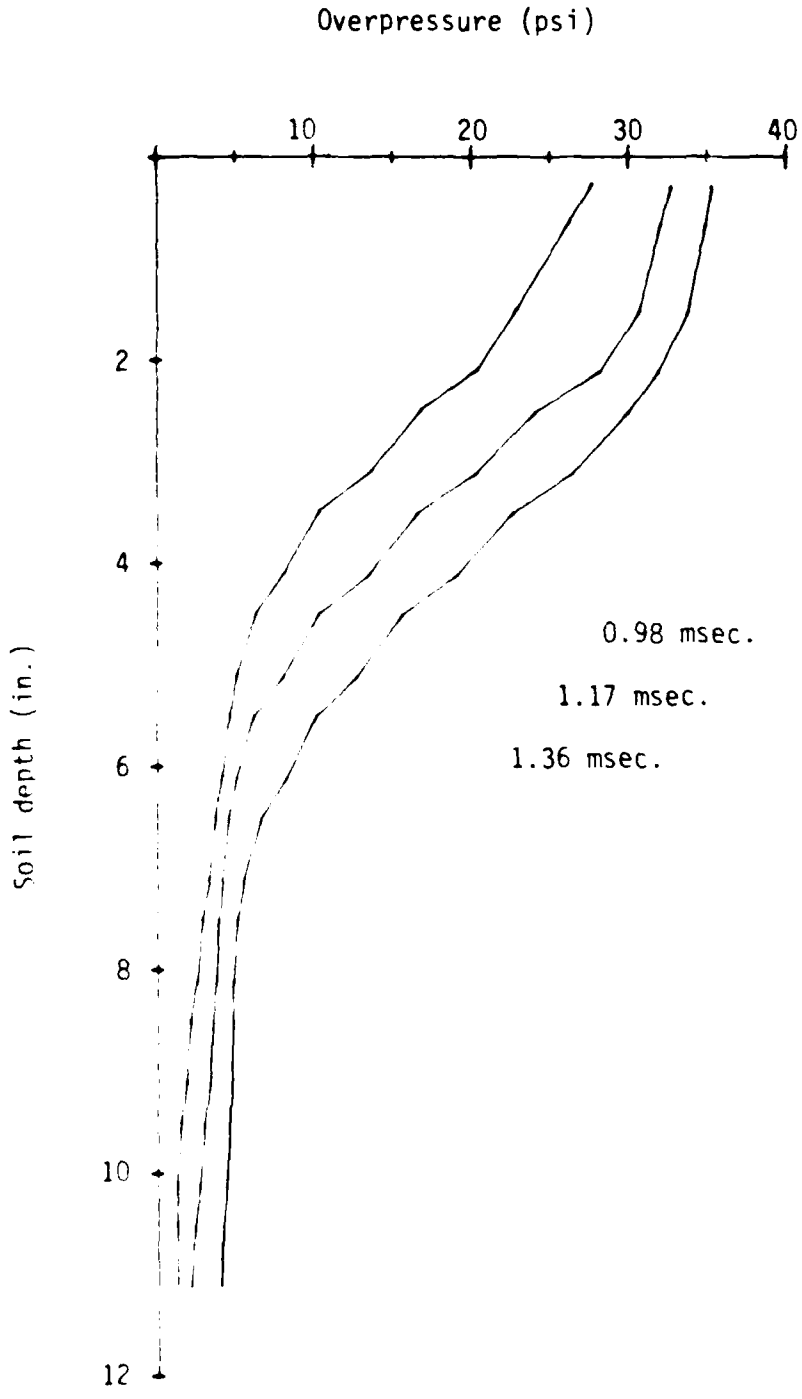

Figure 6.35 Free field pressure profile

CHAPTER VII

RESULTS OF CENTRIFUGE TESTS AND NUMERICAL ANALYSES

The experimental phase of this research was separated into two stages. The first stage, in which the author spent most of his efforts on, included: (1) perfecting the sample preparation scheme to produce high quality samples, (2) obtaining consistent surface overpressure generated by the impact generator, (3) ensuring the accuracy of the contact stress measurements, and (4) investigating the bending response of the contact stress gages.

At the end of the first stage, consistent test results had been obtained. In addition, it has been found that the bending of the micro-concrete pipe was too small to necessitate the bending correction of the contact stress gage reading.

The second stage of the experiments was to initiate a parametric study which later was completed by J.P. Whittaker. The parameters involved in the study included: (1) structure-soil stiffness ratio (pipes with different wall thicknesses were used), (2) soil density, (3) magnitude of the surface overpressure, and (4) depth

of pipe burial. In addition, centrifuge free field experiments were performed. Readers interested in the parametric study are referred to the thesis by Whittaker (1987). However, the effects of the structure-soil stiffness ratio as observed in the test program will be examined herein.

The first section of this chapter shows the experimental results of centrifuge test 1 which was conducted at the end of the first stage. The second section presents the analytical results of the same test. In addition, results of non-linear analyses with and without the application of the body forces are also compared.

The third section shows the analytical results of centrifuge tests 2 and 6 which were conducted in the parametric study. Comparisons between the experiments and the analysis are presented for the pipe deflections in test 2 and the contact pressures in test 6.

The fourth section shows the results of the free field analysis. The free field stresses obtained are used in the study of the effects of structure-soil stiffness ratio on the contact pressures, the results of which are presented in the fifth section.

7.1 Experimental Results of Centrifuge Test 1

Figure 7.1 shows a summary of centrifuge test 1. The wall thickness of the pipe was 0.2 inches, and the burial depth measured to the crown was 3.825 inches. The figure includes three surface overpressure measurements and five contact stress measurements. Surface stress gages numbers 8, 9, and 10 were positioned on the soil surface as shown in the figure. Since the distribution of the surface overpressure was uniform along and symmetrical about the y-axis, these three gages positioned from the center, and along the x-axis, would be enough to define the pressure distribution on the soil surface. The contact stress gages were labeled with letters "a" through "e". Their positions on the pipe are shown in the figure. The surface overpressures were the input pressures in the analysis, whereas the contact pressures were the ones to be compared between the analysis and experiments.

Figure 7.1 shows the stress histories up to 2.0 milliseconds after the application of the surface overpressure. The records after which are not shown due to the increase in pressures caused by the reflected wave from the boundary.

Figure 7.1 also shows the failure mode of the 0.2-inch-thick micro-concrete pipe. The pipe failed by four tension cracks, two at the outer wall of the pipe

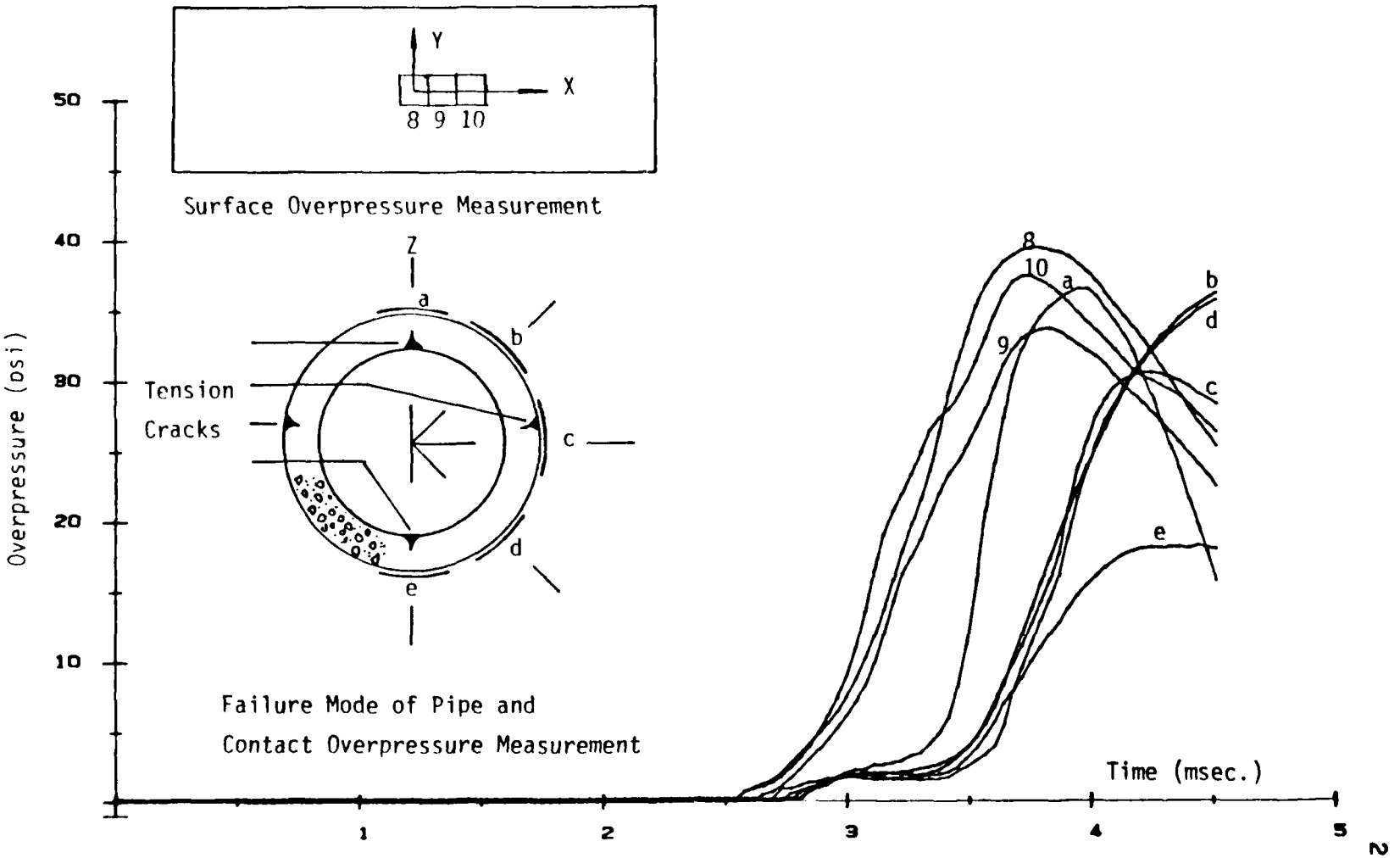

Figure 7.1 Summary of centrifuge test 1

located about 5 degrees above the springlines, and the other two at the inner wall of the pipe located at the crown and the invert of the pipe.

7.2 Analytical Results of Centrifuge Test 1

Centrifuge test 1 was analyzed by linear and non-linear analyses. In the linear analysis the behavior of the soil and the micro-concrete is described by using the Young's modulus and the Poisson's ratio. On the other hand, the constitutive relationships of these materials in the non-linear analysis are represented by the cap model and the engineering model, respectively. The Young's moduli and the Poisson's ratios used in the linear analysis, and the model parameters used in the non-linear analysis have been discussed in Chapter 6.

Figure 7.2 compares the contact pressure histories at the crown, springline, and invert of the pipe. The plots show that: (1) the analyses agree with the experiment in the peak pressures at these three locations; (2) the analyses shows a slower pressure rise; and (3) the crown pressure is smaller in the linear analysis than in the non-linear analysis, whereas the pressures at the springline and invert are about the same for both cases.

A non-linear analysis without the application of the body forces was conducted for the same test. The results are compared to those from the non-linear

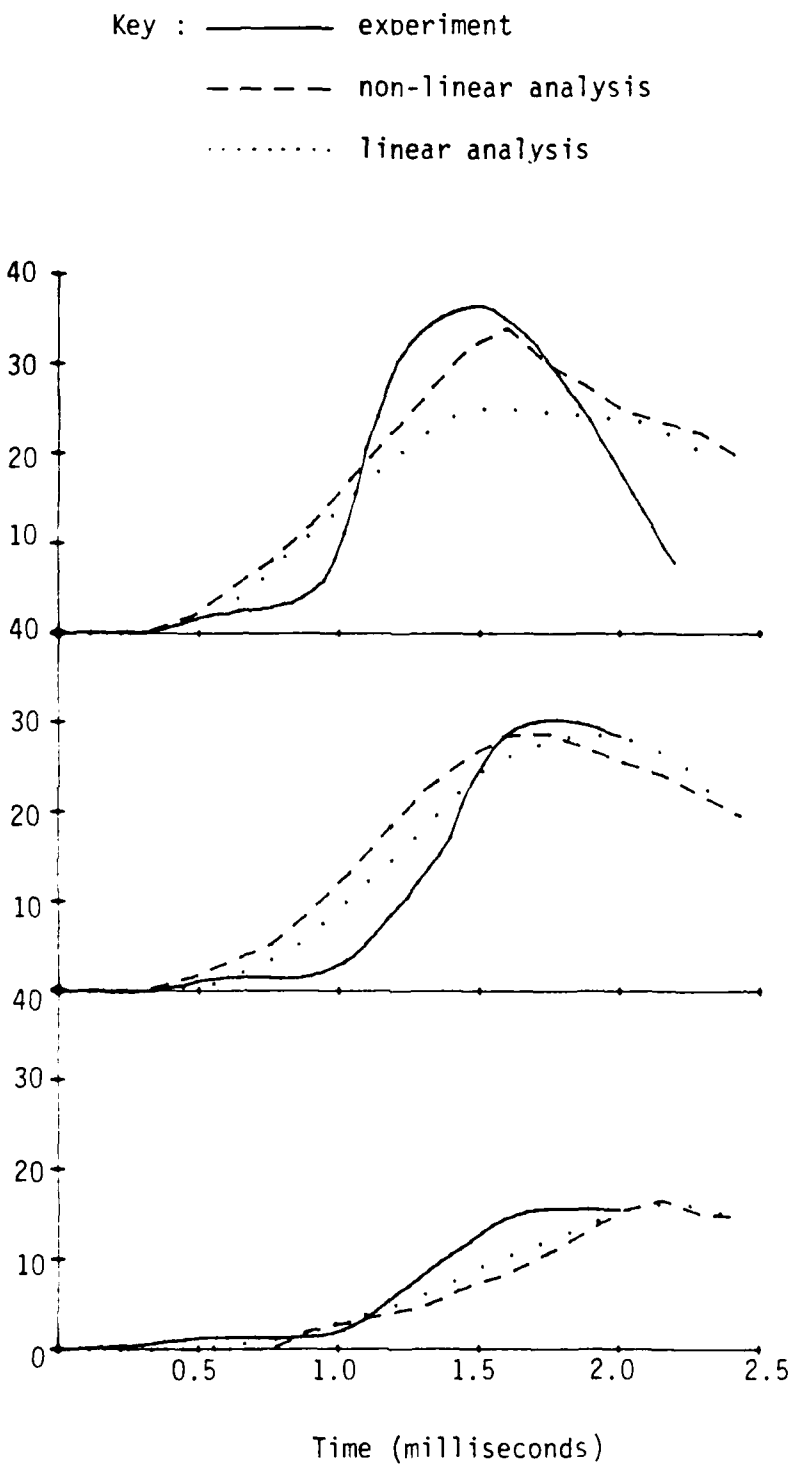

Figure 7.2 Comparisons between the experiment and the analyses. Test 1

analysis with the body forces and are shown in Figure 7.3. The results indicate that when the body forces are absent, the rate of pressure rise remains about the same but the pressures are lower.

7.3 Analytical Results of Centrifuge Tests 2, 6 and 24

Centrifuge tests 2, 6 and 24 were conducted in the parametric study in this research program. These tests were analyzed by the non-linear analysis with three intentions: first, to compare (between the experiment and the analysis) the pipe deflections in test 2, in which proximeters were used to measure the pipe deflections at the crown, springline and invert of the pipe; second, to compare the contact pressure in test 6, in which the thickest pipe (0.8 in.) in the test program was used; and third, to compare the contact pressure in test 24 which was conducted under 1-g conditions. The tests followed the procedures described in Chapter 5. Detailed description of the proximeter and its calibration can be found in the thesis by Whittaker (1987).

Figure 7.4 shows the comparisons of the pipe deflections between the experiment and the analysis of test 2. The figure indicates that the analysis does not agree with the experiment quantitatively. In addition, the deflections reach a maximum value earlier in the analysis.

Key : Non-linear analysis with body forces

---- Non-linear analysis without body forces

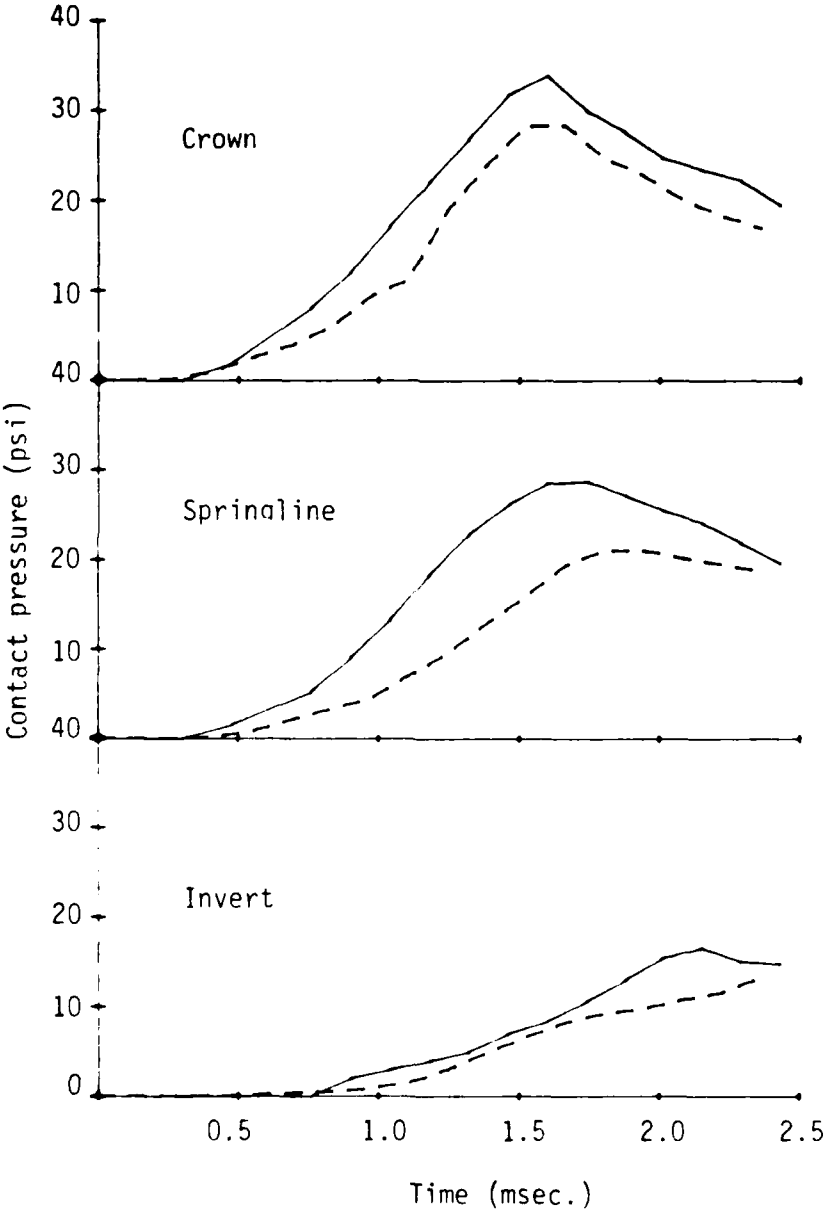

Figure 7.3 Comparisons between the analyses with and without body forces

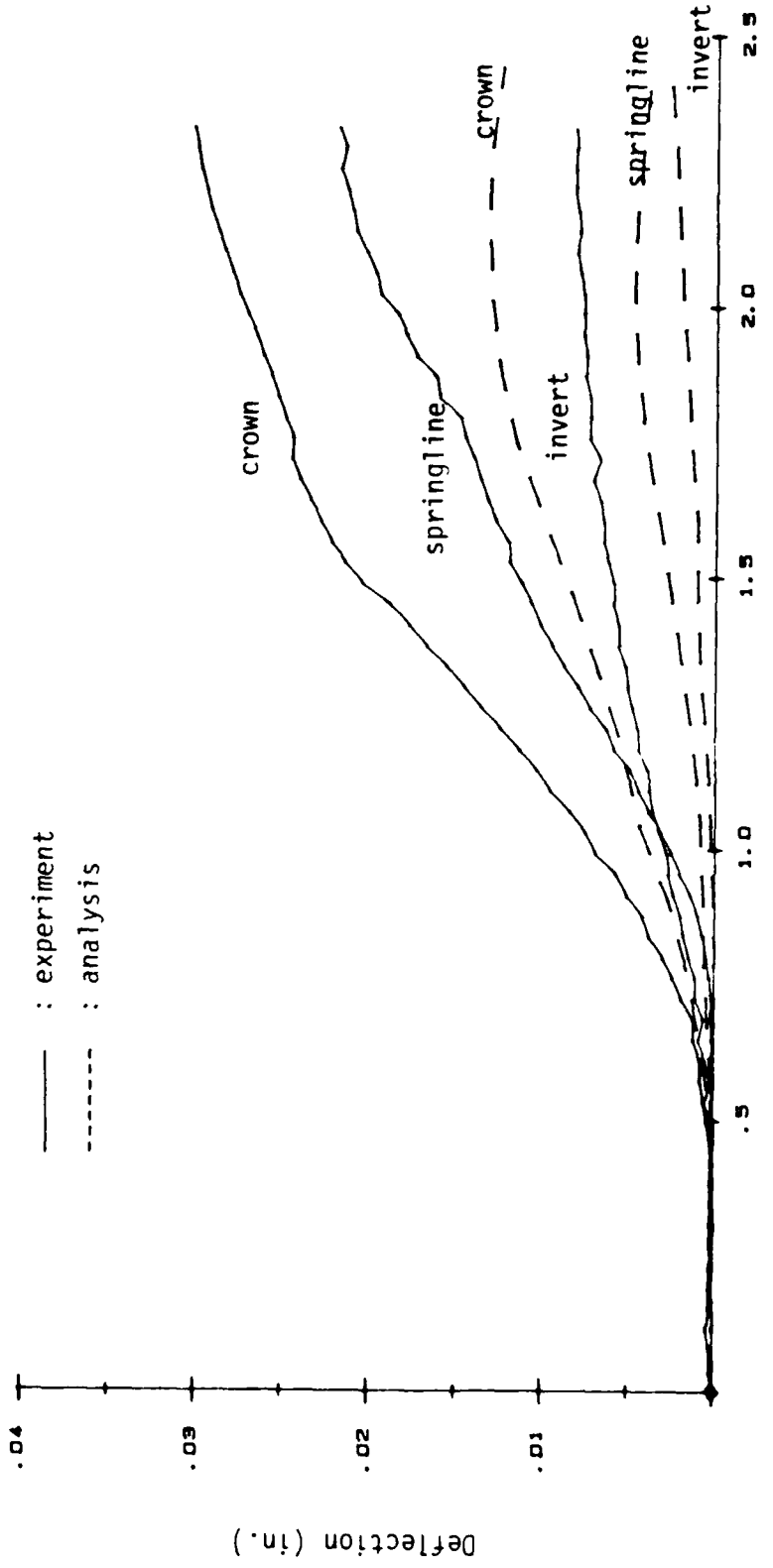

Figure 7.4 Comparisons of the pipe deflections between the analysis and the experiment

The comparisons of the contact pressures of test 6 are shown in Figure 7.5. The figure shows that except at the springline, the contact pressures are smaller in the analysis than the experiment. In addition, the pressures rise more slowly in the analysis than in the experiment. This was also one of the conclusions in the case of 0.2 inch thick pipe shown in Figure 7.2.

The comparisons of the contact pressures of test 24 are shown in Figure 7.6. The test was conducted under 1-g conditions and the analysis was performed without the application of body forces. The figure indicates poor agreement between the experiment and the analysis.

7.4 Results of Free Field Analyses

Free field stresses are the stresses in the soil when the structure is not present. These stresses can be used to indicate the effect of the existence of the structure. Normalizing the contact stresses by the free field stresses allows the comparisons to be made of the aforementioned effects for different structures.

Seven non-linear analyses were performed to compute the free field stresses, using surface overpressures with the peak value ranging from 30 to 110 psi. The impulse applied to the soil had the same shape as that in the centrifuge tests. Vertical free field stresses at the locations of crown and invert (if the pipe exist), and horizontal free field stresses at the springline

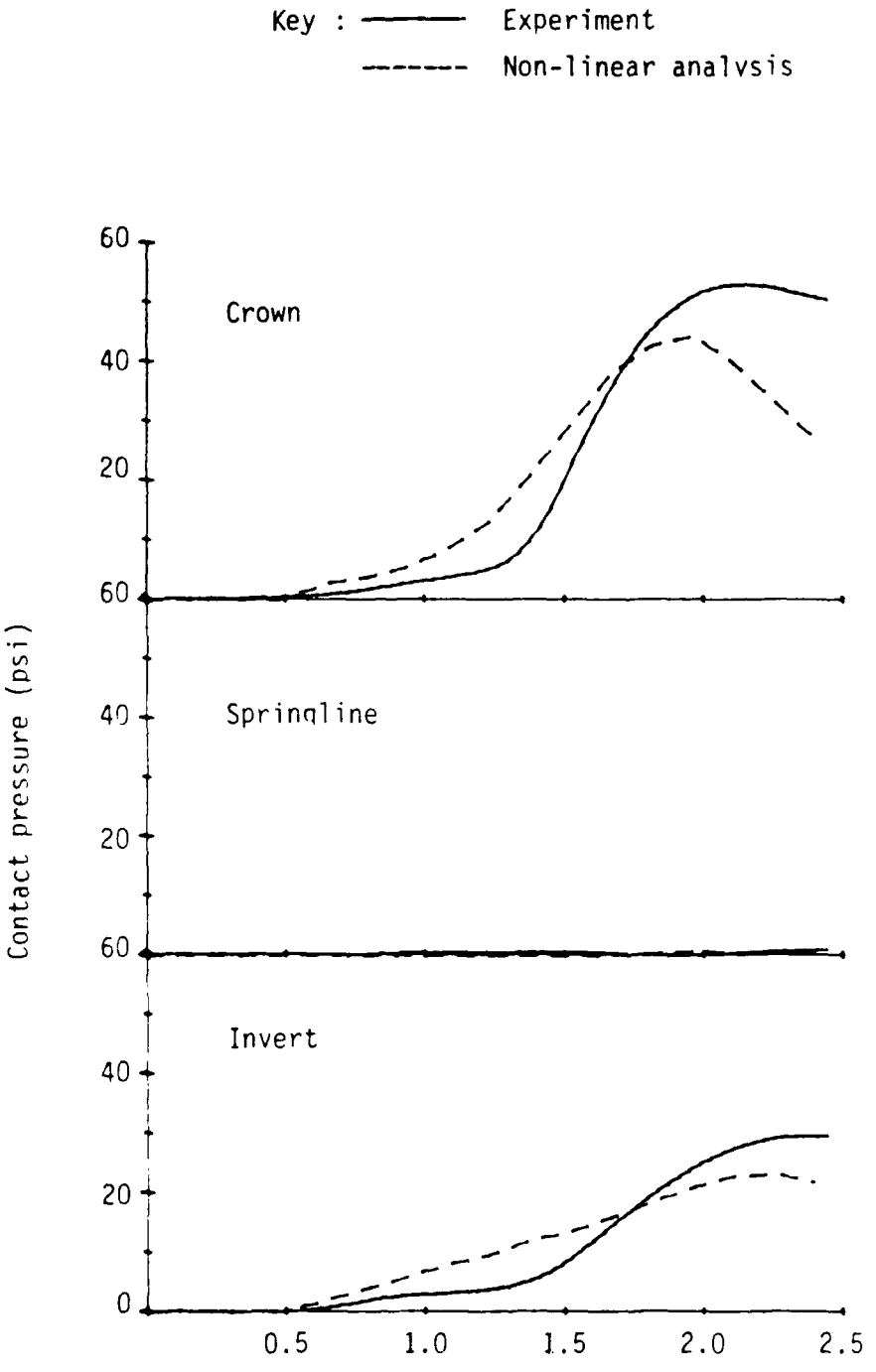

Figure 7.5 Comparisons between the experiment and the analysis, Test C

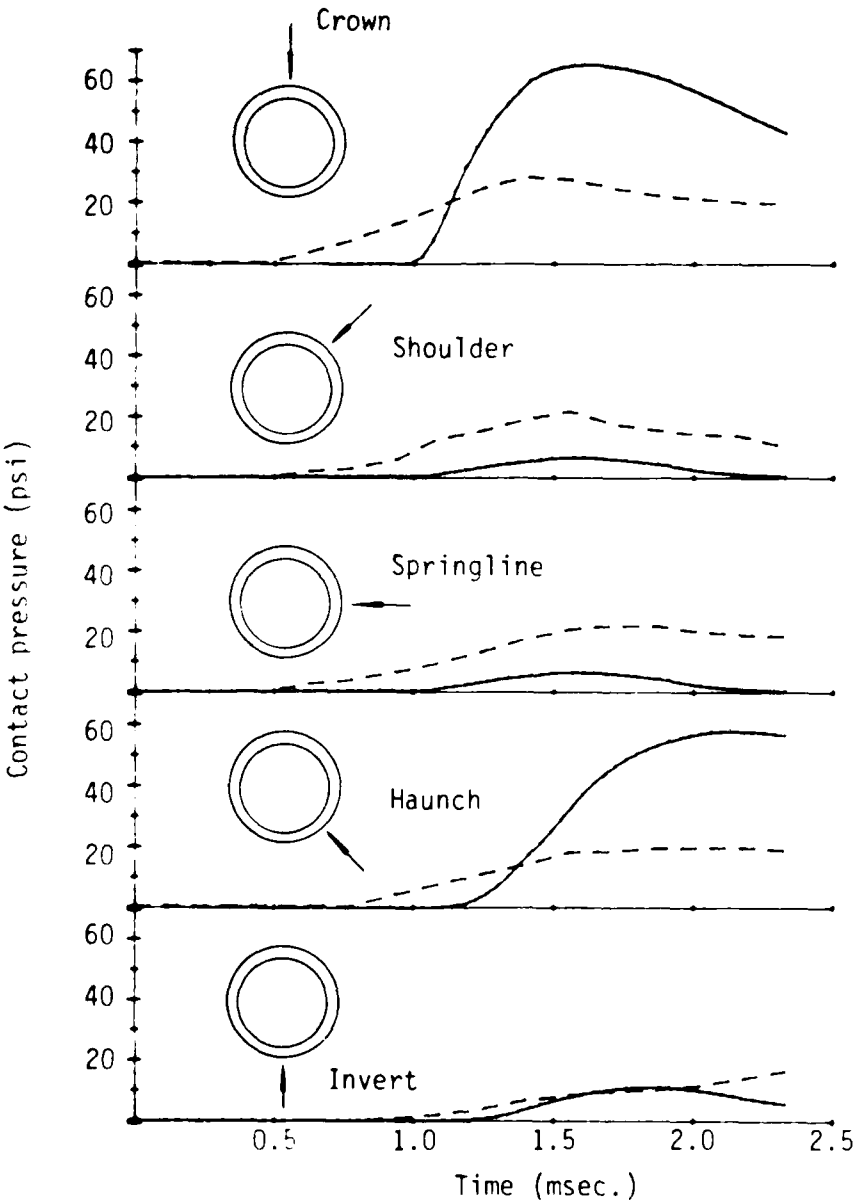

Figure 7.6 Comparisons between the experiment and the analysis. Test 24

were obtained in these analyses. The results are summarized in Figure 7.7. The free field stress ratio plotted as the ordinate is the ratio of the maximum free field stress to the maximum surface overpressure. Figure 7.7 allows the determination of the maximum free field stress for any given maximum surface overpressure. Figure 7.7 also shows the results of a free field centrifuge experiment. The test was conducted by Whittaker in the parametric study of the research program.

Note that the relationship between the free field stress ratio and the maximum surface overpressure is linear and the free field stress ratio decreases with the increase of the maximum surface overpressure, indicating the effects of nonlinearity. In addition, the free field stress ratio at the location of crown (if the pipe exists) is greater than unity for the maximum surface overpressure less than 100 psi implying stress amplification at this location.

The plot of the free field stress ratio versus the maximum surface overpressure at the invert is parallel to that at the crown but the magnitude is lower. This indicates stress attenuation along the depth of the soil.

The free field stress ratio at the springline also decreases with the increase of the surface overpressure,

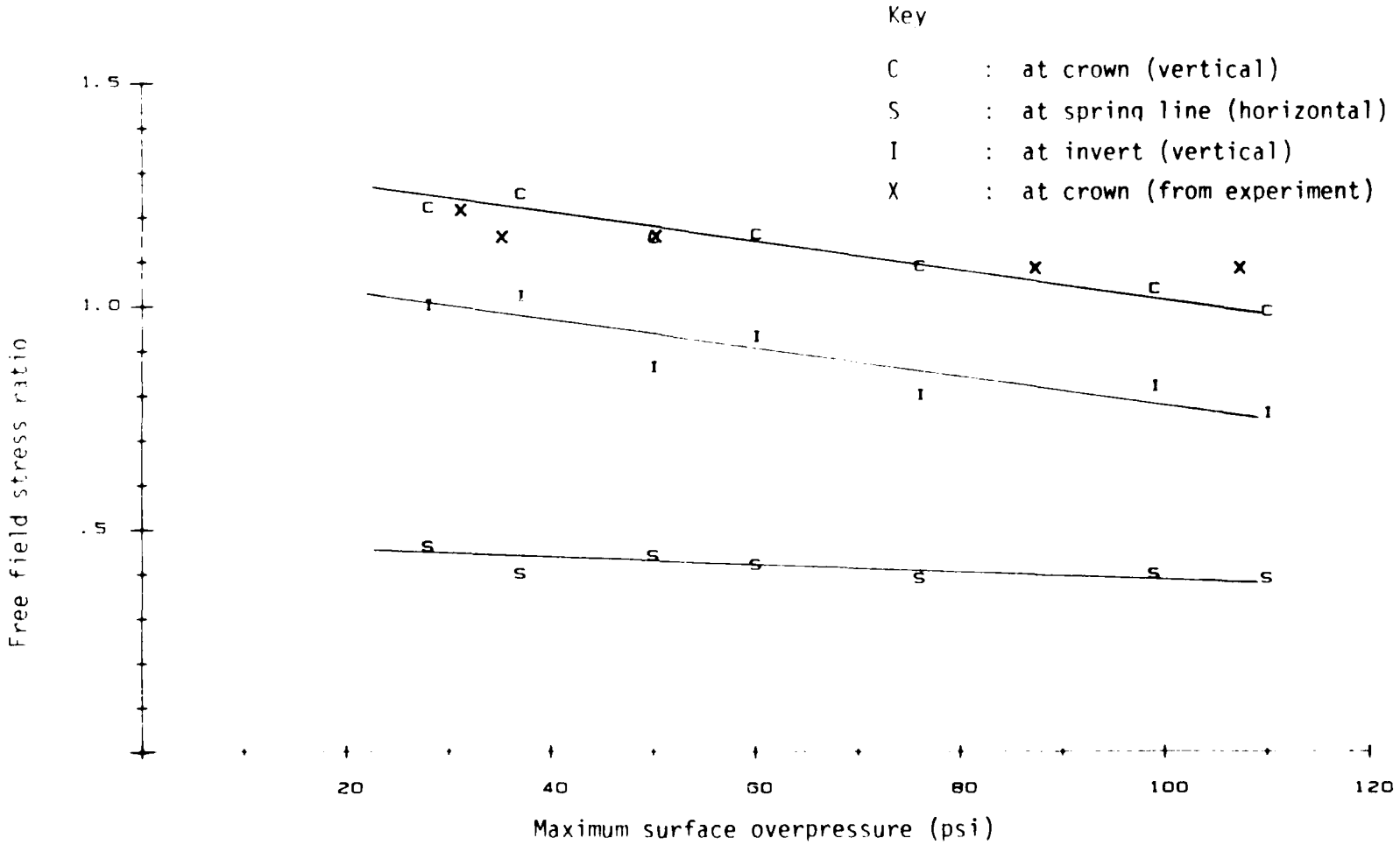

Figure 7.7 Plot shows stress ratio vs. maximum surface overpressure at different locations

but the decreasing rate is smaller than those at the crown and invert. This implies that the ratio of lateral to vertical pressure at the springline increases with the increase of the surface overpressure.

7.5 Effect of Structure-Soil Stiffness Ratio

The effects of structure-soil stiffness ratio on the contact pressures (at the crown, springline and invert) were investigated in centrifuge tests 2 to 11. These tests were also analyzed by non-linear analysis.

Centrifuge tests 2 to 6 had micro-concrete pipes with wall thicknesses of 0.2, 0.3, 0.4, 0.6 and 0.8 inches, respectively. Similarly, tests 7 to 11 had the same set of wall thicknesses. The magnitude of the surface overpressure in tests 2 to 6 was in the range of 30 to 40 psi, whereas the surface overpressure in tests 7 to 11 was 90 to 100 psi.

The structure-soil stiffness ratio is defined as:

$$K_{ss} = EI/MD_o^3$$

where K_{ss} = structure-soil stiffness ratio,

E = Young's modulus of the structural material,

I = $t^3/12$, moment of inertia per unit length of the pipe,

t = pipe thickness,

M = constrained modulus of the soil, and

D_o = outer diameter of the pipe.

In order to show the effect of the presence of the pipes, and the change in this effect due to the changes in the structure-soil stiffness ratio, a contact stress ratio is used which is defined as:

$$R_c = \frac{P_p}{P_f}$$

where R_c = contact stress ratio,

P_p = maximum contact pressure, and

P_f = maximum free field stress.

According to this definition, a contact stress ratio greater than one indicates stress concentration on the structure and a value less than one implies stress relief from the structure.

The maximum free field stresses had been obtained as described in the previous section. Hence, the contact stress ratio at the crown, springline and invert of the pipe can be obtained by dividing the maximum contact pressure at these locations by the corresponding maximum free field stress.

Figure 7.8 shows the relationship between the contact stress ratio at the crown and the structure-soil stiffness ratio. Starting from the left of the plot, the

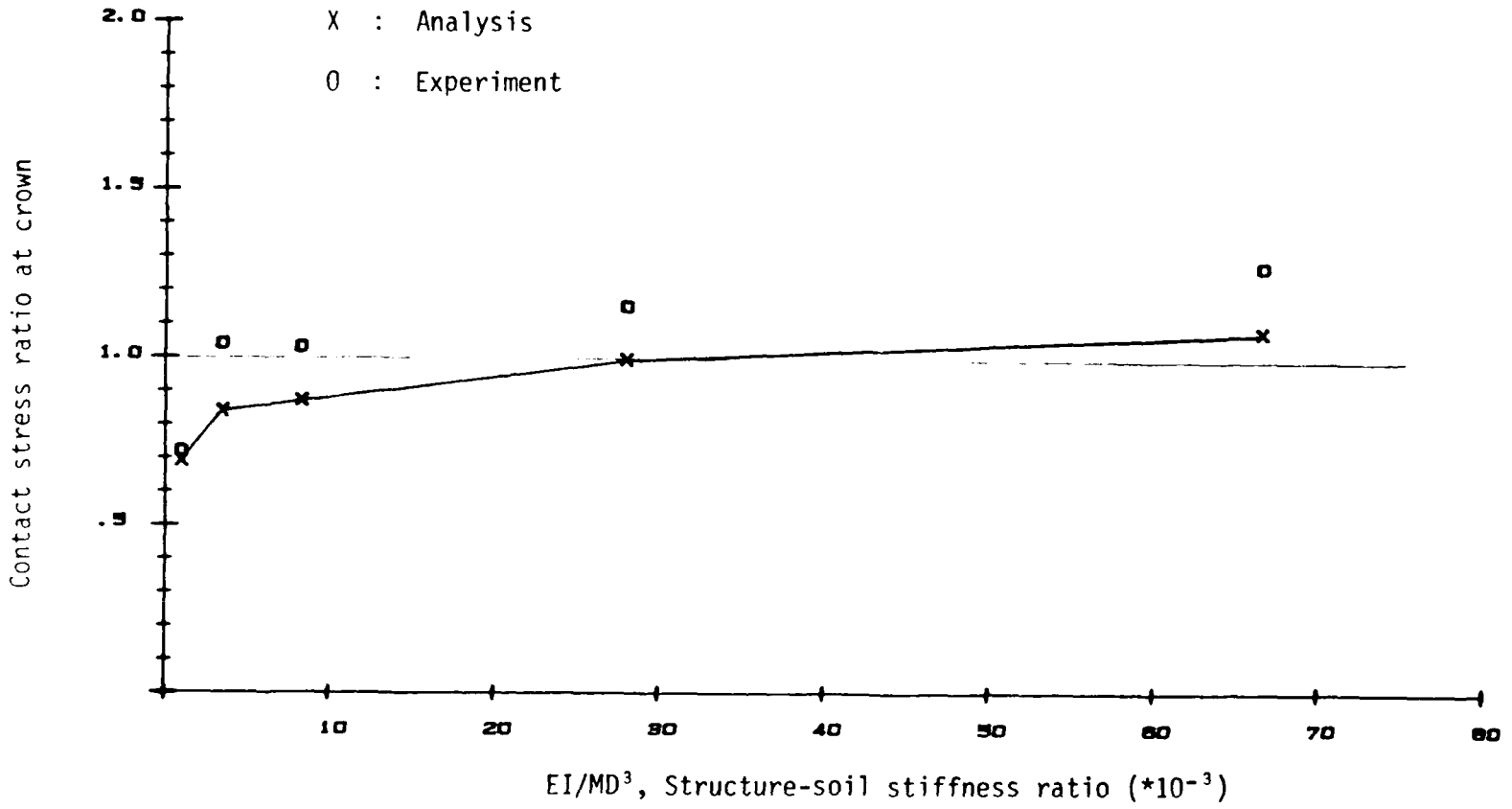

Figure 7.8 Contact stress ratio at crown vs. structure-soil stiffness ratio for surface overpressure of 30-40 psi

five data points represent the tests with wall thicknesses of 0.2, 0.3, 0.4, 0.6 and 0.8 inches, respectively.

Figure 7.8 shows that the data from the experiment and the analysis fall in a narrow band, and they all show the common trend, which indicates that the contact stress ratio increases with increasing structure-soil stiffness ratio.

Allgood and Takahashi (1972) defined the rigid, intermediate, and flexible pipes by the following criteria:

1. Rigid: $EI/MD_o^3 > 0.1$
2. Intermediate: $10^{-4} \leq EI/MD_o^3 \leq 0.1$, and
3. Flexible: $EI/MD_o^3 < 10^{-4}$.

According to these criteria, all of the micro-concrete pipes used in the experiments were intermediate pipes. However, in order to explain the results in Figure 7.8, it is necessary to divide the micro-concrete pipes into two groups. The pipes of the first group induced stress relief at the crown and the pipes of the second group induced stress concentration at the crown, or equivalently, the first group has a contact stress ratio at the crown less than one and the second group has the contact stress ratio at the crown greater than one.

In spite of the criteria given by Allgood and Takahashi, the author categorizes the first group as flexible pipes and the second group as rigid pipes. Therefore, the pipes with wall thicknesses of 0.2, 0.3, and 0.4 inches were flexible pipes, and those with wall thicknesses of 0.6 and 0.8 inches were rigid pipes. The reason for this distinction will soon become clear.

After the distinction was made, the trend in Figure 7.8 can be explained as follows. For the flexible pipes, as the wall thickness of the pipe increased, in other words, as the structure-soil stiffness ratio increased, the deflection at the crown decreased. This decrease in deflection reduced the stress relief at the crown, and thus increased the contact stress ratio. For the rigid pipe, there was no stress relief at the crown, and the tendency of the stress concentration increased with the increase in the structure-soil stiffness ratio.

The results from the experiments showed that the pipes with wall thicknesses of 0.2, 0.3 and 0.4 inches always failed with four tension cracks (two at the inner wall, located at the crown and invert of the pipe, the other two at the outer wall, located at the springlines of the pipe). On the other hand, the pipes with wall thicknesses of 0.6 and 0.8 inches always remained intact after the tests.

Note that the above experimental evidences are reflected in Figure 7.8 which shows that the pipes with the wall thicknesses of 0.2, 0.3, and 0.4 inches have contact stress ratio at the crown less than one, and the pipes with wall thicknesses of 0.6 and 0.8 inches have contact stress ratio at the crown greater than one. From these experimental results one can see that it is rational to use the contact stress ratio equal to one to distinguish between flexible and rigid pipes.

Figure 7.9 shows the relationship between the contact stress ratio at the springline and the structure-soil stiffness ratio from the same set of tests. The figure shows a qualitative agreement between the experiment and the analysis.

The decreasing trend of the contact stress ratio at the springline can again be explained by considering the conditions of flexible and rigid pipes. For the flexible pipes, the deformation of the pipes caused the pipe to bulge at the springline. This forces the soil in that region to change from an at-rest state to a passive state. Since the free field stress is the stress at rest, it is by definition smaller than the passive stress. Hence, the contact stress ratio at the springline is greater than one for the flexible pipes.

As the stiffness of the pipe increased, the deformation of the pipe reduced, hence, the contact

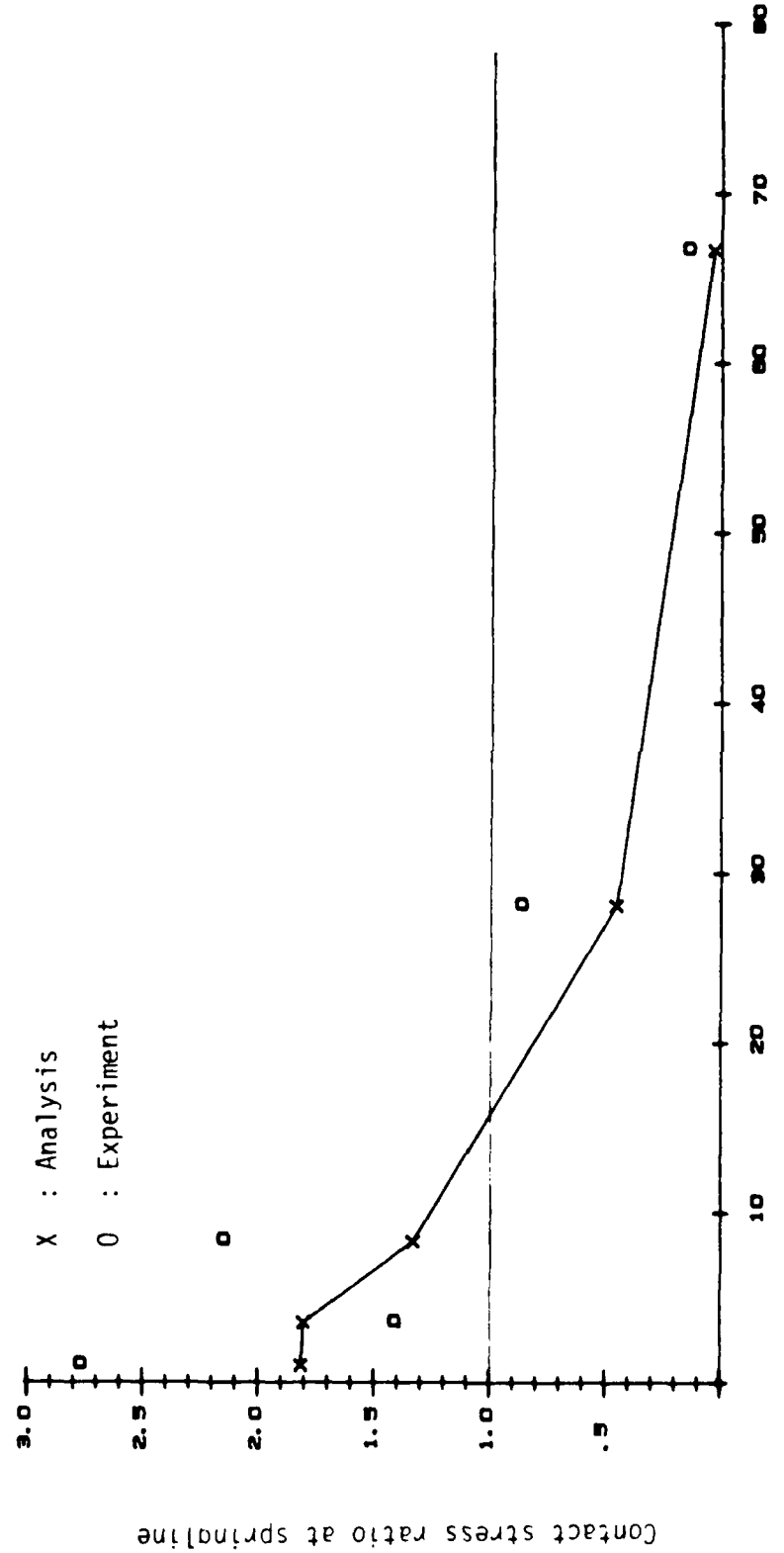

Figure 7.9 Contact stress ratio at springline vs. structure-soil stiffness ratio for surface overpressure of 30-40 psi

stress ratio at the springline decreased. This trend continued until the factor was equal to one, then, the second condition started to apply.

The second condition applied to rigid pipes. As discussed before, rigid pipes caused a stress concentration at the crown. This stress concentration reduced the soil stress at the areas outside the crown of the pipes. Although the pipes would still bulge at the springline, the deformation must be small so that the net effect produced a horizontal stress smaller than the free field stress.

For the rigid pipes, the decreasing trend of the contact stress ratio at the springline was believed due to the increase of the stress concentration at the crown as the structure-soil stiffness ratio increased.

Note that the failure of the pipes is also reflected in Figure 7.9. The figure shows that for the pipes that failed in the experiments, their contact stress ratios at the springline were greater than one and for the pipes which remained intact, their contact stress ratios at the springline were less than one.

Figure 7.10 shows a plot of contact stress ratio at the invert of the pipe versus the structure-soil stiffness ratio. The plot shows good agreement between the experiments and analysis. The trend in this figure is similar to that in Figure 7.8. However, all the

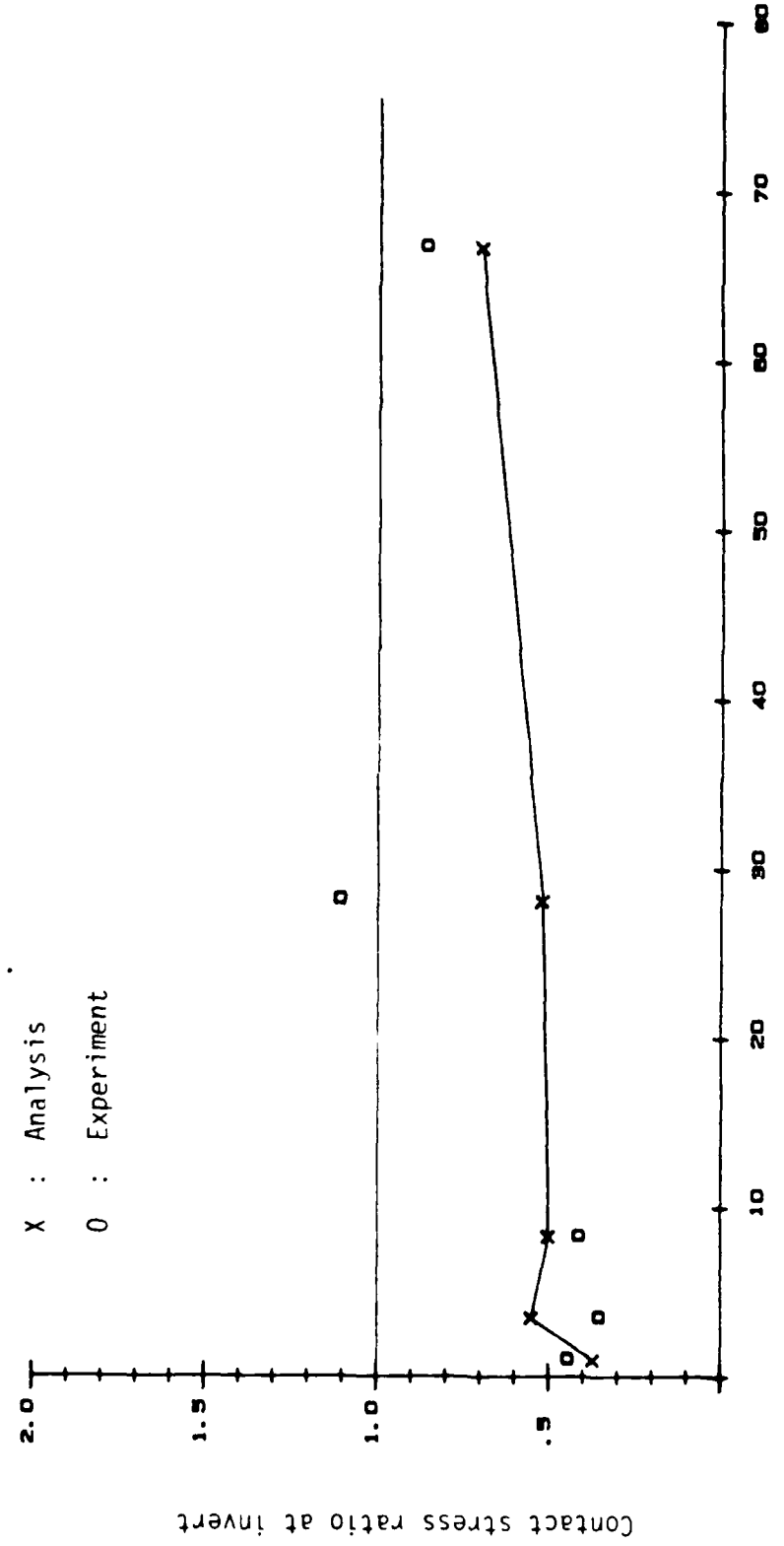

Figure 7.10 Contact stress ratio at invert vs. structure-soil stiffness ratio for surface overpressure of 30-40 psi

contact stress ratios at the invert are less than one. The fact that this factor was less than one for flexible pipes could be due to the possible inward deflection of the pipe causing stress relief at the invert. This was similar to the phenomenon occurring at the crown except that the magnitude was smaller. For rigid pipes, it was believed that the stress concentration at the crown would transmit the stress to the invert and cause a passive state for the soil beneath the pipe. However, Figure 7.10 shows the opposite is true. At this time, no reason can be given to explain this result.

The effects of structure-soil stiffness ratio under a higher surface overpressure were investigated in centrifuge tests 7 to 11. Figures 7.11 to 7.13 shows the structure-soil stiffness ratio versus the contact stress ratio at the crown, springline and invert of the pipe, respectively. The conclusions drawn from tests 2 to 6 are also applied to the current case except that the contact stress ratios in the latter are slightly higher.

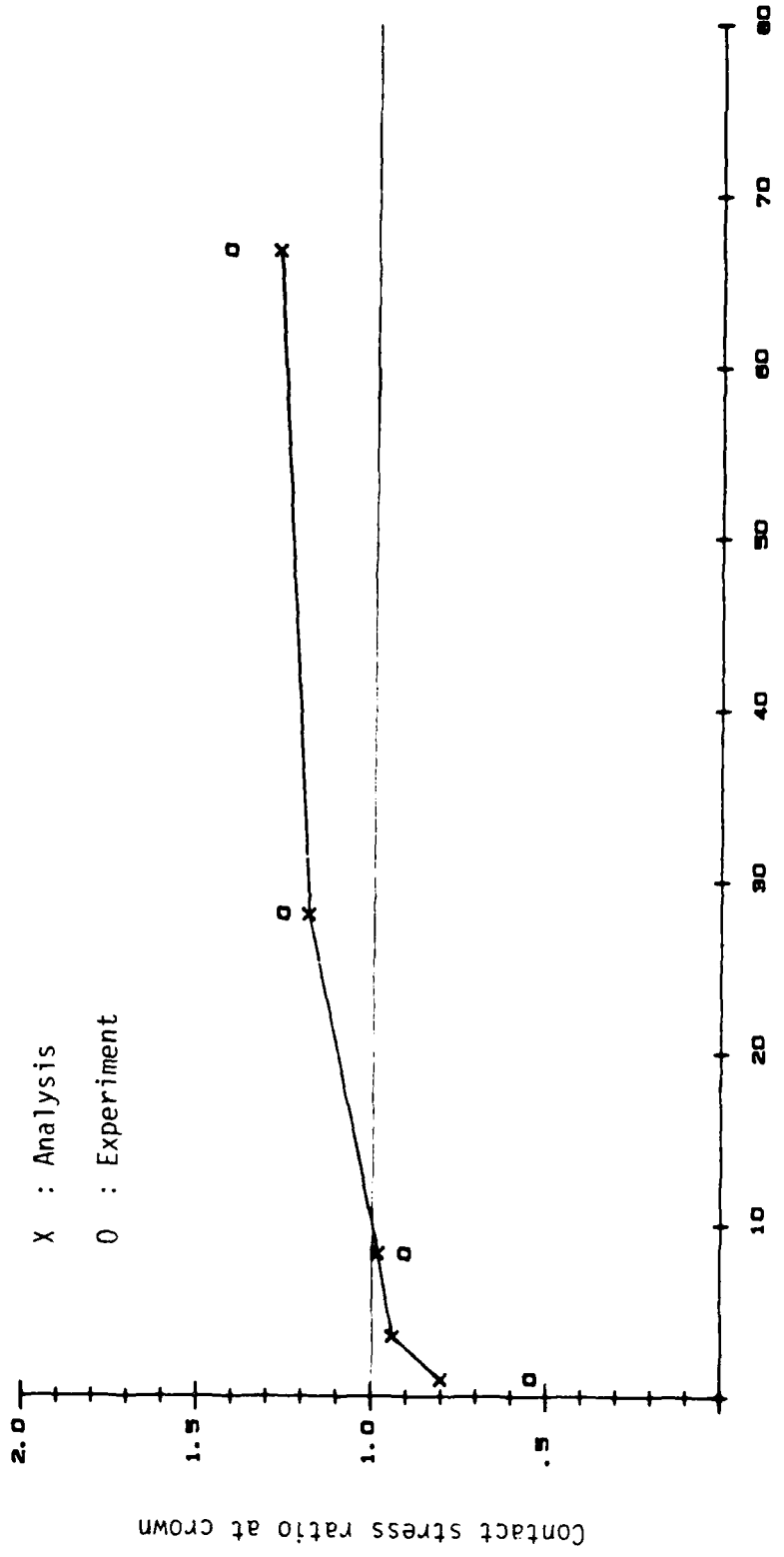

Figure 7.11 Contact stress ratio at crown vs. structure-soil stiffness ratio for surface overpressure of 90-100 psi

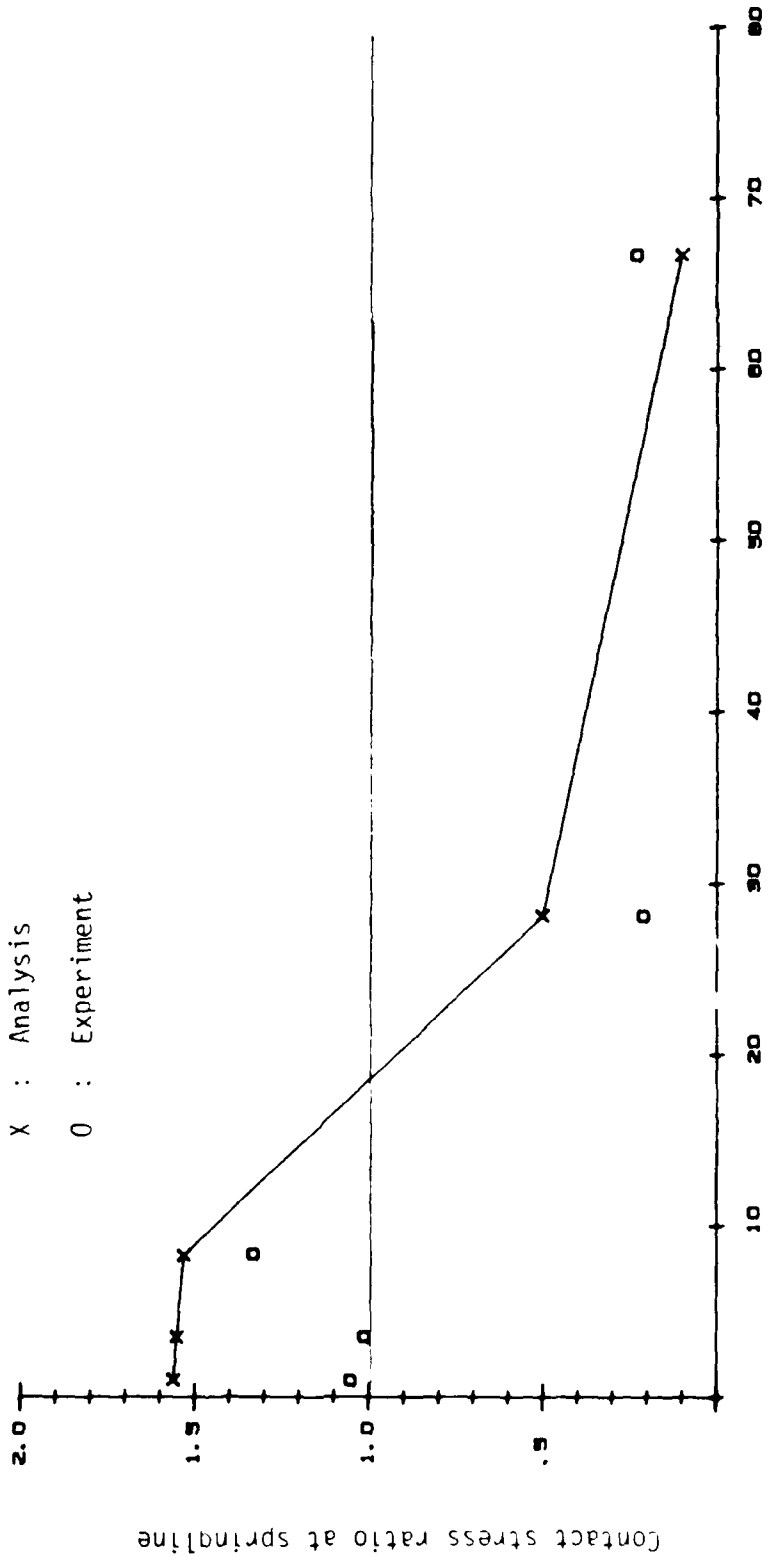

Figure 7.12 Contact stress ratio at springline vs. structure-soil stiffness ratio for surface overpressure of 90-100 psi

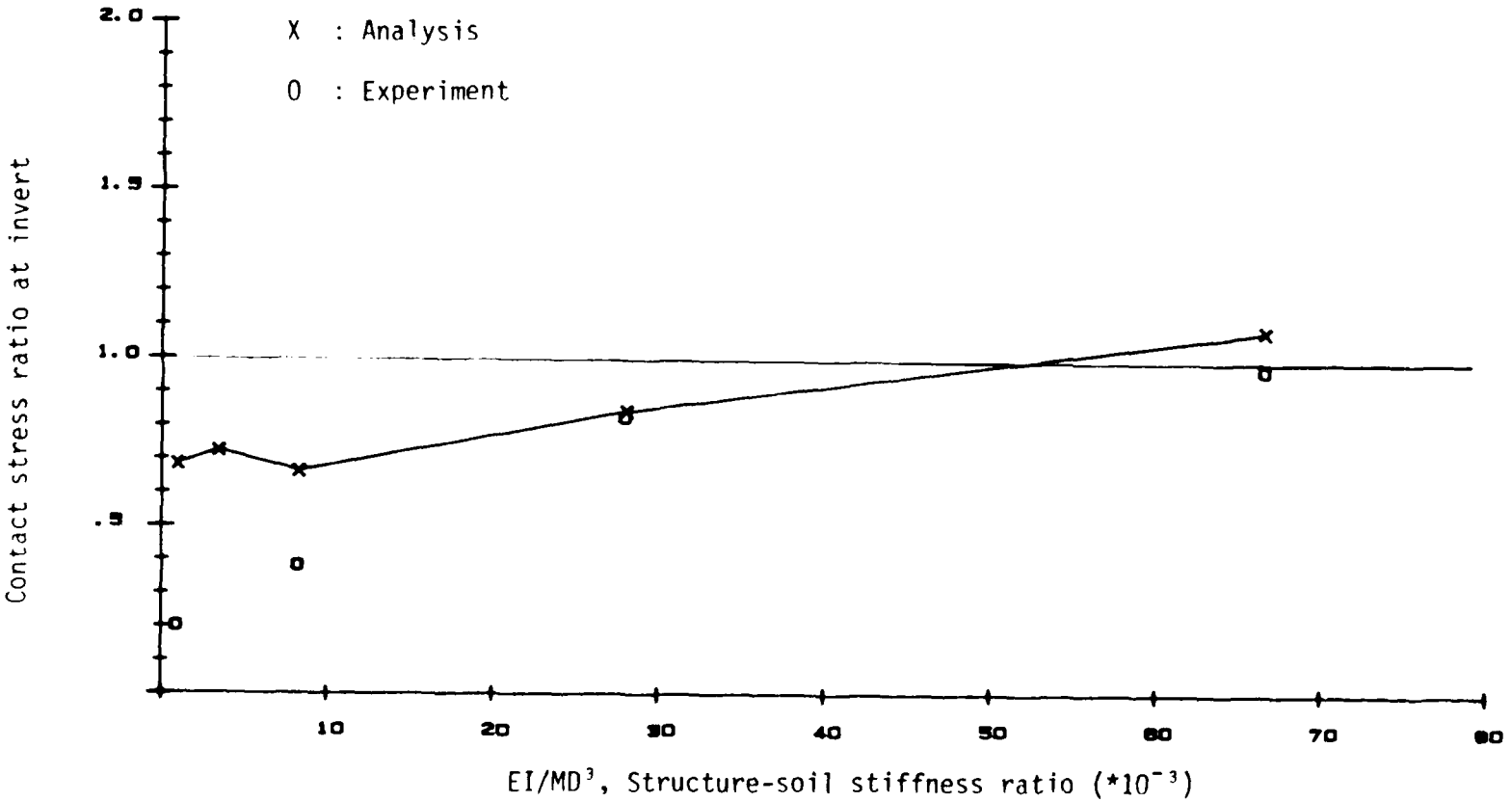

Figure 7.13 Contact stress ratio at invert vs. Structure-soil stiffness ratio for surface overpressure of 90-100 psi

CHAPTER VIII

SUMMARY, CONCLUSIONS AND RECOMMENDATIONS

8.1 Summary

Soil-structure interaction under blast loading was investigated both experimentally in a 10 g-ton centrifuge and analytically by finite element simulation. In the centrifuge experiments, circular pipes made of micro-concrete were buried in a dry sand and tested in the centrifuge to simulate the effects of gravity-induced overburden stresses which played a major role in controlling the soil stiffness and, subsequently, the response of the pipe.

The blast loading was simulated by a pressure pulse generated by rupturing a burst disc in an impact generator. Surface stress gages and contact stress gages both made of polyvinylidene fluoride, were built and calibrated to measure air blast magnitudes and contact pressures.

The centrifuge experiments provided insight into the dynamic response of buried pipes and a data base for the verification of numerical results. These results were obtained by linear and non-linear finite element

analyses of the experiments duplicating the surface overpressure loading. The suitability of constitutive relations for both soil and micro-concrete were verified by comparing test results and analyses. The effects of soil arching around the buried pipe was also delineated from both experiment and analysis.

8.2 Conclusions

1. Micro-concrete has shown to work satisfactorily. It has properties similar to conventional concrete but uses finer aggregates. The material allows the construction of thin-walled structures which are necessary for the model tests.
2. The friction-reducing membrane placed at the soil-container boundary can reduce the coefficient of friction from 56% to less than 8% and the membrane allows local straining of the soil.
3. The impact generator can produce controlled airblast in the centrifuge. The magnitude of the airblast can be controlled by the upstream pressure and the thickness of the rupture disc.
4. Dynamic stress gages constructed of piezoelectric materials have proven to be excellent instruments for measuring airblast

magnitudes and the stresses transmitted from soils onto buried structures. Both surface and contact stress gages respond linearly to dynamic overpressures. The response of the contact stress gage is independent of the initial density of soils and the type of soil. In addition, the contact stress gage does not introduce inclusion effects in the soil.

5. The comparisons between the experiments and the analysis show that (1) the contact pressures are in agreement, (2) the contact pressures rise more slowly in the analysis, (3) the pipe deflections are not in agreement, and (4) in the study of structure-soil stiffness effects, both quantitative and qualitative agreement are obtained for the behaviors at the crown and the invert, but only qualitative agreement is obtained for the behavior at the springline. The results of analysis also show that the linear analysis has a smaller crown pressure than the non-linear analysis, but the pressures at the springline and the invert are about the same for both cases. Non-linear analysis without the application of the body forces has shown to produce lower contact pressures than the analysis with the body forces.

6. The investigation on the effects of the structure-soil stiffness ratio indicates that arching effects had dominated the interaction of the soil-pipe system, and that the interaction can be quantified using the stress concentration factor.

8.3 Recommendations

1. Further development of the stress gages can be fruitful. The following aspects of gage's performance are recommended for investigation: (1) the possibility of using the contact stress gage to measure a slower and longer duration dynamic event such as earthquake type of loading; (2) use the gage to measure dynamic stresses in a wet or saturated soil; (3) the development of a new gage to measure stresses in two directions independently; (4) investigation on the smallest possible sizes for the surface and the contact stress gages; and (5) the development of a new gage to measure shear stresses in soils.

2. The impact generator can be used to generate airblast loadings in centrifuges for other studies, or, it can be used in the dynamic characteristic test of soils.

3. The centrifuge test results provide a data base for the problem of dynamic soil-structure interaction. It is recommended that this data base be used for the calibration of other solution schemes. The incorporation of body forces is recommended in these attempts.

BIBLIOGRAPHY

Albritton, G.E. "The Elastic Response of Buried Cylinders Critical Literature Review and Pilot Study," U.S. Army Waterways Experiment Station Technical Report 1-720. 1966.

Allgood, J.R. and Takahashi, S.K. "Balanced Design and Finite Element Analysis of Culverts," Highway Research Record, No. 413, 1972.

Baylor, J.L. and Wright, J. P. "Three dimensional Transient Nonlinear Analysis," Finite Element analysis of Transient Nonlinear Structural Behavior, ASME, AMD Vol. 14, Winter Annual Meeting, Houston, Texas, 1975, pp. 179-191.

Baylor, J.L., Wright, J.P. and Chung, C.F. "TRANAL User's Guide, Part I (Small Strain, Small Displacement Version)," Report No. DNA4960F. Weidlinger Associates, New York, N.Y., 1979.

Bulson, P.S. Buried Structures, Static and Dynamic Strength, New York, Chapman and Hall. 1985

Chung, R.M., Bur, A.J., and Reasner, E. "Development of an NBS Polymer Gage for Dynamic Soil Stress Measurement," U.S, Department of Commerce, National Bureau of Standards, Report number NBSIR 85-3135, 1985.

Corotis, R.B. and Krizek, R.J. "Analysis and Measurement of Soil Behavior Around Buried Concrete Pipe," ASTM Technical Publication 630, 1976, pp. 91-134.

Das, B.M. Fundamentals of Soil Dynamics, New York, Elsevier.
1983.

Desai, C.S. "Behavior of Interface between Structural and Geologic Media," International Conference on Recent Advance in Geotechnical Earthquake Engineering and Soil Dynamics, Rolla, Missouri, Vol. 2, 1981.

DiMaggio, F.L. and Sandler, I.S. "Material Model for Granular Soils," Journal of the Engineering Mechanical

Division, American Society of Civil Engineers EM3, June, 1971, pp. 935-949.

Dorris A.F. "Response of Horizontally Orientated Buried Cylinders to Static and Dynamic Loading," U.S. Army Waterways Experiment Station. Technical Report 1-682. 1965.

Dorris. A.F. and Alberitton, G.E. "Response of a Buried Prototype Communications Conduit to Static and Dynamic Loading," U.S. Army Waterways Experiment Station, Technical Report 1-750.

Ducan, J.M. and Clough, G.W. "Finite Element Analyses of Port Allen Lock," Journal of the Soil Mechanics and Foundations Division, American Society of Civil Engineers
No. Sm8, 1971. pp. 1053-1068.

Feynman, R.P., Leighton, R.B. and Sands, M. "The Feynman Lectures on Physics," Vol. II, Addison-Wesley Publishing Company, 1964. pp. 6-2 to pp. 6-5 and pp. 11-6 to pp. 11-8.

Fragaszy, R.J., Voss, M.E. "Laboratory and Centrifuge Modeling of Blast-Induced Liquefaction," Eight International Symposium on Millitary Application of Blast Simulation. Spieq, Switzerland, 20-24 June, 1983.

Getzler, Z., Komornik, A. and Mazurik, A. "Model Study on Arching above Buried Structures," Journal of the Soil Mechancial and Foundation Division, American Society of Civil Engineers, SM5, Sept. 1968, pp. 1123-1141.

Ghaboussi, J., Wilson, E.L., and Isenberg, J. "Finite Element for Rock Joints and Interfaces," Journal of Soil Mechancial and Foundation Division, American Society of Civil Engineers, Vol. 99 No.SM10, 1973.

Goodman, R.E., Taylor, R.L.and Brekke, T.L. "A Model for the Mechanics of Jointed Rock," Journal of soil Mechanical and foundation Division, American Society of Civil Engineers
Vol. 94, No. SM3, 1968.

Höeg, K. "Stresses against Underground Structural Cylinders," Journal of the Soil Mechanical and Foundation Division, American Society of Civil Engineers, Sm4, July 1968. pp. 833-857.

Holsapple, K.A. "The Equivalent Depth of Burst for Impact Cratering," Proceeding of the 11th Conference on Lunar Planet Science, pp. 2379-2401, 1980.

Humphreys, J., Ward, I.M., McGrath, J.C., Nix, E.L. and Road, D. "The Measurement of the piezoelectric Coefficients d_{31} and d_{3h} for Uniaxially Oriented Polyvinylidene Fluoride",, Report of THORN EM1 central Research Laboratories.

Hvorslev, M.J. "The changeable Interaction between Soils and Pressure Cells", Tests and Reviews at the Waterways Experiment Station, June, 1976.

Jackson, J.G. Jr., Ehrgott, J.Q. and Rohani, B. "Loading Rate Effects on Compressibility of Sand," Journal of the Geotechnical Engineering Division, American Society of Civil Engineers, GT8, 1980, pp. 839-852.

Katona, M.G., Smith, J.M., Odello, R.J., and Allgood, J.R. "CANDE: Engineering Manual-A modern Approach for the Structural Design and Analysis of Buried Culverts," Report to the Federal Highway Administration, Civil Engineering Laboratory, Port Hueneme, CA. 1976.

Ko, H.Y., Shin, C.J., Ketchan, S.A. and Sture, S. "Dynamic Soil Properties Characterization in Support of Hard Mobile Launcher and Soil Response STudies," University of Colorado at Boulder, July, 1984.

Liepmann, H.W., Roshko. A. Elements of Gasdynamics John Wiley and Sons, INc., New York 1957.

Linger, D.A. "Historical Development of the Soil-Structure Interaction Problem," Highway Research Record, No. 413. 1972, pp. 5-11.

Marston, A., and Anderson, A.O. "The Theory of loads on Pipes in Ditches and Tests on Cement and Clay Drain Tile and Sewer Pipe," Engineerint Experiment Staation Iowa State College, Bull. 31, 1913.

McDonough, G.F., Jr., Dynamic Loads on Buried Structures, Ph.D. thesis, University of Illinois, Urbana, Ill., 1959.

McGrath, J.C., Holt, L., Jones, D.M., and Ward I.M. "Recent Measurements on Improved Thick Film Piezoelectric PVDF Polymer Materials for Hydrophone Application," Report of THORN EMI Central Research Laboratories.

McNulty, J.W. "An Experimental Study of Arching in Sand," U.S. Army Engineering Waterways Experiment Station, Technical Rep. 1-674, 1965.

Moore, P.J. "The Response of Soils to Dynamic Loadings; Report 21, One-Dimensional Compression and Wave Propagation," Research Report R63-64, Department of Civil Engineering, Massachusetts Institute of Technology, Cambridge, Mass., 1963.

Monfore, G.E. "An Analysis of the Stress Distribution In and Near Stress Ganges Embedded in Elastic Solid," Structural Laboratory Report No. SP26, U.S. Bureau of Reclamation, 1950.

Newmark, N.M. "The Basis of Current Criteria for the Design of Underground Protective Construction," Proceeding, Symposium on Soil-Structure Interaction, University of Arizona, Tucson, 1964, pp. 1-24.

Nelson, I. and Goldstein, G. "Blast Wave Reflections in Soil from a Buried Rigid Dome," International Symposium on Dynamic Soil-Structure Interaction Minneapolis, 1984, pp.153-158.

Nielson, F.D. "Soil Structure Arching Analysis of Buried Flexible Structures," Highway Research Record 185, 1967 pp. 36-50.

Ni, J.C. Centrifugal and Analytical Modeling of a Buried Flexible Culvert, Ph.D. Thesis, University of Colorado at Boulder, Boulder, CO., 1985.

Nix E.L. "A Direct Method for Measurement of the Film-Thickness Piezoelectric Coefficient of Polyvinylidene Fluoride," Report of THORN EM1 Central Research Laboratories.

Nix, E.L., Holt, L., McGrath, J.C. Ward, I.M. "Highly Drawn Polyvinylidene Fluoride with Enhanced Mechanical and Electrical Properties," Report of THORN EM1 Central Research Laboratories, 1980.

Nix, E.L., Ward, I.M. "The Measurement of the Shear Piezoelecctric Coefficient of Polyvinylidene Fluoride," Report of THORN EM1 Central Research Laboratories.

Peattie, K.R., Sparrow R.W. "The Fundamental Action of Earth Pressure Cells," Journal of the Mechanics and Physics of Solids, Vol 2, No. 3, April 1954, pp. 141-155.

Sandler, I.S., Dimaggio, F.L., and Baladi, G.Y. "Generalized Cap Model for Geological Materials", Journal of Geotechnical Engineering Division, American Society of Civil Engineers, Vol. 102, No. GT7, July, 1976, pp. 683-699.

Sandler, I.S. and Rubin, D. "An Algorithm and a Modular Subroutine for the Cap Model," International Journal for Numerical and Analytical Methods in Geomechanics, Vol. 3, 1979, pp. 173-186.

Schindler, L. "An Improved Facility for Testing Soils in One-Dimensional Compression," Proceedings, International Symposium on wave Propagation and Dynamic Properties of Earth Materials, University of New Mexico, Albuquerque, N.M., Aug. 1968, pp. 847-860.

Schmidt, R.M. "Centrifuge Simulation of the Johnie Boy 500 Ton Cratering Event," Proceeding of the 9th Conference on Lunar Planet Science, pp. 3877-3889, 1978.

Schmidt, R.M. "Meteor Crater: Energy of Formation-Implications of Centrifuge Scaling," Proceeding of the 11th Conference on Lunar Planet Science, pp. 2099-2128, 1980.

Schmidt, R.M. and Holsapple, K.A. "Theory and Experiments on Centrifuge Cratering," Journal of Geophysical Research, Vol. 85, No. 2, Jan 10, 1980.

Seed, H.B. and Lundgren, R. "Investigation of the Effect of Transient Loading upon the Strength and Deformation Characteristics of saturated sands," Proceeding, ASTM, Vol. 54, 1954, pp.1288.

Selig, E.T., McVay, M.C. and Chang, C.S. "Finite Element Modeling of Buried Concrete Pipe Installations," Transportation Research Record 878, 1982, pp. 17-23.

Spangler, M.G. and Handy, R.L. Soil Engineering, New York, Harper and Row, 1982.

Soil Pressure Cell Investigation, Technical Memorandum No. 210-1, Waterways Experiment Station, 1944.

Taylor, D.W. "Review of Pressure Distribution Theories and Earth Pressure Cell Investigation," Chapter 2 in Report to U.S. Army Waterways Experiment Station, Vicksburg, Miss., Nov. 1945.

Terzaghi, K. "Stress Distribution in Dry and in Saturated Sand and above a Yielding Trapdoor," Proceeding International Conference on Soil Mechanics, Vol. 1, 1936.

Terzaghi, K. Theoretical Soil Mechanics, New York, John Wiley and Sons, 1943.

Tory, A.C., Sparrow, R.W. "The Influence of Diaphragm Flexibility on the Performance of an Earth Pressure Cell",
Journal of Scientific Instruments, Vol. 44, No. 9, Sept. 1967, pp. 781-785.

Townsend, F.C., McVay, M.C., Bradley, D.M., Cunningham, C.H. and Yovaish, D.J. "Numerical and Centrifugal Modeling of Buried Structure Response to Near Field Blast," Proceeding of Second Symposium on The Interaction of Non-Nuclear Munitions with Structures, Panama City Beach, FL, April, 1985, pp. 482-487.

Walters, J.V. and Thomas, J.N. "Shear Zone Development in Granular Materials," Proceeding of the Fourth International Conference on Numerical Method in Geotechanics, Vol. 1, Edmonton, Canada, 1982, pp. 263-274.

Weiler, W.A., and Kulhawy, F.H. "Factors Affecting Stress Cell Measurements in Soil" American Society of Civil Engineers Journal of the Geotechnical Engineering Division, GT12, Dec. 1982, pp. 1529-1548.

Watkin, R.K. "Failure Conditions of Flexible Culverts Embedded in Soil," HRB Proc., Vol. 39, 1960, pp. 36-371.

White, H.L., and Layer, J.P. "The Corrugated Metal Conduit as a Compression Ring," HRB Proceeding Vol. 39, 1960, pp. 389-397.

Whitman, R.V., Getzler, Z. and Hoeg, K. "Static Tests upon Thin Domes Buried in Sand," Massachusetts Institute of Technology, Cambridge, Mass., Report 12 to U.S. Army Engineer Waterways Experiment Station, 1962.

Whitman, R.V. "The Response of Soils to Dynamic Loadings; Report 17, Stress-Strain-Time Behavior of Soil in One-Dimensional Compression," Research Report R63-25, Department of Civil Engineering, Massachusetts Institute of Technology, Cambridge, Mass., May 1963.

Whiteman, R.V., and Healy, K.A. "Shear Strength of Sands During Rapid Loadings," Transactions, American Society

of Civil Engineers Vol. 128, Part I, 1963, pp. 1553-1594.

Whitman, R.V., "The Response of Soils to Dynamic Loadings; Report 26, Final Report," Contract Report No. 3-26, U.S. Army Engineer Waterways Experiment Station, 1970.

Whittaker, P. James, M.S. Thesis, University of Colorado at Boulder, Boulder, CO., 1987.

Wilson, S.D., and Sibley, E.A. "Ground Displacement from Air Blast Loading," Journal, Soil Mechanics and Foundation Division, American Society of Civil Engineers, Vol. 88, No.SM6, Dec. 1962, pp. 1-31.

END

12-87

DTIC